Cranfield University

Pauline Loilier

Numerical Simulation of Two-Phase Gas-Liquid Flows in Inclined and Vertical Pipelines

School of Engineering

Ph.D. Thesis

Cranfield University

School of Engineering

Applied Mathematics and Computing Group

Ph.D. Thesis

Academic Year 2005-2006

Pauline Loilier

Numerical Simulation of Two-Phase Gas-Liquid Flows in Inclined and Vertical Pipelines

Supervisor: Prof. Chris P. Thompson

August 2006

This thesis is submitted in partial fulfilment of the requirements for the degree of Doctor of Philosophy

BLANK IN ORIGINAL

Abstract

The present thesis describes the advances made in modelling two-phase flows in inclined pipes using a transient one-dimensional approach. The research is a developement of an existing numerical methodology, capable of simulating stratified and slugging two-phase flows in horizontal or inclined single pipes. The aim of the present work is to extend the capabilities of the approach in order (i) to account for the effect of the pipe topography in the numerical solution of the two-fluid model, and (ii) to simulate vertical bubbly two-phase flows at various pressures in large diameter pipes, and (iii) to model stratified and terrain-induced slugging in two-phase flow pipelines made of several uphill, downhill and level sections.

A transient compressible two-fluid model based on the one-dimensional form of the mass and momentum conservation equations for the gas and liquid phases, is developed to predict those flow configurations. The wall to fluid and the interphase interactions are accounted for by constitutive relations which are flow regime dependent. The conservation equations are discretized using a finite volume method.

An algorithm is created to enable simulations on pipelines made of several sections, and account for the effect of the topography in the simulations. The methodology is applied to the compressible model in order to evaluate the robustness and accuracy of the numerical schemes, especially for the high-resolution Advection Upwinding Splitting Method (AUSM) associated to the compressible model. It also assesses the ability of the method to predict three physical flow regimes, namely stratified, bubbly and terrain-induced slug flows.

The terrain-induced slugging study is performed on a slightly inclined ($\pm 1.5^{o}$) V-section system. The use of hydrodynamic slug correlations for hilly-terrain slugging is discussed. It shows to be conclusive with a good agreement with experimental measurements obtained for slug frequency and slug length predictions. Mechanisms such as the wave formation at the interface, the slug growth and propagation as well as merging slugs, can also be observed by the model. The bubbly model is extensively tested against available data collected by Nottingham University from experimental systems of $70mm$ and $189mm$ vertical pipes. In some cases, void fraction predictions are within 10% with experimental data, and pressure predictions within 4%. The simulation results compare well in overall with the measurements. In large diameter pipes, some variations are observed between the numerical and the measured results: especially the model underpredicts the flow at the

bottom of the pipe. Limitations of the model for this particular case are highlighted. It is also observed that, in fully-developed flows, the model does give satisfactory predictions.

Acknowledgements

This work has been undertaken within the Joint Project on Transient Multiphase Flows. The Author wishes to acknowledge the contributions made to this project by the Engineering and Physical Sciences Research Council (EPSRC), the Department of Trade and Industry and the following: - Advantica; AspenTech; BP Exploration; Chevron; ConocoPhillips; ENI; ExxonMobil; FEESA; Granherne / Subsea 7; Institutt for Energiteknikk; Institut Français du Pétrôle; Norsk Hydro; Petrobras, Scandpower; Shell; SINTEF; Statoil and TOTAL. The Author wishes to express their sincere gratitude for this support.

In addition, I would like to thank my supervisor, Prof. Chris Thompson, for having given me the opportunity to carry out research on multiphase flow modelling. I would like to thank him for his guidance, support and his encouragement.

I wish to express my immense gratitude to Dr Christian Omgba-Essama for his help, patience, "debugging support", proof-reading of the thesis and friendship throughout the years. He is the Thierry Henry of multiphase, and quite frankly, this would have taken much longer without his precious advices. Thanks a lot, Christian.

Special thanks are due, in no particular order, to my past and present colleagues and friends in the Applied Mathematics and Computing (AMAC) group: Stuart Barnes, Dulcéneia Becker, Jean Charpin, Alexandre Dugarry, Shan Fu, George Goudinakis, Mustapha Gourma, Ouahid Harireche, James Nelson, Hans-Dieter Reuter, Peter Sherar, Homa Sutherland, Julian Turnbull, Kath Tipping, Judith Weissinger, and Bo Xu. They have all contributed to make the group a very enjoyable place to work. A very special thanks is due to Rachael Wiseman for her extremely good work and patience with all of us. I would also like to thank Dr Lahcen Hanich for his rich guidance on multifluid modelling during the first two years. I am also very grateful to Dr Liz Wren and Karl Omebere-Iyari, from the School of Chemical, Environmental and Mining Engineering of Nottingham University, who kindly provided vertical flow experimental data. Finally, in the work section of my acknowledgements, my sincere thanks to Dr Mohammed Louaked and Dr Jean Lejeune, from the Département de Mathématiques et Mécanique de l'Université de Caen in France, without whom I would not have come to Cranfield.

Obviously, it would not have been quite the same without Aaron, Fatou, Jéjé, Pat and Yvos, whose friendship, laughters, discussions and coffee breaks were priceless throughout

the years. I will miss the Team!

A big thank you to all the friends back in France for their support and encouragement, and to everyone that I have known over the years at Cranfield University and from the Cranfield Volleyball Club, it made my student life a very memorable and special one.

Aaahh... I do not know how many times I thought about this very moment when the thesis will be written up, all wrapped up, ready for submission. To be honest, I have a hard time believing I did it (I guess the Viva is there to remind me it is not over yet!)... Something tells me I am not the only one not to believe it though. How many times have my family and close friends been answered "next month, I think... " to the fierce but legitimate question "when are you finishing?". And for the constant patience, the omnipresent and inexhaustible support they showed me thoughout the past few years, I am truly and endlessly grateful. A huge, enormous, oceansize merci to my parents and to Fafate, Tom, Mag, Claire and Jim for being there. Yes, it has been a long journey, especially last year, however "nothing is a waste of time if you use the experience wisely"[1].

[1]Rodin (1840 - 1917)

Contents

List of Figures

List of Tables

Nomenclature

Symbol	Definition	Unit
Roman		
A	Cross-sectional area of the pipe ($A = A_g + A_l = \pi D^2/4$)	$[m^2]$
A_g	Cross-sectional area of the gas phase	$[m^2]$
A_l	Cross-sectional area of the liquid phase	$[m^2]$
a_{ik}	Interfacial area concentration	-
B_{fk}	Body or gravity force of phase k	-
C_1	Coefficient used in the drag formulation	-
C_D	Drag coefficient	-
C_{D1}	Coefficient used for the drag coefficient formulation	-
C_{D2}	Coefficient used for the drag coefficient formulation	-
C_{D3}	Coefficient used for the drag coefficient formulation	-
C_{VM}	Virtual mass coefficient	-
c	Concentration term	-
c_1, c_2	Coefficients used for the pressure relaxation equation	-
c_k^2	Speed of sound of phase k	$[m.s^{-1}]$
D	Pipe diameter	$[m]$
D_b	Bubble diameter	$[m]$
D_{hk}	Hydraulic diameter of phase k	$[m]$
D_g, D_{hg}	Gas hydraulic diameter	$[m]$
D_l, D_{hl}	Liquid hydraulic diameter	$[m]$
dP/dx	Pressure gradient	$[Pa.m^{-1}]$
d_{sm}	Sauter mean diameter	$[m]$
Eo	Eotvos number	-
F	Vector of the physical flux terms	-
$\tilde{F}$	Vector of the numerical flux terms	-
F^c	Convective term numerical flux	-
F^p	Pressure term numerical flux	-
F_i	Interfacial shear force	$[Pa.m^{-1}]$
F_{wk}	Wall shear force of phase k	$[Pa.m^{-1}]$
Fr_k	Froude number of phase k ($Fr_k = V_{sk}/\sqrt{gD}$)	-

f_i	Interfacial friction factor	-
f_k	Wall friction factor of phase k	-
f_m	Friction factor used in drag formulation	-
G_k	Mass velocity of phase k	$[kg/(m^2s)]$
G_g	Mass velocity of gas-phase	$[kg/(m^2s)]$
G_l	Mass velocity of liquid-phase	$[kg/(m^2s)]$
g	Gravitational acceleration constant	$[m.s^{-2}]$
H	Matrix of non-conservative terms	
h_l	Liquid height	$[m]$
L_S	Length of the slug body	$[m]$
M_A, M_B	Matrices for system of equations	
M_j	Jacobian of the flux vector F $(M_J = \partial F/\partial U)$	
M_{ki}	Momentum transfer of phase k	
n_1	Coeffeicient used in the drag formulation	-
$P_k(x)$	Polynomial function of the k-index	$[Pa]$
P	Common pressure	$[Pa]$
P_c	Pressure correction term	$[Pa]$
P_g	Pressure of the gas phase	$[Pa]$
P_i	Interfacial pressure	$[Pa]$
P_k	Pressure of phase k	$[Pa]$
P_{ki}	Interfacial pressure of phase k	$[Pa]$
P_l	Pressure of the liquid phase	$[Pa]$
$P^{\pm}$	Split pressure functions	
R	Cross-sectional pipe radius	$[m]$
R_b	Radius of small bubbles	$[m]$
Re_k	Reynolds number of phase k	-
Re_g	Reynolds number of the gas phase	-
Re_l	Reynolds number of the liquid phase	-
Re_m	Reynolds number of the gas-liquid mixture	-
S	Vector of source terms	
S_i	Interfacial wetted perimeter	$[m]$
S_k	Wall wetted perimeter of phase k	$[m]$
T	Flow temperature	[Kelvin]
t	Time variable	$[s]$
U	Vector of conservative variables	
$\bar{U}$	Intermediate vector solution	
V_D	Drift velocity	$[m.s^{-1}]$
V_b	Bubble rise velocity	$[m.s^{-1}]$
V_k	Velocity of phase k	$[m.s^{-1}]$
V_i	Interfacial velocity	$[m.s^{-1}]$
V_g	Gas phase velocity	$[m.s^{-1}]$
V_l	Liquid phase velocity	$[m.s^{-1}]$
V_m	Mixture velocity	$[m.s^{-1}]$

V_{sk}	Superficial velocity of phase k ($V_{sk} = \alpha_k V_k$)	$[m.s^{-1}]$
V_r	Relative velocity ($V_r = V_g - V_l$)	$[m.s^{-1}]$
$\bar{V}_r$	Average local relative velocity	$[m.s^{-1}]$
$\tilde{V}^{\pm}$	Split velocity functions	
We	Mixture Weber number	-
X^2	Martinelli parameter ($X^2 = (dP/dX)_l/(dP/dx)_g$)	-
x	Space variable	$[m]$
Y	Inclination parameter	-
Z^2	Chilsholm parameter ($Z^2 = (dP/dX)_{g0}/(dP/dx)_{l0}$)	-

Greek

α_k	Volume fraction or holdup of phase k	-
α_g	Volume fraction or holdup of the gas phase	-
α_l	Volume fraction or holdup of the liquid phase	-
β	Pipe inclination	[rad]
χ_L, χ_R	Parameters (AUSM formulation)	
ΔP_{ki}	Pressure correction term of phase k	$[Pa]$
$\Delta\rho$	Density difference	$[kg.m^{-3}]$
Δt	Integration time step	$[s]$
Δx	Mesh spacing of the computational grid	$[x]$
ϵ	Tolerance	-
ϕ	Smoothing function (AUSM formulation)	
ζ	Parameter	
Γ_k	Mass transfer of phase k	$[kg/(m^{-3}.s)]$
κ_1, κ_2	Coefficients used for the function ϕ	-
λ	Characteristic value or eigenvalue	$[m.s^{-1}]$
λ_k	k^{th} characteristic value or eigenvalue ($k = 1, 2, \ldots$)	$[m.s^{-1}]$
λ_{max}	Maximum of the absolute value of eigenvalues	$[m.s^{-1}]$
λ_L	Non-slip liquid holdup	-
θ_i	Angle (pipeline interpolation)	[rad]
ρ_k	Density of phase k	$[kg.m^{-3}]$
ρ_g	Density of the gas phase	$[kg.m^{-3}]$
ρ_l	Density of the liquid phase	$[kg.m^{-3}]$
ρ_m	Density of the gas-liquid mixture	$[kg.m^{-3}]$
μ	Relaxation parameter	-
μ_k	Viscosity of phase k	$[kg/(m.s)]$
μ_g	Viscosity of the gas phase	$[kg/(m.s)]$
μ_l	Viscosity of the liquid phase	$[kg/(m.s)]$
μ_m	Viscosity of the gas-liquid mixture	$[kg/(m.s)]$
σ	Surface tension	$[N.m^{-1}]$
τ	Ratio timestep/mesh size	$[m.s^{-1}]$
τ_i	Interfacial shear stress	$[N.m^{-2}]$

τ_k	Viscous shear stress of phase k	$[N.m^{-2}]$
τ_k^{Re}	Reynolds or turbulent viscous shear stress of phase k	$[N.m^{-2}]$
τ_{wk}	Wall shear stress of phase k	$[N.m^{-2}]$
τ_{wg}	Wall shear stress of the gas phase	$[N.m^{-2}]$
τ_{wl}	Wall shear stress of the liquid phase	$[N.m^{-2}]$
ξ, ξ_0	Coefficients used for pressure correction terms	-
ω_s	Slug frequency	$[s^{-1}]$

Superscripts

D	Diffuse
AD	Anti-Diffuse
$AUSMD^\star$	AUSMD* numerical scheme
$AUSMV^\star$	AUSMV* numerical scheme
$AUSMDV^\star$	AUSMDV* numerical scheme
B	Basset
C	Collision
D	Drag or Diffuse (Chapter 4)
FCT	Flux Corrected Transport numerical scheme
$force$	First Order Centred numerical scheme
HLL	Harten Lax and van Leer scheme
L	Lift (Chapter 2, 3), Left state (Chapter 4 5)
LF	Lax-Friedrichs numerical scheme
R	Right state
Ri	Richtmyer scheme
$TVDLF$	Total Variation Diminishing (TVD) Lax-Friedrichs numerical scheme
TD	Taitel and Dukler
VM	Virtual Mass
$'$	First derivative
c	Convective flux term
n	Current time step
$n+1$	Next time step
p	Pressure flux term

Subscripts

gO	Gas Overall
lO	Liquid Overall
g	Gas phase
l	Liquid phase
m	Mixture gas-liquid
r	Relative

w	Wall
j	Cell centre index
$j+1/2$	Cell border index
$j-1/2$	Cell border index
acc	Acceleration term
$fric$	Frictional term
$grav$	Gravitational term
$crit$	Critical value
$visc$	Relative to the viscosity
x	Axial coordinate
$\langle\rangle$	Area-average

Acronyms

AMR	Adaptive Mesh Refinement
AUSM	Advection Upwinding Splitting Method
CFD	Computational Fluid Dynamics
CFL	Courant-Friedrichs-Levy number
EMAPS	Eulerian Multiphase Adaptive Pipeline Solver
FCT	Flux Corrected Transport
Force	First-Order Centred
FVS	Flux Vector Splitting
FDS	Flux Difference Splitting
IKH	Inviscid Kelvin-Helmholtz
PDE	Partial Differential Equation
PFM	Pressure-Free Model
SPM	Single Pressure Model
TFM	Two-Fluid Model
TMF	Transient Multiphase Flow
TPM	Two-Pressure Model
TVD	Total Variation Diminishing

1 Introduction

1.1 Overview

In this chapter multiphase flow is briefly introduced, together with a statement of its industrial significance. The most common interfacial arrangements or "flow patterns" are then described for horizontal and vertical flows. The focus is then quickly shifted to two-phase gas-liquid flow modelling, its importance and the different available techniques. Next, the most common methods are described which help to establish the position of two-fluid models within gas-liquid systems. Having examined where two-fluid models fit in, reasons are given for studying two-phase flows in multiple pipe systems, and particularly for a compressible two-fluid model. This leads to a statement of the main objective of the work presented in this thesis and a description of the strategy for meeting this objective. Based on this description, a brief summary of each chapter is finally presented together with details of how each one helps to reach this goal.

1.2 Multiphase flow

Multiphase flow is a common phenomenon. It occurs both in nature and in technology. One of the most trivial examples in nature is that of clouds which are composed of droplets of liquid moving as a gas. Examples where multiphase flow occurs in industrial applications include: energy conversion, paper manufacturing, food manufacturing and medical applications.

For the successful design and operation of any process plant, a knowledge of the chemical and physical properties of the materials being processed is essential. However, an understanding of the way these materials flow around the system is also essential since all processes at some point involve movement of material from one region of the plant to another. In many cases, the materials being processed do not flow as a single phase such as gas, liquid or solid. Instead complex combinations of two or more of these phases may predominate with gas-liquid, gas-solid, liquid-solid, liquid-liquid and even gas-liquid-solid flows commonly encountered. In particular, gas-liquid flows frequently occur in all types of process equipment from boilers and condensers to refrigerators, absorbers to heat exchangers and even within air-conditioners. They are also prevalent in many gas and oil

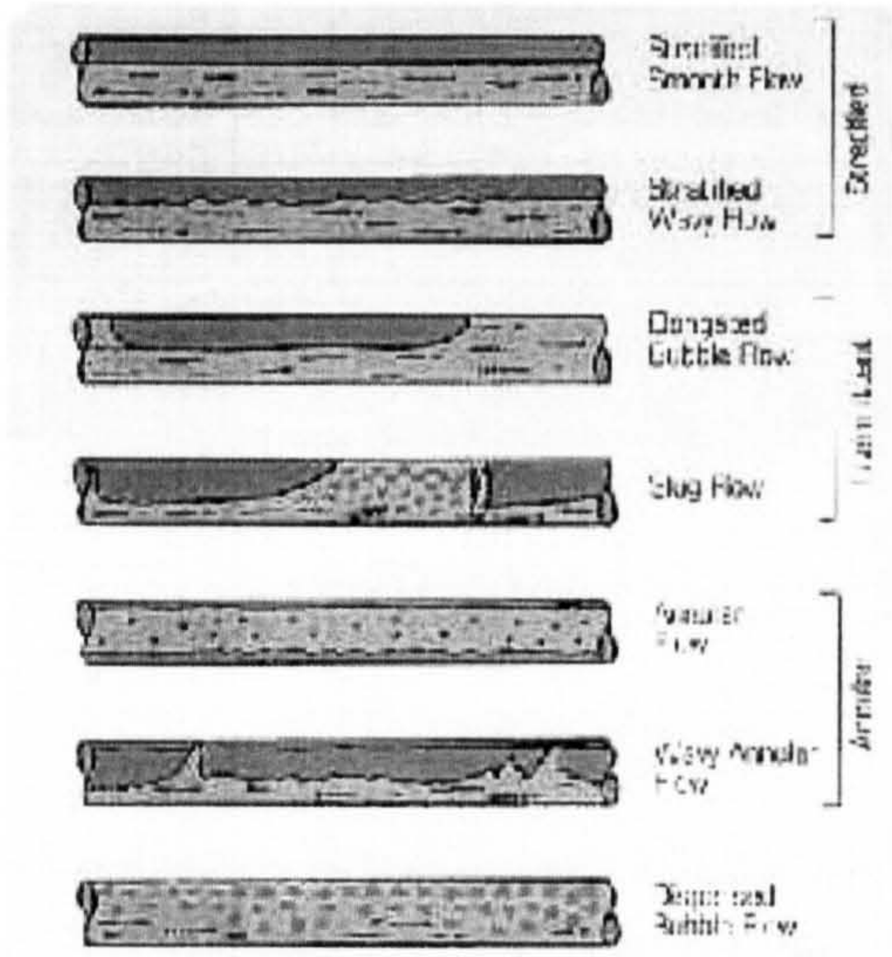

Figure 1.1 : *Different flow regimes in horizontal pipes.*

pipeline systems.

In addition to being the most common of the two-phase cases, gas-liquid flow is also the most complex since it combines the characteristics of a deformable interface with those of a compressible phase. This means that for a specified channel design and inclination and for given fluids fed into the system at known flow-rates the gas-liquid interface can arrange itself into a wide variety of forms. As a result, many investigators have concluded that, although theoretically possible, it is simply too difficult to solve the two-phase flow problem using the classic Navier-Stokes equations. This has led to the adoption of a phenomenological approach in which the flow distributions are classified into several different "patterns"; enabling the main characteristics of each distinct type of flow to be studied separately.

1.3 Flow patterns

There is no agreement of a general map with all flow regimes and it may differ from one author to another. One can define "new" regimes depending on small parameters. However, we tend to present in this section the main configurations usually referred to as in the literature.

Two-phase air-water flows can appear in different configurations, called *flow regimes* or *flow patterns*. These classifications are: separated, intermittent and distributed flow. The different flow regimes occurring in horizontal and nearly horizontal pipes are:

- Stratified: The two phases are separated by a curved mean interface (concave towards the gas) in a straight-pipe section. The shear between the gas and the liquid leads to wave formation when the velocity difference is high which is referred

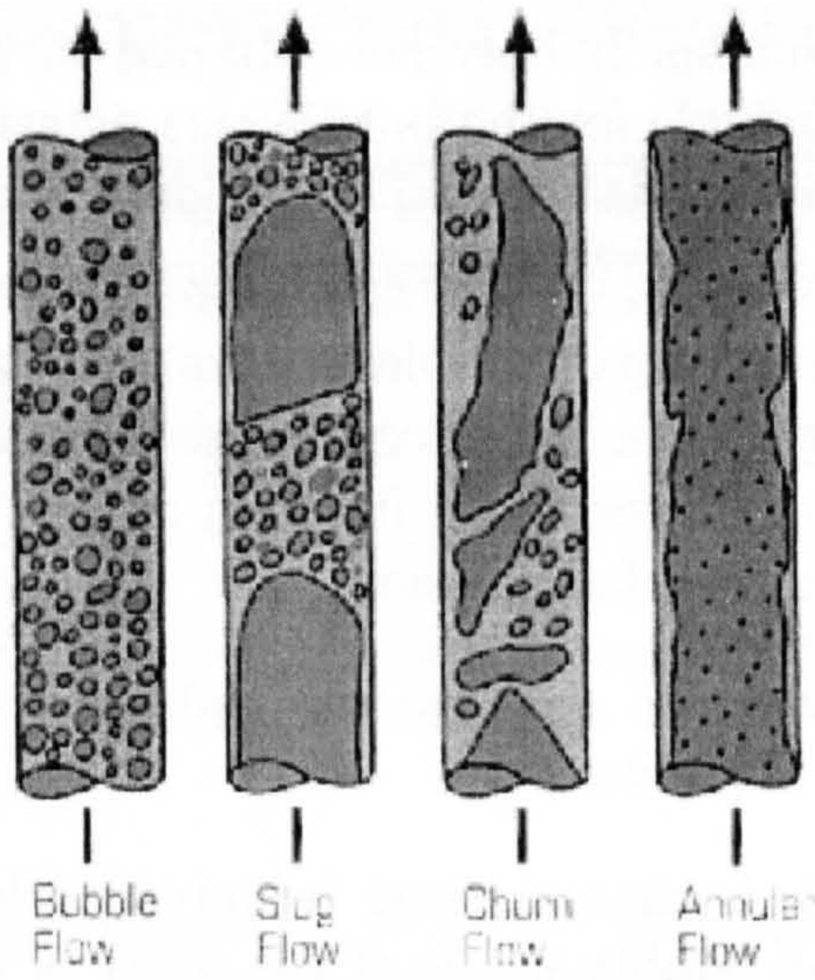

Figure 1.2 : *Different flow regimes in vertical pipes.*

to as *stratified wavy*. When in contrast, the interface is smooth, the flow pattern is called *stratified smooth*. Droplets can be present in wavy-stratified flow.

- Bubbly Flow: The gas is dispersed in the continuous liquid phase in the form of droplets. Most flow in the upper part of the pipe. However their pipe distribution becomes more uniform as the liquid flow rate increases.

- Slug or Intermittent Flow: Pockets of gas separated by regions of full-liquid are observed. Small gas bubbles appear in the liquid in each side of the slug.

- Plug Flow: Same regime as in *slug flow* with smaller gas bubbles.

- Annular Flow: This configuration can be seen as a particular case of stratified flow when the mean interface is cylindrical, with no contact with the wall. The gas flows in the center of the pipe, surrounded by the liquid phase which creates a film along the wall. This film may contain some gas bubbles. In the same way, the gas phase may carry some liquid droplets and even bigger liquid pockets. Some do differentiate these two annular regimes into two categories, respectively, *annular with droplets* and *wispy annular*.

The classification in vertical configuration is:

- Bubbly Flow: The liquid paths are continuous and contain a dispersion of bubbles. The gas or vapour bubbles are of approximate uniform size. Void fractions range from the extreme case of a single isolated bubble in a large container to the quasi continuum flow of foam. Different bubble shapes and trajectories can occur as a result of the interactions between forces due to surface tension, viscosity, inertia and buoyancy. It can be separated into two sub-regimes:

- Low-Reynolds Number bubbly flow. Liquid turbulence is absent or does not play an important role for the bubble size determination. Therefore inlet device, gas flow rate and interfacial effects determine the bubble size.
- High-Reynolds Number bubbly flow, also called finely dispersed bubbly flow. Assuming that break-up of bubbles occurs if the inertial forces due to turbulent eddies are stronger than the forces due to surface tension, the resulting maximum size can be expressed as a function of the turbulence energy dissipation, liquid viscosity and surface tension.

In this thesis, no turbulence is considered and thus there is no distinct separation between Low-Re and High-Re.

- Slug/Plug Flow: This is characterised by large pockets of gas, followed by large pockets of liquid. The bubble size is of the order of the pipe diameter, leading to a large rise in velocity of the gas phase. This flow regime is therefore strongly non-stationary. A falling film of liquid can be observed near the wall. A dispersion of smaller bubbles region through the liquid can be observed as well. The elongated bullet-shaped bubbles observed in this flow regime are called Taylor bubbles.

- Churn Flow: Increasing flow velocity breaks down the slug flow bubbles and leads to an unstable regime. Flow is of an oscillatory nature with the liquid near the outer tube wall continuously pulsing. This regime represents the transition between slug and annular flow.

- Annular Flow: This is characterised by a continuous phase all along the pipe, flowing in the pipe center. Liquid mostly flows along the wall as an irregular film and in droplets entrained in the gas core. When the liquid loading in the core is greater, the regime may be called *wispy annular*.

1.4 Two-phase gas-liquid flow modelling

In this thesis we are mainly concerned with analytical and numerical investigation of transient phenomena in long pipelines. Even if pipelines are designed to operate in steady-state conditions, transient phenomena can be observed in pipelines and occur from changes in the geometry or changes in the inlet flow rates. And there is a real need to be able to predict flow characteristics (current flow regime, fluid amounts, pressure drop, or liquid holdup) in the line. Certain flow configurations or flow regimes, such as slug flow, can pose serious problems to the operator and designer of two-phase flow systems. Large and fluctuating rates of gas and liquid can severely reduce the production and even shut down or damage equipment in the worst cases. As a result, prediction of flow characteristics is essential for an optimal, efficient and economically feasible design and operation of two-phase gas-liquid systems.

No consensus exists on modelling gas-liquid flow with an Eulerian approach. The main

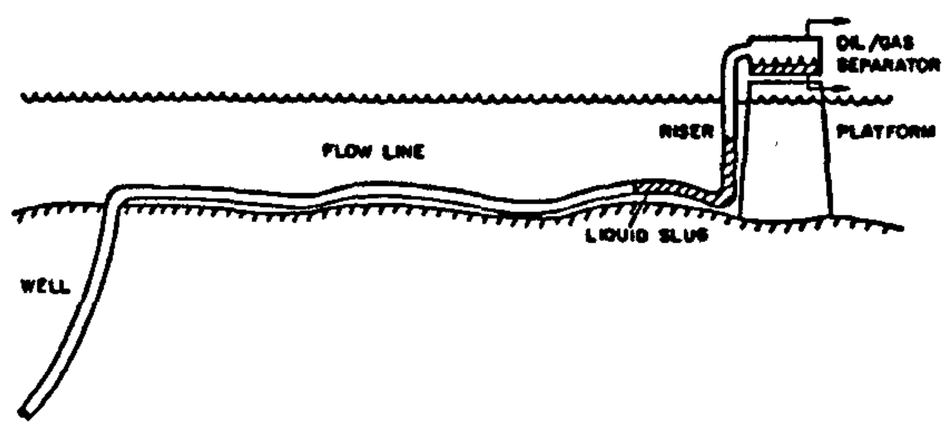

Figure 1.3 : *Schematic representation of a pipeline: from well to offshore.*

reasons account the complex phenomena to be modelled (phases interactions, chemical reactions, interfacial forces,...), and the numerous different flow configurations. All Eulerian models are a simplification of the instantaneous local formulation. This formulation describes two-phase flow as monophasic domains with mobile boundaries or interfaces between each phase. The monophasic regions are described with the Navier-Stokes equations and the interfaces are expressed by algebraic and evolution laws. One should notice that this formulation assumes the position of interfaces as an unknown. This formulation is tedious to use for the purpose of the approximation of two-phase flow; in the case of bubbly flow, for instance, the number of interfaces is a radical obstacle and the characteristic scale of bubbles is too small for the current approximation methods. Therefore to overcome this restriction, we looked at two different ways already existing, that enable the modelling of two-phase flow with the numerical methods developed nowadays. The first one consists of only using the equation of the mixing two-phase (mono-fluid model). The second one uses the averaging technique on the Navier-Stokes equations to obtain the phase quantities weighted by the volume fraction of each phase (two-fluid model).

The study of bubbly flow in vertical pipes is particularly challenging for computational schemes and resolving it accurately will provide a reliable tool for future predictions since this is the common flow of vertical configurations. In the past, bubbly flow has been considered with homogeneous or averaged-mixture models [5, 8] in the mid 70s. Current models include equations for each phase and are referred to as two-fluid models. The derivation of this class of model was carried out by many researchers [6, 2, 13]. Transfer terms are usually unknown and one requires some additional consideration for their formulation (experimental data or simplified models). They differ from one model to another depending on which flow regime is being investigated.

The present study investigates a two-fluid model using a two-pressure approach. Single-pressure models assume constant pressure across the fluid medium, while in two-pressure models, distinct pressure is assumed for each phase. Many contributions with this approach exist in the literature such as Baer and Nunziato [1], Saurel and Abgrall [13] or Glimm *et al.* [3]. This approach is chosen in this work for its mathematical properties as well as its physical representation.

A serious problem in the development of two-phase two-component flows is that in many circumstances the basic set of equations is ill-posed in the sense that the solution does not depend continuously on the initial data and has, as a consequence, complex characteristics. Considerable literature exists concerning the modelling of such problems. The ill-posed nature can be removed either by the addition of small second order viscous terms (Trapp and Ransom, 1982; Doster, 1996), by a pressure correction (Sainsaulieu [11, 12]) or by adding virtual mass terms (Tiselj [14]). Ramshaw and Trapp [9] or Hancox et al. [4] consider a two-pressure model which includes interfacial pressure relationships. Real characteristics were found at low volume fractions of the dispersed phase. Ransom and Hicks [10], or, Saurel and Abgrall [13] supplemented the standard set of equations by adding a void fraction propagation equation. Real characteristics were obtained; the physical motivation of the void fraction propagation equation seems still unclear but provides a real interest, and is the approach retained in this study.

1.5 Principal objectives of this project

This work is related to the Transient Multiphase Flows (TMF) project, funded by the UK Engineering and Physical Sciences Research Council (EPSRC) and by the Oil and Gas industries and their contractors. The aim of this programme is to improve the oil and gas industry's tools for the prediction, design and optimisation of pipeline transportation and process plants.

The aim of this thesis is the mathematical simulation of two-phase gas-liquid flow with the Finite Volume method. More precisely the purpose is to extend the capabilities of the Eulerian Multiphase Adaptive Pipeline Solver (EMAPS) in order to take into account the pipeline topography effect in the computations, and to simulate vertical two-phase bubbly flows in large pipe diameters.

1.6 Strategy

In the petroleum industry, the transport of multiphase flows usually occurs in elaborate pipelines which go from the extraction point, where the natural source is, to the shore, where the substances are being processed. By their topography, pipelines induce various flow configurations, or flow regimes, some of them such as slug flow being crucial to avoid considering damage that may result. Therefore it becomes essential to produce a reliable tool that can predict flows along any pipeline geometry.

Since any attempt to model complex two-phase flow regimes with an incompressible approach is too restrictive, a more detailed description is required instead. This description needs to take into account the gas compressibility in the flow, as it becomes a requirement when modelling certain flow regimes, such as slug or bubbly flows.

The most popular technique is the two-fluid approach which represents a more general model for two-phase flow by considering each phase separately and allowing to distinguish

between the velocity and pressure of each phase. Examples of two-fluid models range from incompressible, single-pressure and two-pressure models.

Although existing single-pressure models are adequate to predict many situations, they are limited to a certain range of validity where the set of equations remains well-posed. By envisaging a two-pressure approach, leading to an extra equation in the model but increasing the domain of validity, improved transient models may be developed.

Consequently to provide information on these operations, this project was divided into several distinct parts:

- Development of an accurate mathematical and numerical model for transient two-phase bubbly flow in vertical pipelines and the evaluation of its limitations.

- Robust and accurate discretisation can significantly allow better predictions of the behaviour of the system. Therefore a relative review of different numerical schemes and their behaviour was performed, and the developement of an existing advanced high-resolution method was investigated.

- Design and development of an algorithm that will efficiently interpolate any geometry and enable simulations on pipelines with such topologies. Application to slugging in V-section pipe system was studied.

Therefore, as a final objective of this research, we will simulate the transient behaviour of two-phase flow in vertical risers and inclined pipe systems.

1.7 Summary of subsequent chapters

In Chapter 2, a physical description of the two-phase flow phenomenon in pipelines is given followed by a review of the current capabilities for modelling two-phase flow in pipelines. More precisely, upward vertical flow and bubbly flow regime are detailed as well as the current flow regime transition models. The formulation of the two-fluid model for one-dimensional isothermal flow is also presented in the chapter.

In Chapter 3, a detailed description of the two mathematical models is presented, their basic conservation equations are derived and the constitutive relations required to close the equation set are given. The first model considers no phase pressure in its formulation and was mainly used for stratified approximation, and for the validation of the geometry algorithm presented in Chapter 5. The model used for transient two-phase bubbly flow and terrain-induced slugging is a compressible two-fluid model with five equations. Its main feature is that the phase pressures are not assumed equal at all points and at all times, contrary to many models used in commercial codes. Basically a relaxation term makes it possible to recover the equilibrium in an infinitely short time. However, the first attempt to obtain a simple compressible two-fluid model led us to consider instantaneous pressure relaxation, which arguably revealed the model to become a single-pressure model.

And yet it is still remarkably interesting to use such a model, since the characteristics of the system remain easier to compute than for other models. The first section deals with the general process to obtain the governing equations which covers the assumptions made, the averaged equations and the additional relations to close the system. At the same time, we study the hyperbolicity of both models and the stability limit is presented in Appendix C.

Chapter 4 deals with the numerical model and solution procedure developed, implemented and employed to solve the mathematical models. The first part describes the explicit finite volume approach adopted in this work. The conservative flux schemes applied to the models are also reported in this chapter, as well as the numerical schemes for the non-conservative terms required in some two-phase flow models. Constraints on time step and boundary condition treatment are also examined. These issues are fundamental in most numerical schemes in order to ensure convergence to a reliable solution. The final section examines the results from classical benchmarks simulations used to validate two-phase flow models implemented in this study. This corresponds to a note [7] presented to the 12^{th} *International Conference on Multiphase Production Technology* held in Barcelona, Spain, from 25 to 27 May 2005 (co-written with Christian Omgba-Essama and Chris Thompson).

Chapter 5 focuses on the algorithmic technique used to interpolate pipelines, and solve physical problems on any topology. It is split into three parts. The first one describes in detail the algorithm and its implementation into the code. It also stresses some issues that occurred during the realisation of this stage. These issues are highlighted and discussed in the next part where we present some tests about the single-phase problem of Shallow-Water equations. The final part presents the results from two-phase flow simulations performed on pipelines with small inclination change. Stratified flow on a downhill elbow pipeline is first reported with a comparison between compressible and incompressible models answers. To close the chapter, we present the validity of the compressible model to predict the complex features of two-phase terrain-induced slugging. Review of slug flow key parameters and the numerical approaches to this complex flow regime is presented. The analysis of the numerical predictions of a terrain-induced slugging case is performed and compared with available numerical and experimental data.

Chapter 6 presents the validation of the compressible model for bubbly flow. Predictions for steady-state and transient gas-liquid bubbly flow in vertical pipelines are compared to available numerical and experimental data. Validations for two-phase air-water mixtures on a 70mm-diameter pipe are investigated, followed by large pipe diameter (189mm) predictions for naphtha-nitrogen flows. Assessment on some required closures are also discussed in the chapter.

The main conclusions are summarised in Chapter 7. Suggestions as to how this work could be usefully extended are also discussed in this chapter.

References - 1

[1] BAER, M., AND NUNZIATO, J. A two-phase mixture theory for the deflagration to detonation (ddt) transition in reactive granular materials. *Int. J. Multiphase Flow 12-6* (1986), 861–889.

[2] CHENG, L., DREW, D., AND LAHEY JR, R. An analysis of wave propagation in bubbly two-component, two-phase flow. *Journal of Heat Transfer 107* (May 1985), 402–408.

[3] GLIMM, J., S. D., AND SHARP, D. Two-phase modelling of a fluid mixing layer. *Journal of Fluids Mechanics 378* (1999), 119–143.

[4] HANCOX, W. T., FERCH, R. L., LIU, W. S., AND NIEMAN, R. E. One-dimensional models for transient gas-liquid flows in ducts. *Int. J. of Multiphase Flow 6*, 1-2 (Feb-Apr 1980), 25–40.

[5] ISHII, M. *Thermo-Fluid Dynamic Theory of Two-Phase Flow.* Ph.D. thesis, Eyrolles Press, Paris, 1975.

[6] LAHEY JR, R., AND DREW, D. The virtual mass and lift force on a sphere in rotating and straining inviscid flow. *Int. J. of Multiphase Flow 13* (1987), 113–121.

[7] LOILIER, P., OMGBA-ESSAMA, C., AND THOMPSON, C. Numerical experiments of two-phase flows in pipeline with a two-fluid compressible model. In 12^{th} *International Conference on Multiphase Production Technology, Barcelona, Spain* (25-27 May 2005).

[8] NIGMATULIN, R. *Dynamics of multiphase media.* Hemisphere, New York, 1991.

[9] RAMSHAW, J., AND TRAPP, J. Characteristics, stability and short- wavelength phenomena in two-phase flow equation systems. *Nuclear Science and Engineering 66* (1978), 93–102.

[10] RANSOM, V., AND HICKS, D. Hyperbolic two-pressure models for two-phase flow. *Journal of Comp. Phys. 53* (1984), 124–151.

[11] SAINSAULIEU, L. *Contribution à la modélisation mathématique et numérique des écoule- ments diphasiques constitués d'un nuage de particules dans un écoulement de gaz.* Thèse d'habilitation, Université Paris VI, France, 1995.

[12] SAINSAULIEU, L. Finite volume approximations of two phase-fluid flows based on approximate roe-type riemann solver. *J. Comp. Phys. 121* (1995), 1–28.

[13] SAUREL, R., AND ABGRALL, R. A multiphase godunov method for compressible multifluid and multiphase flows. *Journal of Computational Physics 150* (1999), 425–467.

[14] TISELJ, I., AND PETELIN, S. Modelling of two-phase flow with second-order accurate scheme. *J. Comp. Phys. 136* (1997), 503–521.

2 Two-phase flow modelling

2.1 Overview

The purpose of this chapter is to familiarize the reader with the problem of two-phase flow in pipelines and to review the current capabilities for modelling two-phase flow in pipelines.

The chapter reviews the current technology for modelling two-phase flow in pipelines with an accent on upward vertical flow and bubbly flow regime. The various models for flow regime transitions are briefly described in Section 2.2, followed by a discussion of state-of-art steady-state and transient two-phase flow models (Section 2.3). In Section 2.4, a brief review of bubbly flow modelling in upward vertical flow is provided. The formulation of the two-fluid model for one-dimensional isothermal flow closes the chapter.

The purpose of this literature review is to highlight the limitations and deficiencies of existing two-phase flow models.

2.2 Transition models

It is recognised that accurate predictions of liquid fraction and pressure drop for two-phase flow in pipelines cannot be obtained without some means to determine the flow regimes. Dukler [24] suggested that only three basic flow regimes exist: separated, intermittent and dispersed, the other flow patterns being a combination of the three basic regimes. The separated flow pattern usually includes the stratified smooth and wavy regimes and the annular regime. The intermittent flow regime comprises slug flow and elongated bubble flow. The dispersed flow pattern encompasses liquid droplets in the gas and gas bubbles in the liquid phase. A full description of the structure of possible flow regimes can be found in Taitel and Dukler [57].

There are essentially two approaches to predict flow regime transitions. On one hand, flow regime maps obtained from visual observations of experiments. The transition boundaries are then mapped using a coordinate system based on the phases superficial velocities. Such maps were given for instance by Mandhane *et al.* [41] for horizontal flows and by Spedding and Nguyen [54] and Barnea *et al.* [3] for vertical and inclined flows. Such flow regime

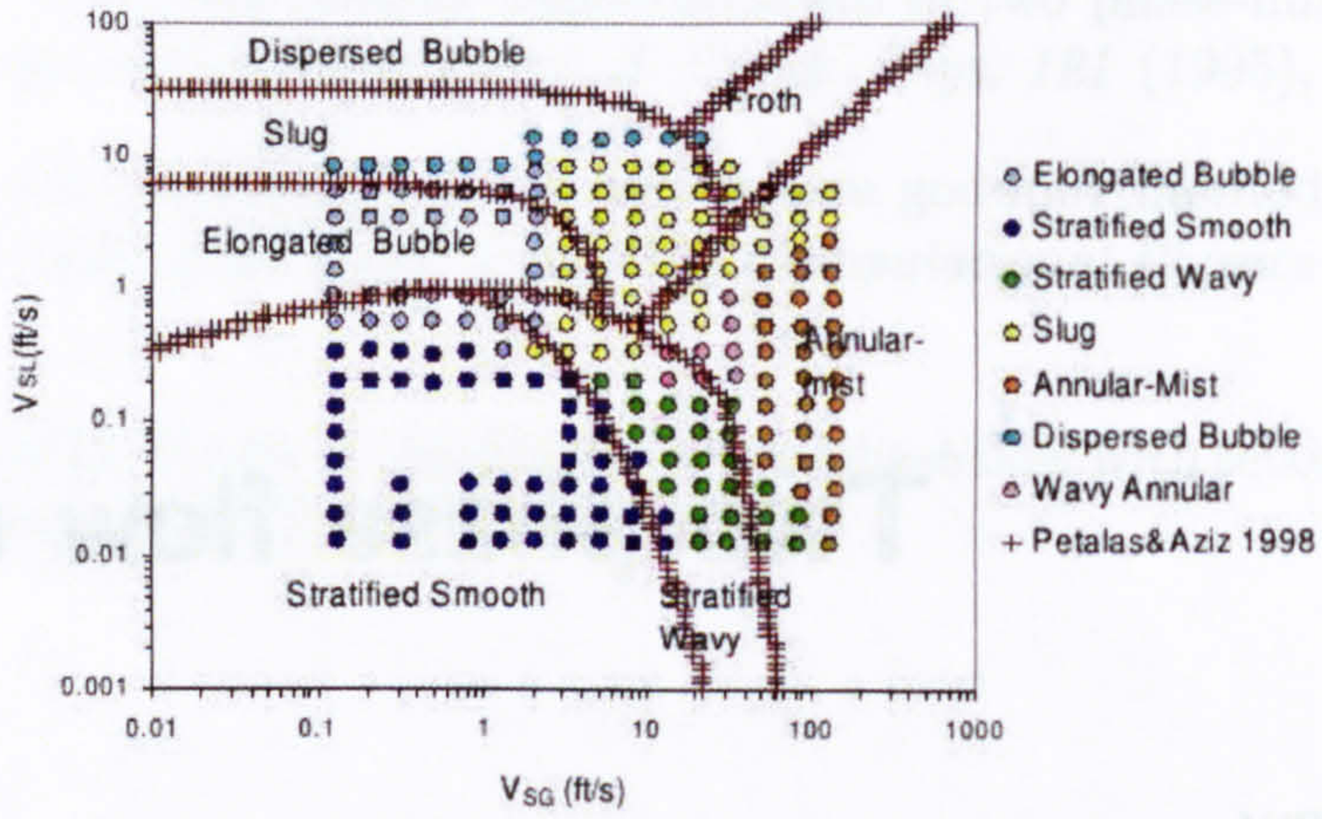

Figure 2.1 : *Example of flow regime map: comparison of transition boundaries [9] (air-water system, horizontal flow, $D = 1.0inch$).*

maps are not universal in that position of the transition boundaries varies with the pipes diameter and inclination, as well as with the fluid properties. It is therefore mainly useful as a tool to validate empirical and theoretical models.

On the other hand, flow regime transitions are based on the development of either empirical correlations or analytical expressions which represent the transition lines. Mukherjee and Brill [45] presented empirical equations to predict flow patterns for downward vertical and upward vertical pipe flows. Their correlations obtained by fitting the best curves through experimental data, predict the influence of the pipe inclination on the flow regimes boundaries. Comparisons with their predictions and experimental data of other workers indicated a good agreement.

In the analytical approach, the flow regime transitions are derived from balances of the physical forces responsible for the distribution of the phases. The forces considered are friction, gravity, lift, buoyancy and forces resulting from turbulence fluctuations. Taitel *et al* [57] proposed such models for flow transitions in horizontal [57] and vertical [56] tubes. Subsequently, Barnea [2] published extensions of these models, adapting them to flows in the whole range of pipe inclinations. Recently, Petalas and Aziz [48] published a mechanistic model which encompasses all the relations that were proposed in the earlier publications.

The advantage of the analytical over the empirical model for predicting flow regimes lies in the fact that less empiricism is involved. Empirical techniques are accurate when conditions in which they are applied are similar to the ones for which they were developed. It is therefore expected that analytical models would be more accurate for a wider range of situations.

With regards to flexible risers problem, accurate predictions cannot be obtained if the

correct flow regime is not determined. Hence flow regime transition models are essential.

2.3 Two-phase flow modelling

A fundamental problem to the theory of two-phase flow is the interface and despite the fact that each flow regime has a distinct average interfacial topology, the interfaces can fluctuate in space and time. Therefore it has to be mathematically and numerically treated with rigour.

Mainly two approaches are used: Eulerian-Eulerian models, or Eulerian-Lagrangian models [34, 19]. Eulerian approach defines the particle characteristics at each node of the grid, whereas Lagrangian description follows a single point moving at its own (independent) velocity. In the Eulerian-Lagrangian method, the dispersed phase is treated from a Lagrangian point of view and the continuous phase from an Eulerian point of view, with effects of the dispersed phase taken into consideration in the source terms of the constitutive equations. The Lagrangian approach gives a direct physical interpretation of the fluid-particle interaction and is not subjected to the numerical diffusion. Due to the fact that it models the particles as volume-less points, it is not suited for applications where the volume fraction of the dispersed phase (number of bubbles) is high [6]. We choose an Eulerian-Eulerian approach, mainly because Eulerian approach allows to deal with both phases with a consistent numerical scheme on a consistent numerical grid which becomes a distinct accuracy advantage in two-way coupling and can reduce the computational costs. The two-fluid model in which each phase is seen from an Eulerian point of view, is a common Eulerian-Eulerian approach of two-phase flow modeling. The phases are considered as two mixed continua, where local averaged quantities for each phase is defined at each point of the physical space. The two-fluid approach is the method chosen in this study.

Besides the standard models, applicable for a large range of flow patterns, there are models dedicated to specific two-phase flow patterns. Such models include bubbly gas/liquid flows which are characterized by a strong coupling between the phases due to rapid interphase transfers of mass, momentum and energy. The large velocity differences cannot be sustained and the assumptions that the phase pressures and the phase temperatures are equal at any cross-section appear consistent with experimental observations.

The more or less established models for two-phase flows include continuity, momentum and energy equations for each phase. They are obtained by averaging the single-phase equations over space and time and result in additional terms that describe the phase interactions. They are the mass transfer terms in the continuity equation, the momentum transfer terms in the momentum equations and the heat or energy exchange transfer terms in the energy equations. Since their exact expression is most of the time unknown, additional considerations, from experimental data or simplified models, are required to

formulate them.

The next step consists of writing the local instantaneous conservation equations for mass, momentum and energy separately, for each phase, with the appropriate transport properties. Averaging techniques lead to a set of equations that approximate the mean values of the desired flow variables and interfacial transfer effects. Four different averaging techniques are proposed in the literature [30, 20], spatial (volume or area averaging) without time averaging, time averaging without spatial averaging, ensemble averaging with no spatial average and ensemble/space averaging or time/space averaging. Despite their significant variations, they usually lead to the same forms of averaged balance equations. An ensemble average is more general than the other techniques [20] and is the technique retained in this work. It generally leads to a full set of three-dimensional equations. Since in the petroleum industries, pipelines are much longer than wide, a one-dimensional approach is considered, obtained by integrating the set of equations over a cross-section. Note that averaging techniques do lose some information from the equations and therefore some extra constitutive equations, called *closure relations* have to be supplied to the set of equations.

These constitutive relations are functions of the fluid velocities and their local properties and the two-phase flow regime. They gather together pressure terms (phase pressures, interfacial pressure and pressure correction term), wall shear force and interfacial force terms (drag, lift, virtual mass). They may contain derivative terms that would change the formulation of the general two-fluid model and are discussed more in detail in this chapter and in Chapter 3.

2.3.1 Steady-state models

Many two-phase flow calculation methods used by the petroleum industry rely on steady-states models. The performance of a complete pipeline made of several uphill and downhill sections is obtained by analysing section separately. The inlet volume flow rates of any given section are based on the local fluid densities and on the pipeline inlet mass flow rates. From the volume flow rates and the local fluid properties, the flow regime, the pressure drop and the liquid holdup in the section are determined from the empirical or mechanistic models for steady-state two-phase flow.

The development of empirical correlations for pressure drop and liquid holdup evolved from flow regime independent methods [38] to more accurate methods which are flow regime sensitive [5]. Many of the original correlations are based on experimental data for horizontal and vertical flows; in the case of inclined pipes, modified vertical flow correlations are frequently used. Mukherjee and Brill [45] developed empirical pressure drop and liquid holdup equations for inclined pipes from experimental data for inclination angles ranging from $-90°$ to $+90°$. This model yields reasonable agreements with steady-state field data.

Mechanistic models for steady-state two-phase flow in pipelines are based on the mass

and momentum conservation equations for the gas and liquid phases. These models are flow regime dependent. For stratified flow, for instance, models have been developed for pressure drop and liquid fraction using the simple one-dimensional form of the momentum equations for each phase [1, 57].
Models for bubbly flow are commonly obtained from a one-dimensional analysis and assume the gas phase velocity is equal to the summation of the liquid phase velocity and a rise velocity due to bubble buoyancy. Rise velocities for bubbles of different shapes and sizes have been derived by Ishii and Zuber [33]. This relationship between the gas and the liquid phase velocities fixes the liquid fraction for a steady-state bubbly flow.

Although obtained from basic conservation principles, all mechanistic models depend on empirical correlations for their closure relationships. The reliability of such models is therefore strongly related to the accuracy of these closure relationships.

2.3.2 Transient models

The equations of motion of a Newtonian flow are given by the Navier-Stokes equations. These equations depend on the three-dimension of space and time. When multiphase flow occur in pipelines, the problem is usually formulated in a one-dimensional framework with respect to the pipe axis, since pipelines are much longer than wide. Basically, the single-phase Navier-Stokes equations in each phase are averaged with a procedure through which the multi-dimensional case is reduced to one spatial dimension. The flow characteristic variables such as the density, the velocity, or the temperature are averaged on a transverse pipe section, assumed circular in the case of pipelines.

Mathematical models for two-phase flows range from homogeneous models to multi-field models. A usual approach in two-phase flow modelling is to average the local instantaneous conservation laws (time-, space- or ensemble-averaged). And this set of averaged equations can be written for each field (or fluid). This approach simplifies the mathematical aspects of the equations, but will lose some informations about the local gradients at interfaces and walls. Therefore, closure relations have to be provided for interfacial and wall transfer of heat, mass and momentum.

A simple model is the *homogeneous model* that treats the two-phase mixture as a pseudo-fluid. The model properties are determined by the relative quantity of each phase [44, 50]. It is built from the mass, momentum and energy conservation equations of the mixture. Another equation usually given by either gas or liquid mass conservation is added to complete the system. This formulation is only valid when the two phases have the same temperature and the same velocity. It is a reasonable assumption when the flow is really dispersed and where the slip velocity is not important.

In order to get a relative gas velocity with respect to the liquid phase, the model must be built with two different velocities. The simplest approach is the *drift-flux model* [68, 30]. It is built from the same conservation equations as the homogeneous model, but the closure equation is given by a *slip law* between the two phases. This closure equation can

have different forms: it can be a correlation of the liquid holdup, an empirical relation on the gas velocity, or a slip law between the two phases. All these equations assume a steady-state flow.

One major advantage of drift-flux models is to eliminate the need to model the interactions at the interface, such as the momentum transfer or the effects due to the interfacial pressure. However, a more rigorous approach is given by the *two-fluid method* where the velocities and/or the pressures of each phase are distinct.

Two-fluid models enable both mechanical and thermal non-equilibrium to be taken into account and represent a more general model for two-phase flow. The two-fluid model can be seen as a separated-fluid approach for Eulerian description. It assumes that both the carrier phase (liquid) and the particle involves two separate but inter-mixed continua. This representation does not keep track on the individual bubble but represents volume-averaged description of each element of the domain. Therefore it accounts for relative inter-phase velocity and temperature differences. The treatment of these inter-phase expressions have to be dealt with when modelling two-phase flows.

Two-fluid models allows to account two distinct velocities and also different pressures. Several forms have been developed: pressure-free models [65], where the pressure does not appear in the equations (global momentum equation), single-pressure models [55], in which the two phase pressures are assumed to be equal and two-pressure models, which consider two different pressures [47, 53, 51] by introducing a local constitutive relation that accounts for this pressure difference due to dynamic and interfacial effects.

2.4 Vertical flow modelling

The purpose here is not to enumerate all the models presented in the literature for two-phase vertical flow with application to bubbly flow but to briefly show the various approaches adopted by researchers for modelling these flows configuration.

In Eulerian methods, a general transient two-phase flow problem can be formulated by using a two-fluid model or a drift-flux model, depending on the degree of the dynamic coupling between the phases.

To account for the velocity differences between the phases induced by gravity and centrifugal forces, a model has been developed that uses a single momentum equation with an additional term to represent the effect of velocity differences between the phases. Depending on the formulation of the constitutive equations used to determine the velocity differences, the model has various names in the literature, however it shall be referred to as drift-flux model in the rest of the thesis. The notable feature of the drift-flux model is that the restriction on equal phase velocities is relaxed and the momentum exchange between the phases and the pipe is modelled separately with different gas and liquid velocities. The relaxation of equal velocities is most important when the densities between the phases are quite different in the presence of a gravitational potential field or large pres-

sure gradients. It has first been introduced for two-phase flow by Zuber and Findlay [68] and Ishii [30]. Because of its simplicity and applicability to a wide range of practical interest, the drift-flux model has been and is still studied extensively [28] and is used in some current commercial codes. The governing equations for the drift-flux model are not presented here, but can be found in the thesis by Théron [58] as well as in numerous articles [68, 42, 52].

In his drift-flux model, Ishii [30] developed a simple correlation for upward two-phase flow and was the first to consider fully developed bubbly flow. He assumed that the distribution parameter would depend on the density ratio and on the Reynolds number. He proposed drift velocity correlations for four regimes: bubbly, slug, churn and annular flow. Later, Hibiki and Ishii [28] modified the constitutive equations of the distribution parameter for vertical bubbly flow by introducing the bubble dynamics. They concluded that a dominant factor to determine the distribution parameter in vertical upward flow was the bubble diameter. The drift-flux model has been extended to study vertical upward pipe in large diameter pipes by Hills [29], Ishii and Kocamustafaogullari [31] and Hibiki and Ishii [28]. More details on general drift-flux applications can be found in Pauchon, Masella [42], Ishii and co-workers [30, 28] and Zuber and Findlay [68].

The drift-flux model is widely used in the literature however it is an approximate formulation in comparison with the more rigorous multi-fluid formulation. The two-fluid model is generally formulated by a set of conservation equations governing the balance of mass, momentum and energy of each phase. In the formulation of the model, the transport processes of each phase is expressed by their own balance equation. Therefore it can be expected that the model can predict more detailed changes and phase interactions than a mixture model such as the drift-flux model.

Several authors have investigated the application of a two-fluid model for two-phase bubbly flow. Basically these studies differ in the formulation of the interfacial momentum transfer and more precisely in the formulation of the standard drag force. The momentum transfer is often formulated as combination of the following forces:

$$M_{ki} = F_D + F_{VM} + F_L + F_C \tag{2.1}$$

where the subscripts D, VM, L and C stand for the steady-state drag, virtual mass, lift and collision forces respectively. Bubbly flow models usually contain a drag force (except in Chung *et al.* [11, 13, 15, 14, 12] where only virtual mass forces coupled with an interfacial pressure jump terms are considered) and the interfacial momentum transfer often combines the drag force with either the virtual mass, lift and/or collision forces. The non-drag forces will be discussed in more details later in the chapter and in Chapter 3. Due to the derivative terms in their formulation, the addition of some of the non-drag forces in the model will modify the nature of the systems of governing equations (hyperbolicity) and thus the stability of the model. Some of them are reported to have a small effect in the simulation [10, 43], and including these forces in the momentum transfer may not always be required. Hence, in this study, we will only consider the drag terms in the

formulation of the interfacial momentum transfer. Drag forces are of great importance when modelling two-phase flow and despite this fact, the formulation is not always known accurately. The standard drag force approach varies significantly from researchers and can be classified for bubbly flow into two categories presented below.

A first group of studies (Ishii and Mishima [43], Tomiyama *et al.* [60], Park *et al.* [46], Cheng *et al.* [10], Drew *et al.* [21, 35, 36], Geurst [25], Chahed and Masbernat [8], Drew and Lahey [22], Lopez de Bertodano [39], Lucas *et al.* [40], Politano *et al.* [49]) follows the approach where the standard drag is function of the dimensionless drag coefficient which depends on the gas volume fraction, the bubble diameter, the liquid viscosity and the relative velocity:

$$F_D = \frac{3}{4}\frac{\rho_l \alpha_g C_D}{D_b}|\bar{V}_r|\bar{V}_r. \tag{2.2}$$

As pointed out by Ishii *et al.* [32], the weakest link in two-fluid model formulation is the constitutive equations for the interfacial interaction terms and the difficulties arise due to the complicated motion and transitions of the flow pattern of gas phase. It is therefore indispensable to introduce constitutive relations for interfacial transfer terms, in particular the drag correlation and interfacial area concentration. Hence, with his approach, Ishii led to the development of a second class of two-fluid models which introduce the interfacial area per unit volume in the interfacial transfer terms (Ishii and Mishima [32], Ishii and Kocamustafaogullari [31], Delhaye [18], Wu *et al.* [66], Hatta *et al.* [26], Fu *et al* [27], Lhuillier *et al.* [37]). All the phase interaction terms in the governing equations can be written as a product of the interfacial area concentration a_{ig} and the driving force, where the interfacial area concentration specifies the geometric capability of the interfacial transfer. Since the interfacial area depends upon the two-phase structure, it changes dramatically following the two-phase flow regime evolution. For each model following this approach, the interfacial area concentration a_{ig} mainly accounts in the formulation of the standard drag force as follows:

$$F_D = \frac{1}{8}\rho_l a_{ig} C_D V_r |V_r| \tag{2.3}$$

where a_{ig} is flow regime dependent and for instance, is given for bubbly flow as:

$$a_{ig} = \frac{6\alpha_g}{d_{sm}} \tag{2.4}$$

where d_{sm} is the Sauter mean diameter. More details are given in Chapter 3.

The main advantage of using the interfacial area method over another one is the capability it provides for vertical flow transition modelling. Indeed, one can formulate a different interfacial area concentration a_{ig} for each flow regime which offers having to modify only one term in the interfacial momentum transfer to switch from flow regimes.

In this section, a brief description of general two-phase flow modelling tools and the current

available approaches for modelling bubbly flow in vertical upward flow is presented. The purpose was to review the actual capabilities in the process of developing a model for two-phase flow in upward vertical pipes. The next section describes in more details the one-dimensional two-fluid model and the additional closure laws required by this approach.

2.5 The two-fluid model

As discussed earlier in this chapter, of the different two-phase models abounding in the literature, the two-fluid model is chosen in the present work and its formulation is detailed in this section. The governing equations and the closure laws for adiabatic flows are presented. The constitutive relations for interfacial transfer terms are described for both stratified and bubbly flow regimes.

2.5.1 Governing equations

The purpose of this subsection is to remind how the set of equations is obtained, from the generic two-fluid equations. The generic formulation of the two-fluid model is :
Mass conservation:

$$\frac{\partial}{\partial t}(\alpha_k \rho_k) + \frac{\partial}{\partial x}(\rho_k \alpha_k V_k) = \Gamma_k \tag{2.5}$$

Momentum conservation:

$$\begin{aligned}\frac{\partial}{\partial t}(\alpha_k \rho_k V_k) + \frac{\partial}{\partial x}(\rho_k \alpha_k V_k^2) = -\alpha_k \frac{\partial P_k}{\partial x} - \Delta P_{ki} \frac{\partial \alpha_k}{\partial x} + \frac{\partial}{\partial x}\alpha_k \left(\tau_k + \tau_k^{Re}\right) \\ + M_{ki} + M_{kw} + \Gamma_k V_{ki} - \rho_k \alpha_k g \sin\beta\end{aligned} \tag{2.6}$$

where β is the pipe inclination with the horizontal, $\rho_k, P_k, V_k, \alpha_k$ are respectively the density, the pressure, the velocity and the volume fraction of phase k; Γ_k represents the mass transfer; V_{ki} gives the interfacial velocity for each phase; τ_k and τ_k^{Re} are respectively the viscous stress and the Reynolds (turbulent) viscous stress terms; and ΔP_{ki} represents the pressure correction terms; M_{ki}, M_{kw} are the interfacial and wall shear forces.

Three extra relations are added to the set of equations:

$$\alpha_g + \alpha_l = 1 \tag{2.7}$$

$$\Gamma_g + \Gamma_l = 0 \tag{2.8}$$

$$\textstyle\sum_k M_{ki} + \Gamma_k V_{ki} = 0 \tag{2.9}$$

Of course, the number of unknowns is bigger than the number of equations and constitutive relations are required to close the system.

The following general assumptions have also been made:

- no mass transfer between the phases is considered which implies $\Gamma_k = 0$;

- the Reynolds viscous stress, τ_k^{Re}, is not accurately modeled in two-phase flow, even though Park *et al.* [46] formulated a correlation, no conclusive study has been established whether or not its presence in the equations has an important effect on the results. Therefore it will be neglected in the present work;

- the viscous terms τ_k which is found to have a minor effect on the flows under consideration will also be neglected.

With these assumptions and the extra relations, the generic two-fluid model is reduced to 6 equations for 14 unknowns. To close the system, the required constitutive relations are defined by complicated functions of the fluid velocities and their local properties, as well as the two-phase flow patterns. Some of them contain derivative terms which might change the structure of the generic two-fluid model, its convective terms and therefore its wave propagation behaviour. Most of these closure relations are presented in the following section.

2.5.2 Closure laws

This section describes the different modelling approach available in the literature for the interfacial force, wall shear and pressure terms. It will also help the reader in understanding the assumptions made for the formulation of two specific two-fluid models in Chapter 3.

2.5.2.1 Interfacial stress term

The interfacial stress term M_{ki} arises from stresses acting on the interface. It is the most crucial transfer law in modelling multiphase isothermal flows and can be expressed as a linear combination of several important physical forces, namely:

$$F_{ki} = F_{ki}^{D} + F_{ki}^{VM} + F_{ki}^{L} + F_{ki}^{C} \tag{2.10}$$

where the superscripts D, VM, L and C stand for the steady-state drag, virtual mass, lift and collision forces respectively. Closure models for the interfacial drag and virtual mass forces are presented respectively in the next chapter and in the next sub-sections. Lift and collision forces are not considered in this work, following Ishii and Mishima [43] who suggested that the functional forms are not well known.

a. Interfacial shear force

In all specific two-phase flow models described later, the virtual mass force mentioned in the next sub-section will be neglected, making the interfacial drag law the only closure term for modelling two-phase flows that were investigated in the present work.

The total interfacial shear force greatly depends upon the flow regime considered and despite its great importance, its real expression is not always known accurately. However, Ishii and Mishima [43] suggested modelling it as the combination of two terms as:

$$F_{ki}^{D} = \langle -\tau_{ki}\alpha_k \rangle_x + \bar{F}_{ki} \tag{2.11}$$

The first term on the right-hand side represents the effect of the interfacial shear and the void gradient and is particularly important for a separated flow. The second term is regarded as the generalized area-averaged particle drag and is important for a dispersed flow.

Formulation for stratified flow

In a stratified or annular flow, the contribution of the interfacial shear and void gradient is the dominant drag force. Ishii and Mishima[43] have shown that, for separated flows in a tube, it can be given as:

$$F_{ki}^{D} = \langle -\tau_{ki}\alpha_k \rangle_x = -\frac{\tau_{gi} S_i}{A} \tag{2.12}$$

where A is the pipe cross-section and S_i is the wetted perimeter of the interface or the gas core, which will be defined in next chapter. The constitutive relation for the gas interfacial shear stress τ_{gi}, which will be renamed τ_i in the remaining of the thesis, is given in terms of the standard interfacial friction factor as:

$$\tau_i = \frac{1}{2} f_i \rho_g |V_g - V_l|(V_g - V_l). \tag{2.13}$$

There is a number of correlations for the interfacial friction factor f_i. They depend upon the fluid's local properties and the flow regime. They are not presented here, but some of them will be reviewed in the next chapter.

Formulation for dispersed flow

As previously mentioned, the average drag force on a single particle, drop or bubble is the force acting on that object as it moves steadily through the surrounding fluid. It is usually given in terms of a dimensionless coefficient C_D, where the drag force for a dispersed bubble flow is defined as:

$$\bar{T}_{ki} = \frac{3}{4} \frac{\rho_l \alpha_g C_D}{D_b} |\bar{V}_r| \bar{V}_r \tag{2.14}$$

Here, the drag coefficient C_D is assumed to be a function of the gas volume fraction α_g, the bubble diameter D_b, the relative velocity $\bar{V}_r$ and the liquid viscosity. The dependence of C_D on these parameters has been studied and many correlations for the drag coefficient C_D have been suggested in the literature. They are summarized in the book by Clift et al. [16] and in the reference papers by Ishii and Zuber [33] and Tomiyama et al. [61, 62].

A similar formulation for the drag force is given in terms of the interfacial area concentration a_{ig} which is flow regime dependent [30]. Hence it reads:

$$\bar{T}_{ki} = \frac{1}{8} \rho_l a_{ig} C_D |\bar{V}_r| \bar{V}_r \tag{2.15}$$

where $a_{ig} = \dfrac{6\alpha_g}{d_{sm}}$ for bubbly flow regime. d_{sm} represents the Sauter mean diameter and is defined in Chapter 3.

It should be noticed that the averaged local relative velocity $\bar{V}_r$ is not equal to the difference

between the area averaged mean velocity of phases ($V_g - V_l$), also referred to as slip velocity). The difference between them can be very large and is explained by the fact that two different effects can cause slip between two phases in one-dimensional formulation: the local relative motion between two phases at a local point and the integral effect of the phase and velocity distributions arising due to the area averaging [68, 30]. However, in this work, $\bar{V}_r$ is assumed equal to $V_r = V_g - V_l$.

b. Virtual mass force

The virtual mass term in Eq. 2.10 represents the interphase force resulting from the displacement of adjacent fluid mass in the case of relative acceleration between the phases. The form of the virtual mass term in realistic two-phase flows is not known exactly and different forms of the virtual mass term is used in different computer codes for nuclear thermal hydraulics simulations [7, 59]. The most general form of the virtual mass contains first order space and time derivatives [21] and can be expressed as:

$$T_{li}^{VM} = C_{VM}\rho_l\alpha_g\left\{\frac{\partial V_r}{\partial t} + V_l\frac{\partial V_g}{\partial x} - V_g\frac{\partial V_l}{\partial x} + (\kappa - 1)V_r\frac{\partial V_r}{\partial x}\right\}. \tag{2.16}$$

where V_r is the relative velocity and the parameter κ should be a function of the gas volume fraction with the value 2 when α_g tends to 0 and 0 for α_g tends to 1. In the hydraulics codes [59], the parameter κ is set equal to 1. Toumi and Kumbaro [63] also used the same value of κ in their numerical model and in all three cases, the liquid density ρ_l in Eq. 2.16 is replaced by the product of the liquid volume fraction α_l by the mixture density ρ_m . The corresponding expression used is therefore:

$$T_{li}^{VM} = C_{VM}\rho_M\alpha_l\alpha_g\left[\left(\frac{\partial V_g}{\partial t} + V_l\frac{\partial V_g}{\partial x}\right) - \left(\frac{\partial V_l}{\partial t} + V_g\frac{\partial V_l}{\partial x}\right)\right] \tag{2.17}$$

The open parameter C_{VM} in the virtual mass term can be used to adjust the interfacial momentum coupling with respect to different flow regimes. For idealised dispersed droplet or bubbly flow, a value of $C_{VM} = 0.5$ has been derived from classical potential flow. For completely separated flows (such as stratified flow), it is expected that C_{VM} tends to zero, but in the case of churn-turbulent two-phase flow with strong interfacial momentum coupling, a value of $C_{VM} > 0.5$ might be more appropriate. For slug flow, Ishii and Mishima [43] calculated a factor of $C_{VM} = 3.3$ to 5 depending on the form of slugs.

To account for the interaction effects between phases, Zuber [67] suggested using the following expression of the virtual mass coefficient

$$C_{VM} = \frac{1}{2}\left(\frac{1 + 2R_d}{1 - R_d}\right) \tag{2.18}$$

where R_d is the discontinuous phase fraction. However, C_{VM} is defined in [63] by a condition necessary to obtain a hyperbolic system. Thus for their set of equations they found that the system is hyperbolic if:

$$C_{VM} \leq C_{VM}^{o} = \sqrt{4c(1-c)} \tag{2.19}$$

where c is a concentration term defined as follows:

$$c = \frac{\rho_g \alpha_g}{\rho_g \alpha_g + \rho_l \alpha_l} \tag{2.20}$$

In conclusion, it is worth noting that for many interesting cases, the inclusion or neglect of the virtual mass force in the phasic momentum does not appreciably change the momentum results. However, the inclusion of this term with its temporal and spatial derivative terms has an effect on the hyperbolicity of the system and the numerical scheme. Although it adds an extra complexity on the numerical scheme, Watanabe et al. [64] claimed that the virtual mass force improves the computation efficiency of the solution scheme.

2.5.2.2 Wall shear stress

The wall shear stress represents the stresses acting on the phase at the wall. Different methodologies have been proposed to calculate it and have been reviewed in many books. The wall shear stress is generally based on closure laws derived from fully developed steady state two-phase flows and usually given as:

$$T_{kw} = -\frac{\tau_k S_k}{A} \tag{2.21}$$

where S_k is the part of the wall wetted by phase k and τ_k is the wall shear stress of the same phase. The constitutive relation for the wall shear stress is given in term of the standard wall friction factor f_k as:

$$\tau_k = \frac{1}{2} f_k \rho_k |V_k| V_k. \tag{2.22}$$

It is common practice to model two-phase wall friction factors using single-phase pipe formulae and thus correlations for gas and liquid wall frictions abound in the literature. These single-phase relations are not presented here, but will be reviewed in the next chapter.

2.5.2.3 Pressure terms

In the literature, three equivalent formulations are found for the pressure terms appearing in the momentum Eq. 2.6. These forms are:

$$\alpha_k \frac{\partial P_k}{\partial x} + \Delta P_{ki} \frac{\partial \alpha_k}{\partial x} = \frac{\partial (\alpha_k \Delta P_{ki})}{\partial x} + \alpha_k \frac{\partial P_{ki}}{\partial x} = \frac{\partial (\alpha_k P_k)}{\partial x} - P_{ki} \frac{\partial \alpha_k}{\partial x} \tag{2.23}$$

where the ΔP_{ki} is defined by $\Delta P_{ki} = P_k - P_{ki}$. This term is referred in the literature as a pressure correction term.

The system of equations contains then four distinct pressure terms (P_k, P_{ki} for $k = g, l$) which have to be linked by additional relations. In consequence, several two-fluid models formulations can be made depending upon the pressure formulation and the closure relationships. This complicates the selection of a specific model for practical applications and notably when the way to obtain these closure laws is not always clarified.

a. Phasic pressure

The phasic pressure in a compressible fluid is related to the temperature and density of the fluid through a thermodynamic equation of state. However, for isothermal flows considered here, the phase pressure equation only depends upon the fluid density and can be given as:

$$P_k = P_k(\rho_k) \tag{2.24}$$

The usual approach to model pressure differences between the phases is to assume pressure equilibrium in both fluids. However, for the two-pressure model, non-equilibrium in pressures is adopted. Different relations representing this difference can be found in the literature, from instantaneous pressure relaxation to formulation from surface tension effects [51, 12].

b. Interfacial pressure

The difference between the two interfacial pressures is generally related to the surface tension force and appears to depend on the flow pattern considered. When this force becomes important, Barnea and Taitel [4] suggested an expression for the stratified flow regime. Drew and Passman [23] gave an alternative expression for bubbly flow. Both relations are defined by:

$$\begin{cases} P_{gi} - P_{li} = \sigma \dfrac{\partial h_l^2}{\partial x^2} & \text{Stratified} \\ P_{gi} - P_{li} = \dfrac{2\sigma}{R_b} & \text{Bubbly flow} \end{cases} \tag{2.25}$$

where σ is a constant surface tension, h_l is the height of the liquid in the pipe if stratified flow and R_b is the radius of bubbles.

However, the simplest way to obtain the interfacial pressure difference is to assume equal interface pressure, thereby neglecting the effect of surface tension. Mathematical models considered later in this chapter always use the equal interfacial pressure assumption and subsequently adopt the following relation:

$$P_{gi} = P_{li} = P_i \tag{2.26}$$

c. Pressure correction term

Early two-fluid models did not consider this term in their formulation. However, its inclusion in the momentum equations allows, for example, an accurate propagation of gravity waves in stratified flow and may have a significant effect on the hyperbolicity of the model. Therefore, recent models tend to include it in their formulation and, as a consequence, numerous expressions depending on the flow regime abound in the literature. In what follows, an account of pressure correction closure models for stratified and dispersed bubbly flow is given.

Formulation for stratified flow

In stratified flow, the pressure correction is generally associated to the hydrostatic head. An expression is obtained by averaging the liquid pressure P_l over any cross-section as [4]:

$$P_l = \frac{1}{A_l}\int_0^{h_l}(P_{li} + \rho_l g\cos\beta(h_l - y))bdy \tag{2.27}$$

where b is the chord length $[b(y)]$ and β is the angle of the pipe with the horizontal. Using the Leibniz rule for differentiation, they obtained:

$$\frac{\partial}{\partial x}(P_l A_l) = \frac{\partial}{\partial x}(P_{li} + A_l) + A_l\rho_l g\cos\beta\frac{\partial h_l}{\partial x} \tag{2.28}$$

A similar expression is obtained for the gas phase; hence for a constant cross-section, combining Eq. 2.5 and 2.23 gives the following relations:

$$\begin{cases} \dfrac{\partial(\alpha_l\Delta P_l)}{\partial x} = \alpha_l\rho_l g\cos\beta\dfrac{\partial h_l}{\partial x} \\ \dfrac{\partial(\alpha_g\Delta P_g)}{\partial x} = \alpha_g\rho_g g\cos\beta\dfrac{\partial h_l}{\partial x} \end{cases} \tag{2.29}$$

Many authors [57, 65, 4] use this expression in their momentum equations and it is therefore the same expression that will be used for the incompressible model formulation presented in the next chapter.

Formulation for dispersed bubbly flow

The pressure correction term is sometimes considered as a stabilizing term for two-fluid models. It is often neglected in favour of the virtual mass term in numerous codes dealing with dispersed flows. However, a detailed study of closure models for bubbly flows is presented in [23] where the following relation is proposed:

$$\begin{cases} P_g - P_{gi} = 0 \\ P_l - P_{li} = \xi(Re_L, \alpha_l)\rho_l(V_g - V_l)^2 \end{cases} \tag{2.30}$$

It is suggested that for dilute flow, $\xi = 1/4$ when the boundary layer remains attached to the spherical particle. For low Reynolds number flows, the calculation of the averaged fields indicates that $\xi = -9/32$.

Some authors take into account pressure corrections for all configurations in such a way that they always have a conditionally hyperbolic system for the test cases studied. The following expression is suggested in [63, 7, 17]:

$$\Delta P_g = \Delta P_l = \delta(\alpha_k, \rho_k)(V_g - V_l)^2 \tag{2.31}$$

with

$$\delta = \begin{cases} \xi\rho_l\alpha_g & \text{Toumi [63]} \\ \dfrac{\rho_g\rho_l\alpha_g\alpha_l}{\rho_g\alpha_g + \rho_l\alpha_l} & \text{CATHARE code [7]} \end{cases} \tag{2.32}$$

where ξ is an adjustable coefficient used to ensure that the resulting two-fluid model remains hyperbolic during numerical simulations.

2.6 Summary

The literature review reveals that to date there exists no two-phase model that can treat all the aspects of two-phase flows in a satisfactorily way.

Steady-state two-phase flow models do not account for transient effects and are insensitive to upstream and downstream influences.

Transient mixture models are simple to derive but rely on closure relationships which are flow regime dependent. In addition, because mixture models are based on a mixture momentum equation, they are not appropriate for certain flow patterns such as slug flow. In the case of the more general transient two-fluid model, the main difficulty resides in the modelling of the interphase interactions. Because two-fluid models are based on basic conservation principles and treat the interphase interactions at a more fundamental level than other models, they can be applied to a wider range of complex two-phase flow problems.

In the present study, it is proposed to solve two-phase flow problems with transient, one-dimensional, isothermal two-fluid models. The description of the proposed models is given in the next chapter.

References - 2

[1] AGRAWAL, S., GREGORY, G., AND GOVIER, G. An analysis of horizontal stratified two-phase flow in pipes. *Can. J. Chem. Eng 51* (1973), 280–286.

[2] BARNEA, D. A unified model for predicting flow pattern transitions for the whole range of pipe inclinations. *Int. J. Multiphase Flow 13*, 1 (1987), 1–12.

[3] BARNEA, D., SHOHAM, O., TAITEL, Y., AND DUKLER, A. Gas-liquid flows in inclined tubes: flow pattern transitions for upward flow. *Chem. Eng. Sci. 40*, 1 (1985), 131–136.

[4] BARNEA, D., AND TAITEL, Y. Interfacial and structural stability of separated flow. *Int. J. Multiphase Flow 20* (1994), 387–414.

[5] BEGGS, H. D., AND BRILL, J. A study of two-phase flow in inclined pipes. *J. Petroleum Technology, Trans. 25* (1973), 607–617.

[6] BERTOLA, F., VANNI, M., AND BALDI, G. Application of computational fluid dynamics to multiphase flow in bubble columns. *Int. J. of Chem. Reactor Engineering 1* (2003). Article A3.

[7] BESTION, D. The physical closure laws in the CATHARE code. *Nuclear engineering design 124* (1990), 229–245.

[8] CHAHED, J., AND MASBERNAT, L. Forces interfaciales et turbulence dans les écoulements à bulles. *C. R. Acad. Sci. Paris 326* (1998), 635–642.

[9] CHEN, Y. *Modeling gas-liquid flow in pipes: flow pattern transitions and drift-flux modeling.* MSc thesis, Departement of Petroleum Engineering, Stanford University, 2001.

[10] CHENG, L., DREW, D., AND LAHEY JR, R. An analysis of wave propagation in bubbly two-component, two-phase flow. *Journal of Heat Transfer 107* (May 1985), 402–408.

[11] CHUNG, M.-S., CHANG, K.-S., AND LEE, S.-J. Wave propagation in two-phase flow based on a new hyperbolic two-fluid model. *Numerical Heat Transfer, Part A 38* (2000), 169–191.

[12] CHUNG, M.-S., CHANG, K.-S., AND LEE, S.-J. Numerical solution of hyperbolic two-fluid two-phase flow model with non-reflecting boundary conditions. *Int. J. of Eng. Sci. 40* (2002), 789–803.

[13] CHUNG, M.-S., CHANG, K.-S., LEE, S.-J., AND LEE, W.-J. An interfacial presure jump model for two-phase bubbly flow. *Numerical Heat Transfer, Part B 40* (2001), 83–97.

[14] CHUNG, M.-S., LEE, S.-J., AND CHANG, K.-S. Effect of interfacial pressure jump and virtual mass terms on sound wave propagation in the two-phase flow. *Journal of Sound and Vibration 244*, 4 (2001), 717–728.

[15] CHUNG, M.-S., AND LEE, W.-J. On the wave dispersion relevant to the virtual mass terms in the two-phase two-fluid model. *Numerical Heat Transfer, Part A 40* (2001), 239–251.

[16] CLIFT, R., GRACE, J., AND WEBER, M. *Bubbles, Drops, and Particles.* Academic Press, New York, 1978.

[17] COQUEL, F., EL AMINE, E., GODLEWSKI, B., PERTHAME, B., AND RASCLE, P. A numerical method using upwind schemes for the resolution of two-phase flows. *J. Comp. Phys. 136* (1997), 272–288.

[18] DELHAYE, J. Some issues related to the modeling of interfacial areas in gas-liquid flows. I. The conceptual issues. *C. R. Acad. Sci. Paris 329*, II (2001), 397–410.

[19] DELNOIJ, E., KUIPERS, J., AND VAN SWAAIJ, W. Dynamic simulation of gas-liquid two-phase flow: effect of column aspect ratio on the flow structure. *Chem. Eng. Sci. 52*, 21/22 (1997), 3759–3772.

[20] DREW, D. Mathematical modeling of two-phase flows. *Annual Review of Fluid mechanics 15* (1983), 261–291.

[21] DREW, D., CHENG, L., AND LAHEY JR, R. The analysis of virtual mass effects in two-phase flow. *Int. J. of Multiphase Flow 5* (1979), 233–242.

[22] DREW, D., AND LAHEY JR, R. On the development of multidimensional two-fluid models for vapor/liquid two-phase flows. *Chem Eng Commun 118* (1992), 125–139.

[23] DREW, D., AND PASSMAN, S. L. *Theory of Multicomponent Fluids*, vol. 135 of *Applied Mathematical Sciences.* Springer Verlag, 1999.

[24] DUKLER, A. Modelling two-phase flow and heat transfer. In 6^{th} *International Heat Transfer Conference* (August 1978), vol. 22. Toronto, Canada.

[25] GEURST, A. Variational principles and two-fluid hydrodynamics of bubbly liquid/gas mixtures. *Physica 135A* (1986), 455–486.

[26] HATTA, N., FUJIMOTO, H., ISOBE, M., AND KANG, J.-S. Theoretical analysis of flow characteristics of multiphase mixtures in a vertical pipe. *Int. J. of Multiphase Flow 24*, 4 (1998), 539–561.

[27] HATTA, N., FUJIMOTO, H., ISOBE, M., AND KANG, J.-S. Theoretical analysis of flow characteristics of multiphase mixtures in a vertical pipe. *Int. J. of Multiphase Flow 24*, 4 (1998), 539–561.

[28] HIBIKI, T., AND ISHII, M. One-dimensional drift-flux model for two-phase flow in a large diameter pipe. *Int J of Heat and Mass Tranfer 46* (2003), 1773–1790.

[29] HILLS, J. The operation of a bubble column at high throughputs i. gas holdup measurements. *Chem Eng Sci 12* (1976), 89–99.

[30] ISHII, M. One-dimensional drift-flux model and constitutive equations for relative motion between phases in various two-phase flow regimes. *Argonne National Lab Report, ANL 77-47* (October 1977).

[31] ISHII, M., AND KOCAMUSTAFAOGULLARI, G. Private communication. also maximum fluid particle size for bubbles and drops. In *ASME Winter Annual Meeting* (1985), pp. 99–107. Miami Beach, FL, USA.

[32] ISHII, M., MISHIMA, K., KATAOKA, I., AND KOCAMUSTAFAOGULLARI, G. Two-fluid model and importance of the interfacial area in two-phase flow analysis. In *9th U.S. National Congress of Applied Mechanics* (1982), pp. 73–80. Ithaca, New-York.

[33] ISHII, M., AND ZUBER, N. Drag coefficient and relative velocity in bubbly, droplet or particulate flows. *AIChE Journal 25*, 5 (September 1979), 843–855.

[34] KUO, T., PAN, C., AND CHIENG, C. Eulerian-Lagrangian computations on phase distribution of two-phase bubbly flows. *International Journal for Numerical Methods in Fluids 24* (1997), 579–593.

[35] LAHEY JR, R., AND DREW, D. The virtual mass and lift force on a sphere in rotating and straining inviscid flow. *Int. J. of Multiphase Flow 13* (1987), 113–121.

[36] LAHEY JR, R., AND DREW, D. The analysis of two-phase flow and heat transfer using a multidimensional, four field, two-fluid model. *Nuclear Engineering and Design 204* (2001), 29–44.

[37] LHUILLIER, D., MOREL, C., AND DELHAYE, J. Bilan d'aire interfaciale dans un mélange diphasique: approche locale vs approche pariculaire. *C.R. Acad. des Sci. Paris, T 328 II b* (2000), 143–149.

[38] LOCKART, R., AND MARTINELLI, R. Proposed correlation of data for isothermal two-phase, two component flow in pipes. *Chem. Eng. Prog. 1* (1949), 39–48.

[39] LOPEZ DE BERTODANO, M., LAHEY JR., R., AND JONES, O. Phase distribution in bubbly two-phase flow in vertical ducts. *Int. J. of Multiphase Flow 20* (1994), 805–818.

[40] LUCAS, D., KREPPER, E., AND PRASSER, H.-M. Prediction of radial gas profiles in vertical pipe flow on the basis of bubble size distribution. *Int. J. Therm. Sci. 40* (2001), 217–225.

[41] MANDHANE, J., GREGORY, G., AND AZIZ, K. A flow pattern map for gas-liquid flow in horizontal pipes. *Int. Journal of Multiphase Flow 1* (1974), 537–553.

[42] MASELLA, J. M. *Quelques Méthodes Numériques Pour Les Ecoulements Diphasiques Bi-Fluide En Conduites Pétrolières.* Ph.D. thesis, Université Pierre et Marie Curie, Paris VI, 1997.

[43] MISHIMA, K., AND ISHII, M. Flow regime transition criteria for two-phase flow in vertical pipes. *Int. J. of Heat Mass Trans 27* (1984), 723–734.

[44] MORI, Y., HIJIKATA, K., AND OHMORI, T. Propagation of a pressure wave in two-phase flow with very high void fraction. *Int. J. Multiphase Flow 2* (1976), 453–464.

[45] MUKHERJEE, H., AND BRILL, J. P. Empirical equations to predict flow patterns in two-phase inclined flows. *Int. J. Multiphase Flow 13* (1987), 299–315.

[46] PARK, J. W., DREW, D. A., AND LAHEY JR., R. T. The analysis of void wave propagation in adiabatic monodispersed bubbly two-phase flows using an ensemble-averaged two-fluid model. *Int. J. of Multiphase Flow 24* (1998), 1205–1244.

[47] PAUCHON, C., AND BANERJEE, S. Interphase momentum interaction effects in the averaged multifluid model. *Int. J. of Multiphase Flow 12*, 4 (1986), 559–573.

[48] PETALAS, N., AND AZIZ, K. A mechanistic model for multiphase flow in pipes. In *49th Annual Technical Meeting of the Petroleum Society of the Canadian Institute of Mining, Metallurgy and Petroleum* (8-10 June 1998). Calgary, Alberta, Canada.

[49] POLITANO, M., CARRICA, P., AND CONVERTI, J. A model for turbulent polydisperse two-phase flow in vertical channels. *Int. J. of Multiphase Flow 29* (2003), 1153–1182.

[50] RAMOS, J. One-dimensional, time-dependent, homogeneous two-phase flow in volcanic conduits. *Int. J. for Num. Meth. in Fluids 21* (1995), 253–278.

[51] RANSOM, V., AND HICKS, D. Hyperbolic two-pressure models for two-phase flow. *Journal of Comp. Phys. 53* (1984), 124–151.

[52] ROMATE, J. Developing a second-order tvd scheme for one-dimensional two-phase flow model. In *AMIF-ESF Workshop âĂŞ Computing Methods for Two-Phase Flow, Paper 22, Aussois, France* (January 12-14 2000).

[53] SAUREL, R., AND ABGRALL, R. A multiphase godunov method for compressible multifluid and multiphase flows. *Journal of Computational Physics 150* (1999), 425–467.

[54] SPEDDING, P., AND NGUYEN, V. Regime maps for air-water two-phase flow. *Chem. Eng. Sci. 35* (1980), 779–793.

[55] STUHMILLER, J. H. Influence of interfacial pressure forces on the character of two-phase flow model equations. *Int J Multiphase Flow 3*, 6 (Dec 1977), 551–560.

[56] TAITEL, Y., BARNEA, D., AND DUKLER, A. Modelling flow pattern transitions for stratified flow in vertical tubes. *AIChE Journal 26*, 3 (1980), 345–354.

[57] TAITEL, Y., AND DUKLER, A. A model for predicting flow regime transitions in horizontal and near horizontal gas-liquid flow. *AIChE Journal 22*, 1 (1976), 47–55.

[58] THÉRON, B. *Ecoulements instationnaires intermittents de gas et de liquide en conduite horizontale.* Thèse, Institut National Polytechnique, Toulouse, France, 1989.

[59] TISELJ, I., AND PETELIN, S. Modelling of two-phase flow with second-order accurate scheme. *J. Comp. Phys. 136* (1997), 503–521.

[60] TOMIYAMA, A. Struggle with computational bubble dynamics. In *Third Int. Conf. on Multiphase Flow, ICMF 98* (8-12 June 1998). Lyon, France.

[61] TOMIYAMA, A., KATAOKA, I., AND SAKAGUCHI, T. Drag coefficients of bubbles, 1st report: Drag coefficient of a single bubble in a stagnant liquid. *Trans. JSME 61*, B (1995), 23–57.

[62] TOMIYAMA, A., KATAOKA, I., AND SAKAGUCHI, T. Drag coefficients of single bubbles under normal and microgravity conditions. *JSME Int. J. 41*, B (1998), 472–479.

[63] TOUMI, I., AND KUMBARO, A. An approximate linearized Riemann solver for a two-fluid model. *J. Comp. Phys. 124* (1996), 286–300.

[64] WATANABE, T., HIRANO, M., TANABE, F., AND KAMO, H. The effect of virtual mass force term on the numerical stability and efficiency of systems calculations. *Nuclear Engineering and Design 120* (1990), 181–192.

[65] WATSON, M. Non-linear waves in pipeline two-phase flows. In *Proceedings of 3rd Conference on Hyperbolic Problems* (11-15 June 1990).

[66] WU, Q., KIM, S., ISHII, M., AND BEUSS, S. One-group interfacial area transport in vertical bubbly flow. *Int. J. of Heat Mass Transfer 41* (1998), 1103–1112.

[67] ZUBER, N. On the dispersed two-phase flow in the laminar flow regime. *Chemical Engineering Science 19* (1964), 897–917.

[68] ZUBER, N., AND FINDLAY, J. Average volumetric concentration in two-phase flow systems. *Journal of Heat Transfer* (1965), 453–468.

3 The mathematical model

3.1 Overview

This chapter describes the differential transport equations and the accompanying constitutive relationships that form the one-dimensional time averaged two-fluid models used in the present study. The models assume isothermal flow, enabling us to neglect the equations of energy. This assumption is a reasonable approximation for pipelines which have a large surface area to volume ratio and a constant wall temperature.

Section 3.2 presents the first model used in this study, which is a transient incompressible two-fluid model developed for stratified flows. The motivation for this model is to test and validate the geometry algorithm described in Chapter 5.

The second model presented in Section 3.3 is a more complete model, specific for bubbly flows, flow regime where the gas compressibility can no longer be neglected. Hence we detail the formulation of the compressible two-fluid equations adopted in the present research, and investigate the mathematical character of the equations.

Section 3.4 will mainly focus on the constitutive equations for the wall and interphase momentum transfer for stratified and bubbly flows. Parametric studies illustrate how the correlations for bubbly flows are selected. Thermodynamic models and treatment of interfacial velocity and pressure are also described in this section.

3.2 Incompressible model

The model describes an incompressible two-phase flow of gas and liquid in a circular pipe inclined at an angle β to the horizontal [44]. It is based upon the multi-fluid model where the pressure is eliminated leading to a conservative formulation, and is sometimes referred to as Pressure-Free Model (PFM). An algebraic constraint between the volume fractions and the phase velocities is introduced in order to reduce the number of equations adding together the phases mass conservation. This constraint states that, for incompressible cases, the mixture velocity V_m is a function of time only.

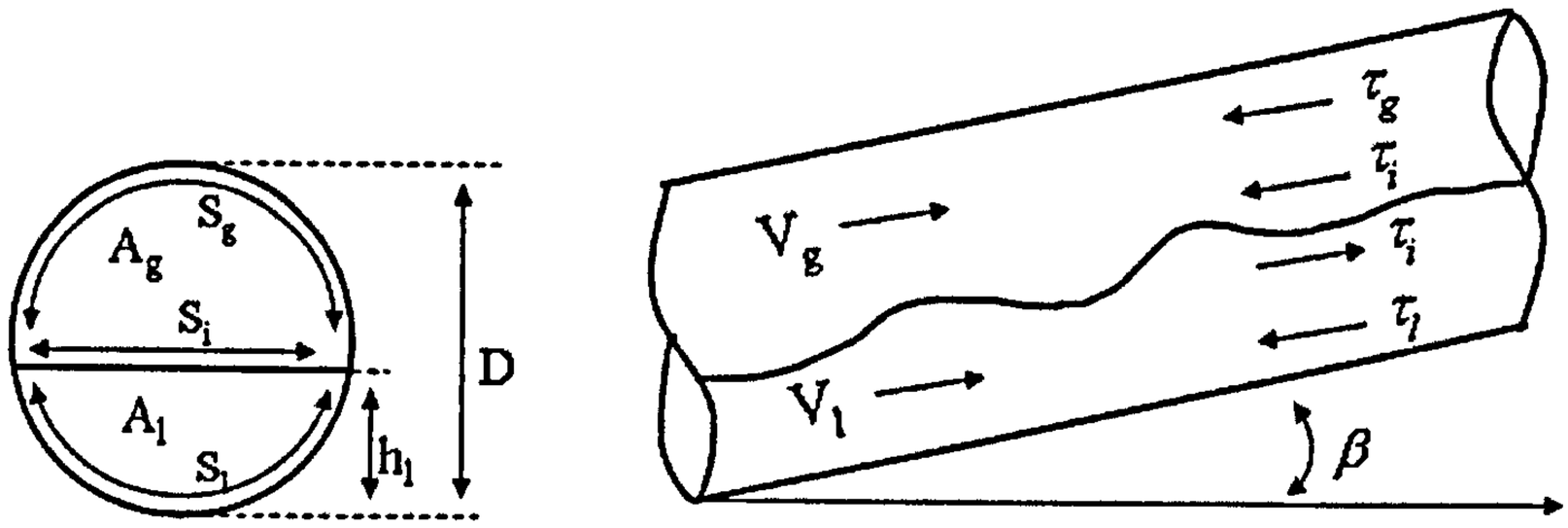

Figure 3.1 : *Description of the stratified two-phase flow: cross-section and side views of a stratified flow in a circular pipe.*

3.2.1 The governing equations

Starting from the general formulation of the two-fluid model:

- Mass Conservation:

$$\frac{\partial}{\partial t}(\rho_k A_k) + \frac{\partial}{\partial x}(\rho_k A_k V_k) = 0 \tag{3.1}$$

- Momentum Conservation:

$$\frac{\partial}{\partial t}(\rho_k A_k V_k) + \frac{\partial}{\partial x}(\rho_k A_k V_k^2) = -A_k \frac{\partial P_i}{\partial x} - A_k \rho_k g \cos\beta \frac{\partial h}{\partial x} - A_k \rho_k g \sin\beta \pm \tau_i S_i - \tau_{wk} S_k \tag{3.2}$$

with $k = g, l$ and h is the liquid height. The coefficients τ_{wk} and τ_i represent the shear stresses. S_i and S_k designate the interfacial width and the gas wetted perimeter respectively.
To eliminate the pressure gradient, we combine the two momentum equations to obtain the *global momentum equation.* The *conservation of the total mass* is obtained by summation of the two mass conservation equations.
Hence, the governing equations can be written as follows:

- Conservation of total mass

$$\frac{\partial}{\partial t}\Big(\rho_L A_L + \rho_G A_G\Big) + \frac{\partial}{\partial x}\Big(\rho_L A_L V_L + \rho_G A_G V_G\Big) = 0 \tag{3.3}$$

- Global momentum equation

$$\frac{\partial}{\partial t}\Big(\rho_L V_L - \rho_G V_G\Big) + \frac{\partial}{\partial x}\Big(\frac{1}{2}\rho_L V_L^2 - \frac{1}{2}\rho_G V_G^2 + (\rho_L - \rho_G) g h_L \cos\beta\Big) = -(\rho_L - \rho_G) g \sin\beta + \Big(\frac{1}{A_L} + \frac{1}{A_G}\Big)\tau_i S_i + \frac{\tau_G S_G}{A_G} - \frac{\tau_L S_L}{A_L} \tag{3.4}$$

with the algebraic constraint

$$V_m = A_L V_L + A_G V_G = A(V_{SL} + V_{SG}) \tag{3.5}$$

$$A = A_L + A_G \tag{3.6}$$

This model makes the assumptions of incompressible and isothermal flow. This slightly restricts the domain of application. Nevertheless our first objective in this work is to investigate this fairly simplified model. Single-pressure models efficiency have been previously studied in other works [26].

3.2.2 Model analysis

The governing equations of any specific model can be algebraically re-written into a matrix or primitive form expressed as:

$$M_B(U)\frac{\partial U}{\partial t} + M_A(U)\frac{\partial U}{\partial x} = S(U) \tag{3.7}$$

where M_A and M_B are two non-singular square matrices whose coefficients are functions of the flow variables. U represents the vector of conservative or primitive variables and S contains the source terms of interfacial and wall transfers of mass and momentum.

Hence the study of the model characteristics can be reduced to the evaluation of the equation

$$det(M_A - \lambda M_B) = 0 \tag{3.8}$$

where λ is a characteristic value.
If we consider the conservative vector U given by:

$$U = \begin{pmatrix} \alpha_l \\ V_g \end{pmatrix} \tag{3.9}$$

and let the density difference and the relative velocity be defined by $\Delta\rho = \rho_l - \rho_g$ and $V_r = V_g - V_l$, the expression of the matrices M_A and M_B read:

$$M_A = \begin{pmatrix} \Delta\rho V_g & \Delta\rho\alpha_l \\ \rho_l V_l \dfrac{V_r}{\alpha_l} + \Delta\rho g \cos\beta \dfrac{A}{A'_l} & -(\rho_g V_g + \rho_l V_l \dfrac{\alpha_g}{\alpha_l}) \end{pmatrix} \tag{3.10}$$

and

$$M_B = \begin{pmatrix} \Delta\rho & 0 \\ \rho_l \dfrac{V_r}{\alpha_l} & -(\rho_g + \rho_l \dfrac{\alpha_g}{\alpha_l}) \end{pmatrix} \tag{3.11}$$

Hence,

$$M_A - \lambda M_B = \begin{pmatrix} \Delta\rho(V_g - \lambda) & \Delta\rho\alpha_g \\ \rho_l \dfrac{V_r}{\alpha_l}(V_l - \lambda) + \Delta\rho g \cos\beta \dfrac{A}{A_l'} & -\Big(\rho_g(V_g - \lambda) + \rho_l(V_l - \lambda)\dfrac{\alpha_g}{\alpha_l}\Big) \end{pmatrix} \quad (3.12)$$

and when evaluating $det(M_A - \lambda M_B) = 0$, one finds the following expression

$$-\frac{\Delta\rho(V_g - \lambda)}{\alpha_l}(\rho_g\alpha_l(V_g - \lambda) + \rho_l\alpha_g(V_l - \lambda)) + \frac{\Delta\rho\alpha_g}{\alpha_l}\Big((\rho_l V_r(V_l - \lambda)) + \Delta\rho g\cos\beta\frac{A}{A_l'}\Big) = 0. \quad (3.13)$$

If $\phi = \dfrac{\rho_g\alpha_l}{\rho_l\alpha_g}$ and dividing Eq.3.13 first by $\dfrac{\Delta\rho}{\alpha_l}$, rearranging and dividing by $\dfrac{1}{\alpha_l\rho_l}$, the polynomial becomes:

$$-\lambda^2(1+\phi) + 2\lambda(V_l + \phi V_g) - \Big(V_l^2 + \phi V_g^2 - \frac{\Delta\rho g\cos\beta A_l}{\rho_l A_l'}\Big) = 0. \quad (3.14)$$

The discriminant Δ must always be greater than or equal to zero to ensure the roots of the polynomial are all real.

$$\Delta = (V_l + \phi V_g)^2 - (1-\phi)(\Big(V_l^2 + \phi V_g^2 - \frac{\Delta\rho g\cos\beta A_l}{\rho_l A_l'}\Big). \quad (3.15)$$

and $\Delta \geq 0$ gives a simple relation, called the Inviscid Kevin-Helmholtz (IKH) condition, which reads here:

$$(V_g - V_l)^2 \geq \frac{\Delta\rho(\rho_l\alpha_g + \rho_g\alpha_l)}{\rho_g\rho_l} g\cos\beta\frac{A}{A_l'}. \quad (3.16)$$

And the two characteristics of the model are given by:

$$\lambda_1 = \frac{(V_l + \phi V_g) + \sqrt{\Delta}}{1+\phi} \quad (3.17)$$

$$\lambda_2 = \frac{(V_l + \phi V_g) + \sqrt{\Delta}}{1+\phi} \quad (3.18)$$

where the discriminant Δ is given by Eq.3.15 and ϕ is the density ratio as previously defined.

3.3 Compressible model

Two-fluid models with an equilibrium pressure assumption have some drawbacks. In particular, they do not remain hyperbolic for the entire domain of calculation (the whole

range of volume fraction), which leads to an initial value problem which is "ill-posed" for many initial conditions. Using a two-pressure approach will allow a formulation with the unconditional hyperbolicity of the system and this approach will remove instabilities which occur with other models. Additionally, the expression of the characteristics of a two-pressure model is far simpler than for single-pressure models, simplifying the computations. Different researchers [37, 34, 12, 27, 25, 42] have already presented some results of two-pressure based model on classical two-phase benchmarks. Their works differ by some variations in either the model formulation [37, 34] or the numerical method associated with [12, 42]. The model presented in this work is based on a two-fluid model with two distinct pressures in which a relaxation stage at the interface is included. The computation process is thus divided into two stages: (1) solving the hyperbolic system assuming different pressures, followed by (2) a relaxation on the pressures towards equilibrium at the interface.

3.3.1 The governing equations

The one-dimensional system governing two-phase compressible flows contains five time-dependent partial differential equations, four obtained from the conservation of mass and momentum for each phase. A fifth equation is added to the mass and momentum equations, which expresses the evolution of the volume fraction and is obtained by an averaging procedure [37, 34]: this equation indicates that the volume fraction propagates with the mean interfacial velocity, which is not necessarily equal to the local fluid velocity. For the rest of the thesis, the compressible model will be referred to as TPM5 (Two-Pressure Model 5 equations). The system can be expressed as follows:

$$\frac{\partial}{\partial t}(\rho_g \alpha_g) + \frac{\partial}{\partial x}(\rho_g \alpha_g V_g) = 0 \tag{3.19}$$

$$\frac{\partial}{\partial t}(\rho_l \alpha_l) + \frac{\partial}{\partial x}(\rho_l \alpha_l V_l) = 0 \tag{3.20}$$

$$\frac{\partial}{\partial t}(\rho_g \alpha_g V_g) + \frac{\partial}{\partial x}(\alpha_g(\rho_g V_g^2 + P_g)) = P_i \frac{\partial}{\partial x}\alpha_g + F_{wg} + F_i + B_{fg} \tag{3.21}$$

$$\frac{\partial}{\partial t}(\rho_l \alpha_l V_l) + \frac{\partial}{\partial x}(\alpha_l(\rho_l V_l^2 + P_l)) = -P_i \frac{\partial}{\partial x}\alpha_g + F_{wl} - F_i + B_{fl} \tag{3.22}$$

$$\frac{\partial}{\partial t}\alpha_g + V_i \frac{\partial}{\partial x}\alpha_g = \mu(P_g - P_l) \tag{3.23}$$

where α_k is the void fraction of phase k. ρ_k, V_k are the density and the velocity of phase k, $(k = g, l)$. The mass fraction is defined $m_k = \alpha_k \rho_k$ and the pressure P_k of phase k. μ is a positive function of pressure relaxation. $V_i(U)$ and $P_i(U)$ represent the averaged values of the interfacial velocity and the interfacial pressure over the two-phase control volume and must be modelled by closure laws. Modelling of the averaged interfacial variables is rather delicate and this is discussed in the following sections.

The terms B_{fk} represent the body forces. They are composed of the gravity force and the buoyancy force, used for bubbly flow. The terms F stand for the frictional forces per

unit volume between each phase and the wall and between the phases themselves (at the interface). These terms are the constitutive relations, which are flow regime dependent; they are required to close the system of equations and are subject of investigation in Section 3.4.

3.3.2 Pressure relaxation

Two-phase flow problems imply a dynamic difference in the mean pressures and leave us with three quantities to deal with (P_g, P_l and P_i). In the present model, they all can be linked by the parameter μ. This homogenisation variable depends on the fluid compressibilities, on their nature and on the two-phase mixture topology. Baer and Nunziato [5] showed theoretically the existence of this variable, and experimental measurements of this variable have been conducted for a medium of low density foam. Thus in certain cases, a full formulation for these quantities is known [5, 6, 34], however there is no general expression. In many physical situations, it is reasonable to assume that pressure tends to equilibrium instantaneously. Different constant values of μ have however been tested and compared with answers when $\mu = \infty$. The results from this study are not reported in this work, but it indicated that the most satisfying choice was to select the infinite value. Therefore we use $\mu = \infty$ for all calculations presented in this thesis.

In this context, the system of equations is solved in two steps. The variables are evolved over time by the solution of a strictly hyperbolic system, followed by a pressure relaxation step which equalises the pressures. This is different from single-pressure models that solve a system where the pressure equilibrium is already assumed in the equations, leading to a system which is not hyperbolic for certain conditions; which makes the system very difficult to solve.

The following section describes the procedure of instantaneous relaxation used in this work.

3.3.2.1 Numerical procedure

For all test problems presented in this thesis, the following approximate resolution method is used, which says that the instantaneous pressure relaxation process consists in finding the solution of:

$$F(\alpha_g) = P_g(\rho_g) - P_l(\rho_l) = 0. \tag{3.24}$$

The pressures are given by their equations of state, with input $\rho_k = \frac{(\alpha_k \rho_k)^0}{\alpha_k}$, where the superscript 0 denotes the value after the resolution of the hyperbolic system. The problem is now to look at the value of α_g for which the two pressures are equal. This is achieved by an iterative resolution of $F(\alpha_g) = 0$.

A common iterative procedure used for solving this equation is the Ridders' procedure [31] but it requires an average of 5 or 6 iterations, in each cell and at each time step to converge the pressure to a few decimals. Therefore, in order to reduce the number of iterations a

second root–finding method has been introduced. It is more efficient but is only applicable when using linear equations of state such as:

$$P_k - P_{0,k} = a_k^2(\rho_k - \rho_{0,k}) \tag{3.25}$$

where $P_{0,k}$ and $\rho_{0,k}$ are respectively the initial pressure and density of phase k.

This problem can be re-stated as:

$$\textit{finding } \alpha \textit{ such as } F(\alpha) = 0 \tag{3.26}$$

is the same as

$$\textit{finding } P \textit{ such as } \alpha_g + \alpha_l = 1, \tag{3.27}$$

hence replacing α_g and α_l by $\frac{m_g}{\rho_g}$ and $\frac{m_l}{\rho_l}$ in Eq. 3.27, combining with Eq. 3.25, the pressure relaxation procedure becomes equivalent to solving the second-order polynomial

$$P^2 + c_1 P + c_2 = 0 \tag{3.28}$$

with

$$\begin{cases} c_1 = -a_g^2 m_g - a_l^2 m_l - P_{0,l} + a_l^2 \rho_{0,l} \\ c_2 = -a_g^2 m_g - (-P_{0,l} + a_l^2 \rho_{0,l}) \end{cases} \tag{3.29}$$

Hence the value that equilibrates the pressure is the positive root of Eq. 3.28 when it exists; the density and the volume fraction are updated from this new value.

3.3.3 Model analysis

This section presents the study of the hyperbolicity of the system. The TPM5 model can be re-written in the form

$$B(U)\frac{\partial U}{\partial t} + A(U)\frac{\partial U}{\partial x} = S(U) \tag{3.30}$$

where, when U is considered as a vector of conservative variables, $B(U)$ is clearly equal to the identity matrix. Intuitively, one expects the system to be hyperbolic if it propagates information at a finite speed through space [45]. The system (3.30) (or the convective operator) is said to be hyperbolic if the matrix $A(U)$ can be diagonalised on $\mathbb{R}$ (all the eigenvalues of A are real and distinct, and the corresponding eigenvectors are linearly independent). As an initial boundary value problem, a two-phase flow model would be ill-posed if complex eigenvalues were present. Discussions on hyperbolicity can be found in several papers (Stuhmiller [38], Ghidaglia et al [13]) where many ways to detect whether a model is or not well-posed in the domain of validity of the variables are investigated.

Prosperetti and Satrape [32] analysed the stability of various incompressible two-fluid

models and concluded that the stability is independent of the wavelength. This implies that if the existence of complex characteristics leads to instability of the system at short scale, the same instability will also be present at all scales. Therefore if a model is non-hyperbolic, it ought to be unstable and any numerical result showing the contrary must be a consequence of an excessive dissipative numerical scheme and a possibly slow growth rate of the instability.

The hyperbolicity analysis must be carefully examined each time a two-phase model is proposed. Not only the domain of validity of the model is given by the characteristic study, but it is also useful when developing numerical methods used to solve the physical model.

If we rewrite the equations, the system under consideration reads:

$$\frac{\partial U}{\partial t} + \frac{\partial F(U)}{\partial x} = H(U)\frac{\partial N}{\partial x} + S(U) \tag{3.31}$$

$$\frac{\partial U}{\partial t} + \frac{\partial F(U)}{\partial x} = H(U)\frac{\partial \alpha_g}{\partial x} + S(U) \tag{3.32}$$

with
$H(U)$: interface matrix, and, N: vector of non-conservative variables.

$$\begin{aligned} U &= (\rho_g\alpha_g, \rho_g\alpha_g V_g, \rho_l\alpha_l, \rho_l\alpha_l V_l, \alpha_g)^T \\ F(U) &= (\rho_g\alpha_g V_g, \rho_g\alpha_g V_g^2 + \alpha_g P_g, \rho_l\alpha_l V_l, \rho_l\alpha_l V_l^2 + \alpha_l P_l, 0)^T \\ H(U) &= (0, P_i(U), 0, -P_i(U), -V_i(U))^T \end{aligned}$$

In the two-fluid two-pressure model, the system (3.19) can be expressed in a quasi-linear formulation as:

$$\frac{\partial U}{\partial t} + M_J(U)\frac{\partial U}{\partial x} = S(U) \tag{3.33}$$

where $M_J = (M_J^{ij})_{i,j=1,\ldots,5}$ is the Jacobian matrix based on the conservative vector U.

Hence the study of their characteristics can be reduced to the investigation of the equation:

$$det(M_J - \lambda I) = 0 \tag{3.34}$$

where λ is a characteristic value and I is the identity matrix.

a. Evaluation of the Jacobian matrix M_J

$$U = \begin{pmatrix} \alpha_g\rho_g \\ \rho_g\alpha_g V_g \\ \rho_l\alpha_l \\ \rho_l\alpha_l V_l \\ \alpha_g \end{pmatrix} = \begin{pmatrix} \widehat{\rho_g} \\ m_g \\ \widehat{\rho_l} \\ m_l \\ \alpha_g \end{pmatrix} \text{ and } H = \begin{pmatrix} 0 \\ P_i \\ 0 \\ -P_i \\ -V_i \end{pmatrix} \tag{3.35}$$

From there, we identify M_J from the system (3.30) and the fact that M_J must satisfy

$$\frac{\partial U}{\partial t} + M_J(U)\frac{\partial U}{\partial x} = 0, \tag{3.36}$$

which gives:

- **gas mass equation**

$$\frac{\partial(\rho_g \alpha_g V_g)}{\partial x} = 0 \;\Rightarrow\; \frac{\partial m_g}{\partial x} = 0 \Rightarrow \begin{cases} M_J^{12} = 1 \\ M_J^{11} = M_J^{13} = M_J^{14} = M_J^{15} = 0 \end{cases} \tag{3.37}$$

- **gas momentum equation**

$$\frac{\partial(\rho_g \alpha_g V_g^2 + P_g)}{\partial x} = P_i \frac{\partial \alpha_g}{\partial x} \tag{3.38}$$

The left-hand side gives,

$$\frac{\partial(\rho_g \alpha_g V_g^2 + P_g)}{\partial x} = V_g \frac{\partial m_g}{\partial x} + m_g \frac{\partial V_g}{\partial x} + \alpha_g \frac{\partial P_g}{\partial x} + (P_g - P_i)\frac{\partial \alpha_g}{\partial x} = 0$$

however,

$$V_g = \frac{m_g}{\widehat{\rho}_g} \;\Rightarrow\; m_g \frac{\partial V_g}{\partial x} = m_g \frac{\partial}{\partial x}\left(\frac{m_g}{\widehat{\rho}_g}\right) = \frac{m_g}{\widehat{\rho}_g}\frac{\partial m_g}{\partial x} - \frac{m_g^2}{\widehat{\rho}_g}\frac{\partial \widehat{\rho}_g}{\partial x}$$

$$m_g \frac{\partial V_g}{\partial x} = V_g \frac{\partial m_g}{\partial x} - V_g^2 \frac{\partial \widehat{\rho}_g}{\partial x}$$

Besides, as a barotropic flow, $P_g = P_g(\rho_g)$ which leads to the following relation:

$$\frac{\partial P_g}{\partial x} = \frac{\partial P_g}{\partial \rho_g}\frac{\partial \rho_g}{\partial x}.$$

If we define $\zeta_k = \dfrac{\partial P_k}{\partial \rho_k}$, then,

$$\alpha_g \frac{\partial P_g}{\partial x} = \alpha_g \zeta_g \frac{\partial \rho_g}{\partial x}$$

and,

$$\begin{aligned} \alpha_g \frac{\partial \rho_g}{\partial x} &= \frac{\partial(\alpha_g \rho_g)}{\partial x} - \rho_g \frac{\partial \alpha_g}{\partial x} \\ &= \frac{\partial \widehat{\rho}_g}{\partial x} - \rho_g \frac{\partial \alpha_g}{\partial x}. \end{aligned}$$

And so,

$$\alpha_g \frac{\partial P_g}{\partial x} = \zeta_g \frac{\partial \widehat{\rho}_g}{\partial x} - \zeta_g \rho_g \frac{\partial \alpha_g}{\partial x}.$$

Hence, gas momentum equation reads:

$$2V_g\frac{\partial m_g}{\partial x} - V_g^2\frac{\partial \widehat{\rho_g}}{\partial x} + \zeta_g\frac{\partial \widehat{\rho_g}}{\partial x} - \zeta_g\rho_g\frac{\partial \alpha_g}{\partial x} + (P_g - P_i)\frac{\partial \alpha_g}{\partial x} = 0.$$

However,

$$M_J^{21}\frac{\partial \widehat{\rho_g}}{\partial x} + M_J^{22}\frac{\partial m_g}{\partial x} + M_J^{23}\frac{\partial \widehat{\rho_g}}{\partial x} + M_J^{24}\frac{\partial m_g}{\partial x} + M_J^{25}\frac{\partial \alpha_g}{\partial x} = 0 \tag{3.39}$$

therefore leading to

$$\begin{cases} M_J^{21} = -V_g^2 + \zeta_g \\ M_J^{22} = 2V_g \\ M_J^{23} = M_J^{24} = 0 \\ M_J^{25} = P_g - \zeta_g\rho_g - P_i \end{cases}$$

- The same method applied to the **liquid mass and momentum equations** gives (recalling that $\frac{\partial \alpha_l}{\partial x} = -\frac{\partial \alpha_g}{\partial x}$):

$$\begin{cases} M_J^{31} = M_J^{32} = M_J^{33} = M_J^{35} = 0 \\ M_J^{34} = 1 \\ M_J^{41} = M_J^{42} = 0 \\ M_J^{43} = -V_l^2 + \zeta_l \\ M_J^{44} = 2V_l \\ M_J^{45} = -P_l + \zeta_l\rho_l + P_i \end{cases} \tag{3.40}$$

- The **void fraction equation** gives:

$$V_i(U)\frac{\partial \alpha_g}{\partial x} = 0 \;\Rightarrow\; \begin{cases} M_J^{51} = M_J^{52} = M_J^{53} = M_J^{54} = 0 \\ M_J^{25} = V_i \end{cases} \tag{3.41}$$

Finally, the Jacobian M_J can be written in quasi-linear formulation as:

$$M_J = \begin{bmatrix} 0 & 1 & 0 & 0 & 0 \\ M_J^{21} & M_J^{22} & 0 & 0 & M_J^{25} \\ 0 & 0 & 0 & 1 & 0 \\ 0 & 0 & M_J^{43} & M_J^{44} & M_J^{45} \\ 0 & 0 & 0 & 0 & V_i \end{bmatrix} \tag{3.42}$$

b. Determination of the characteristics of the system

The system of equations can be written as:

$$\frac{\partial U}{\partial t} + A(U)\frac{\partial U}{\partial x} = 0. \tag{3.43}$$

Observing that

$$det(\lambda I - A) = P_5(\lambda),$$

where

$$P_5(\lambda) = [(\lambda - V_l)^2 - \zeta_l][(\lambda - V_g)^2 - \zeta_g](\lambda - V_i),$$

the five roots of P_5 are:

$$V_k \pm c_k \quad \text{and} \quad V_i. \tag{3.44}$$

where V_i is the interface velocity, defined next Section. A detailed analysis of the eigenvectors [34] states that the model is *hyperbolic* if and only if one of the following cases is obtained:

$$\begin{cases} \text{Case1} & : \quad c_k^2 = (V_k - V_i)^2, (k = g, \text{ and } k = l),\ P_g = P_l = 0; \\ \text{Case2} & : \quad c_g^2 = (V_g - V_i)^2, P_g = 0; \\ \text{Case3} & : \quad c_l^2 = (V_l - V_i)^2, P_l = 0; \\ \text{Case4} & : \quad c_k^2 \neq (V_k - V_i)^2, (k = g, \text{ and } k = l); \end{cases}$$

The model has therefore always real eigenvalues, but there are cases, namely when $c_k^2 = (V_k - V_i)^2$ (for $k = g$ or $k = l$), when the number of eigenvectors drops from 5 to 4 leading to an incomplete set. Thus the system is no longer hyperbolic.

3.4 The constitutive equations

The constitutive equations, or closure laws, replace the information that has been lost during the averaging process of the local instantaneous conservation equations. They model the interphase and wall to fluid momentum transfer and the interphase mass transfer. For an isothermal flow with no mass transfer, only the momentum transfer needs to be considered. Thermodynamic equations of state and interfacial velocity and pressure are also formulated in this section.

3.4.1 Thermodynamic

Pressure is associated to temperature and density of the fluid, governed by an equation of state. As the assumption of barotropic flow is made, the pressure only depends on the density ρ_k:

$$P_k = P_k(\rho_k) \tag{3.45}$$

and we assume the simplified linear thermodynamic relations

$$\rho_k = \rho_{k,0} + \frac{P_k - P_{k,0}}{c_k^2}. \tag{3.46}$$

The compressibilities are constant, given by

$$\frac{\partial P_k}{\partial \rho_k} = c_k^2. \tag{3.47}$$

Throughout this work, different parameters are used for the liquid phase depending of the nature of the liquid and the operating pressure. For instance, the parameters for water at atmospheric pressure are:

$$P_{l,0} = 1bar = 10^5 Pa, \tag{3.48}$$
$$\rho_{l,0} = 1000kg/m^3 \tag{3.49}$$

and

$$c_l^2 = 10^6 m/s. \tag{3.50}$$

For the gas phase we set

$$P_{g,0} = 0, \tag{3.51}$$
$$\rho_{l,0} = 0 \tag{3.52}$$

and

$$c_g^2 = 10^5 m/s. \tag{3.53}$$

This constitutes an approximate model of the behaviour of air and water.

3.4.2 Interface velocity and pressure

The non-conservative terms in the system 3.19 are always present whatever the physical processes occurring at the interfaces. Their modelling must be achieved with great care in order to obtain a well-posed mathematical model, i.e. hyperbolic. In two-phase gas-liquid flows, many authors consider the liquid as incompressible. They write that liquid and interfacial pressures equal the gas pressure, yielding ill-posed mathematical models. This results in numerical instabilities and in the necessity of using an extremely large numerical viscosity. In this approach, since each phase is assumed compressible, there is no need to make an artificial choice. There are different definitions of interfacial parameters [37, 34, 14, 7]. A way to estimate the mean interfacial pressure is to consider it like Ransom & Hicks [34] proposed,

$$P_i(U) = P_g - \delta \frac{\alpha_g \rho_g \alpha_l \rho_l V_R^2}{\alpha_g \rho_g + \alpha_l \rho_l} \tag{3.54}$$

where V_R is the relative velocity, and δ has to be chosen greater than 1 to ensure the hyperbolicity of the system [7]. In the computations, $\delta = 2.0$.

The second difficulty with non-conservative terms and equations lies in the estimate of the

averaged interfacial velocity. In most references, V_i is taken equal to the incompressible or the less compressible phase [37, 36, 5]. In the simulations, the interface velocity [29] is estimated as the velocity of the centre volume:

$$V_i = \sum_k \alpha_k V_k \tag{3.55}$$

3.4.3 Body forces

The body forces contain the gravity term and the buoyancy effect. For each phase, this force reads:

$$B_{fg} = \alpha_g \rho_g g \sin\beta - C_B(\rho_l - \rho_g)V_b g \tag{3.56}$$
$$B_{fl} = \alpha_l \rho_l g \sin\beta - C_B(\rho_l - \rho_g)V_b g \tag{3.57}$$

where g is the gravity $g = 9.81\, m.s^{-1}$; C_B is the coefficient of buoyancy, equal to 0 for stratified flow and 1 for bubbly and slug flow.
The bubble axial rise velocity V_b is given as follows:

$$V_b = 1.53 \left[\frac{\sigma g \Delta\rho}{\rho_l^2}\right]^{1/4} \sin\beta \tag{3.58}$$

3.4.4 Shear forces

There are three shear stresses (τ_{wg}, τ_{wl} and τ_i) involved in the momentum balances of a two-phase flow model. Appropriate shear stresses relationships are therefore very important in order to achieve satisfactory predictions in liquid holdup and pressure drop for the flow system. Various correlations either theoretical [39] or based on experimental studies [3] in gas-liquid pipe flows are available for shear stress evaluations. However no general model that could predict frictional pressure drop and liquid holdup for any flow situations exists. Instead the literature provides successful models, dependent of the flow and sometimes also dependent of the pipe size and the nature of the fluid.

The interfacial and wall shear forces are expressed as in by:

$$F_{wk} = \frac{-\tau_{wk} S_k}{A} \tag{3.59}$$

and

$$F_i = \frac{-\tau_i S_i}{A} \tag{3.60}$$

respectively. In the above equations, A is the pipe cross-sectional area, S_i and S_k designate the interfacial width and the phase wetted perimeter respectively, as shown in Fig.3.1.

The interfacial and wall shear stresses τ_i and τ_{wk} are commonly related to the dynamic pressure by:

$$\tau_{wg} = \frac{1}{2} f_g \rho_g V_g |V_g| \qquad \tau_{wl} = \frac{1}{2} f_l \rho_l V_l |V_l| \tag{3.61}$$

$$\tau_i = \frac{1}{2} f_i \rho_g V_r |V_r| \quad \text{with} \quad V_r = V_g - V_l \tag{3.62}$$

where the coefficients f_g, f_l and f_i are defined as the Darcy or Fanning friction factors and V_r is the relative or slip velocity between the phases.

In what follows, we detail the wall and interfacial friction factors used in this study.

3.4.4.1 Wall friction factors

In two-phase flow computations, it is common practise to model the fluids wall friction factors using single-phase pipe flow formulae. Therefore, we firstly present some useful formulae validated for single-phase pipe flow.

The oldest, simple and widely used formula for friction factors in single phase turbulent flow is the Blasius equation. This formula, which is only valid for smooth walls and for Reynolds number (Re) ranging between 2.5×10^3 and 10^5, can be found in most fluid dynamics textbooks and is given by:

$$f = 0.0792 Re^{-0.25} \tag{3.63}$$

For fully developed laminar flow in a round tube a simple formula derived by Hagen and Poiseuille is generally used for practical applications and is given by:

$$f = \frac{16}{Re} \tag{3.64}$$

New correlations have been derived from two-phase flow studies and a slightly different expression of the Blasius equation has been used in the work of Taitel and Dukler [39]. The expression for the gas wall friction factor is:

$$f_g = C_g Re_g^{-n_g} \tag{3.65}$$

where the Reynolds number is defined as:

$$Re_g = \frac{D_g V_g \rho_g}{\mu_g}. \tag{3.66}$$

The hydraulic diameter D_g is defined as:

$$D_g = \frac{4 A_g}{(S_g + S_i)}. \tag{3.67}$$

The coefficients C_g and n_g respectively have values of 0.046 and 0.25 if the flow is turbulent ($Re_g > 2100$), or 16 and 1 if the flow is laminar ($Re_g \leq 2100$).

The correlation used for calculating the liquid-wall friction factor f_l, is that of Kowalski [22]. It is expressed as:

$$f_l = c_l(\alpha_l Re_{sl})^{n_l} \tag{3.68}$$

where c_l and n_l are correlated coefficients, α_l is the liquid volume fraction and Re_{sl} is a Reynolds number based on the liquid superficial velocity and the pipe inner diameter.

Kowalski proposed to use $c_l = 0.263$ and $n_l = -0.5$. Hand [16] found that this choice was not in agreement with his experimental results and suggested the values 0.062 and -0.139 respectively for c_l and n_l.

Many models have been proposed to calculate the gas or liquid wall friction factors, but for turbulent flow, most of the recent models seem to use the modified Blasius equation (Eq. 3.63) for gases and the Kowalski type of equation (Eq. 3.68) for liquids. In the laminar region, the Hagen-Poiseuille equation (Eq. 3.64) is still preferred.

3.4.4.2 Interfacial friction factors

It is clear in the literature that the formulation of the interfacial friction factor is of crucial importance when modelling two-phase flows. Many authors ([11, 16]) have discussed the various approaches and models, which have been used in the past to evaluate the interfacial shear stress. Some of those useful for stratified and bubbly flow will be mentioned below.

The drag force is the most important force and highly depends on the flow regime considered. There is no unique expression. It has however been described as a combination of two terms [24]

$$T_{ki}^D = -\tau_{ki}\frac{\partial \alpha_k}{\partial x} + M_{ki} \tag{3.69}$$

where the first term represents the effect of the interfacial stress, important in separated flow. The second term is an averaged particle drag, important for dispersed flow.

a. Stratified flow

For stratified or annular flow, its expression becomes [24]:

$$T_{ki}^D \cong -\tau_{ki}\frac{\partial \alpha_k}{\partial x} = -\tau_{ki}\frac{S_i}{A} \tag{3.70}$$

with A is the pipe cross section, and S_i is the wetted perimeter of the interface (or gas core, in the case of annular flow). And the interfacial shear stress τ_i is function of the friction factor f_i.

$$\tau_{ki} = \frac{1}{2} f_i \rho_g (V_g - V_l)|V_g - V_l| \tag{3.71}$$

Correlation	Drag Coefficient C_D	Parameters
Govier & Aziz [4]	$C_D = \begin{cases} 180 & Re_B < 0.1 \\ \frac{18+2.7Re_B^{0.687}}{Re_B} & 0.1 \leq Re_B \leq 989 \\ 0.33 & Re_B > 989 \end{cases}$	$Re_B = \frac{\rho_l D_b \lvert V_r \rvert}{\mu_l}$
Wallis [43]	$C_D = \max(\min(\max(C_{D1}, C_{D2}), C_{D3}), \min(C_{D4}, C_{D5}, C_{D6}))$ $C_{D1} = \frac{16}{Re_B}; C_{D2} = \frac{13.6}{Re_B^{0.8}}$ $C_{D3} = \frac{48}{Re_B}; C_{D4} = \frac{Eo}{3}$ $C_{D5} = 0.47Eo^{0.25}\sqrt{We}; C_{D6} = \frac{8}{3}$	$Re_B = \frac{\rho_l D_b \lvert V_r \rvert}{\mu_l}$ $Eo = g\lvert\rho_l - \rho_g\rvert \frac{D_b^2}{\sigma}$ $We = \rho_l V_r^2 \frac{D_b}{\sigma}$
Ishii & Zuber [20]	$C_D = \begin{cases} \frac{24}{Re_B}(1 + 0.1Re_B^{0.75}) & N_{visc} < N_{crit} \\ \frac{8}{3} D_b \sqrt{\frac{g\lvert\rho_l - \rho_g\rvert}{\sigma}} & \text{otherwise} \end{cases}$	$Re_B = \frac{\rho_l D_b \lvert V_r \rvert}{\mu_l}$ $N_{visc} = \frac{\mu_l}{\left(\rho_l \sigma \left(\frac{\sigma}{g\lvert\rho_l - \rho_g\rvert}\right)^{1/2}\right)^{1/2}}$ $N_{crit} = 36\sqrt{2}\left(\frac{1+0.1Re_B^{0.75}}{Re_B^2}\right)$
Clift [8], Delnoij et al.[9] and Park et al.[28]	$C_D = \begin{cases} 240 & Re_B < 0.1 \\ \frac{24+3.6Re_B^{0.687}}{Re_B} & 0.1 \leq Re_B \leq 1000 \\ 0.44 & Re_B > 1000 \end{cases}$	$Re_B = \frac{\rho_l D_b \lvert V_r \rvert \alpha_l^{2.5\mu_m}}{\mu_l}$ $\mu_m = \frac{\mu_g + 4\mu_l}{\mu_g + \mu_l}$

Table 3.1 : *Summary of friction factors for bubbly flow (Part1)*

Correlation	Drag Coefficient C_D	Parameters
Tomiyama [41] and Gupta et al.[15]	$C_D = \max(C_{D1}, C_{D2})$ $C_{D1} = \frac{24+3.6Re_B^{0.687}}{Re_B}; C_{D2} = \frac{\frac{8}{3}Eo}{Eo+4}$	$Re_B = \frac{\rho_l D_b \lvert V_r \rvert}{\mu_l}$ $Eo = g\lvert\rho_l - \rho_g\rvert\frac{D_b^2}{\sigma}$
Kurten [8, (p110)]	$C_D = \begin{cases} \min\left(0.28 + \frac{6}{\sqrt{Re_B}} + \frac{21}{Re_B}, 2400\right) & Re_B \leq 3 \times 10^5 \\ 0.19 & \text{otherwise} \end{cases}$	$Re_B = \frac{\rho_l D_b \lvert V_r \rvert}{\mu_l}$
Brauer [8, (p110)]	$C_D = \begin{cases} \min\left(0.4 + \frac{4}{\sqrt{Re_B}} + \frac{21}{Re_B}, 2400\right) & Re_B \leq 3 \times 10^5 \\ 0.19 & \text{otherwise} \end{cases}$	$Re_B = \frac{\rho_l D_b \lvert V_r \rvert}{\mu_l}$
Tomiyama2 [40]	$C_D = \max(C_{D3}, \min(C_{D1}, C_{D2}))$ $C_{D1} = \frac{24+3.6Re_B^{0.687}}{Re_B}; C_{D2} = \frac{72}{Re_B}$ $C_{D3} = \frac{\frac{8}{3}Eo}{Eo+4}$	$Re_B = \frac{\rho_l D_b \lvert V_r \rvert}{\mu_l}$ $Eo = g\lvert\rho_l - \rho_g\rvert\frac{D_b^2}{\sigma}$

Table 3.2 : *Summary of friction factors for bubbly flow (Part2)*

Correlation	Drag Coefficient C_D	Parameters
Richter [35]	$C_D = \begin{cases} \frac{24}{Re_B} & Re_B < 0.5 \\ 0.4 + \frac{24+\frac{24}{Re_B}}{Re_B} & 0.5 \leq Re_B \leq 1000 \\ 0.42 & 1000 \leq Re_B \leq 10000 \\ 0.13 & Re_B > 10000 \end{cases}$	$Re_B = \frac{\rho_l D_b \lvert V_r \rvert}{\mu_l}$
Peebles [30]	$C_D = \max(\max(C_{D1}, C_{D2}), \min(C_{D3}, C_{D4}))$ $C_{D1} = \frac{24}{Re_B}$ $C_{D2} = \frac{18.7}{Re_B^{0.68}}$ $C_{D3} = 0.0275 \times Eo \times We^2$ $C_{D4} = 0.82 \times Eo^{0.25} \times \sqrt{We}$	$Re_B = \frac{\rho_l D_b \lvert V_r \rvert}{\mu_l}$ $Eo = g\lvert\rho_l - \rho_g\rvert \frac{D_b^2}{\sigma}$ $We = \rho_l V_r^2 \frac{D_b}{\sigma}$
Chawla [18]	$\begin{cases} C_D = \max(C_{D1}, \min(C_{D2}, C_{D3})) \\ C_{D1} = \frac{24}{Re_B} + \frac{24}{Re_B^{0.25}} \\ C_{D2} = \frac{2}{3}\sqrt{Eo} \\ C_{D3} = \frac{8}{3} \end{cases}$	$Re_B = \frac{\rho_l D_b \lvert V_r \rvert}{\mu_l}$ $Eo = g\lvert\rho_l - \rho_g\rvert \frac{D_b^2}{\sigma}$

Table 3.3 : *Summary of friction factors for bubbly flow (Part3)*

The simplest relation for interfacial friction factor is the one used by Taitel & Dukler ([39]). They proposed to take the interfacial shear stress equal to the gas shear stress for smooth and wavy stratified flow.

$$f_i = f_g \tag{3.72}$$

b. Bubbly flow

In this study, we consider bubbly flow as an inhomogeneous flow and assume that the bubbles are rigid and non-deformable spheres.

In bubbly flow modelling, the drag force is the predominant term of the interfacial momentum term. One can also find additional terms acting at the interface, such as virtual mass forces, lift effects. Virtual mass forces can be understood by considering the change in kinetic energy around an accelerating sphere. The acceleration of a bubble gas in a fluid induces a resisting force corresponding to one half the mass of the displaced fluid times the acceleration of the sphere. Effects of virtual mass was reviewed by Drew *et al.* [10]. In general, the inclusion of the virtual mass terms does not perceptibly change the numerical results but the computation efficiency of the solution can be dramatically affected, leading to a change from a hybrid type to a hyperbolic system [33]. However, the hyperbolicity of the system is already ensured with the compressibility therefore virtual mass are neglected in this study.

Lift effects arise from the interaction between bubble and the velocity difference leading to shear stress in liquid. The choice of a lift coefficient is strongly dependent to the nature of the problem, and is not discussed in this work.

Therefore the drag force is the only force considered in the interfacial shear stress in this study. There are many formulations available in the literature. They are all based on the Reynolds number for bubbly flow. Some use the Eotvos number in their formulation as well. A parametric study on the gas velocity and density, holdup, Reynolds number and drag coefficient has been carried out in order to analyse the behaviour of the main variables (see Fig. 3.2 and Fig. 3.3). Two formulations have been investigated in the present work. The formulation from Clift has been chosen for its simplicity to compute and its wide use in the literature. The second one follows the work of Ishii and Tomiyama. Its main advantage over Clift's is the introduction of the interfacial area per unit volume into the formulation which describes the structure of a flow.

The interfacial friction factor described in Park *et al* [28] has the following definition:

$$f_i = \frac{3}{4}\frac{C_D \alpha_g \rho_l}{D_b} \tag{3.73}$$

As summarised in Table 3.4, several formulations are also available for the bubble diameter D_b. With the conditions of the test-cases for vertical bubbly flow, each formulation gives a bubble diameter in the same range and we choose to consider a constant diameter with the Clift-Park formulation.

The formulation proposed by Ishii *et al.* [19] and detailed by Hatta [17] introduces the

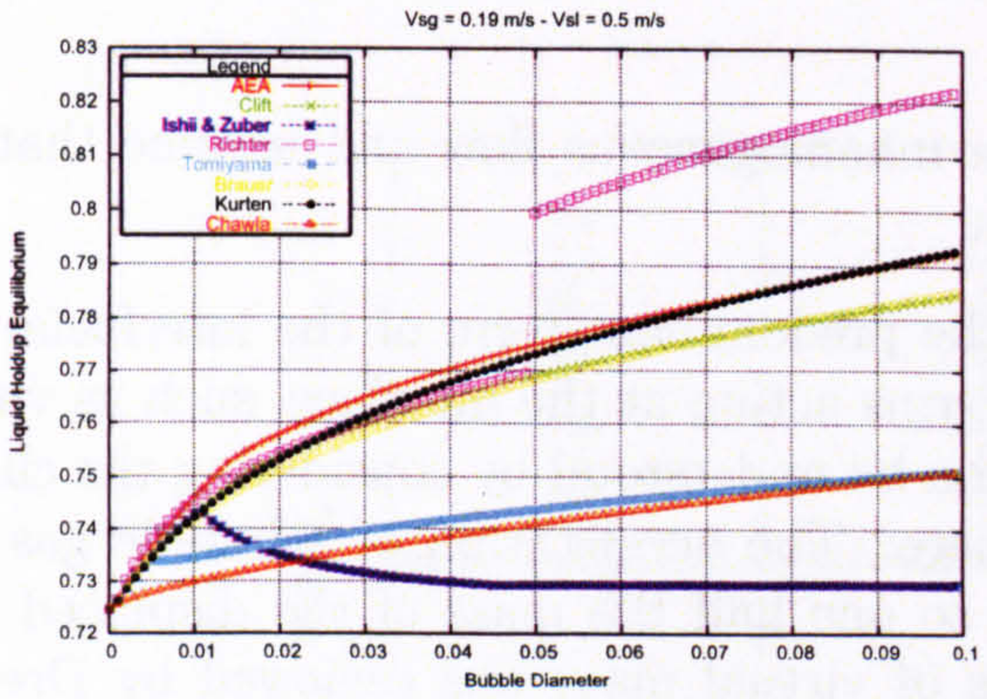

(a) α_l vs D_b

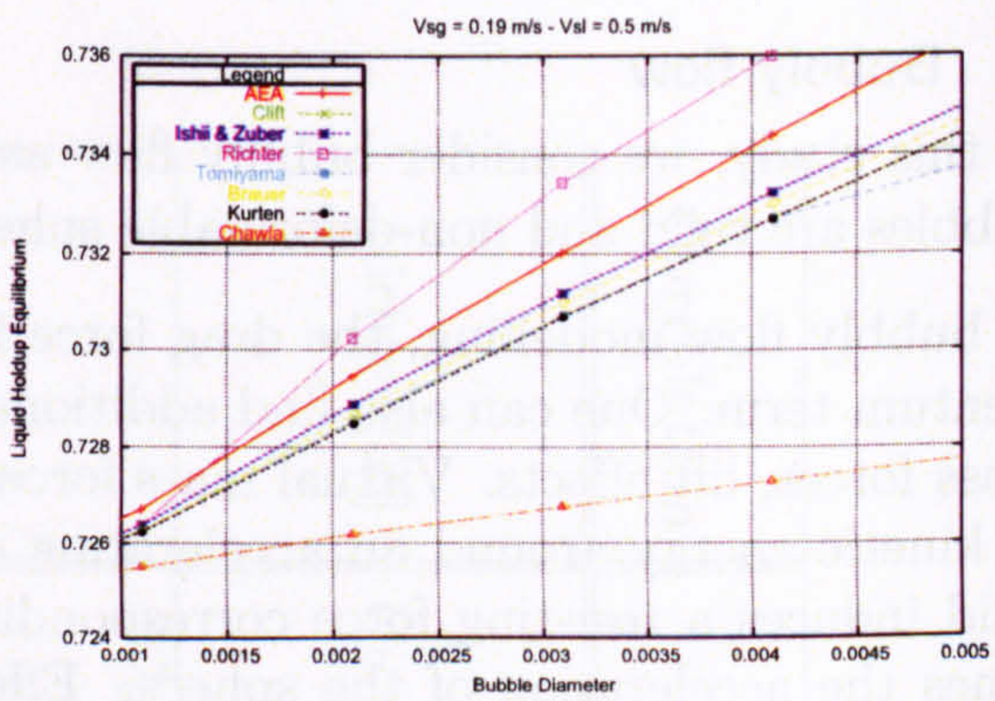

(b) α_l vs D_b

Figure 3.2 : *Parametric study - α_l vs D_b.*

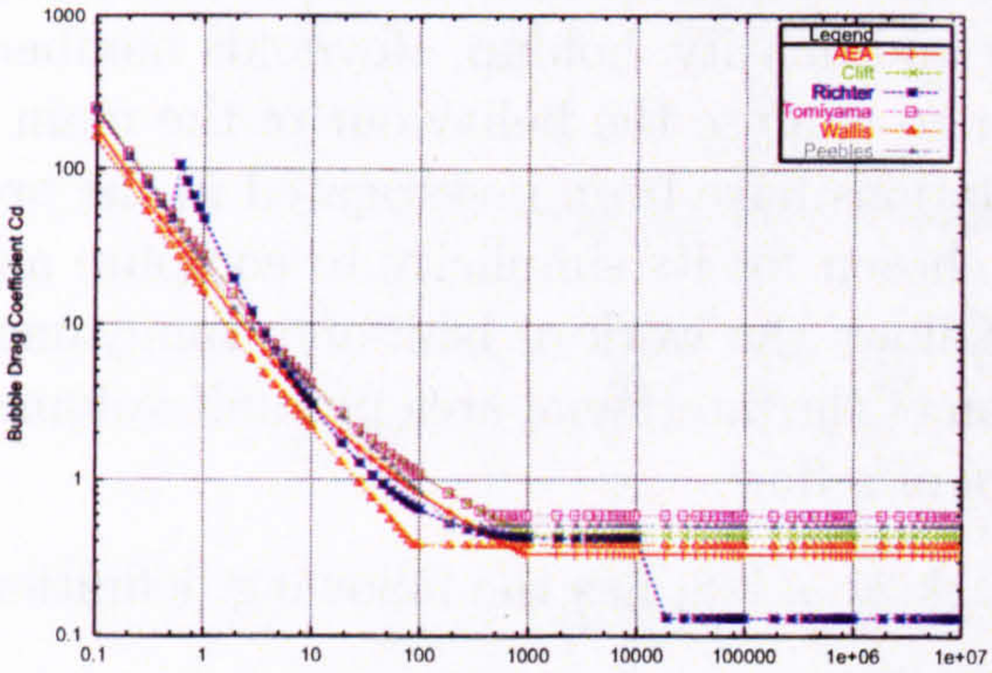

(a) C_D vs Re_b

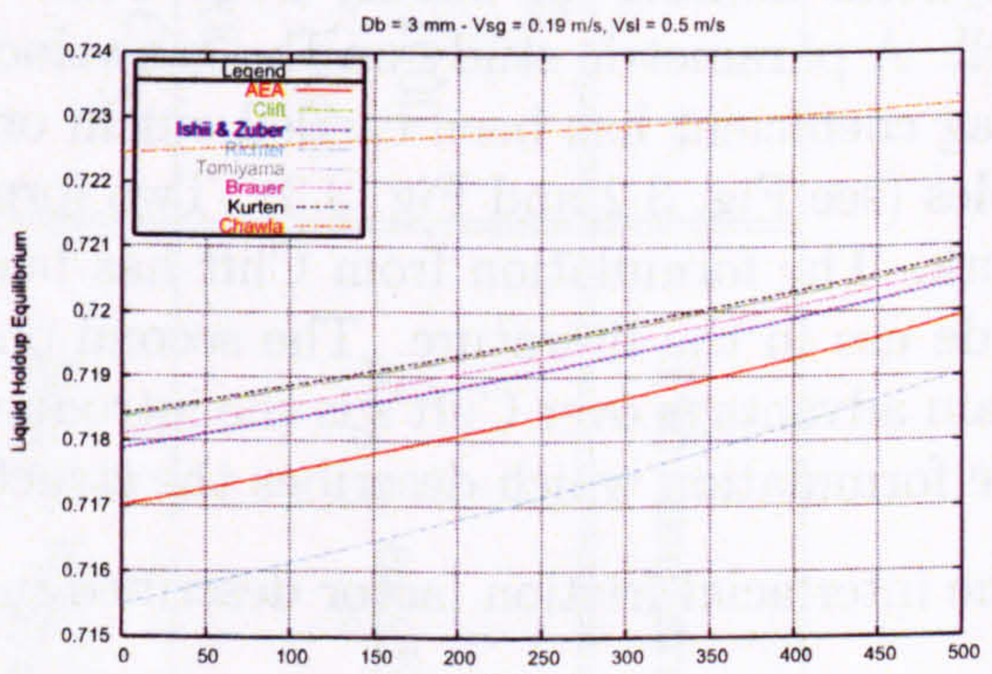

(b) α_l vs ρ_g

Figure 3.3 : *Parametric study.*

Correlation	Bubble Diameter
Tomiyama [41]	$D_b = \text{constant}$
Abdul-Majeed [1]	$D_b = \sqrt{3\dfrac{\sigma}{g\lvert\rho_l - \rho_g\rvert}}$
AEA Technology [2]	$D_b = We_B \dfrac{\sigma}{g\lvert\rho_l - \rho_g\rvert}$
Masella [23]	$D_b = \left(\dfrac{\sigma}{\rho_l V_r^2}\right)^{0.25}$
Hatta [17]	$D_b = d_{sm} = 1.06\left(\dfrac{\sigma}{\rho_l^{1/3}}\right)^{1/3}\left(\dfrac{\alpha_g\alpha_l D^2}{(V_{sg}+V_{sl})(-dP/dx)}\right)^{2/9}$

Table 3.4 : *Summary of bubble diameters.*

interfacial area concentration a_{ig} which characterises the structure of a flow. Its mechanism modelling is based upon the geometrical parameters, gas volumetric fraction and flow [17].

$$f_i = \frac{1}{8} C_D a_{ig} \rho_l \tag{3.74}$$

and

$$C_D = \frac{C_{D0}}{\sqrt{\alpha_l}} \tag{3.75}$$

with C_{D0} is the drag coefficient given by Tomiyama [40]. The interfacial area per unit volume is given for bubbly flow as follows,

$$a_{ig} = \frac{6\alpha_g}{d_{sm}} \tag{3.76}$$

Again the following relation

$$d_{sm} = 1.06\left(\frac{\sigma}{\rho_l^{1/3}}\right)^{1/3}\left(\frac{\alpha_g\alpha_l D^2}{(V_{sg}+V_{sl})(-dP/dx)}\right)^{2/9} \tag{3.77}$$

is given by Kocamustafaogullari et al [21].

For vertical flows, the pressure gradient term in relation 3.77 is composed of a frictional term, a gravitational term and a acceleration term. It is defined as

$$\frac{dP}{dx} = \left(\frac{dP}{dx}\right)_f + \left(\frac{dP}{dx}\right)_{acc} + \left(\frac{dP}{dx}\right)_{grav} \tag{3.78}$$

The pressure drop caused by elevation change depends on the density of the two-phase mixture and is usually calculated using a liquid holdup value. Except for conditions of high velocity, most of the pressure drop in vertical flow is caused by this component. The pressure drop caused by friction losses requires evaluation of a two-phase friction factor. The pressure drop caused by accelerating the fluids is sometimes considered negligible and is usually calculated only for cases of high velocities. Hence the acceleration term is neglected in this study. The equation for the pressure gradient becomes:

$$\frac{dP}{dx} = \left(\frac{dP}{dx}\right)_f + \left(\frac{dP}{dx}\right)_{grav} \tag{3.79}$$

$$= -\frac{1}{2D} f_m \rho_m V_m^2 - \rho_m g \sin\beta \tag{3.80}$$

in which ρ_m is the mixture density given by

$$\rho_m = \alpha_l \rho_l + \alpha_g \rho_g \tag{3.81}$$

and V_m denotes the superficial mixture velocity given by

$$V_m = \alpha_l V_l + \alpha_g V_g. \tag{3.82}$$

The friction factor f_m can be predicted by the Blasius type equation based upon the superficial mixture velocity V_m and the liquid kinematic viscosity μ_l, that is:

$$f_m = C_1 \left(|V_m| D \frac{\rho_l}{\mu_l} \right)^{-n_1}. \tag{3.83}$$

In the calculations, C_1 and n_1 are taken as 0.45 and 0.2.

Another advantage of using this formulation Eq. 3.74 is that the interfacial area per unit a_i can be evaluated for different flow regimes (bubbly, slug and churn flow). It therefore enables the introduction of a simple flow regime transition mechanism by switching to the appropriate interfacial area per unit a_i.

3.4.4.3 Two-phase pipe correlations wetted perimeters

a. Stratified flow

Assuming flat gas-liquid interface and knowing the pipe diameter and the liquid height, the wetted perimeters are given by the following relations:

$$S_l = D\left(\pi - cos^{-1}\left(2\frac{h_l}{D} - 1\right)\right) \tag{3.84}$$

$$S_g = \pi D - S_l \tag{3.85}$$

$$S_i = D\sqrt{1 - \left(2\frac{h_l}{D} - 1\right)^2} \tag{3.86}$$

where h_l is the liquid height in the pipe.

b. Bubbly flow - dispersed flow

In that situation, the wetted perimeters are given by the following relations:

$$S_g = 0 \tag{3.87}$$
$$S_l = 2\pi R \tag{3.88}$$
$$S_i = 2\pi R_b \tag{3.89}$$

3.5 Summary

We have described in this chapter the specific models that have been implemented for the applications presented later in the thesis. The first model we describe here is a two-equation incompressible model. The second model is a two-pressure two-fluid compressible model with five equations (TPM5) and an instantaneous relaxation procedure.

For a better understanding of the main characteristics of the model and for numerical purposes, a stability analysis and more precisely the hyperbolicity condition has been performed. Hence we have shown that the two-pressure model is hyperbolic with its eigenvalues always real. There is yet one case case where the system is no longer hyperbolic, when two eigenvectors are equal implying an incomplete set of eigenvectors.

Furthermore the model TPM5 is always hyperbolic under the condition of finite pressure relaxation, i.e. when the pressures remain not equal at each time. When using an instantaneous relaxation, one can argue that the model becomes a single-pressure model after the relaxation process. Therefore the model characteristics are still the same but the limit validity is similar to single-pressure and pressure-free models, ie critical flow above the same inviscid Kelvin-Helmholtz (IKH) condition.

Additionally, one might be warned against the fact that it has been found that even hyperbolic models can become unstable when algebraic terms, such as drag forces, are added to the momentum equations [32]. Therefore hyperbolicity is necessary but not sufficient for stability.

Closure laws were thoroughly detailed too. Momentum transfer was formulated for different flow regimes. General thermodynamic equation of state and interfacial laws used in the present work were also described. To formulate an accurate mathematical model for two-phase flows with the assumptions mentioned in the introduction of this chapter, accurate estimations of wall friction factors as well as the gas-liquid interfacial friction factor is required. Therefore, we also reviewed and studied in this chapter the different available models in the literature and the combined effect of the liquid wall friction and the interface friction which represent the most uncertain parameters in the modelling of two-phase flows.

References - 3

[1] ABDUL-MAJEED, G. H. Liquid slug holdup in horizontal and slightly inclined two-phase slug flow. *Journal of Petroleum Science and Engineering 27* (2000), 27–32.

[2] AEA TECHNOLOGY. PLAC user guide and technical manual.

[3] ANDRITSOS, N., AND HANRATTY, T. Influence of interfacial waves in stratified gas-liquid flows. *AIChE Journal 33*, 3 (1987), 444–454.

[4] AZIZ, K., AND GOVIER, G. *The Flow of Complex Mixtures in Pipes.* Van Nostrand Reinhold, New York, 1972.

[5] BAER, M., AND NUNZIATO, J. A two-phase mixture theory for the deflagration to detonation (ddt) transition in reactive granular materials. *Int. J. Multiphase Flow 12-6* (1986), 861–889.

[6] BAGNERINI, P., COQUEL, F., MARMIGNON, C., AND ROUY, S. Un principe de relaxation sur le taux de vide dans les modeles diphasiques moyennes. pre-print, Office National des Etudes et Recherches Aerospatiales.

[7] BESTION, D. The physical closure laws in the CATHARE code. *Nuclear engineering design 124* (1990), 229–245.

[8] CLIFT, R., GRACE, J., AND WEBER, M. *Bubbles, Drops, and Particles.* Academic Press, New York, 1978.

[9] DELNOIJ, E., KUIPERS, J., AND VAN SWAAIJ, W. Dynamic simulation of gas-liquid two-phase flow: effect of column aspect ratio on the flow structure. *Chem. Eng. Sci. 52*, 21/22 (1997), 3759–3772.

[10] DREW, D., CHENG, L., AND LAHEY JR, R. The analysis of virtual mass effects in two-phase flow. *Int. J. of Multiphase Flow 5* (1979), 233–242.

[11] ESPEDAL, M. *An Experimental Investigation of Stratified Two-Phase Pipe Flow at Small Inclinations.* Ph.D. thesis, Department of Applied Mechanics, Norwegian University of Science and Technology (NTNU), Trondheim, Norway, 1998.

[12] EVJE, S., AND FLÅTTEN, T. Hybrid flux-splitting schemes for a common two-fluid model. *J. Comp. Phys. 192* (2003), 175–210.

[13] GHIDAGLIA, J.-M., KUMBARO, A., AND LE COQ, G. On the numerical solution to two fluid models via a cell centered finite volume method. *Eur. J. Mech. B, Fluids (France) 20*, 6 (2001), 841–67.

[14] GLIMM, J., S. D., AND SHARP, D. Two-phase modelling of a fluid mixing layer. *Journal of Fluids Mechanics 378* (1999), 119–143.

[15] GUPTA, P., ONG, B., AL-DAHHAN, M., DUDUKOVIC, M. P., AND TOSELAND, B. Hydrodynamics of churn turbulent bubble columns: gasâĂŞliquid recirculation and mechanistic modeling. *Catalysis Today 64*, 3-4 (January 2001), 253–269.

[16] HAND, N. P. *Gas-liquid co-current flow in a horizontal pipe.* Ph.D. thesis, Queen's University Belfast, Northern Ireland, 1991.

[17] HATTA, N., FUJIMOTO, H., ISOBE, M., AND KANG, J.-S. Theoretical analysis of flow characteristics of multiphase mixtures in a vertical pipe. *Int. J. of Multiphase Flow 24*, 4 (1998), 539–561.

[18] ISHII, M., AND CHAWLA, T. Local drag laws in dispersed two-phase flow. *ANL-79-105* (1979). (NUREG/CR-1230).

[19] ISHII, M., MISHIMA, K., KATAOKA, I., AND KOCAMUSTAFAOGULLARI, G. Two-fluid model and importance of the interfacial area in two-phase flow analysis. In *9th U.S. National Congress of Applied Mechanics* (1982), pp. 73–80. Ithaca, New-York.

[20] ISHII, M., AND ZUBER, N. Drag coefficient and relative velocity in bubbly, droplet or particulate flows. *AIChE Journal 25*, 5 (September 1979), 843–855.

[21] KOCAMUSTAFAOGULLARI, G., HUANG, W., AND RAZI, J. Measurement and modeling of average void fraction, bubble size and interfacial area. *Nucl. Eng. and Des. 148* (1994), 437–453.

[22] KOWALSKI, J. E. Wall and interfacial shear stress in stratified flow in a horizontal pipe. *AIChE Journal 33*, 2 (1987), 274–281.

[23] MASELLA, J. M. *Quelques Méthodes Numériques Pour Les Ecoulements Diphasiques Bi-Fluide En Conduites Pétrolières.* Ph.D. thesis, Université Pierre et Marie Curie, Paris VI, 1997.

[24] MISHIMA, K., AND ISHII, M. Flow regime transition criteria for two-phase flow in vertical pipes. *Int. J. of Heat Mass Trans 27* (1984), 723–734.

[25] NIU, Y. Advection upwinding splitting method to solve a compressible two-fluid model. *Int. J. Numer. Meth. Fluids 36* (2001), 351–371.

[26] OMGBA-ESSAMA, C. *Numerical modelling of transient gas-liquid flows (application to stratified and slug flow regimes).* Ph.D. thesis, Cranfield University, Applied Mathematics & Computing group, 2004.

[27] PAILLÈRE, H., CORRE, C., AND GARCIA CASCALES, J. On the extension of the AUSM+ scheme to compressible two-fluid models. *Computers and Fluids 32*, 6 (July 2003), 891–916.

[28] PARK, J. W., DREW, D. A., AND LAHEY JR., R. T. The analysis of void wave propagation in adiabatic monodispersed bubbly two-phase flows using an ensemble-averaged two-fluid model. *Int. J. of Multiphase Flow 24* (1998), 1205–1244.

[29] PAUCHON, C., AND BANERJEE, S. Interphase momentum interaction effects in the averaged multifluid model. *Int. J. of Multiphase Flow 12*, 4 (1986), 559–573.

[30] PEEBLES, F., AND GARBER, H. Studies on the motion of gas bubbles in liquids. *Chem. Eng. Prog. 49*, 2 (1953), 88–97.

[31] PRESS, W. *Numerical Recipes in Fortran90*, 2nd ed. Cambridge University Press, 1996.

[32] PROSPERETTI, A., AND SATRAPE, J. Stability of two-phase flow models. *IMA Volumes in Mathematics and its applications* (1990), 98–117. Springer-Verlag, London.

[33] RAMSHAW, J., AND TRAPP, J. Characteristics, stability, and short-wavelength phenomena in two-phase flow equation systems. *Nuclear Science Engeneering 66* (1978), 93–102.

[34] RANSOM, V., AND HICKS, D. Hyperbolic two-pressure models for two-phase flow. *Journal of Comp. Phys. 53* (1984), 124–151.

[35] RICHTER, S., FLEISCHER, S. ARITOMI, M., AND HAMPEL, R. Transient two-phase flow in arbitrary inclined tubes caused by depressurization of liquid with dissolved gases. *International Journal of Heat and Mass Transfer 44*, 1 (January 2001), 1–15.

[36] SAINSAULIEU, L. Finite volume approximations of two phase-fluid flows based on approximate roe-type riemann solver. *J. Comp. Phys. 121* (1995), 1–28.

[37] SAUREL, R., AND ABGRALL, R. A multiphase godunov method for compressible multifluid and multiphase flows. *Journal of Computational Physics 150* (1999), 425–467.

[38] STUHMILLER, J. H. Influence of interfacial pressure forces on the character of two-phase flow model equations. *Int J Multiphase Flow 3*, 6 (Dec 1977), 551–560.

[39] TAITEL, Y., AND DUKLER, A. A model for predicting flow regime transitions in horizontal and near horizontal gas-liquid flow. *AIChE Journal 22*, 1 (1976), 47–55.

[40] TOMIYAMA, A. Struggle with computational bubble dynamics. In *Third Int. Conf. on Multiphase Flow, ICMF 98* (8-12 June 1998). Lyon, France.

[41] TOMIYAMA, A., KATAOKA, I., AND SAKAGUCHI, T. Drag coefficients of bubbles, 1st report: Drag coefficient of a single bubble in a stagnant liquid. *Trans. JSME 61*, B (1995), 23–57.

[42] TOUMI, I., AND KUMBARO, A. An approximate linearized Riemann solver for a two-fluid model. *J. Comp. Phys. 124* (1996), 286–300.

[43] WALLIS, G. The terminal speed of single drops or bubbles in an infinite medium. *Int. J. of Multiphase Flow 1* (1974), 491–511.

[44] WATSON, M. Non-linear waves in pipeline two-phase flows. In *Proceedings of 3rd Conference on Hyperbolic Problems* (11-15 June 1990).

[45] WHITHAM, G. *Linear and Nonlinear Waves.* Wiley, New York, 1974.

4 Numerical method

4.1 Overview

A numerical method is required in order to solve the set of differential equations derived in Chapter 3. The procedure consists of the following steps:

a) The pipeline is subdivided into finite volumes.

b) The partial differential equations are integrated over the finite volumes and over time to yield to a set of non-linear algebraic equations. The boundary conditions are also put into an algebraic form.

c) The system of equations can be solved numerically by replacing the partial derivatives by finite differences on a discrete numerical grid, and then advancing the solution in time via some numerical schemes algorithm. The process is repeated until steady-state or the desired time level is reached.

This chapter describes in Section 4.3, the finite difference grid conventions used in the present work. Section 4.4 will give details on the conservative numerical schemes, while the non-conservative schemes are described in Section 4.5. The two main constraints, namely the time step size and the boundary conditions, are discussed in Section 4.6.

Finally numerical simulations of classical benchmarks will be the focus of Section 4.7. The various flow conditions they examine, sometimes extreme, enable to thoroughly validate the model, and provide confidence in the convergence and accuracy of the numerical methods, as analytical solutions are known for selected cases.

4.2 Numerical approach

For the past few decades, large efforts of numerical modelling of compressible flow have been developed. Although research performed important advances for the simulation of single-phase flows and has led to stability, robustness and accuracy in numerical solvers, a unique scheme for all models still does not exist.

It is known that systems of PDEs from two-phase modelling involve higher computational

cost and numerical difficulties: conditionally hyperbolicity and non-conservative terms. Therefore numerical schemes need to be dissipative enough to produce stable oscillation free discrete solutions. This is in opposition to the usual expectation of accuracy of the numerical scheme. This is why we will not talk about high order of accuracy in this work.

However numerical methods have been successfully developed for two-fluid models computations. Those schemes are classified into two categories based on the treatment of the pressure term. The first class concerns segregated pressure–based solution algorithms and have been reviewed by Darwish *et al.* [2]. They usually use a Finite Volume approach on staggered grid and one can find among them the inter-phase slip algorithm (IPSA) developed by Spalding [21, 20] and its variants, the implicit multi-field algorithms (IMF) devised by Harlow and Amsdem [5], Stewart [24], and Mahaffy [10]. However while a widespread information is available on single fluid solution procedures, much less information is available for a multi-fluid solution algorithm. This has limited their implementation to a small community, slowed their development and isolated them from the newer developments in single fluid algorithms (all speed flows, pressure-weighted interpolation method,...)

Hence many researchers developed a second class of algorithms which includes approximate Riemann solvers, upwind methods, flux splitting methods and other high resolution shock-capturing methods [22, 27, 25, 17] for two-phase models. All these methods are generally adaptation of single-phase versions, and reviewing these single-fluid schemes is beyond the scope of this thesis.

There is no clear indication in the literature for the selection of an appropriate numerical scheme for two-phase flow applications. Therefore, the approach adopted here is based on this second group of methods because they are much simpler to implement, and their widespread description makes them easy to generalise, which is an important development aspect when designing a solution algorithm for many mathematical models.

However, the purpose of this work is not to create new numerical schemes but use or combine existing ones so that they can handle the mathematical model we chose to represent two-phase flows. For the determination of successful numerical schemes, one has to investigate different mathematical concepts such as consistency, stability and convergence. These studies are not included in this chapter but can easily be found in the various numerical textbooks available [6, 7]. Therefore the following sections only describe the formulation of the numerical schemes implemented in the solver.

4.3 The Finite Volume discretisation

The resolution algorithm is based on a Finite Volume approach. The pipeline is divided into regular cells $M_i = [X_{i-\frac{1}{2}}, X_{i+\frac{1}{2}}]$, the length of each cell being Δx. The unknowns are located at the centre of the cell and let U_i be the variable associated to M_i.

Arising from the derivation of the Navier-Stokes equations, the two-fluid models presented

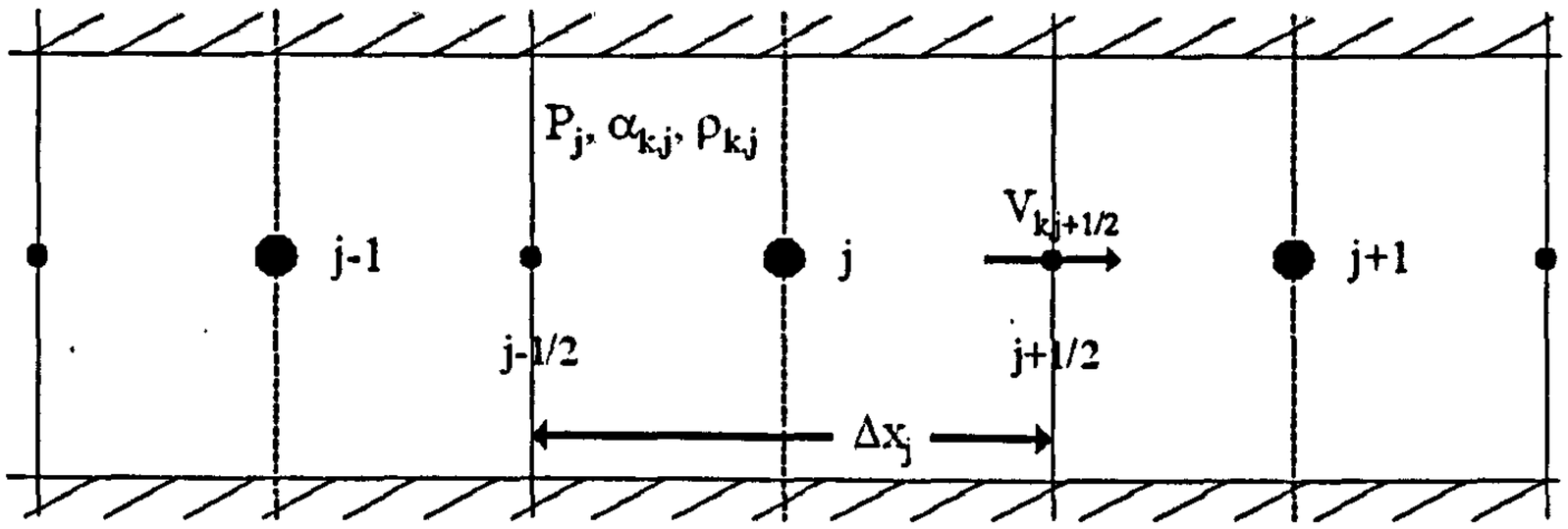

Figure 4.1 : *Finite volume cell.*

in Chapter 3 can be written in the general form:

$$\frac{\partial \mathbf{U}(x,t)}{\partial t} + \frac{\partial \mathbf{F}(\mathbf{U}(x,t))}{\partial x} + \mathbf{H}(\mathbf{U}(\mathbf{x},\mathbf{t}))\frac{\partial \mathbf{U}(x,t)}{\partial x} = \mathbf{S}(\mathbf{U}(x,t)) \tag{4.1}$$

where $\mathbf{U}(x,t)$ represents the vector of conservative variables, $\mathbf{F}$, the flux vector function defining a system of conservation laws and $\mathbf{S}$, the source term vector. $\mathbf{H}\frac{\partial \mathbf{U}}{\partial x}$ is a matrix-vector product that contains all the non-conservative terms present in the model. The general form of equations leads to the general discretisation scheme:

$$U_i^{n+1} = U_i^n - \frac{\Delta t}{\Delta x}\left(\tilde{F}^n_{i+\frac{1}{2}} - \tilde{F}^n_{i-\frac{1}{2}}\right) + \Delta t\left(H\frac{\partial U}{\partial x}\right)_i^n + \Delta t S_j^n \tag{4.2}$$

where $\tilde{F}$ is the numerical flux. Many discretisation schemes are available.

4.4 Conservative schemes

The numerical flux schemes that we used in this work can be classified, in terms of accuracy, as first order, second order and high-resolution methods (second order in the smooth regions of the solution and first order where there are discontinuities or shocks in the solution).

They are often grouped into central and upwind methods. Central schemes offer a general-purpose solver for hyperbolic conservative systems describing multiphase flow phenomena and were selected because there is no requirement of any algebraic manipulation of the Jacobian of the flux vector, or any need of the expressions of the characteristics of the model.

However a lack of accuracy or robustness can be encountered with central schemes and characteristic based schemes have also been implemented to counter-balance these problems.

Central schemes are first described in the following, while the second part presents the characteristics based schemes that were implemented for the present study. A detailed description of the scheme developed for the compressible model closes the section.

4.4.1 Centred schemes

4.4.1.1 Lax-Friedrichs Scheme

The Lax-Friedrichs scheme is the most common explicit numerical scheme found in the literature [26]. It belongs to the Lax family and is first-order in time and second-order in space for independent variations of Δx and Δt. In practise, one operates at a fixed Courant number and the Lax-Friedrichs is thus to be considered as a first order both in space and time. The flux is formulated as follows:

$$\tilde{F}_{i+\frac{1}{2}} = \frac{1}{2}\left(F_{i+1}^n + F_i^n\right) - \frac{\Delta x}{2\Delta t}\left(U_{i+1}^n - U_i^n\right) \tag{4.3}$$

where the numerical flux value at mesh point i is defined by $F_i^n = F(U_j^n)$ with the function F representing the physical expression of the flux terms described by the mathematical model.

This scheme is not applied in its original form any longer due to its lack of accuracy, but several variants with improved accuracy are still in use. It represents however an interesting base for comparisons with other schemes and can be used as intermediate step in higher-order schemes such as in the Richtmyer Lax-Wendroff two-step method described in the following.

4.4.1.2 Lax-Wendroff Scheme

The second-order accurate scheme of Lax and Wendroff is the most important of the space-centred schemes due to its uniqueness for linear equations. Many variants can be defined for non-linear fluxes: they all reduce to the same linear form though and are generally structured as predictor-corrector algorithms with an explicit time integration.

The original scheme requires the evaluation of the Jacobian A which can be a costly operation in a practical computations. Therefore a two-step approach has been introduced to avoid the estimations of such matrices [6]. Two different versions of the two-step scheme exist in the literature, the McCormack version, which is popular in the Aeronautics community, and the Richtmyer version, which is described here. These two versions lead to almost identical solutions, however the Richtmyer which in our view seems the most simpler to implement is presented here. It is characterised by an intermediate first step applying the Lax-Friedrichs scheme to midpoints and a second step that is the application of a leapfrog scheme (for a description of the leapfrog scheme, see for instance the book by Hirsch [6]). In the conservative formulation, this second order flux scheme is defined by:

$$\tilde{F}_{i+\frac{1}{2}} = F(\overline{U}_{j+1/2}^n) \tag{4.4}$$

with the intermediate state

$$\overline{U}_{j+1/2}^n = U_{j+1/2}^n - \frac{1}{2}\frac{\Delta x}{\Delta t}\left(F(U_{i+1}^n) - F(U_i^n)\right) + \frac{\Delta t}{2}S(U_{j+1/2}^n) \tag{4.5}$$

$$U_{j+1/2}^n = \frac{1}{2}\left(U_{i+1}^n + U_i^n\right) \tag{4.6}$$

This scheme is considered to be at the basis of many predictor/corrector methods that are able to handle non-linearities straightforward.

4.4.1.3 The FORCE Scheme

To avoid the extreme diffusion of Lax-Friedrichs scheme and the dispersion (characterised by oscillations or numerical spurious waves) of Richtmyer schemes, the simple deterministic First-ORder CEntred scheme (FORCE) was proposed by Toro [26]. The numerical flux is basically the arithmetic mean of the fluxes for the Lax-Friedrichs and Richtmyer flux:

$$\tilde{F}^{force}_{i+\frac{1}{2}} = \frac{1}{2}\left(\tilde{F}^{LF}_{i+\frac{1}{2}} + \tilde{F}^{Ri}_{i+\frac{1}{2}}\right). \tag{4.7}$$

The advantage of this scheme is that it is significantly simple and efficient [26].

4.4.1.4 The FCT Scheme

The Flux-Corrected Transport (FCT) scheme is based on a two-step Lax-Wendroff method. It can be seen as a "predictor/corrector" method in which a large amount of diffusion is introduced in the predictor stage, and an almost equal amount of anti-diffusion is introduced in the corrector stage. However, the anti-diffusion is limited so that no new maximum or minimum can appear in the solution, nor can existing extrema be accentuated.

It is defined as follows :

$$\tilde{F}_{i+\frac{1}{2}} = F^{c}_{AD,i+\frac{1}{2}} - F^{D}_{i+\frac{1}{2}} \tag{4.8}$$

with

$$F^{D}_{i+\frac{1}{2}} = \eta(U_i - U_{i-1}) \tag{4.9}$$

$$F^{c}_{AD,i+\frac{1}{2}} = S\max\left(0, \min\left(S\Delta Q_{i-\frac{1}{2}}, \min\left(|F^{AD}_{i+\frac{1}{2}}|, S\Delta Q_{i+\frac{1}{2}}\right)\right)\right) \tag{4.10}$$

where

$$\Delta Q_{i+\frac{1}{2}} = \overline{U}_{i+1} - \overline{U}_i \tag{4.11}$$

$$S = sign\left(1, F^{AD}_{i+\frac{1}{2}}\right) \tag{4.12}$$

$$F^{AD}_{i+\frac{1}{2}} = \eta\Delta Q_{i+\frac{1}{2}} \tag{4.13}$$

$$\overline{U}^{n+1}_{i} = U^{n}_{i} - \tau\left(F\left(U^{n+\frac{1}{2}}_{i+\frac{1}{2}}\right) - F\left(U^{n+\frac{1}{2}}_{i-\frac{1}{2}}\right)\right) \tag{4.14}$$

and

$$U_{i+\frac{1}{2}}^{n+\frac{1}{2}} = \overline{\overline{U}}_i^{n+1} - (f_{i+\frac{1}{2}}^{n+1} - f_{i-\frac{1}{2}}^{n+1}) \tag{4.15}$$

$$f_{i+\frac{1}{2}}^{n+1} = \eta\Big(\overline{\overline{U}}_{i+1}^{n+1} - \overline{\overline{U}}_i^{n+1}\Big) \tag{4.16}$$

$$\overline{U}_i^{n+1} = U_i^n - \tau\Big(F\Big(U_{i+\frac{1}{2}}^{n+\frac{1}{2}}\Big) - F\Big(U_{i-\frac{1}{2}}^{n+\frac{1}{2}}\Big)\Big) \tag{4.17}$$

$$\overline{\overline{U}}_i^{n+1} = \overline{U}_i^{n+1} + \eta\Delta x^2 \frac{\overline{U}_{i+1}^{n+1} - 2\overline{U}_i^{n+1} + \overline{U}_{i-1}^{n+1}}{\Delta x^2} \tag{4.18}$$

with $\eta = \frac{1}{8}$, $\tau = \frac{\Delta t}{\Delta x}$ and $f_{i+\frac{1}{2}}^n$ is an approximation of $F(u)$ at position $i\Delta x$ and time $n\Delta t$ (more details can be found in Sod [19]). Comparative studies of high-resolution schemes show that FCT scheme is one of the most competitive for flows with severe gradients. However for our compressible model, the use of FCT becomes more difficult due to the presence of non-conservative terms.

4.4.2 Characterised-based schemes

4.4.2.1 The Rusanov Scheme

In this paragraph, the basic formulation of the Rusanov scheme is outlined. For more details, refer to Saurel [18]. The formulation is written as follows:

$$\tilde{F}_{i+\frac{1}{2}} = \frac{1}{2}\Big(F_i + F_{i+1}\Big) - \frac{\lambda_{max}}{2}\Big(U_{i+1} - U_i\Big) \tag{4.19}$$

$$\lambda_{max} = \lambda_{max}\Big(\frac{U_{i+1} + U_i}{2}\Big) \tag{4.20}$$

with λ_{max} is the maximum eigenvalue of $\dfrac{\partial F(U)}{\partial U}$.
The discretisation in time is totally explicit. It is often associated with the PFM-2 model and has shown to be less diffusive than the FCT scheme.

4.4.2.2 TVD Lax-Friedrichs scheme

The TVD Lax-Friedrichs scheme is a characterised based scheme that uses the maximum eigenvalue of the model studied. It is a high-resolution scheme that uses the Total Variation Diminishing (TVD) approach [6]. Given a mesh function $u^n = u_i^n$, the total variation of u^n is:

$$TV(u^n) = \sum_{i=-\infty}^{\infty} |u_{i+1}^n - u_i^n| \tag{4.21}$$

and a scheme is said TVD if

$$TV(u^{n+1}) \geq TV(u^n). \tag{4.22}$$

The expression of the TVDLF numerical flux is given by:

$$\tilde{F}^{TVDLF}_{j+\frac{1}{2}} = \frac{1}{2}\Big[F(U^L_{j+\frac{1}{2}}) + F(U^R_{j+\frac{1}{2}})\Big] - \frac{1}{2\tau}\Phi^{LR}_{j+\frac{1}{2}} \tag{4.23}$$

with $\tau = \frac{\Delta x}{\Delta t}$.
The left and right state vectors U^L and U^R are formed from an intermediate state $U^{n+\frac{1}{2}}$ and the limited differences $\delta\bar{U}^n$ as:

$$U^L_{j+\frac{1}{2}} = U^{n+\frac{1}{2}}_j + \frac{1}{2}\delta\bar{U}^n, \qquad U^R_{j+\frac{1}{2}} = U^{n+\frac{1}{2}}_{j+1} - \frac{1}{2}\delta\bar{U}^n \tag{4.24}$$

The intermediate step value is given by:

$$U^{n+\frac{1}{2}}_j = U^n_j - \frac{\tau}{2}(F(U^n_j + \frac{1}{2}\delta\bar{U}^n) - F(U^n_j - \frac{1}{2}\delta\bar{U}^n)) + \frac{\delta}{2}S(U^n) \tag{4.25}$$

The dissipative limiter Φ^{LR} is used to reduce the numerical diffusion. The idea of flux limiters is to apply more artificial diffusion in regions of large gradients and less in smooth regions. In this case, it follows the relation:

$$\Phi^{LR} = \frac{\Delta t}{\Delta x}\lambda^{max}_{j+\frac{1}{2}}(U^R - U_L) \tag{4.26}$$

with the relation

$$\lambda^{max}_{j+\frac{1}{2}} = \max_{k=1,neq}\left|\lambda_k\Big(\frac{U^L + U^R}{2}\Big)\right| \tag{4.27}$$

There are several flux limiter functions defined in the literature [3, 26]; we opt for the Minmod function which reads:

$$\delta\bar{U}^n_j = Minmod(U^n_j - U^n_{j-1}, U^n_{j+1} - U^n_j) \tag{4.28}$$

$$Minmod(x,y) = \frac{1}{2}(sign(x) + sign(y))\min(|x|,|y|) \tag{4.29}$$

4.4.2.3 HLL scheme

Another scheme used in this work is the one from Harten, Lax and van Leer, referred to as the HLL scheme, with the following formulation:

$$\tilde{F}^{hll}_{j+\frac{1}{2}} = \begin{cases} F_L & if \quad 0 \le S_L, \\ \frac{S_R F_L - S_L F_R + S_L S_R(U_R - U_L)}{S_R - S_L} & if \quad S_L \le 0 \le S_R, \\ F_R & if \quad 0 \ge S_R \end{cases} \tag{4.30}$$

where S_L and S_R are the fastest signal velocities arising from the solution of the Riemann problem assumed to be known of the two states U_L and U_R. U^{hll} is the constant state vector given by:

$$U^{hll} = \frac{S_R U_R - S_L U_L + F_L - F_R}{S_R - S_L}. \tag{4.31}$$

4.4.3 Hybrid flux-splitting schemes: AUSM formulation

The numerical method used in the present study describes the characteristic-based upwind differencing schemes detailed in [18, 27, 23]. Many of them are categorised as flux difference splitting (FDS) and are based on Godunov-type schemes and Roe-type schemes. They are robust and accurate, but rather time-consuming since they are based on matrix calculations [25, 27]. The flux vector splitting (FVS) method is based on scalar calculations, hence they are more efficient than FDS schemes on a per cell basis but they are also much more diffusive.

During the last few years, many authors have worked on combining both methods: get the efficiency of FVS to the accuracy of FDS. These are called hybrid flux-splitting schemes and are commonly termed the Advection Upstream Splitting Methods (AUSM) family [9, 8]. Based on the upwind concept, they provide an alternative approach to other upwind methods such as Godunov method, FDS methods by Roe, and Solomon and Osher, or FVS methods by Van Leer, and Steger and Warming.

The AUSM first recognises that the inviscid flux consists of two physically distinct parts, convective and pressure fluxes. The convective flux is associated with the flow speed, while the pressure flux is with the acoustic speed. The main reasons for the interest in this upwind differencing scheme are its simplicity and hence its low computational cost, its generalisation to arbitrary equations of state (EOS) and its accuracy. Indeed, the AUSM+ scheme [8] and related mass flux schemes such as AUSMDV, are known to be as accurate as flux difference splitting methods such as Roe's or Osher's approximate Riemann solvers without the cost of field-by-field wave decompositions. Of particular importance is the ability of the scheme to capture contact discontinuities exactly, thereby making the scheme very attractive for viscous flow computations.

Among the several schemes developed with the Advection Upstream Splitting Method (AUSM) [9, 8, 15], two schemes AUSMD* and AUSMV* have been reviewed. Both schemes derive from the AUSM schemes where D and V respectively denote flux-difference biased scheme and flux-vector biased schemes [4].

From the finite volume discretisation (Eq.4.3), the numerical flux $\mathbf{F}$ can be split into a convective flux and a pressure term flux:

$$F_{j+1/2} = F^c_{j+1/2} + F^p_{j+1/2} \tag{4.32}$$

where

$$F^c = \begin{pmatrix} \rho_g \alpha_g V_g \\ \rho_l \alpha_l V_l \\ \rho_g \alpha_g V_g^2 \\ \rho_l \alpha_l V_l^2 \end{pmatrix} \text{ and } F^p = \begin{pmatrix} 0 \\ 0 \\ \alpha_g \Delta P \\ \alpha_l \Delta P \end{pmatrix} \tag{4.33}$$

Hence the mass flux and momentum flux for the AUSMV* scheme are defined as follows:

$$(\rho\alpha V)_{j+1/2} = (\rho\alpha)_L \tilde{V}^+(V_L, c_{j+1/2}, \chi_L) + (\rho\alpha)_R \tilde{V}^-(V_R, c_{j+1/2}, \chi_R) \tag{4.34}$$

$$(\rho\alpha V^2)_{j+1/2} = (\rho\alpha V)_L \tilde{V}^+(V_L, c_{j+1/2}, \chi_L) + (\rho\alpha V)_R \tilde{V}^-(V_R, c_{j+1/2}, \chi_R) \tag{4.35}$$

and the AUSMD* scheme reads:

$$(\rho\alpha V)_{j+1/2} = (\rho\alpha)_L \tilde{V}^+(V_L, c_{j+1/2}, \chi_L) + (\rho\alpha)_R \tilde{V}^-(V_R, c_{j+1/2}, \chi_R) \tag{4.36}$$

$$(\rho\alpha V^2)_{j+1/2} = \frac{1}{2}(\rho\alpha V)_{j+1/2}(V_R + V_L) - \frac{1}{2}|(\rho\alpha V)_{j+1/2}|(V_R - V_L) \tag{4.37}$$

with the splittings velocities formula to remove numerical dissipation:

$$\tilde{V}^{\pm}(V, c, \chi) = \begin{cases} \chi \bar{V}^{\pm}(V, c) + (1-\chi)\frac{V \pm |V|}{2} & \text{if} \quad |V| \leq c \\ \frac{1}{2}(V \pm |V|) & \textit{otherwise} \end{cases} \tag{4.38}$$

$$\bar{V}^{\pm}(V, c) = \begin{cases} \pm\frac{1}{4}(V \pm c)^2 & \text{if} \quad |V| \leq c \\ \frac{1}{2}(V \pm |V|) & \textit{otherwise} \end{cases} \tag{4.39}$$

and a common velocity of sound $c_{j+1/2} = max(c_j, c_{j+1})$ and

$$\chi_L = (1-\phi_L)\frac{2(\rho/\alpha)_L}{(\rho/\alpha)_L + (\rho/\alpha)_R} + \phi_L \tag{4.40}$$

$$\chi_R = (1-\phi_R)\frac{2(\rho/\alpha)_R}{(\rho/\alpha)_L + (\rho/\alpha)_R} + \phi_R \tag{4.41}$$

where ϕ is a smooth symmetric function designed to be equal to 1 near single-phase region and 0 elsewhere. The function ϕ reads

$$\phi = \exp(-\kappa_1 \alpha_g) + \exp(-\kappa_2(1-\alpha_g)) \tag{4.42}$$

with κ_1, κ_2 are constants to determine and represent the degree of smoothness of ϕ. $\kappa_1 = \kappa_2 = 200$ in the present study.

The pressure terms are written as follows

$$F^p_{j+1/2} = (\alpha\Delta P)_{j+1/2} = P^+(V_j, c_{j+1/2})(\Delta P_j) + P^-(V_{j+1}, c_{j+1/2})(\Delta P_{j+1}) \tag{4.43}$$

with

$$P^{\pm}(V, c) = V^{\pm}(V, c) = \begin{cases} \frac{1}{c}\Big(-\frac{V}{c} \pm 2\Big) & \text{if } |V| \leq c \\ \frac{1}{V} & \text{otherwise.} \end{cases} \tag{4.44}$$

Based on observations reported in [4, 15], the following can be noted:

- The AUSMD* is based on matrix calculations whereas AUSMV* is characterised by scalar calculations.

- The FVS scheme possesses outstanding stability properties. The AUSMV* keeps these properties and is able to handle very general flow conditions without introducing instabilities.

- The AUSMD* has a weak dissipation mechanism allowing it to resolve discontinuities with an accuracy comparable to the Roe schemes; however it tends to produce instabilities and overshoots.

This naturally leads Evje and Flatten [4] to develop a hybrid scheme called AUSMDV* combining the FVS/FDS fluxes as follows:

$$F_c^{AUSMDV*} = sF_c^{AUSMV*} + (1-s)F_c^{AUSMD*} \tag{4.45}$$

where s is some parameter for which many choices are possible and the optimal choice might be problem-dependent. We will not discuss this issue in full depth, but propose to use $s = \max(\phi_L, \phi_R)$ where ϕ is the function given in Eq. 4.42. In particular, this simple choice of s will make the scheme able to handle a stiff transition to one-phase flow in a stable and accurate manner. We also note that with this choice AUSMDV* will basically reduce to the stable FVS scheme near one-phase regions and the accurate AUSMD* scheme elsewhere.

For practical problems related to mass transport of oil and gas in pipelines, the main dynamics are associated with slow transients and strong discontinuities are expected to occur at the transition to one-phase flow (such discontinuities will commonly be induced by the buildup of liquid slugs). Therefore it seems that this approach can provide a good basis for methods aiming to resolve such problems.

Section 4.7 is devoted to numerical experiments whose purpose is to highlight the stability and accuracy properties of the AUSM scheme as observed when tested on several well-known flow cases.

4.5 Non-conservative schemes

The generic discretisation involves flux conservative terms that can be dealt with using numerical schemes as stated above and non-conservative terms $\mathbf{H}\frac{\partial \mathbf{U}}{\partial x}$ which are expressed differently by using spatial discretisation schemes. Different schemes are available in the literature and the ones that have been used in this work are now detailed.

4.5.1 Centred scheme

A simple central discretisation, second-order in space, has been implemented for the non-conservative terms and is given by:

$$\left(H\frac{\partial U}{\partial x}\right)_i^n = H_i^n \frac{U_{j+1}^n - U_{j-1}^n}{2\Delta x} \tag{4.46}$$

This centred spatial discretisation usually generates spurious oscillations; therefore the non-conservative terms are generally expressed using a second-order Minmod scheme described in the following sub-section, or a second centred scheme, referred to as Centred-S, given by Masella in [11]. It is expressed as:

$$\left(H\frac{\partial U}{\partial x}\right)_i^n = (H^{ave})_i^n \frac{(U^{mid})_j^n - (U^{mid})_{j-1}^n}{\Delta x} \tag{4.47}$$

where the intermediate matrix U^{ave} and vector U^{mid} are given as:

$$H^{ave} = H(U^{ave}) \tag{4.48}$$

$$(U^{ave})_i^n = \frac{1}{4}(U_{j-1}^n + 2U_j^n - U_{j+1}^n) \tag{4.49}$$

$$(U^{mid})_i^n = \frac{1}{2}(U_j^n + U_{j+1}^n) \tag{4.50}$$

This scheme shows to be more accurate than the previous one and is usually preferred in the computations.

4.5.2 MinMod scheme

This MinMod scheme was suggested by Coquel *et al.* [1] and is given by:

$$\left(H\frac{\partial U}{\partial x}\right)_i^n = \frac{H_i^n}{\Delta x}\text{Min mod}(U_j^n - U_{j-1}^n, U_{j+1}^n - U_j^n) \tag{4.51}$$

$$\text{Min mod}(x,y) = \frac{1}{2}\Big(\text{sign}(x) + \text{sign}(y)\Big)\min(|x|,|y|) \tag{4.52}$$

The scheme is first order accurate in space and was found to be very diffusive. A second formulation, second-order accurate in space, was also used in the computations. It can be expressed as:

$$\left(H\frac{\partial U}{\partial x}\right)_i^n = \frac{H_i^n}{\Delta x}\text{Min mod}(2(U_j^n - U_{j-1}^n), \frac{1}{2}(U_{j+1}^n - U_{j-1}^n), 2(U_j^n - U_{j-1}^n)) \tag{4.53}$$

$$\text{Min mod}(x,y) = \begin{cases} s.\min(|x|,|y|,|z|) & \text{if } \text{sign } x = \text{sign } y = \text{sign } z \\ 0 & \text{otherwise} \end{cases} \tag{4.54}$$

4.6 Constraints

For the numerical schemes described above, appropriate boundary conditions need to be implemented to successfully simulate physical problems. The approach adopted for these conditions is described later in this section, we first present the procedure of selecting time step Δt used by the computational schemes; whereas the mesh size Δx can be specified with no restriction, the time step size is usually restricted to the stability condition of the particular numerical scheme used.

4.6.1 Time Step Size

The mathematical models and numerical schemes described have been implemented in an adaptive mesh refinement (AMR) framework. The full details of this automatic spatial refinement technique is presented in Omgba-Essama thesis [14]. Hence, the spatial discretisation length Δx, appearing in the discrete equations, is generally dictated by the AMR scheme depending upon the desired accuracy. As for the time step Δt, the explicit formulation of the numerical schemes constrains its size with the usual Courant-Friedrichs-Levy (CFL) number. It is therefore given by:

$$\Delta t = CFL \frac{\Delta x}{\lambda_{max}^n} \tag{4.55}$$

where CFL is a positive coefficient restricted to a limiting value, usually one. The closer this coefficient is to its upper limit, the more efficient is the numerical time marching scheme. For all the numerical schemes described above, except for FCT, their stability analysis requires the value $CFL \leq 1$, but for the FCT scheme, it has been showed that the CFL value should be less than 0.5 [19].

The term λ_{max}^n in Eq. 4.55 is the largest wave speed present throughout the domain at time level n. It is estimated for the mathematical model as the largest absolute value of their analytical characteristics defined in the previous chapter. Hence, for a system of k differential equations in a computational domain with M cells (Fig. 4.2), this term is given as:

$$\lambda_{max}^n = \max_j \max_k |\lambda_j^k| \quad \text{for } j = 1, ..., M \text{ and } k = 1, ..., neq. \tag{4.56}$$

4.6.2 Boundary conditions

If a one-dimensional flow problem has to be solved in a $0 \leq x \leq L$ where $x = 0$ is the inflow boundary and $x = L$ the outflow boundary, the application of any scheme requires the knowledge of the flow variables at the points $x = 0$ and $x = L$. These boundary conditions are expected to provide for example the numerical fluxes $\tilde{F}^{1/2}$ and $\tilde{F}^{M+1/2}$, which are required by finite difference discretisation in order to advance the extreme cells 1 and M to the next time level.

For each mesh cell of the computational domain, two numerical fluxes are required to

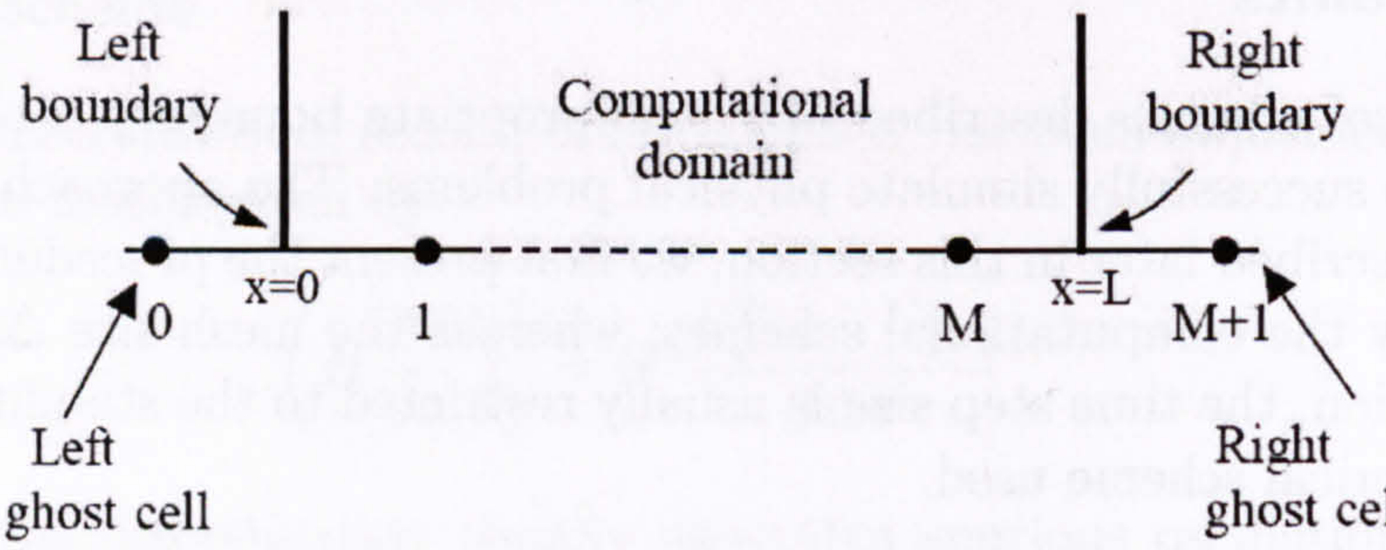

Figure 4.2 : *Boundary conditions. Fictitious or ghost cells outside the domain are created.*

update the vector solution U_j^n. However, for cells 1 and M, which are adjacent to the left and right boundaries respectively, the only known flux is the intercell flux. Hence, some special procedure needs to be implemented. Let us consider the left boundary $x = 0$. As mentioned by Toro [26], one possibility is to assume a boundary function $U_1(t)$ prescribed there. Then we could define an intercell flux at the boundary by setting $\tilde{F}_{1/2} = F(U_1(t))$.

One alternative, adopted in the present work, is to specify a fictitious (or ghost or dummy) cell to the left of the boundary $x = 0$ together with a cell average U_0^n, at each time level n, so that the missing intercell flux $\tilde{F}_{1/2}$ can be solved using (U_0^n, U_1^n). For the right boundary, we also specify a fictitious cell and a cell average U_{M+1}^n to find the intercell flux $\tilde{F}_{M+1/2}$. The imposition of boundary conditions depends entirely on the physics of the problem and have to be treated with great care.

4.7 Classical benchmarks

Considering constant challenges arising in multiphase modelling, one always has to aim for more accuracy, robustness and efficiency in the predicting tool. The AUSM numerical method proposed in [12, 8, 15, 4] is an interesting approach that offers a good compromise between the three notions previously mentioned. The aim of this section is to prove and demonstrate that this scheme and the compressible model presented earlier in the thesis do provide a considerable improvement in those terms for the simulations. A traditional way to do so is to perform classical benchmark test-cases created and developed in order to test numerics on extreme situations, such as strong pressure difference, large velocities, high density difference and near-one phase cases. Throughout these tests, our numerical method is checked to handle difficult conditions and from this strong statement, can be moved forward to industrial-type problems, such as stratified flow, vertical bubbly flow or hydrodynamic slugging.

The following test-cases are classical benchmark tests in the frame of the numerical simulation of two-phase flows.

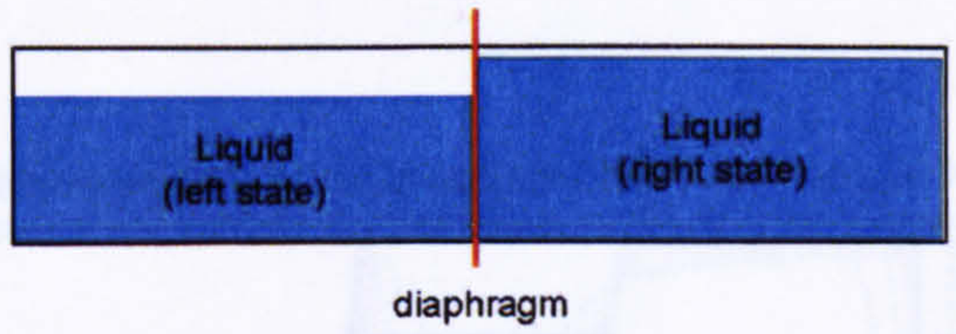

Figure 4.3 : *Two-phase Riemann problem - Toumi test-case sketch.*

4.7.1 Two-phase Riemann problems

In the first class of tests, we assume a strong disequilibrium between both phases in terms of pressure fields. These test-cases are particularly chosen to test the numerical scheme's ability to handle initial data when removed from an equilibrium state. It ensures the scheme's convergence to the same weak solutions when discontinuities in volume fraction and pressure are present.

4.7.1.1 Toumi test-case

The initial solution of the shock-tube problem is composed by two uniform states separated by a discontinuity which is usually located at the origin (Fig. 4.3). The pipe is $10\,m$ long with a diameter of $1\,m$. The initial left and right uniform states are usually introduced by giving the density, the pressure and the velocity. This initial set represents a tube where the left and the right regions are separated by a diaphragm, and filled by the same mixture in two different physical states, with a strong disequilibrium in terms of pressure field. At $t = 0$, the discontinuity between the two initial states breaks into leftward and rightward moving waves, which are separated by a contact surface. Each wave pattern is composed by a contact discontinuity in the middle and a shock or a rarefaction wave at the left and the right sides separating uniform state solution.

The problem initial conditions read for the left and the right states:

$$\begin{cases} \alpha_l^L = 0.25 & \alpha_l^R = 0.1 \\ V_g^L = 0\,m.s^{-1} & V_g^R = 0\,m.s^{-1} \\ V_l^L = 0\,m.s^{-1} \quad \text{and} & V_l^R = 0\,m.s^{-1} \\ P_l^L = 2.0 \times 10^7 Pa & P_l^R = 1.0 \times 10^7 Pa \\ T_l^L = 308.15\,K & T_l^R = 308.15\,K \end{cases} \tag{4.57}$$

The boundary conditions are open at both inlet and outlet of the pipe. The simulations are left running for 0.006 *sec*, with a series of meshes from 100 to 10000 cells.

The mesh dependency study (Fig. 4.4 to 4.6) proved the convergence of the results towards the expected answer proposed in [27]. Overshoots found with coarse meshes ceased with finer meshes. The simulations also captured the wave features created by the shock-tube

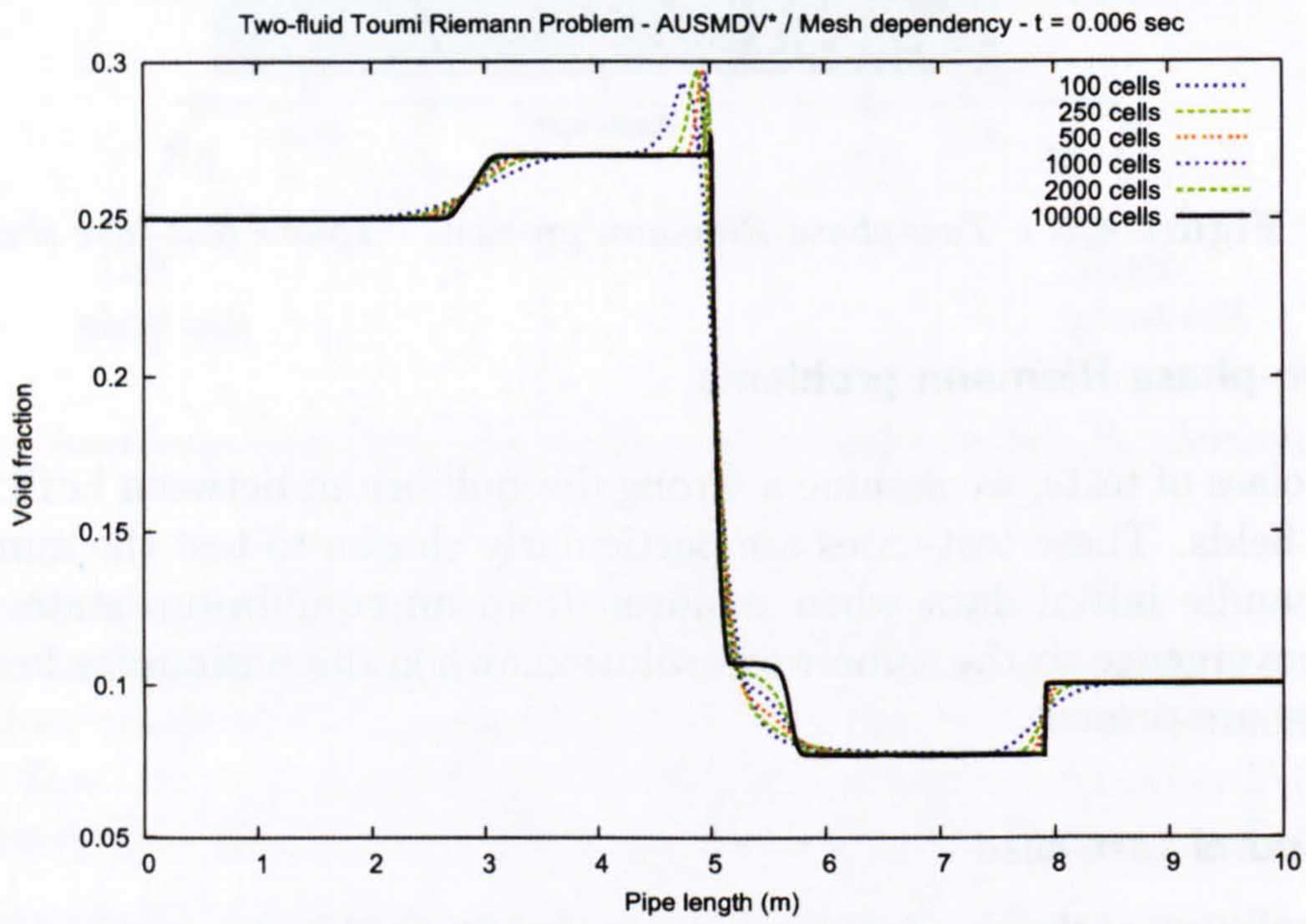

(a) α_g

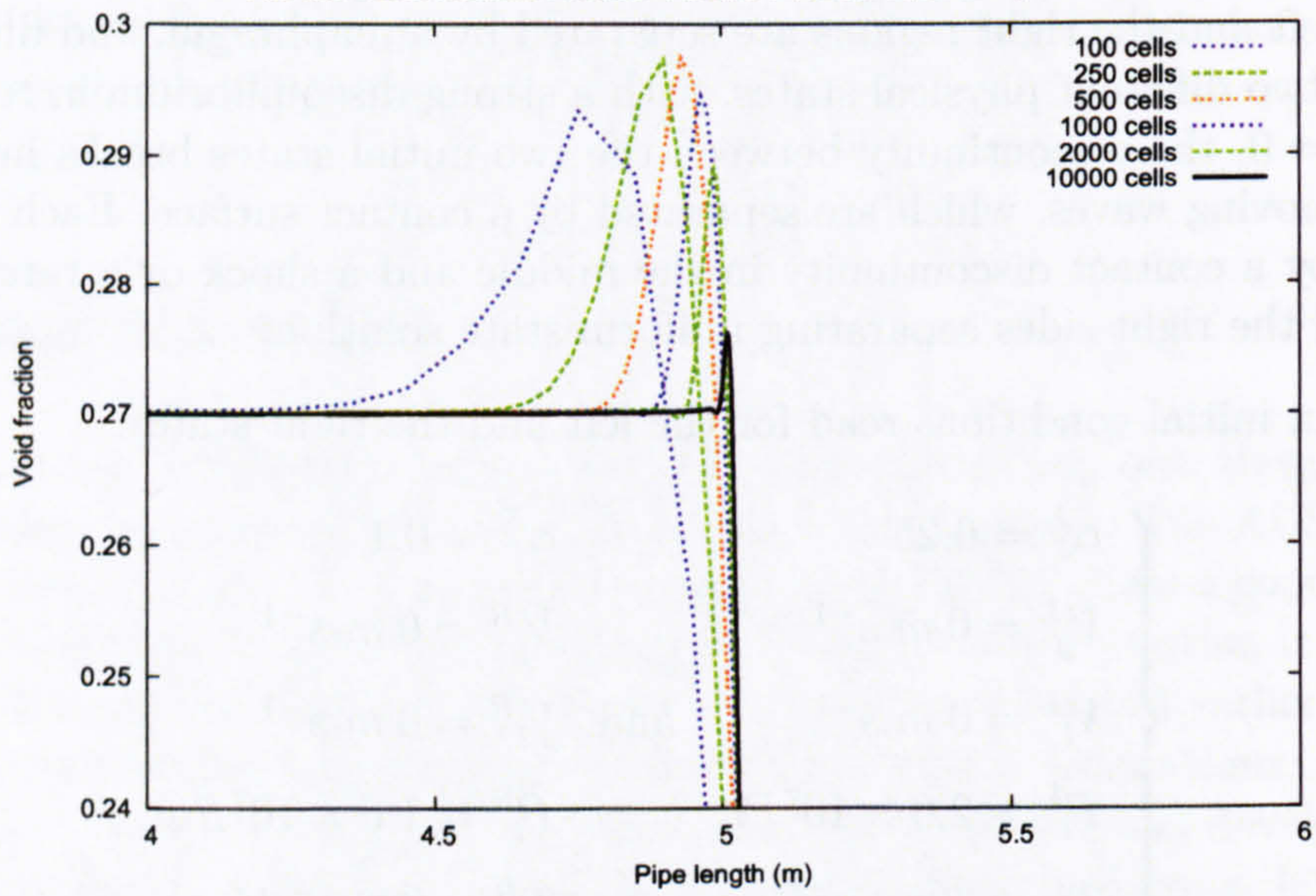

(b) Zoom

Figure 4.4 : *Two-phase Riemann problem - Toumi test-case - TPM5 model. Mesh refinement on the void fraction. Overshoots observed at the shock points tend to decrease with mesh refinement.*

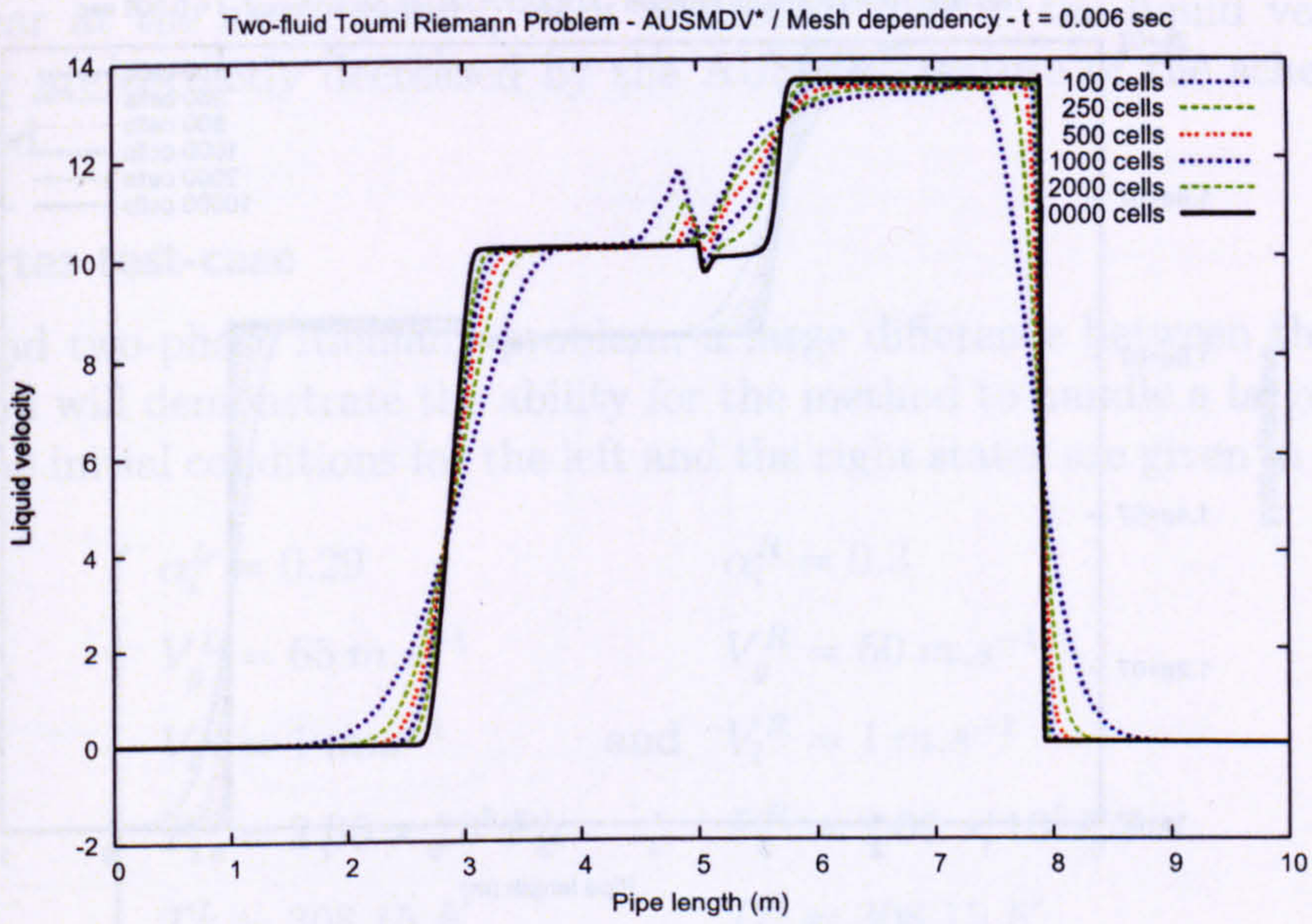

(a) V_l

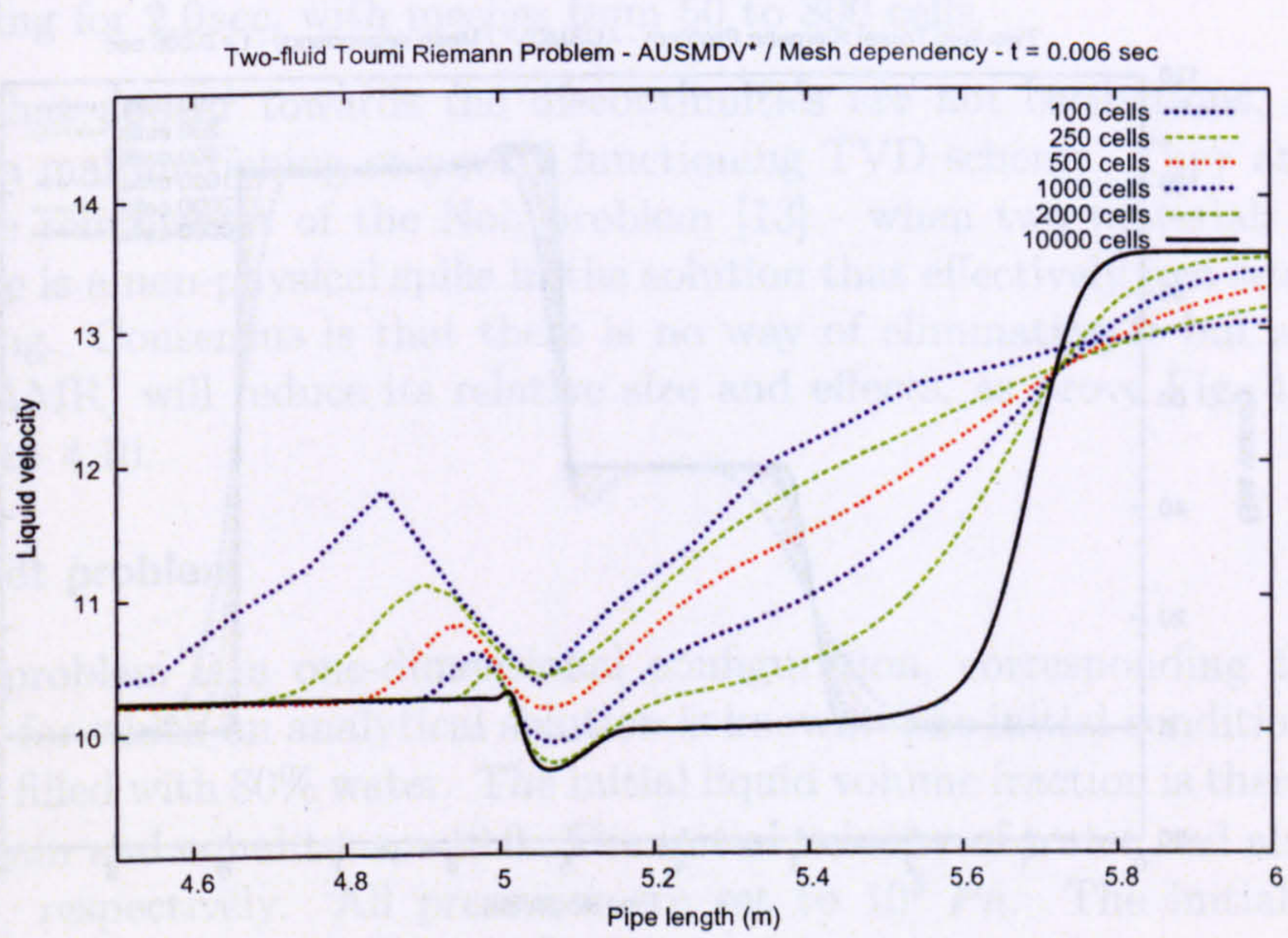

(b) Zoom

Figure 4.5 : *Two-phase Riemann problem - Toumi test-case - TPM5 model. Mesh refinement on the liquid velocity. Again refinement diminished the overshoots observed at the shock points.*

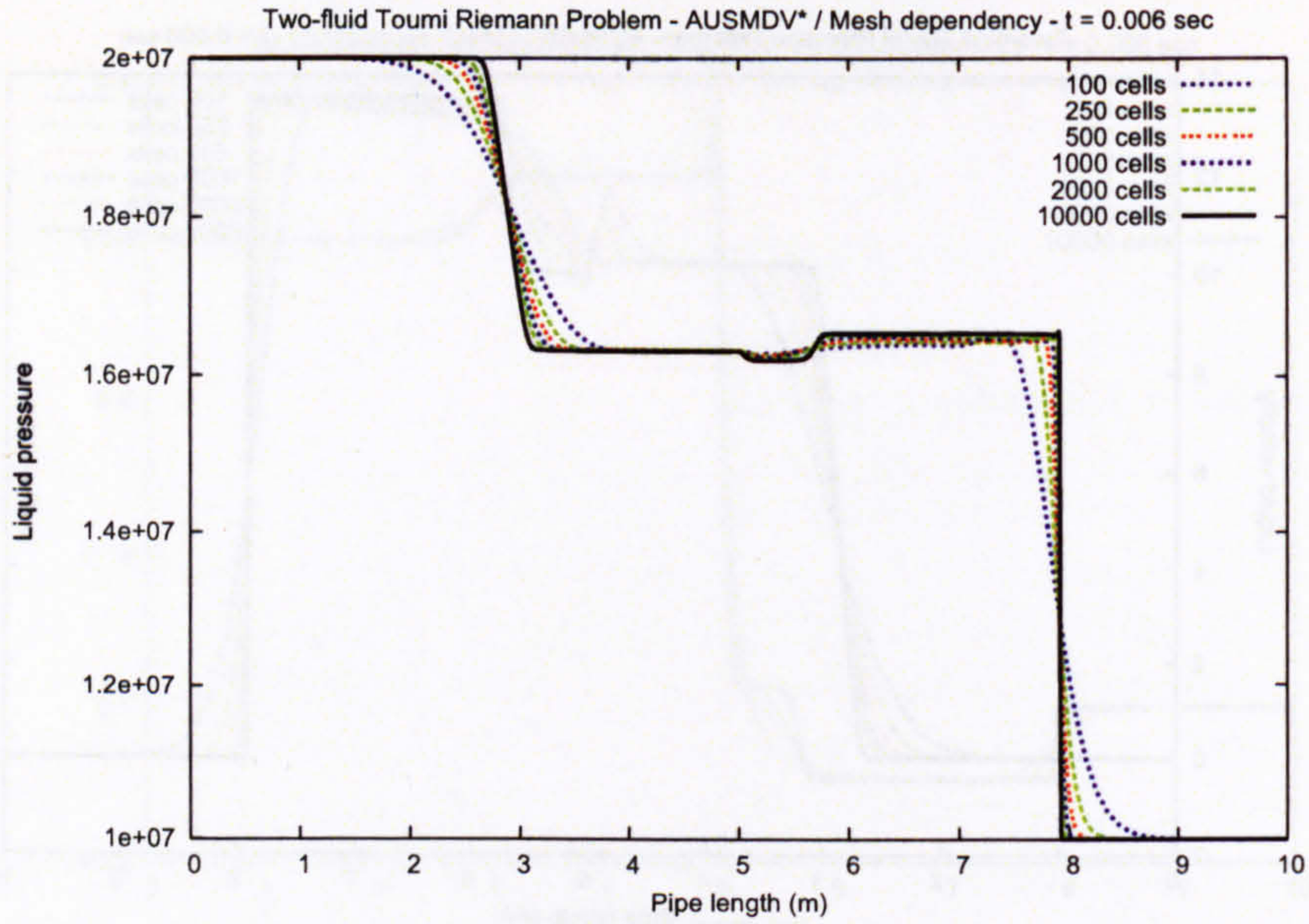

(a) P

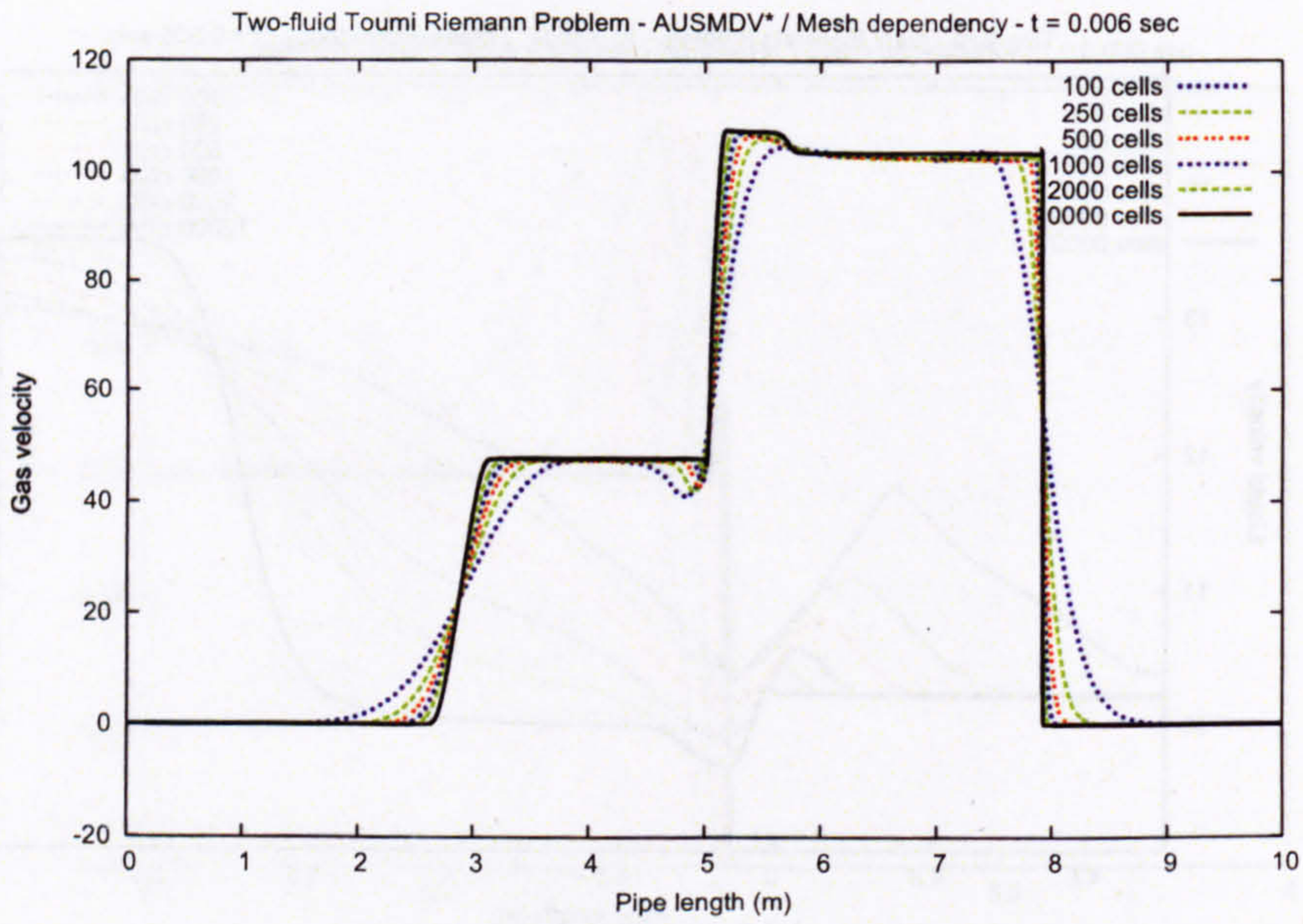

(b) V_g

Figure 4.6 : *Two-phase Riemann problem - Toumi test-case - TPM5 model. Mesh refinement on the liquid pressure and gas velocities. Each wave pattern is composed by a contact discontinuity in the middle of the pipe and a shock or a rarefaction wave at the left and the right sides separating uniform state solution.*

configuration. The rarefaction, the shock-wave and the discontinuity-wave can be identified in the answers, matching with the existing results found in the literature. Overshoots tend to appear at the shock points, such as around $5\,m$ in the liquid velocity profile. However they are correctly decreased by the AUSMV* feature of the scheme when the mesh is refined.

4.7.1.2 Cortes test-case

For this second two-phase Riemann problem, a large difference between the velocities is considered and will demonstrate the ability for the method to handle a large difference in velocities. The initial conditions for the left and the right states are given in the following:

$$\begin{cases} \alpha_l^L = 0.29 & & \alpha_l^R = 0.3 \\ V_g^L = 65\,m.s^{-1} & & V_g^R = 50\,m.s^{-1} \\ V_l^L = 1\,m.s^{-1} & \text{and} & V_l^R = 1\,m.s^{-1} \\ P_l^L = 2.65 \times 10^5 Pa & & P_l^R = 2.65 \times 10^5 Pa \\ T_l^L = 308.15\,K & & T_l^R = 308.15\,K \end{cases} \tag{4.58}$$

The boundary conditions are open at both inlet and outlet of the pipe. The simulations are left running for $2.0sec$, with meshes from 50 to 800 cells.

Overshoots that appear towards the discontinuities are not oscillations, as you would expect from a malfunctioning or poorly functioning TVD scheme. They are a persistent spike and are reminiscent of the Noh problem [13] - when two materials are impacted together there is a non-physical spike in the solution that effectively just sits there or gets advected along. Consensus is that there is no way of eliminating it but adaptive mesh refinement (AMR) will reduce its relative size and effects, as prove Fig. 4.4-(b), 4.5-(b) and Fig. 4.8 to 4.10.

4.7.2 Faucet problem

The Faucet problem is a one-dimensional configuration, corresponding to a $12m$-long vertical pipe, for which an analytical solution is known. The initial condition is a uniform column of air filled with 80% water. The initial liquid volume fraction is therefore constant over the domain and equal to $\alpha_l = 0.8$. The initial velocity of water and air are $10\,m.s^{-1}$ and $0\,m.s^{-1}$, respectively. All pressures are set to $10^5\,Pa$. The initial densities are $\rho_l = 1000\,kg.m^{-3}$ and $\rho_g = 1.16\,kg.m^{-3}$.

The simulation consists in introducing a gravity field at $t > 0$ (Fig. 4.11). The flow is thus only driven by the gravity $g = 9.81\,m.s^{-1}$ and by the boundary conditions; the inlet conditions are similar to the initial conditions ($\alpha_l = 0.8$, $V_l = 10\,m.s^{-1}$ and $V_g = 0\,m.s^{-1}$) and the outlet boundary condition only applies on pressure set constant equal to $10^5\,Pa$.

An analytical transient solution is available with a very simple model assuming that the

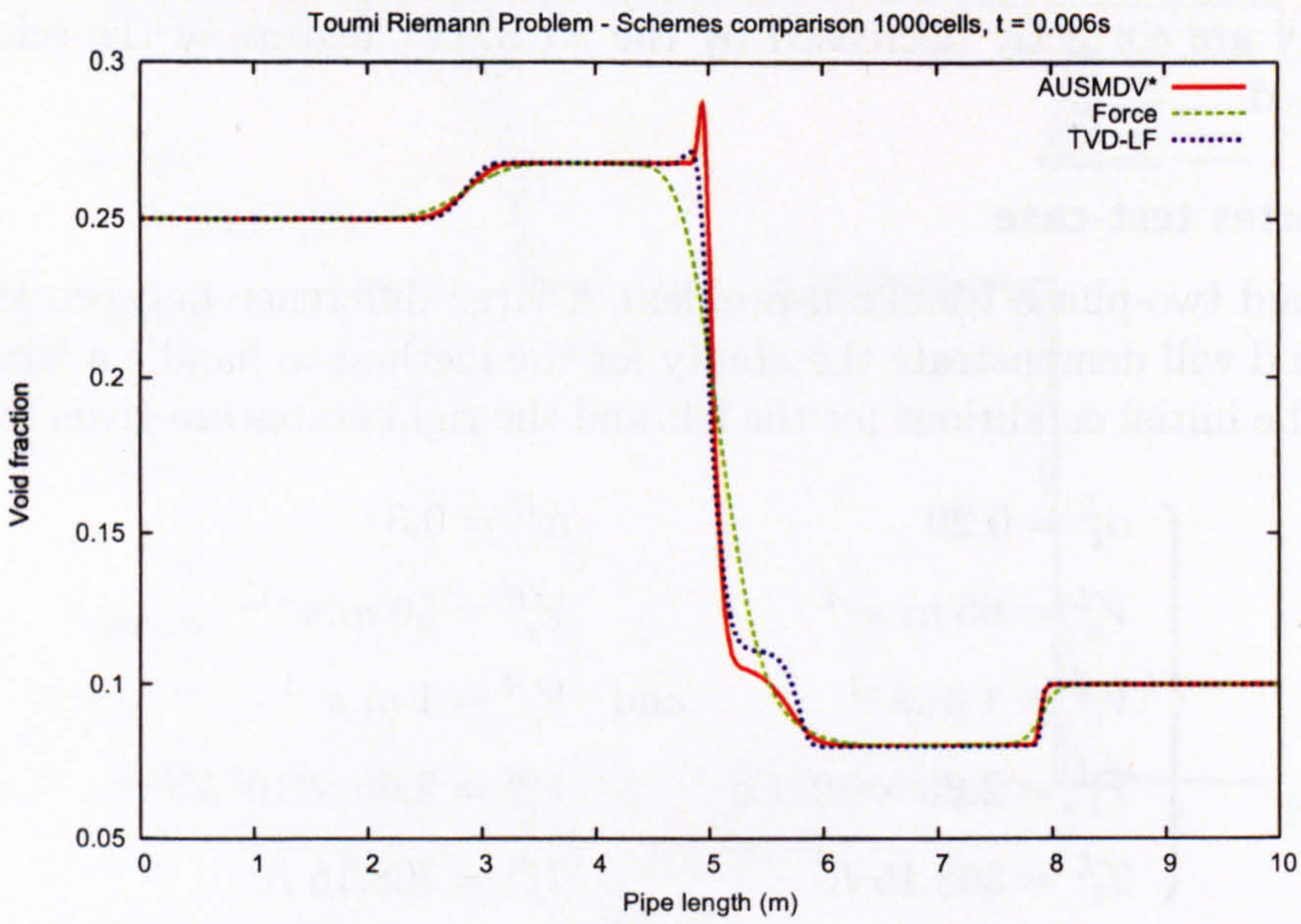

(a) 1000 cells

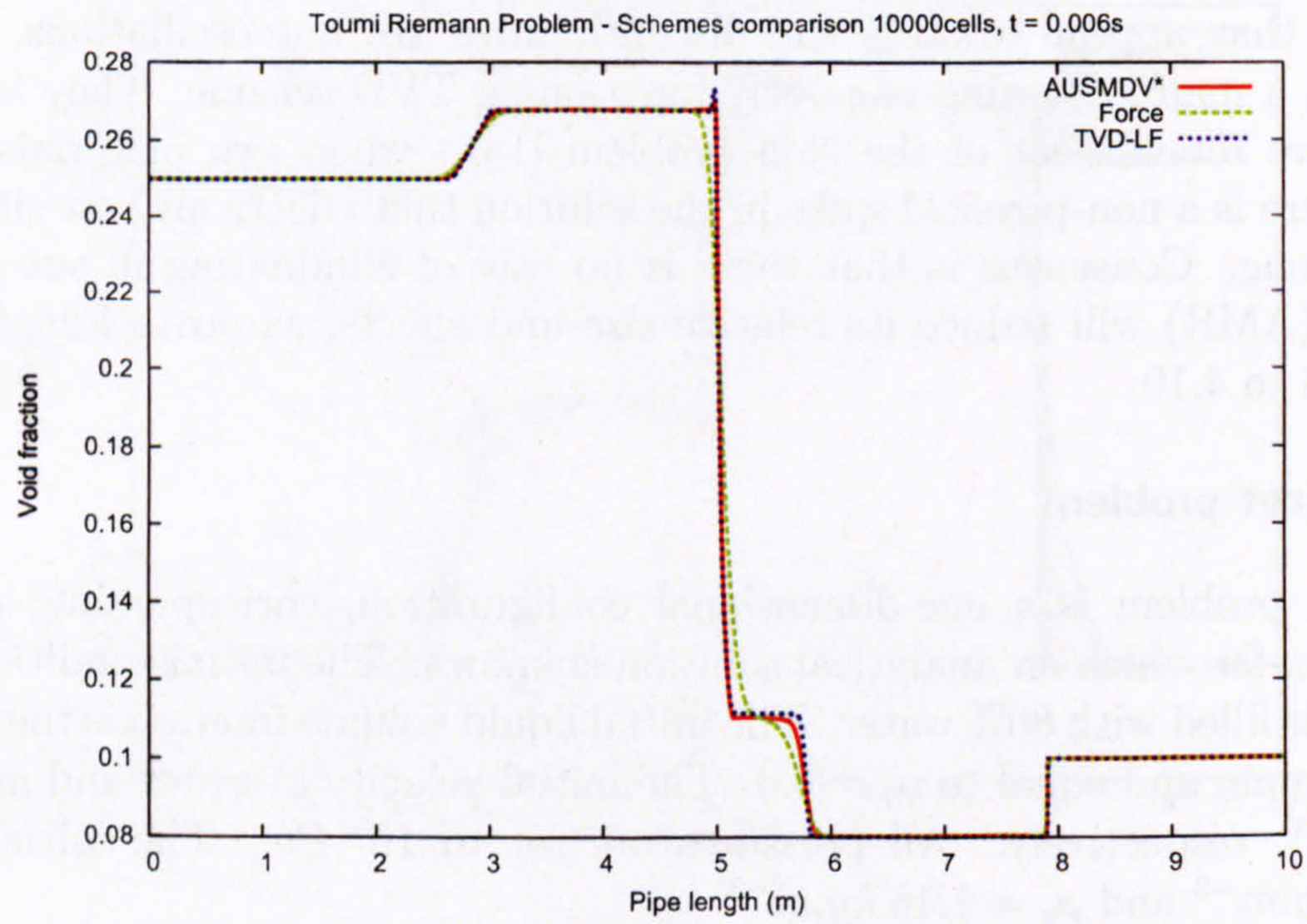

(b) 10000cells

Figure 4.7 : *Two-phase Riemann problem - Toumi test-case - TPM5 model. Mesh refinement decreases the instabilities induced by the discontinuity.*

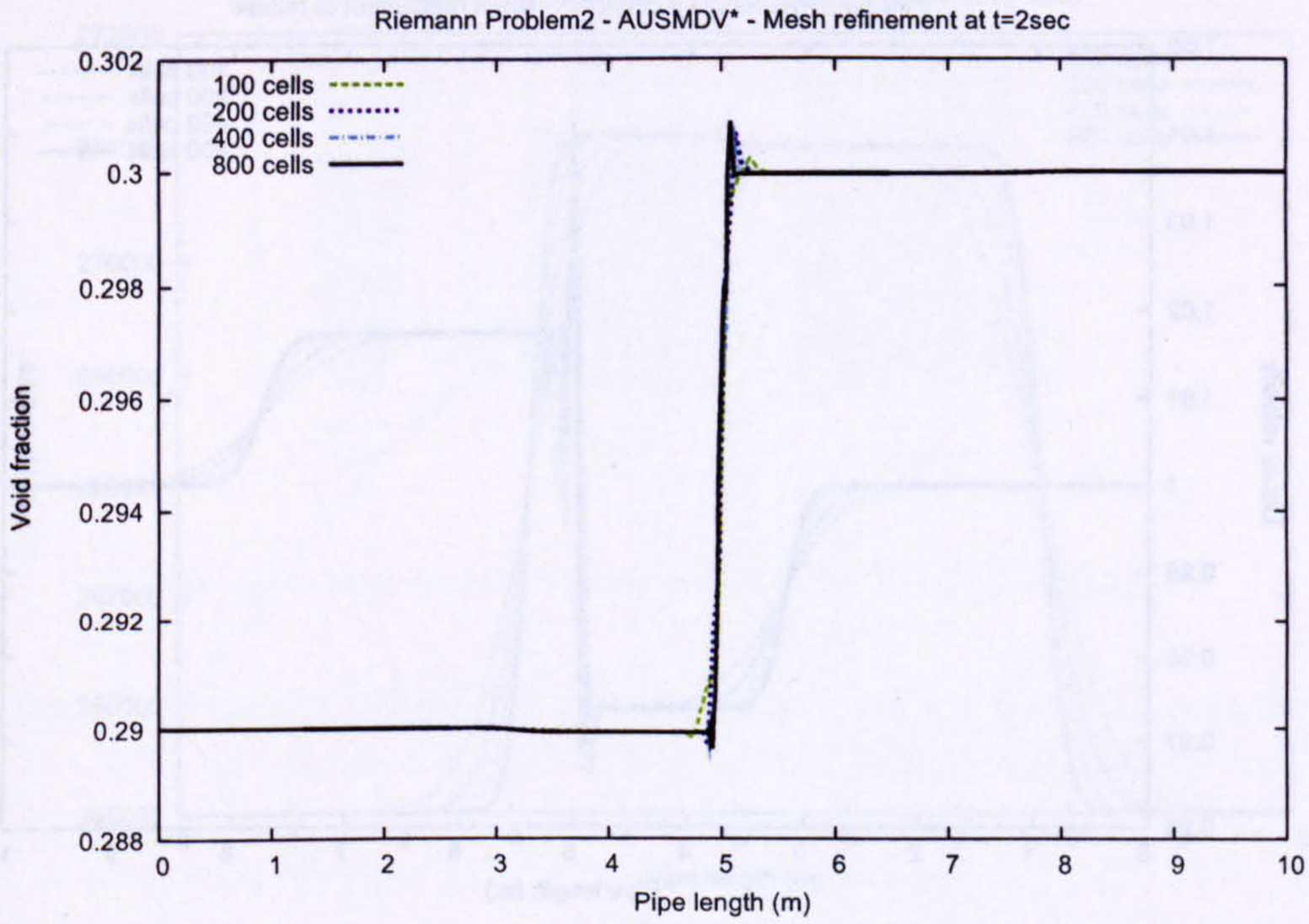

(a) α_g

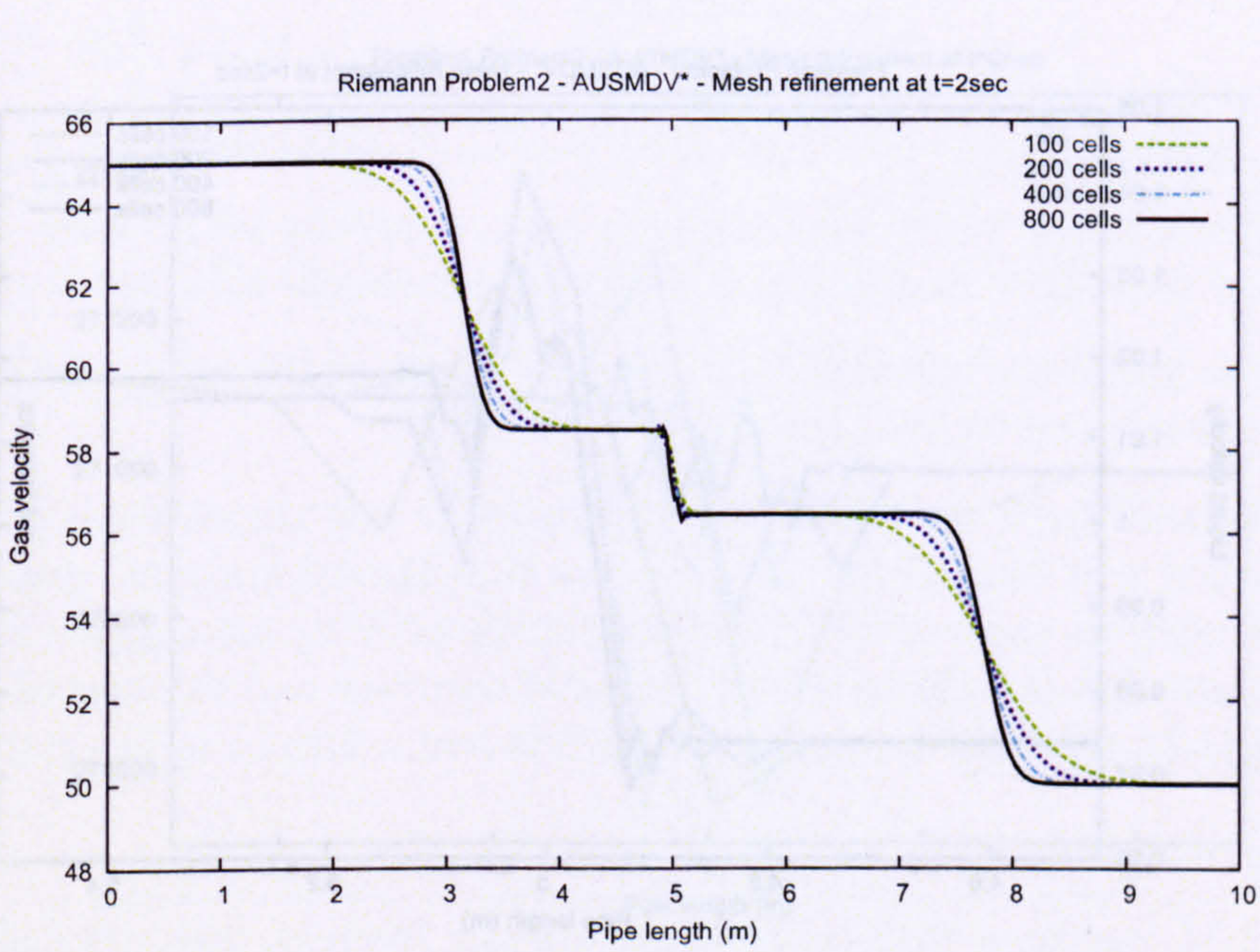

(b) V_g

Figure 4.8 : *Two-phase Riemann problem - Large velocities test-case - TPM5 model. Mesh refinement on the void fraction and gas velocity after 2 seconds of simulation.*

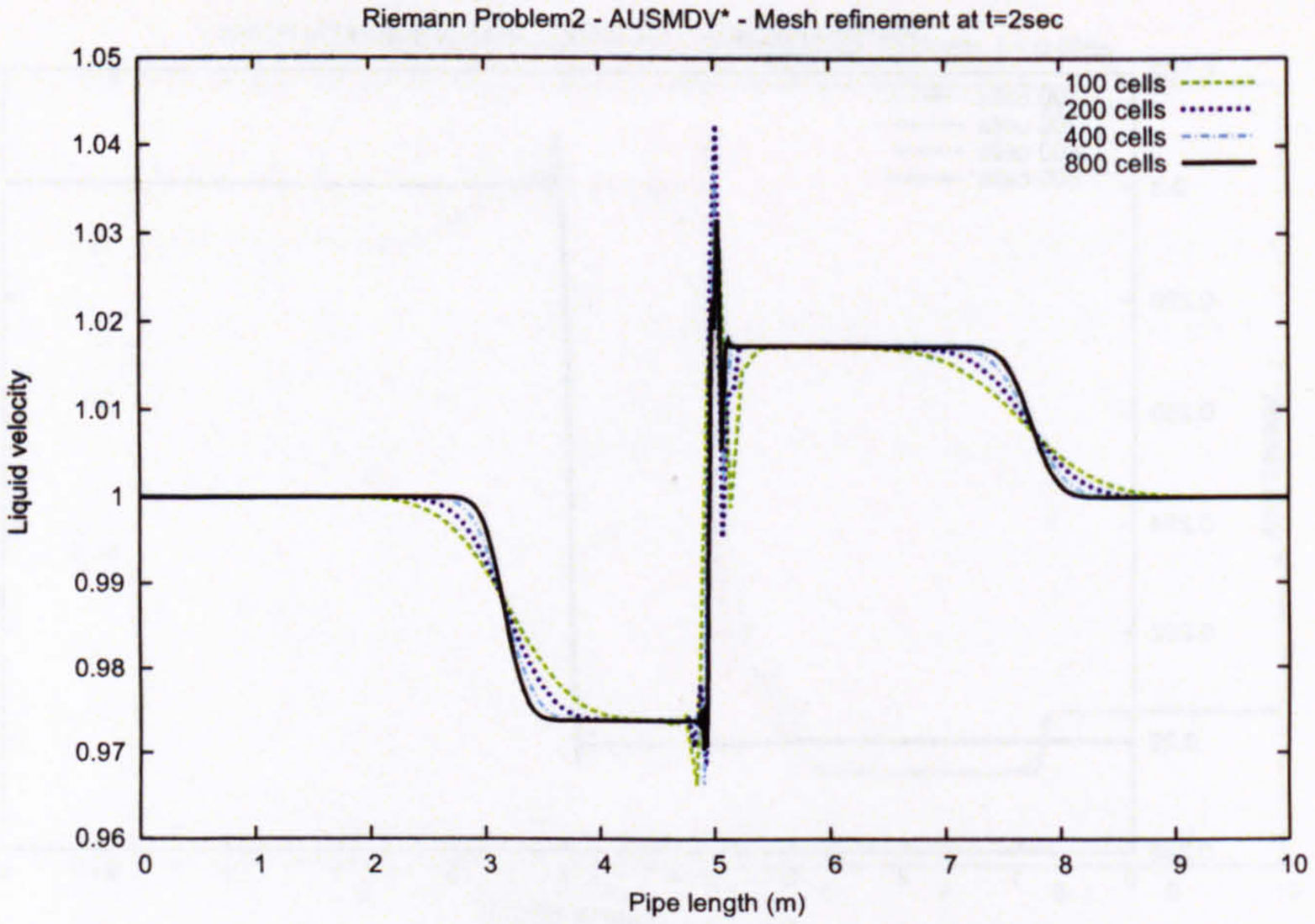

(a) V_l

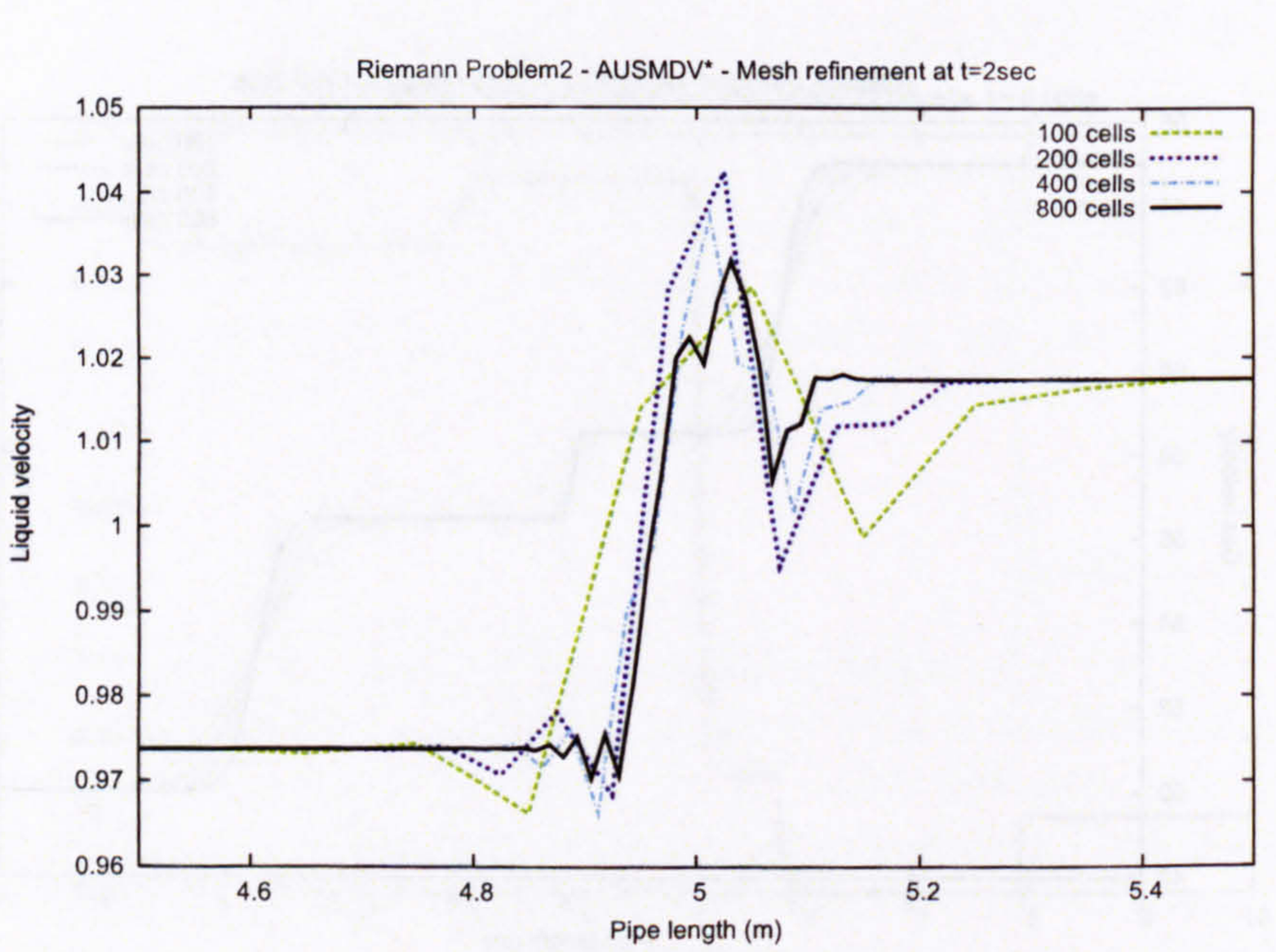

(b) zoom

Figure 4.9 : *Two-phase Riemann problem - Large velocities test-case - TPM5 model. Mesh refinement on the liquid velocity after 2 seconds of simulation. A close-up at the shock shows the discrepancies decreasing with finer meshes.*

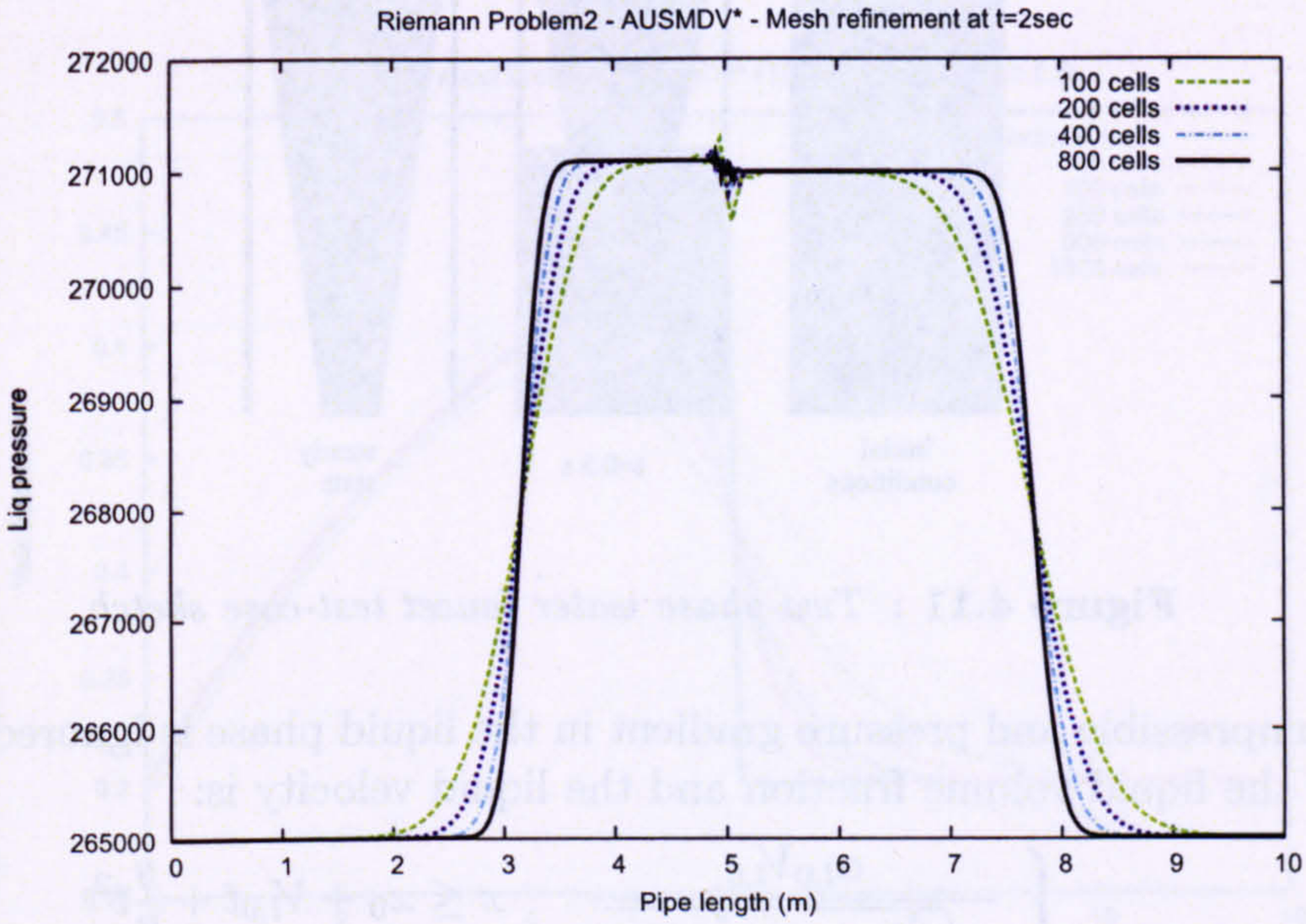

(a) P

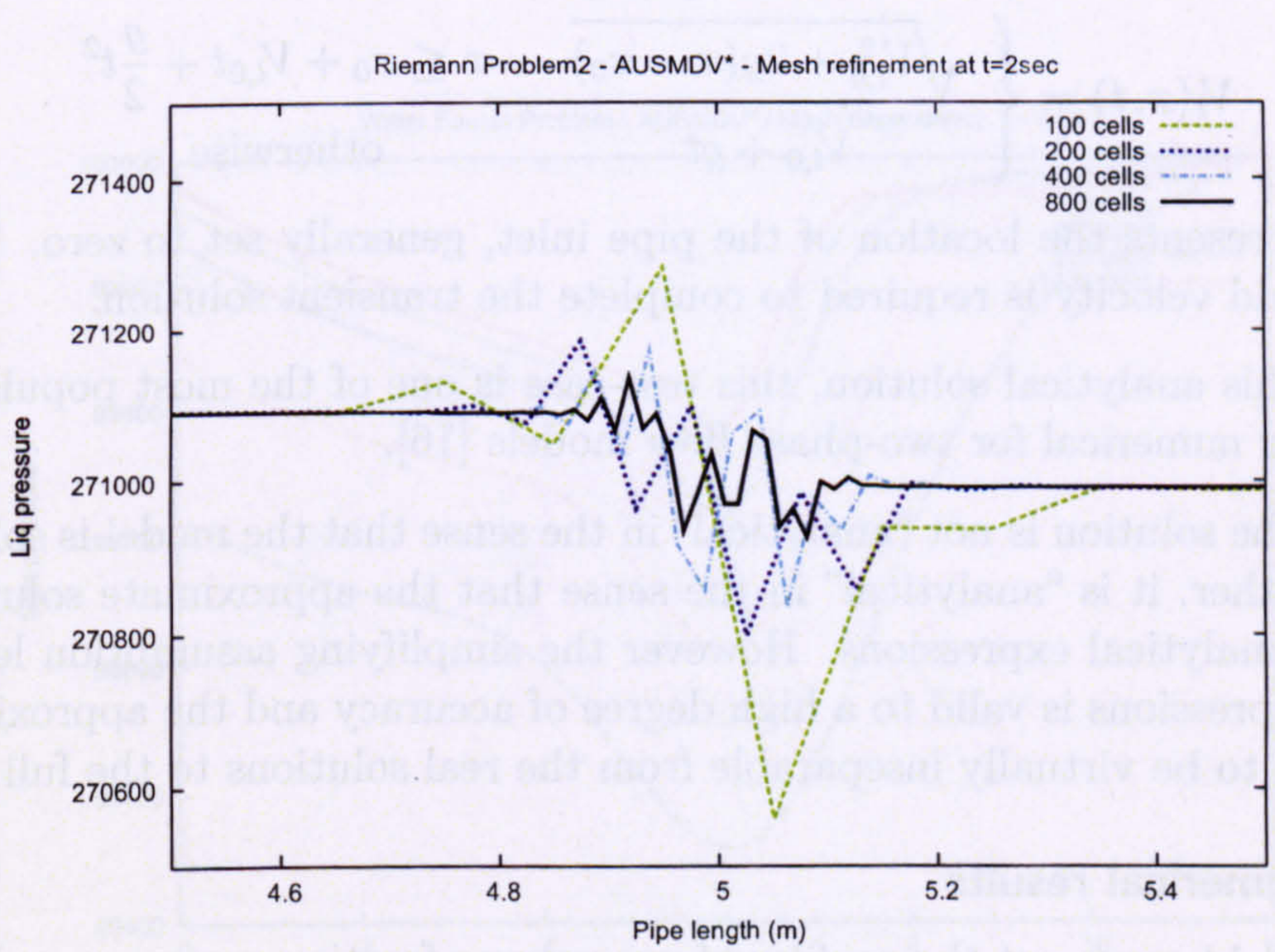

(b) zoom

Figure 4.10 : *Two-phase Riemann problem - Large velocities test-case - TPM5 model. Mesh refinement on the pressure predictions after 2 seconds of simulation. The oscillations appearing at the shock are controlled with mesh refinement.*

Figure 4.11 : *Two-phase water faucet test-case sketch.*

liquid is incompressible and pressure gradient in the liquid phase is ignored. The solution obtained for the liquid volume fraction and the liquid velocity is:

$$\alpha_l(x,t) = \begin{cases} \dfrac{\alpha_{l,0} V_{l,0}}{\sqrt{V_{l,0}^2 + 2g(x-x_0)}} & x \leq x_0 + V_{l,0}t + \dfrac{g}{2}t^2 \\ \alpha_{l,0} & \text{otherwise} \end{cases} \tag{4.59}$$

$$V_l(x,t) = \begin{cases} \sqrt{V_{l,0}^2 + 2g(x-x_0)} & x \leq x_0 + V_{l,0}t + \dfrac{g}{2}t^2 \\ V_{l,0} + gt & \text{otherwise} \end{cases} \tag{4.60}$$

where x_0 represents the location of the pipe inlet, generally set to zero. Therefore only the inlet liquid velocity is required to complete the transient solution.

Because of this analytical solution, this test-case is one of the most popular benchmarks for validating numerical for two-phase flow models [16].

Remark: The solution is not "analytical" in the sense that the model is solved exactly by analysis. Rather, it is "analytical" in the sense that the approximate solutions are given in terms of analytical expressions. However the simplifying assumption leading to these analytical expressions is valid to a high degree of accuracy and the approximate solutions are expected to be virtually inseparable from the real solutions to the full model.

4.7.2.1 Numerical results

Fig. 4.12 to 4.14 represent the profiles of gas volume fraction, pressure and velocity given by the simulations after $t = 0.5sec$. In Fig. 4.12-(a), one can see the mesh dependency effect on the void fraction with AUSMDV* scheme. Meshes from 50 cells to 1000 cells are used. As expected, refinement considerably improves the answer. The same pattern is observed for the gas pressure (Fig. 4.12-(b)) and the gas and liquid velocities (Fig. 4.13-(a) and 4.13-(b)).

Fig. 4.14-(a) and 4.14-(b) display a comparison of different schemes. Answers from the

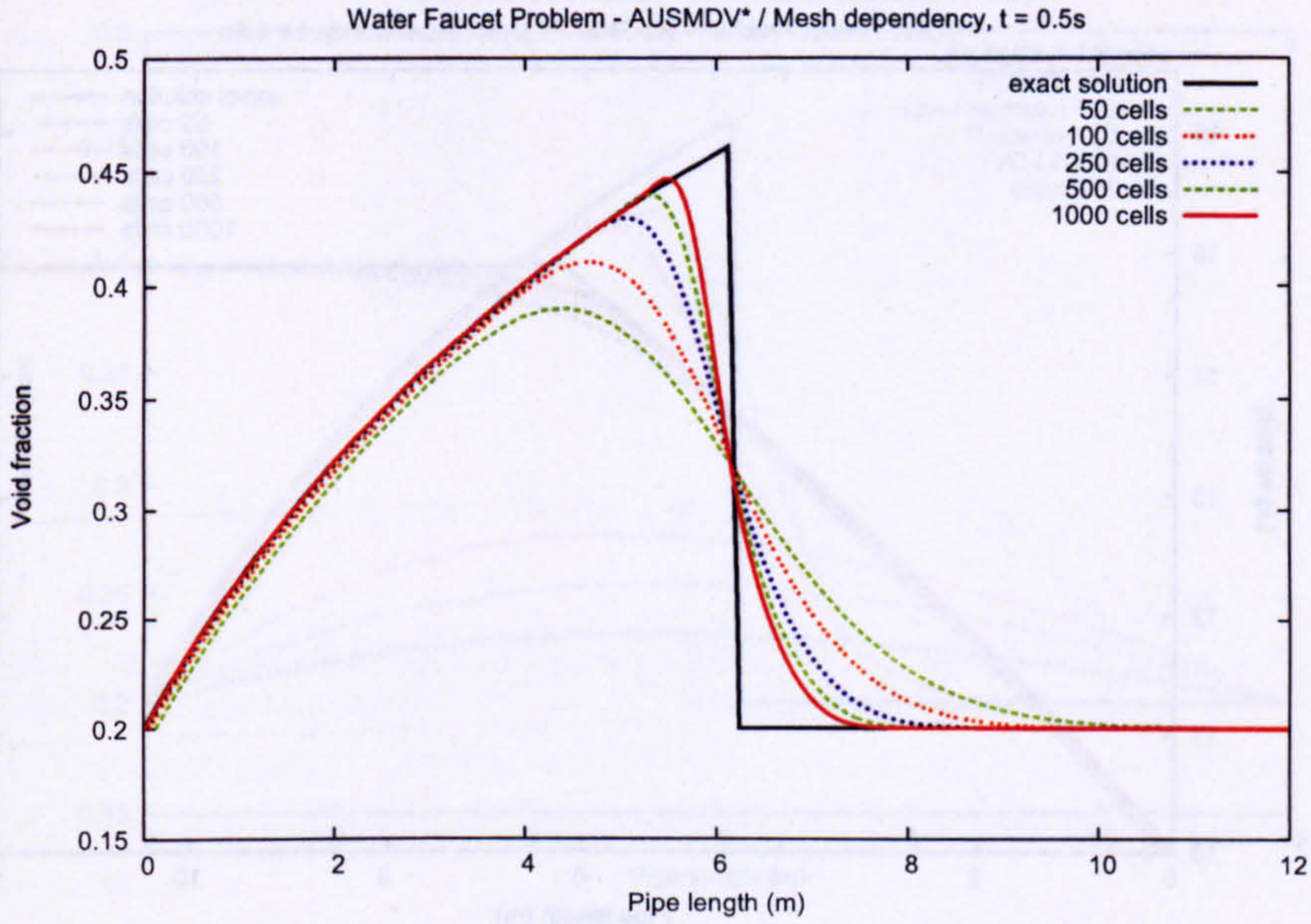

(a) α_g

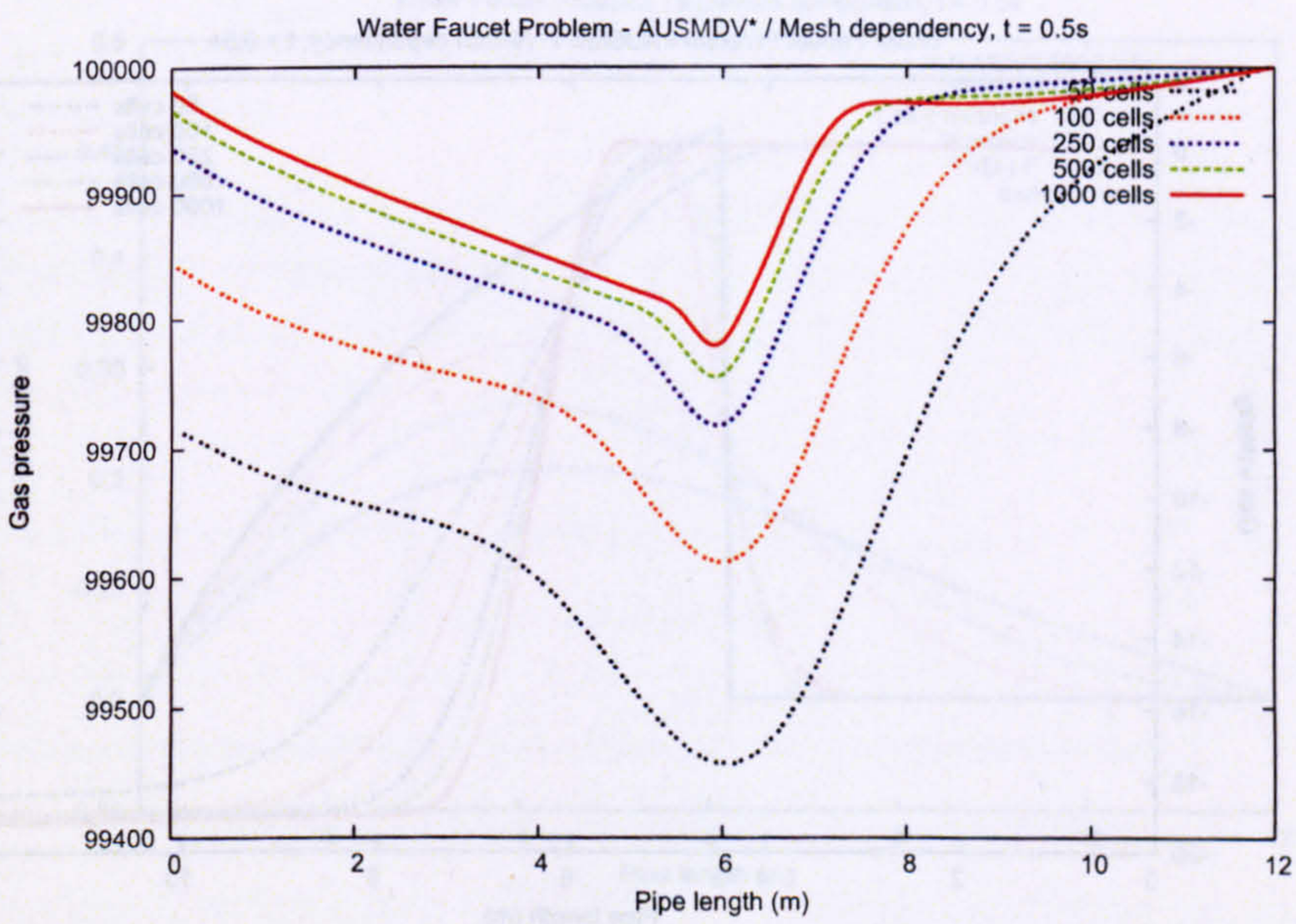

(b) P

Figure 4.12 : *Water faucet problem results - Mesh refinement on void fraction and pressure.*

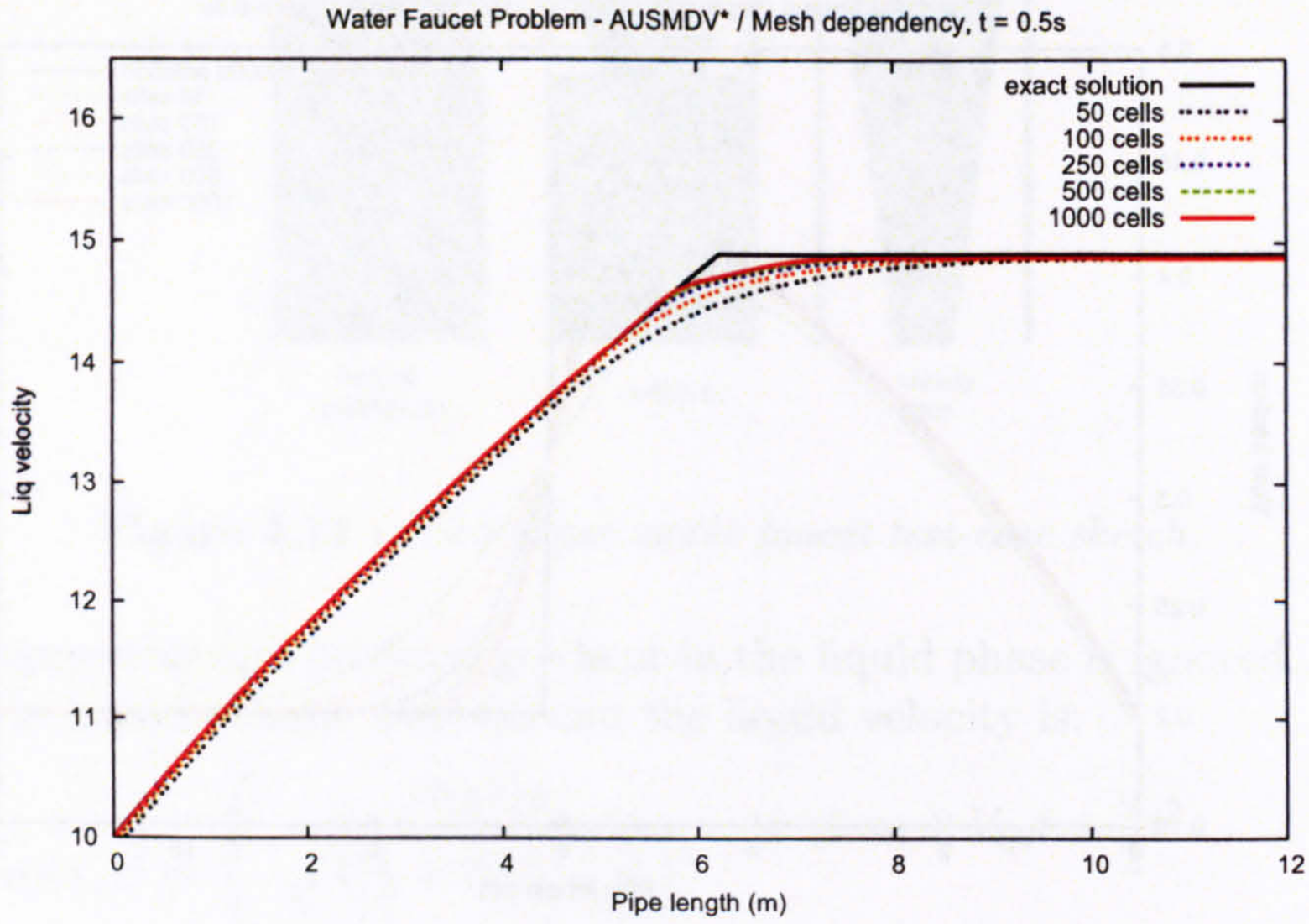

(a) V_l

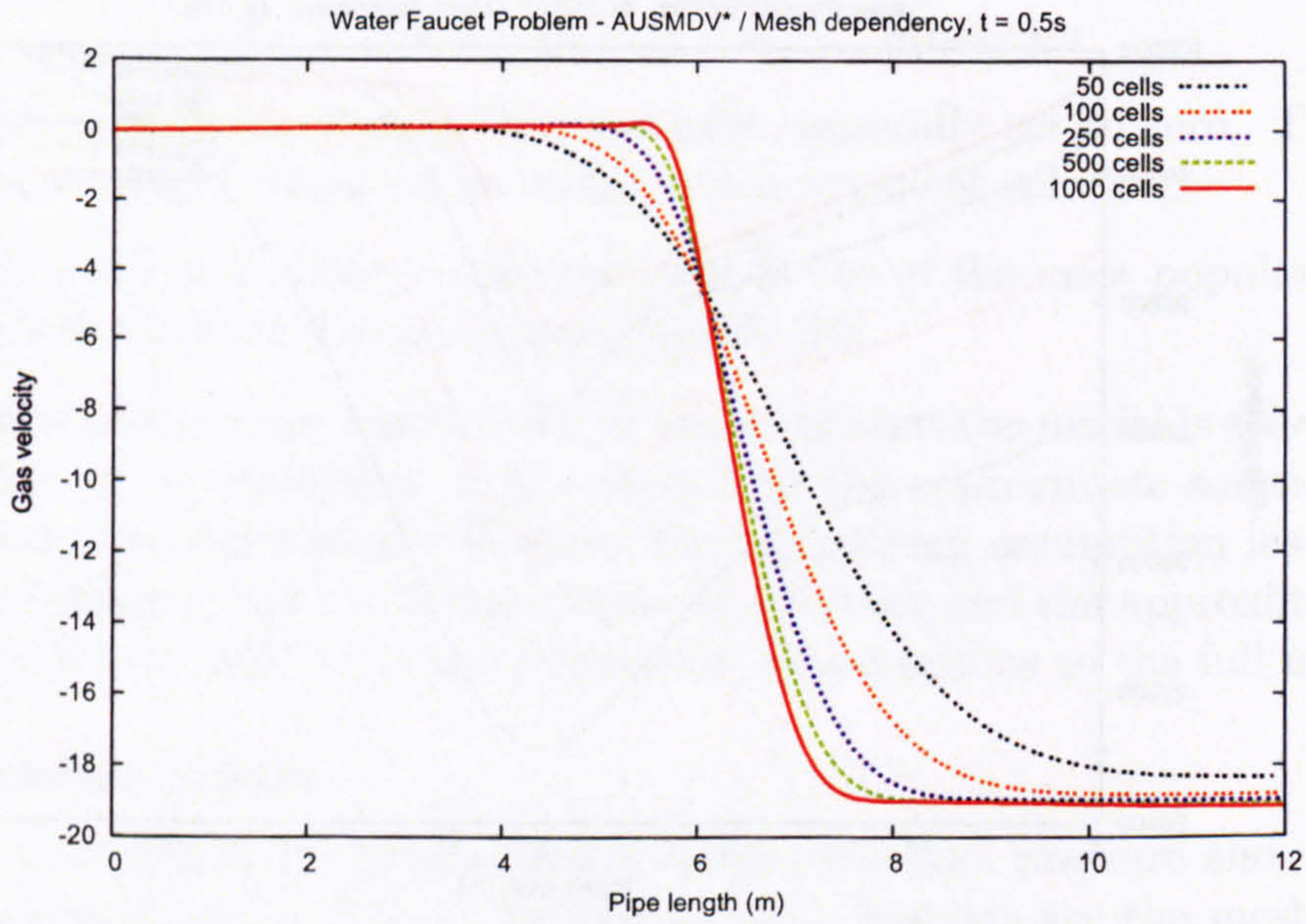

(b) V_g

Figure 4.13 : *Water faucet problem results - Mesh refinement on liquid and gas velocities.*

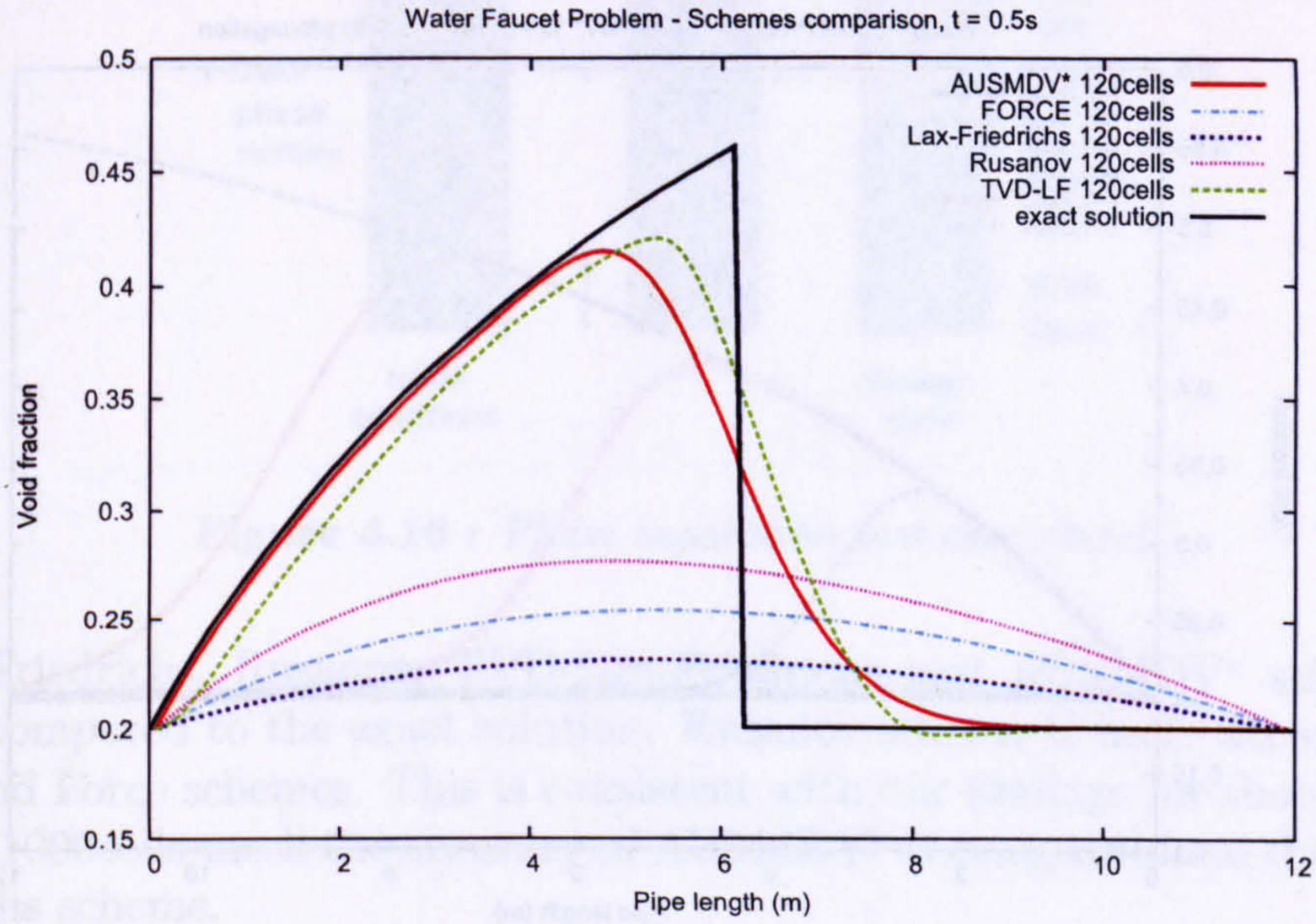

(a) 120 cells

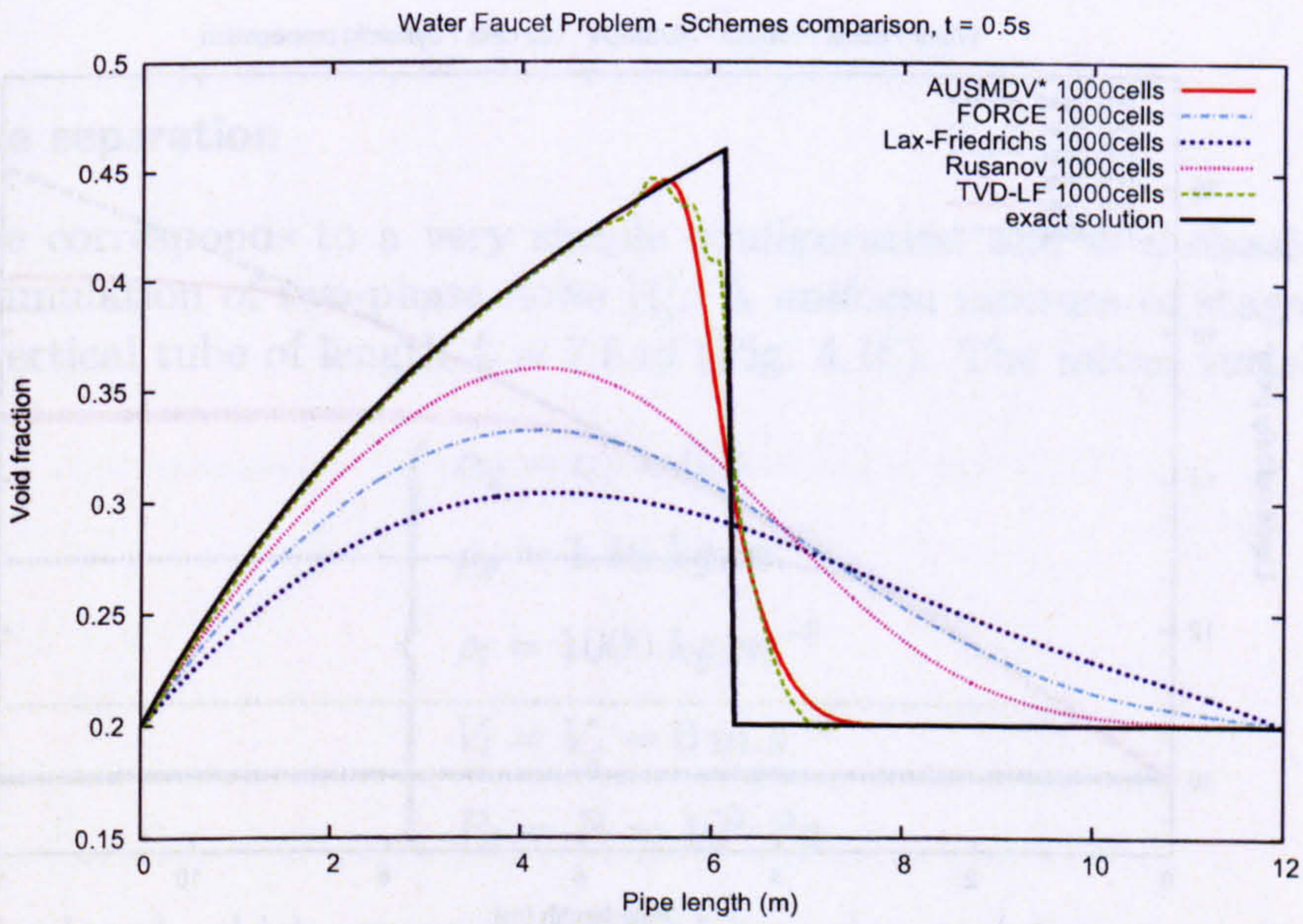

(b) 1000 cells

Figure 4.14 : *Water faucet problem results - Schemes comparison for* 120 *cells and* 1000 *cells showing the accuracy of the AUSMDV⋆ scheme.*

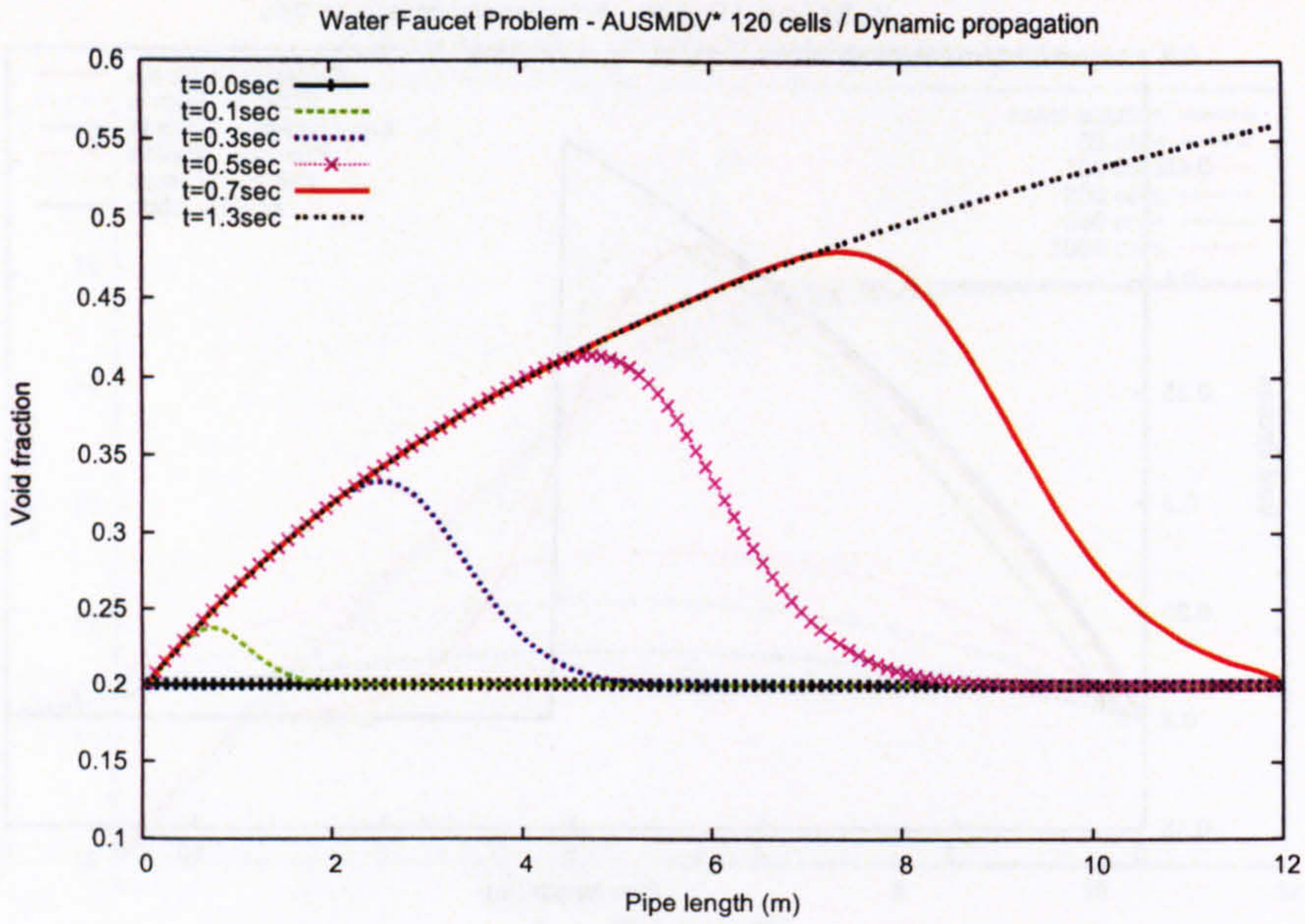

(a)

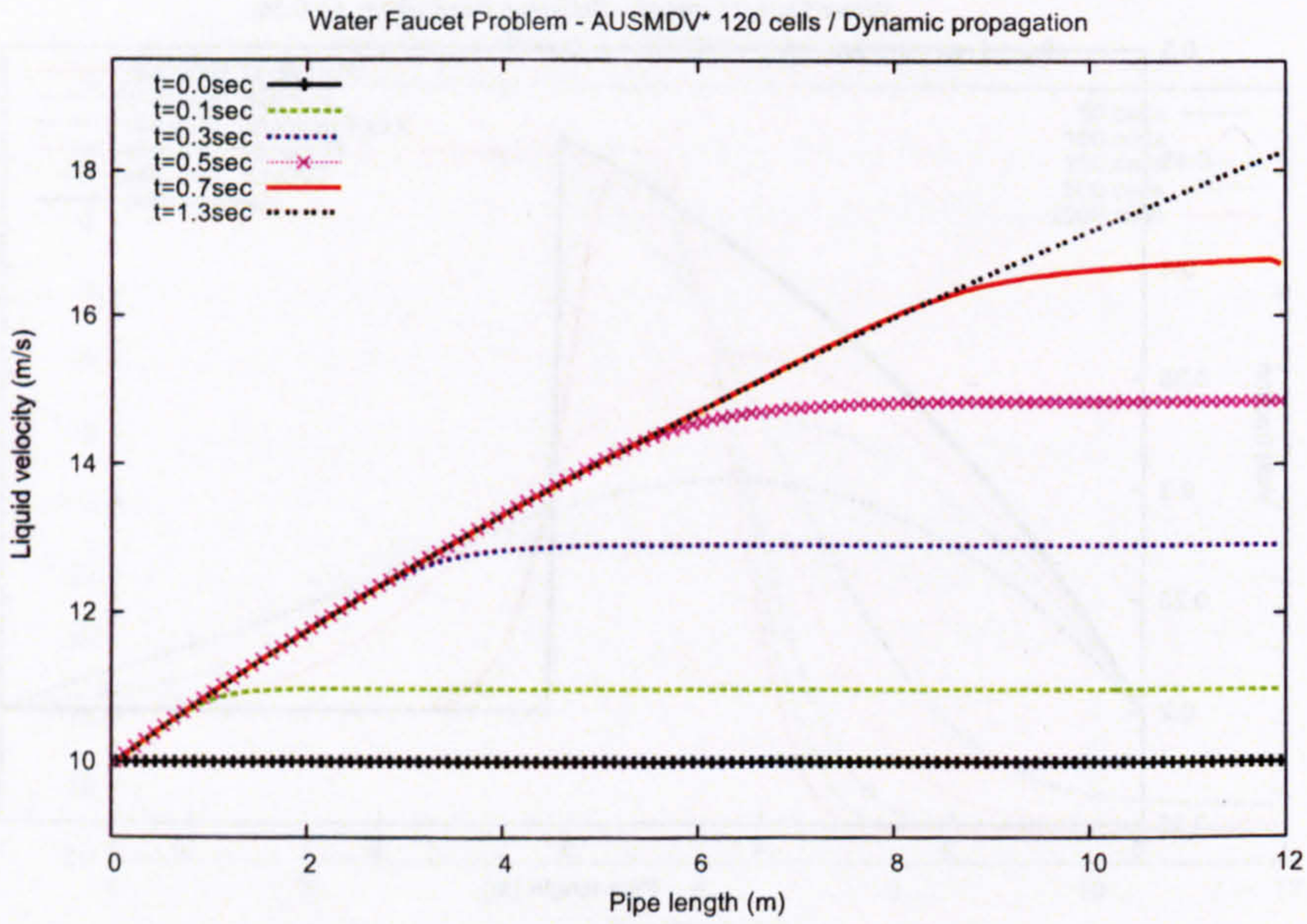

(b)

Figure 4.15 : *Water Faucet problem - TPM5 model - Dynamic propagation of void fraction and liquid velocity.*

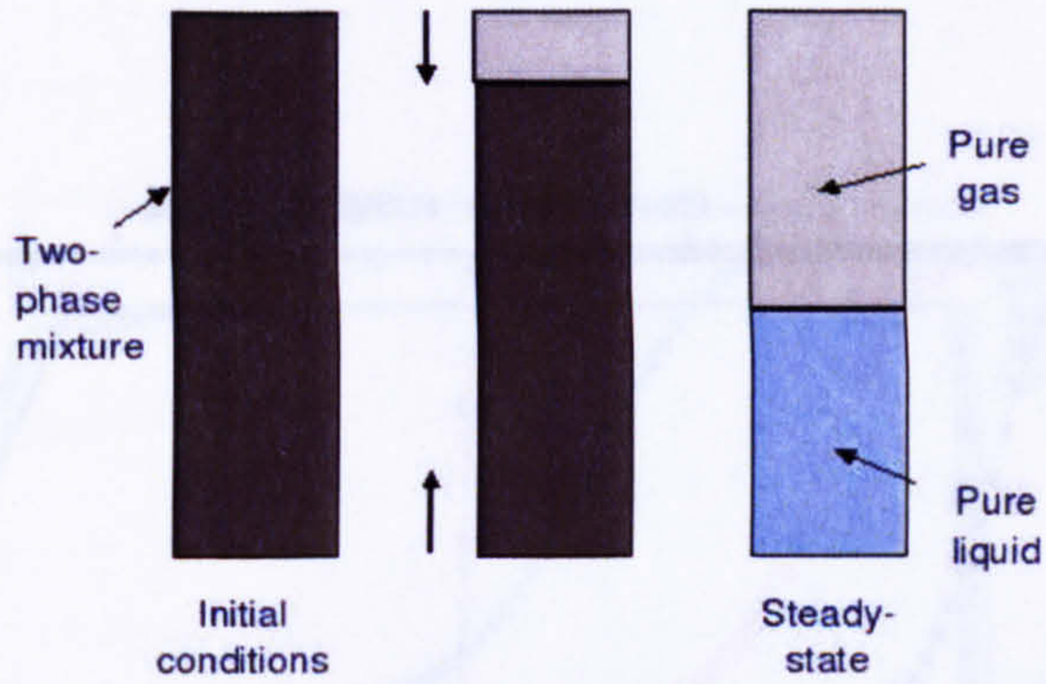

Figure 4.16 : *Phase separation test-case sketch.*

Force, Lax-Friedrichs, Rusanov, TVD-Lax-Friedrichs and AUSMDV* schemes are displayed and compared to the exact solution. Rusanov scheme is more accurate than Lax-Friedrichs and Force schemes. This is consistent with our findings for shocktube problem 1. With the 1000cells-mesh the accuracy of AUSMDV* is comparable to that of the TVD-Lax-Friedrichs scheme.

Fig. 4.15 shows the dynamic propagation of the void and the liquid velocity profiles down the tube until the wave has completely passed out the tube and the steady-state profile remains.

4.7.3 Phase separation

This test-case corresponds to a very simple configuration and is a classical benchmark test for the simulation of two-phase flows [1]. A uniform mixture of stagnant water and air lies in a vertical tube of length $L = 7.5\,m$ (Fig. 4.16). The initial variables are:

$$\begin{cases} \alpha_g = \alpha_l = 0.5 \\ \rho_g = 1.16\ kg.m^{-3} \\ \rho_l = 1000\ kg.m^{-3} \\ V_l = V_g = 0\ m.s^{-1} \\ P_g = P_l = 10^5\ Pa \end{cases} \tag{4.61}$$

The domain is closed, which means that closed boundary conditions are imposed at both extremities $x = 0$ and $x = 7.5$, forcing both velocities to be null at those points.

4.7.3.1 Numerical results

From Fig. 4.17, which shows the time evolution of the void fraction profile for two different mesh sizes, the transient period reveals two volume fraction fronts at the top and the bottom of the pipe. These two fronts slowly meet and a stationary state is then formed:

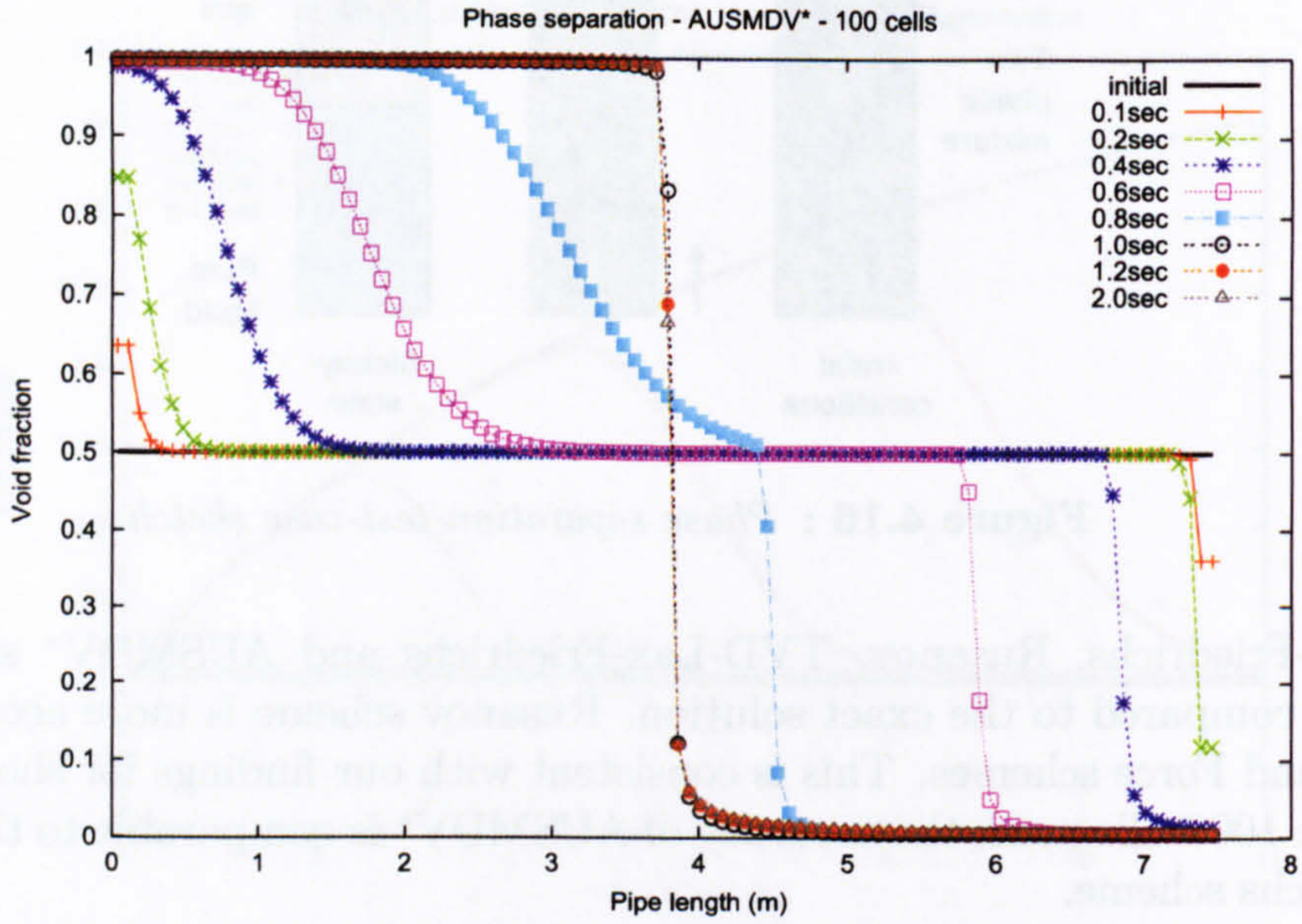

(a) Time evolution - 100 cells

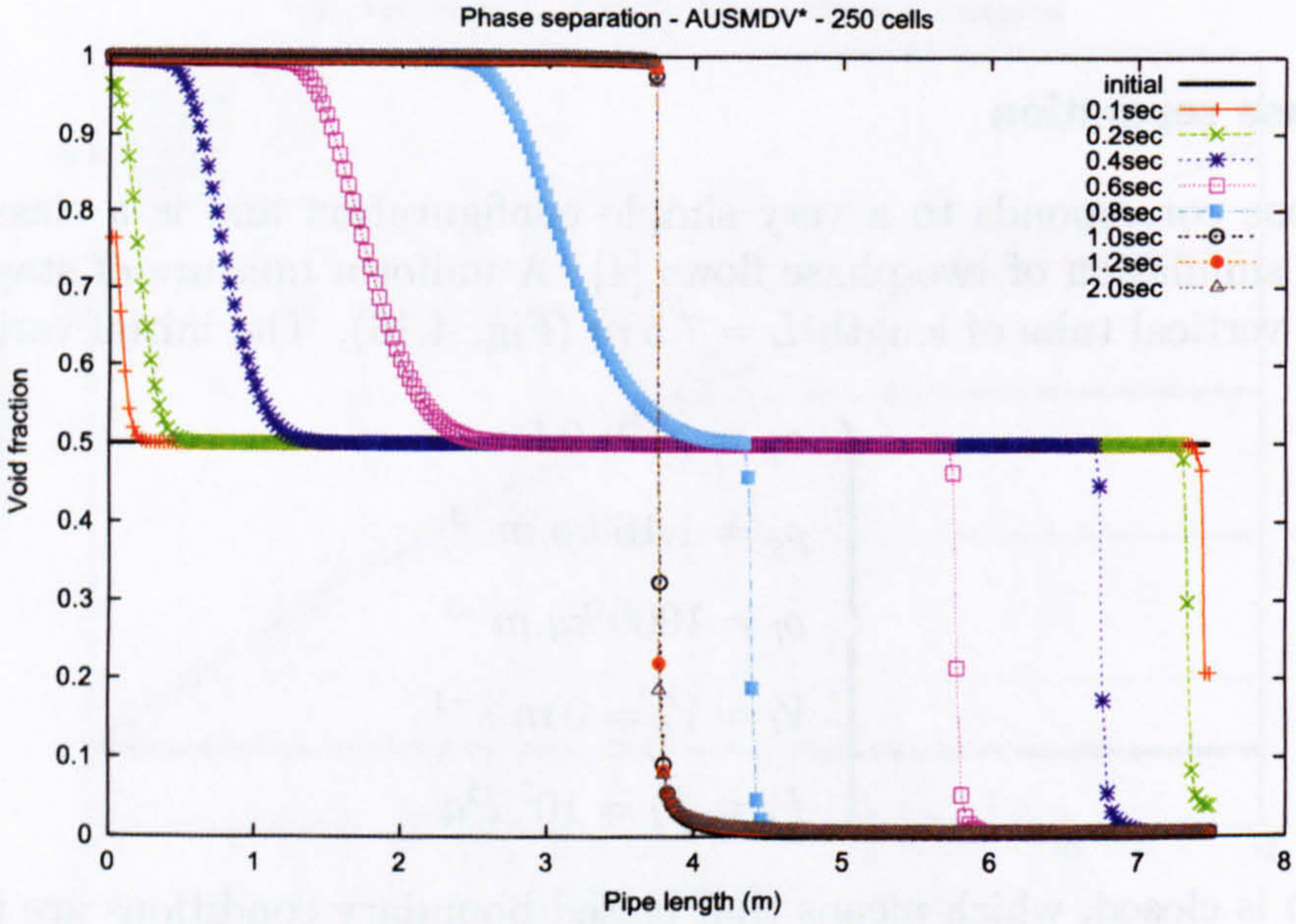

(b) Time evolution - 250 cells

Figure 4.17 : *Phase Separation problem - Time evolution for the void fraction with two different meshes.*

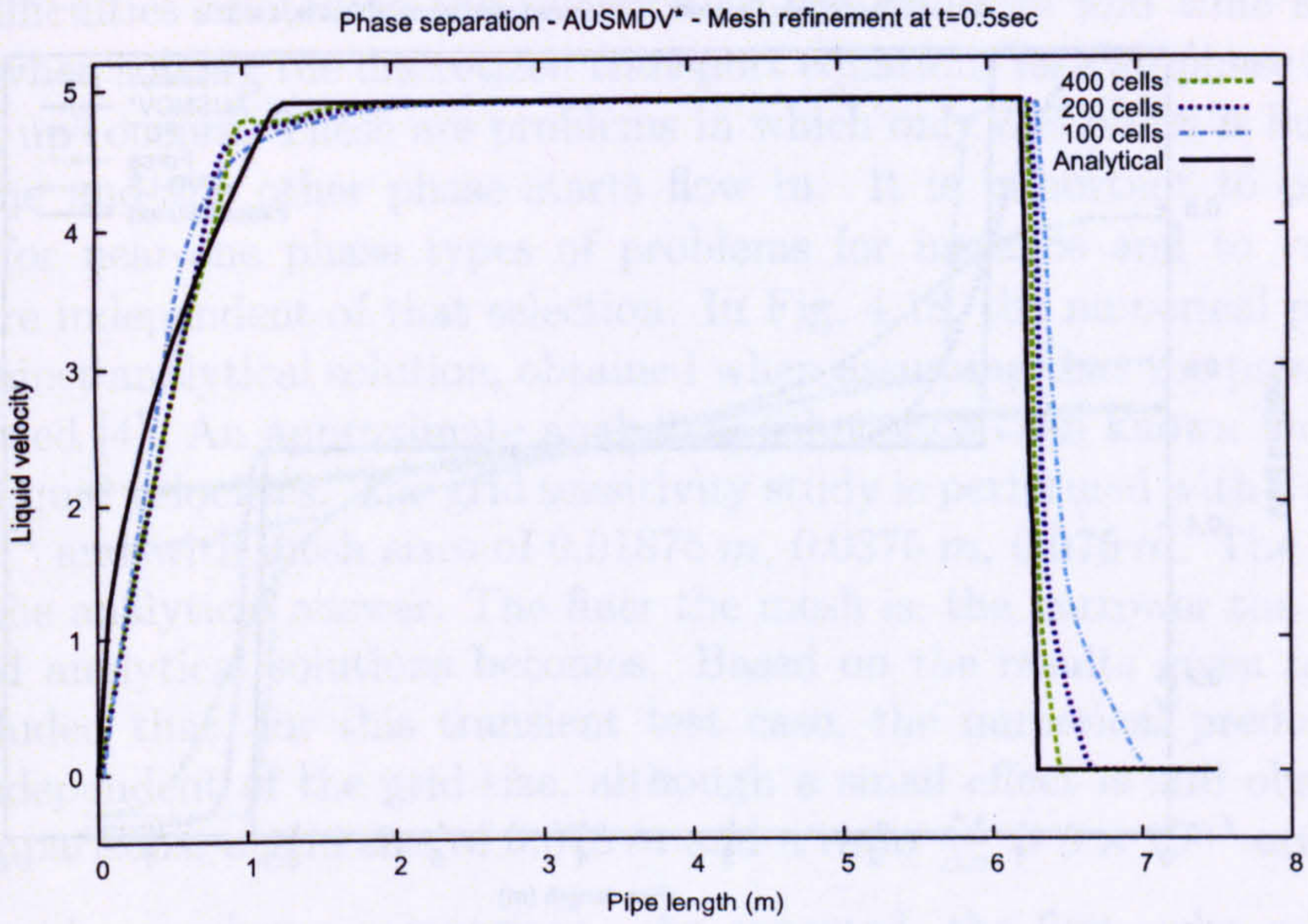

(a) Mesh refinement on V_l profile

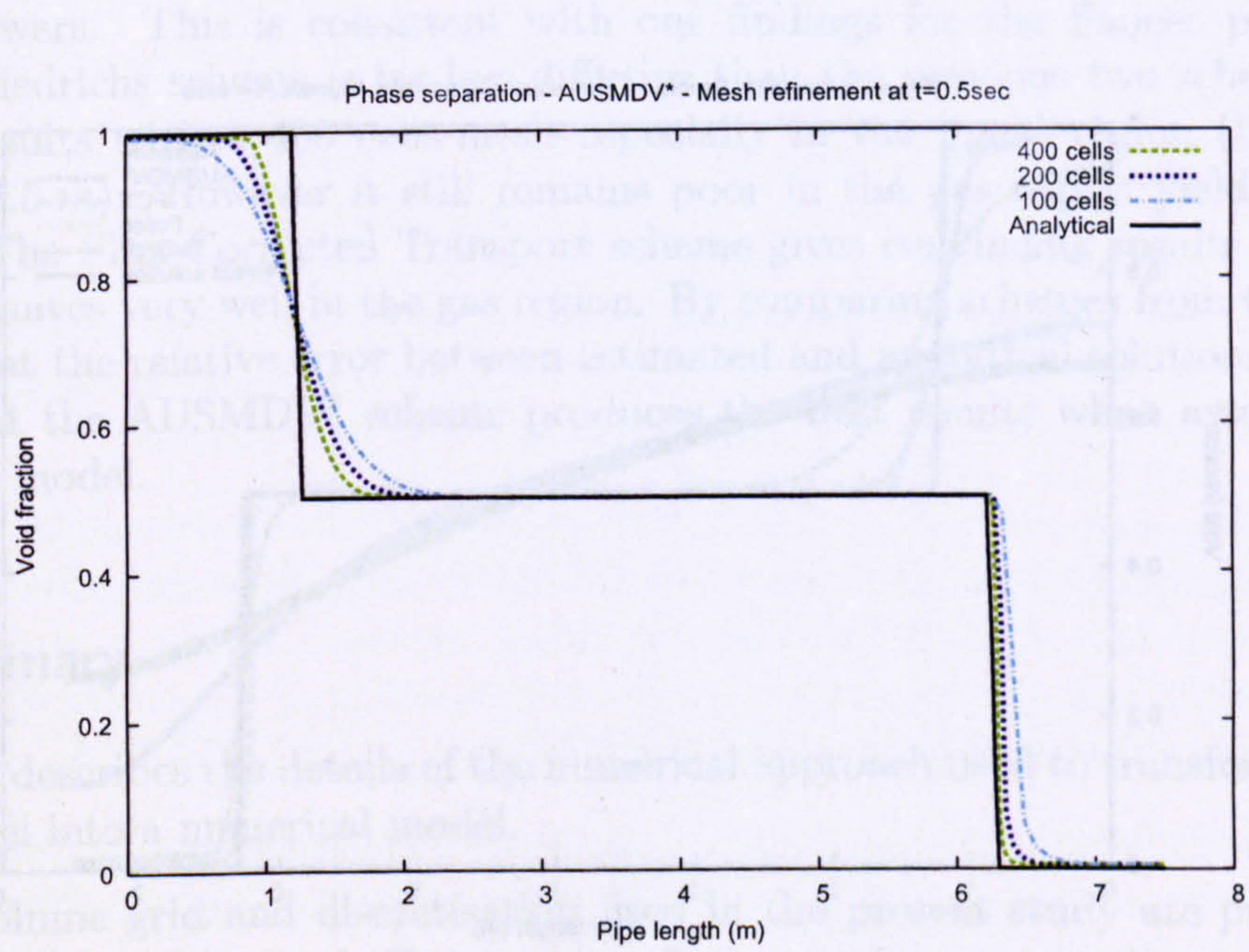

(b) Mesh refinement on α_g profile

Figure 4.18 : *Phase Separation problem - Mesh refinement on liquid velocity and void fraction.*

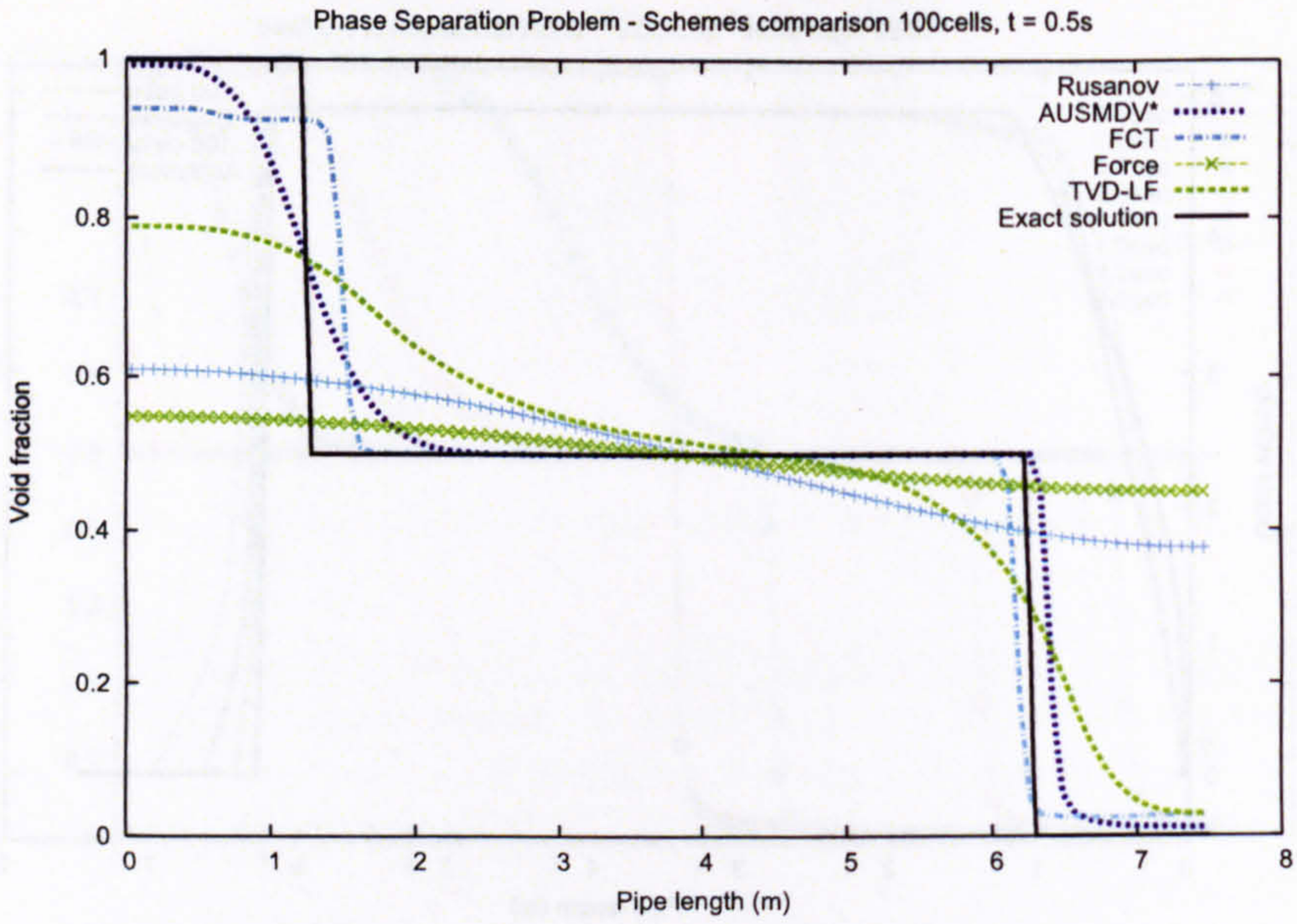

(a) Schemes comparison - 100 cells

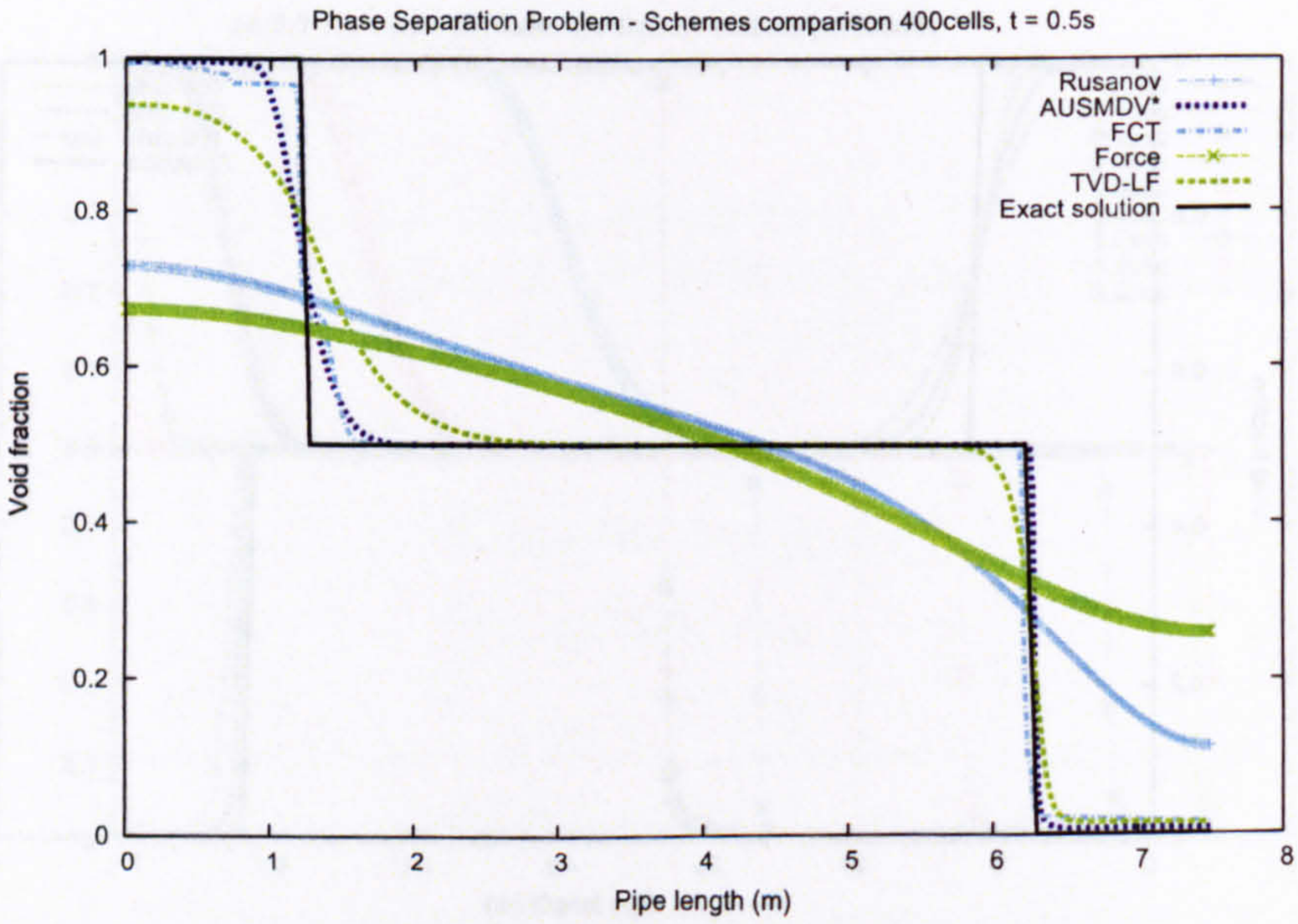

(b) Schemes comparison - 400 cells

Figure 4.19 : *Phase Separation problem - Schemes comparison on the void fraction answers showing that FCT and AUSMDV* are the favouring schemes.*

both phases are fully separated. This steady-state occurs after 1 s, and the later volume fraction results are thus overlapping.

Numerical difficulties related to the selection of the grid size and time step are often encountered when solving the discretized transport equations for two-phase flow problems where "filling up" occurs. These are problems in which only one phase is initially present in the pipeline and the other phase starts flow in. It is important to properly select Δt and Δx for near-one phase types of problems for instance and to verify that the predictions are independent of that selection. In Fig. 4.18, the numerical predictions are compared against analytical solution, obtained when assuming that the pressure variation can be neglected [4]. An approximate analytical solution is then known for both volume fraction and liquid velocities. The grid sensitivity study is performed with a constant ratio $\frac{\Delta t}{\Delta x} = 5 \times 10^{-4}$ and with mesh sizes of $0.01875\,m$, $0.0375\,m$, $0.075\,m$. The three answers converge to the analytical answer. The finer the mesh is, the narrower the error between predicted and analytical solutions becomes. Based on the results given in Fig. 4.17, it can be concluded that, for this transient test case, the numerical predictions become essentially independent of the grid size, although a small effect is still observed. In the following comparisons, a grid size of $0.075\,m$ and a ratio $\frac{\Delta t}{\Delta x} = 5 \times 10^{-4}$ are chosen.

Fig. 4.19 provides a scheme comparison. As expected, the first-order schemes behave poorly compared to the AUSMDV* scheme. The Force and Rusanov schemes give very diffusive answers. This is consistent with our findings for the Faucet problem. The TVD-Lax-Friedrichs scheme is far less diffusive than the previous two schemes and give ostensible results with a 400 cells-mesh especially in the liquid region (bottom of the pipe up to $2.5\,m$). However it still remains poor in the gas region yielding too much dispersion. The Flux-Corrected Transport scheme gives convincing results with a coarse mesh and behaves very well in the gas region. By comparing schemes from the same class and looking at the relative error between estimated and analytical solutions, it is easy to conclude that the AUSMDV* scheme produces the best results when associated to the compressible model.

4.8 Summary

This chapter describes the details of the numerical approach used to transform the mathematical model into a numerical model.

The finite volume grid and discretisation used in the present study are presented. Numerical schemes are described. Two groups of schemes for conservative terms have been investigated: centred schemes and characterised-based schemes. Expressions of the non-conservative schemes used in this work are also formulated. This is followed by a discussion of well-known constraints on the time-step size and on the boundary conditions.

First-order schemes such as Lax-Friedrichs or Rusanov are found very diffusive and second-order schemes such as the Richtmyer Lax-Wendroff scheme are more accurate but create

oscillations at the discontinuity shock. For two-phase flow models, these results have more impact than single-phase flow: spurious oscillations can lead to non-converging solutions and an increasing dispersion might lead to a loss of information for the flow features. Higher-resolution schemes, such as TVD or FCT, are known to be more accurate and capable to handle strong discontinuities in the flow. As previously mentioned, FCT scheme is the most competitive when non-conservative terms are not present in the equations.

An advanced numerical method has been proposed and validated in this chapter. The AUSMDV* scheme is a hybrid scheme between the AUSMD* and AUSMV* schemes and demonstrates to have desirable properties: in particular, AUSMD* possesses an inherent accuracy with a highly reduced computational cost and AUSMV* is stable. Hence, taking advantage of both properties of these two schemes, AUSMDV* has been investigated and implemented with particular focus on the kind of discontinuities expected to appear for slow transients associated with mass transport in pipelines.

Several properties evaluating accuracy and efficiency of the model and the numerical method have been described and emphasised by numerical tests. Comparisons made with several numerical schemes enhance the qualities of the numerical method chosen for the model. Classical extreme benchmarks for the simulation of two-phase flows, namely Riemann problems, water faucet problem and sedimentation problem, have been tested and the features that the different tests require are all reproduced. Some typical problems occurred (overshoots near discontinuities...) but very encouraging results are obtained since computations can be performed over very fine meshes without a loss of stability or physical relevance due to the unconditional hyperbolicity of the model. This highlighted the AUSMDV* to be the most competitive for flow configurations such as near one-phase problems or cases presenting large discontinuities on pressure or velocities. It also has proved that our implemented version combined with the Centred-S scheme is very robust and accurate for the non-conservative models such as our compressible model (TPM5). It is therefore our default schemes that we advocated for this model.

Of course these tests are all benchmark test-cases and when performing practical cases against experimental data, the validation will be more significant. However, the completeness of this first stage is fundamental before moving forward to experimental-type numerical predictions as it provides a good understanding of the model behaviour and a strong base for future numerical experiments.

The scope of the next chapter is the influence of the pipeline geometry into the computations and the algorithm that has been implemented to represent it in the computations.

References - 4

[1] COQUEL, F., EL AMINE, E., GODLEWSKI, B., PERTHAME, B., AND RASCLE, P. A numerical method using upwind schemes for the resolution of two-phase flows. *J. Comp. Phys. 136* (1997), 272–288.

[2] DARWISH, M., MOUKALLED, F., AND SEKAR, B. A unified formulation of the segregated class of algorithms for multifluid flow at all speeds. *Numerical Heat Transfer 40* (2001), 99–137.

[3] DAVIS, S. A simplified tvd finite difference scheme via artificial viscosity. *ICASE report 84-20* (1984).

[4] EVJE, S., AND FLÅTTEN, T. Hybrid flux-splitting schemes for a common two-fluid model. *J. Comp. Phys. 192* (2003), 175–210.

[5] HARLOW, F. M., AND AMSDEN, A. A. Numerical calculations of multiphase flow. *J. Comp. Phys. 17* (1975), 19–52.

[6] HIRSCH., C. *Numerical Computation of Internal and External Flows*, 2nd ed., vol. 2. John Wiley and sons.

[7] LEVEQUE, R. *Numerical Methods for Conservation Laws.* Birkhäuser Verlag, 1990.

[8] LIOU, M. A sequel to AUSM: AUSM+. *J. Comp. Phys. 129* (1996), 364–382. Article no. 0256.

[9] LIOU, M., AND STEFFEN, C. A new flux splitting scheme. *NASA TM104404* (1991).

[10] MAHAFFY, J. H. A stability-enhancing two-step method for fluid flow calculations. *J. Comp. Phys. 46* (1982), 329–341.

[11] MASELLA, J. M. *Quelques Méthodes Numériques Pour Les Ecoulements Diphasiques Bi-Fluide En Conduites Pétrolières.* Ph.D. thesis, Université Pierre et Marie Curie, Paris VI, 1997.

[12] NIU, Y. Advection upwinding splitting method to solve a compressible two-fluid model. *Int. J. Numer. Meth. Fluids 36* (2001), 351–371.

[13] NOH, W. Errors for calculations of strong shocks using an artificial viscosity and an artificial heat flux. *J. Comp. Phys. 72*, 1 (1987), 78–120.

[14] OMGBA-ESSAMA, C. *Numerical modelling of transient gas-liquid flows (application to stratified and slug flow regimes).* Ph.D. thesis, Cranfield University, Applied Mathematics & Computing group, 2004.

[15] PAILLÈRE, H., CORRE, C., AND GARCIA CASCALES, J. On the extension of the AUSM+ scheme to compressible two-fluid models. *Computers and Fluids 32*, 6 (July 2003), 891–916.

[16] RANSOM, V. Numerical benchmark tests. In *Multiphase Science and Technology* (1987), J. D. edited by G.F. Hewitt and W. D. N.Zuber (Hemisphere, Eds., vol. 3.

[17] ROMATE, J. Developing a second-order tvd scheme for one-dimensional two-phase flow model. In *AMIF-ESF Workshop âĂŞ Computing Methods for Two-Phase Flow, Paper 22, Aussois, France* (January 12-14 2000).

[18] SAUREL, R., AND ABGRALL, R. A multiphase godunov method for compressible multifluid and multiphase flows. *Journal of Computational Physics 150* (1999), 425–467.

[19] SOD, G. *Numerical Methods in Fluids Dynamics, Initial and Initial Boundary-Value Problems.* Cambridge University Press, 1985.

[20] SPALDING, D. B. Development in the ipsa procedure for numerical computation of multiphase-flow phenomena with interphase slip, unequal temperatures. In *Numerical Methodologies in Heat Transfer, Proc. Second National Symposium.*

[21] SPALDING, D. B. Numerical computation of multi-phase fluid flow and heat transfer. *Recent Advances in Numerical Methods in Fluid* (1980), 139–167.

[22] STADTKE, H., F. G., AND WORTH, B. Numerical simulation of multi- dimensional two-phase based on hyperbolic flow equations. In *European Two Phase Flow Group Meeting, Piacenza, Italy* (6-8 June 1994).

[23] STADTKE, H., FRANCHELLO, G., AND WORTH, B. Numerical simulation of multi-dimensional two-phase flow based on flux vector splitting. *Nuclear Engineering and Design 177* (1997), 199–213.

[24] STEWART, H. B. Stability of two-phase flow calculation using two-fluid models. *J. Comp. Phys. 33* (1979), 259–270.

[25] TISELJ, I., AND PETELIN, S. Modelling of two-phase flow with second-order accurate scheme. *J. Comp. Phys. 136* (1997), 503–521.

[26] TORO, E. *Riemann Solvers and Numerical Methods for Fluid Dynamics.* Springer Verlag, 1997.

[27] TOUMI, I., AND KUMBARO, A. An approximate linearized Riemann solver for a two-fluid model. *J. Comp. Phys. 124* (1996), 286–300.

5 Geometry

5.1 Overview

In this chapter, we present the description, numerical implementation and subsequent validation of the algorithm which has been developed to simulate fluid flows in multiple pipes topography. The geometry algorithm is described in the first part of the chapter, and evaluated in the second by performing various testcases on single- and two-phase flows which secure the procedure validity. The main objective being to explain the methodology of the geometry algorithm that we have implemented, the majority of our description and validation will be dedicated to this purpose.

Section 5.2 outlines the different steps of the algorithm and their implementation in the solver.

The first test is performed on the shallow-water equations in Section 5.3. The motivation is to assess the integrity of the algorithm mechanism, and highlight possible limitations. The next stage in the validation process is focused on two-phase flows problems applied to stratified and slug flow regimes conditions.

Section 5.4 presents the stratified flow case. Details on stratified modelling, correlations for pressure gradient and liquid holdup, and the friction factors used in this case, are first given before performing the simulations on a downward elbow pipeline. The incompressible and the compressible models described in Chapter 3, are both used to perform the simulations and comparisons between the two of them can be drawn.

In Section 5.5, a review of the key parameters for slug flow modelling is presented, followed by a brief description of the various approaches used in the literature to numerically model this flow regime. Finally, numerical simulations carried out for terrain-induced slugging on a V-section pipe system are validated against available measurements. Slug frequency, film length and liquid holdup results are presented.

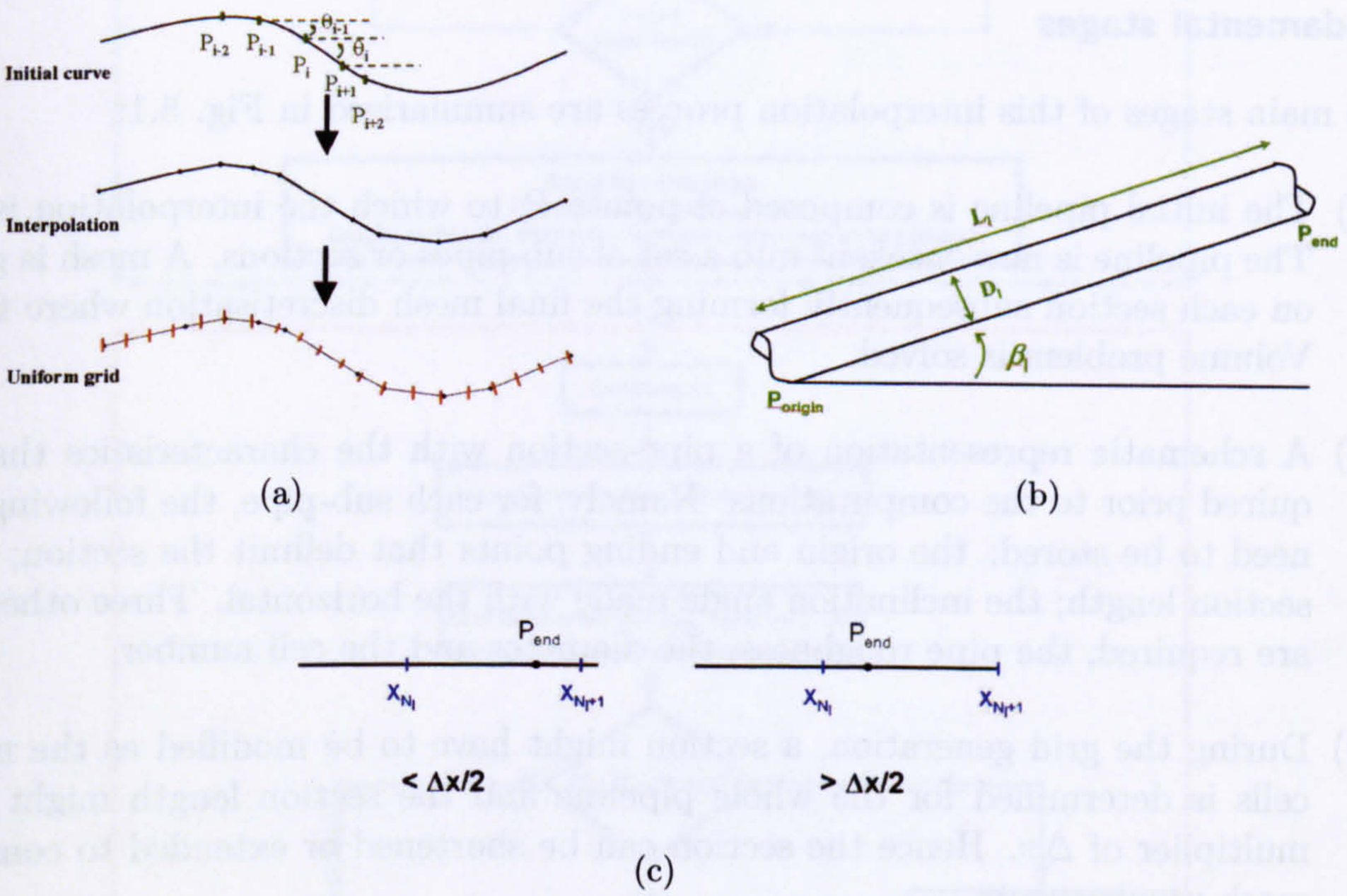

Figure 5.1 : *(a) Different steps of the process; (b) Schematic of sub-pipe features; (c) Grid adjustment.*

5.2 Algorithm

A common method to solve multiphase flow in pipelines is in a one-dimensional framework. The physical space is split up into small volumes where the partial differential equations are integrated over. The variables are then approximated by their average in each volume.

The purpose of this section is to describe the algorithm developed in this thesis for the resolution of multiphase flow problems on any pipeline topography. A one-dimensional space treatment of the pipeline is applied yielding a representation of the pipeline with segments or curves. The idea is thereby to approximate the original curve to obtain a set of segments or sections where the Finite Volume discretisation will be applied.

Fundamental stages

The main stages of this interpolation process are summarised in Fig. 5.1:

(a) The initial pipeline is composed of points P_i to which the interpolation is applied. The pipeline is now "broken" into a set of sub-pipes or sections. A mesh is generated on each section subsequently forming the final mesh discretisation where the Finite Volume problem is solved.

(b) A schematic representation of a pipe-section with the characteristics that are required prior to the computations. Namely, for each sub-pipe, the following features need to be stored: the origin and ending points that delimit the section; the pipe-section length; the inclination angle made with the horizontal. Three other features are required, the pipe roughness, the diameter and the cell number.

(c) During the grid generation, a section might have to be modified as the number of cells is determined for the whole pipeline and the section length might not be a multiplier of Δx. Hence the section can be shortened or extended to complete the mesh requirements.

The core of the geometry algorithm implemented is the region surrounded by a dashed line frame in Fig. 5.2. The region delimited by the plain line represents the grid generation procedure. The whole procedure [25], interpolation and meshing, can be described with the following algorithm:

Interpolation: Get the sub-pipes partition

a) Compute each Θ_i angle formed by $[P_iP_{i+1}]$ and the horizontal.

b) Get the set of nodes and the sub-pipes. For the approximation, a tolerance ϵ is required. The typical value is 10^{-3} and is chosen to provide the best approximation without drastically affecting the computing time.

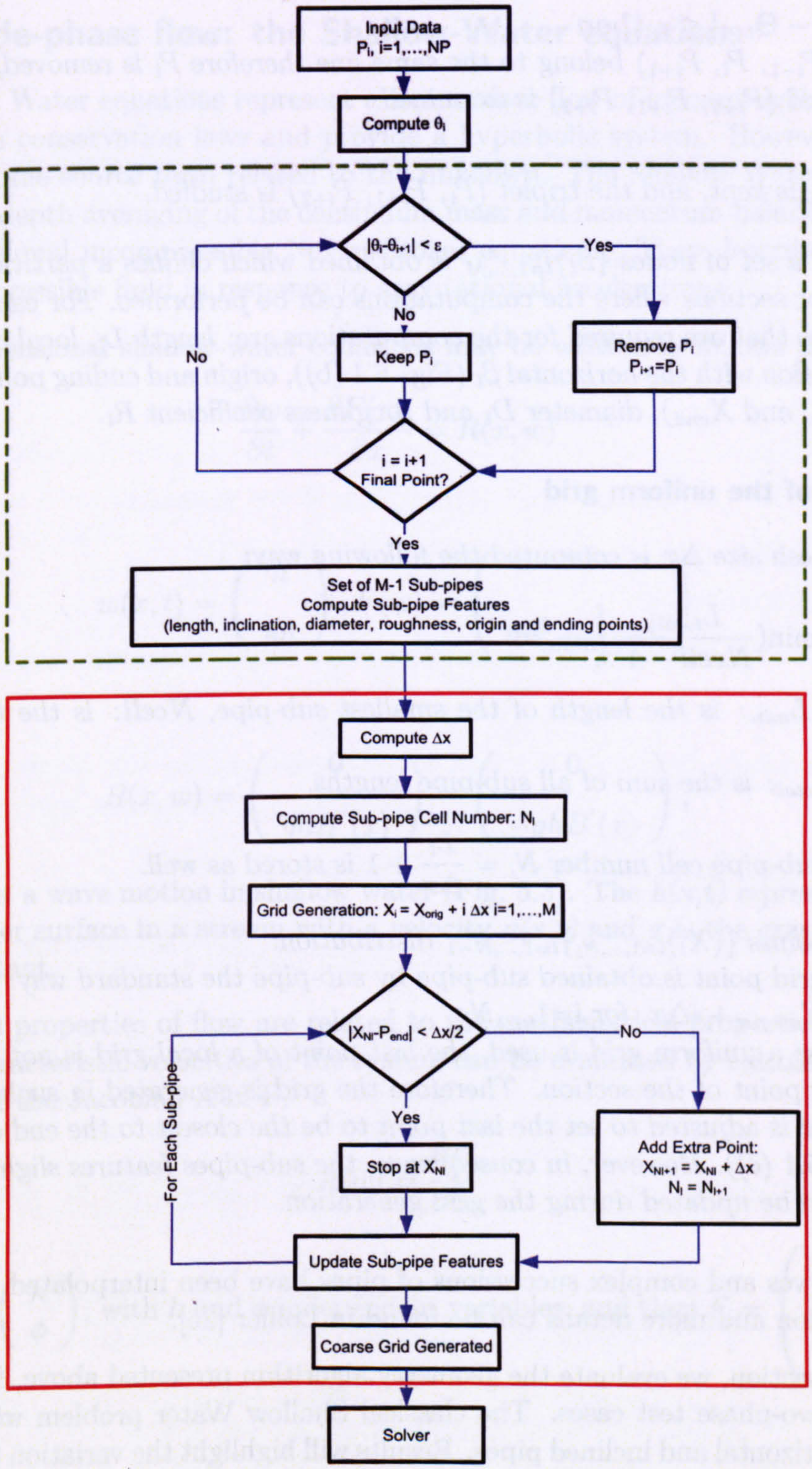

Figure 5.2 : *Flowchart that describes the algorithm for the interpolation algorithm and the grid generation. The first part (dashed line) represents the original topography interpolation procedure. The grid generation is described in the second part (plain line).*

if $|\Theta_i - \Theta_{i+1}| \leq \epsilon$ ***then***

(P_{i-1}, P_i, P_{i+1}) belong to the same line therefore P_i is removed, and $(P_{i-1}, P_{i+1}, P_{i+2})$ is examined.

else

P_i is kept, and the triplet (P_i, P_{i+1}, P_{i+2}) is studied.

c) *Hence, a set of nodes $\{S_l\}_{l=1,...,M}$ is obtained which defines a partition of M-1 sub-pipes or sections where the computations can be performed. For each of them, the features that are required for the computations are: length L_l, local cell number N_l, inclination with the horizontal β_l (Fig. 5.1 (b)), origin and ending points coordinates (X_{origin} and X_{end}), diameter D_l and roughness coefficient R_l.*

Generation of the uniform grid

a) *The mesh size Δx is computed the following way:*

$$\Delta x = \min(\frac{L_{total}}{Ncell - 1}, L_{min})$$

where L_{min}: is the length of the smallest sub-pipe, Ncell: is the total cell number,
and L_{total}: is the sum of all sub-pipe lengths.

b) *Each sub-pipe cell number $N_l = \frac{L_l}{\Delta x} + 1$ is stored as well.*

c) *Grid points $\{(X_i)_{i=1,...,N_l}\}_{l=1,...,N-1}$ distribution:*
Each grid point is obtained sub-pipe by sub-pipe the standard way:
$X_i = X_{origin} + i\Delta x$, for i=1,...,$N_l$.
Because a uniform grid is used, the last point of a local grid is not necessarily the ending point of the section. Therefore the grid is generated in such a way the cell number is adjusted to set the last point to be the closest to the end of the sub-pipe (Fig. 5.1 (c)). However, in consequence, the sub-pipes features slightly change and need to be updated during the grid generation.

Different curves and complex successions of pipes have been interpolated to validate the grid generation and more details can be found in Loilier [25].

In the next section, we evaluate the geometry algorithm presented above, for both single-phase and two-phase test cases. The classical Shallow Water problem will first be presented on horizontal and inclined pipes. Results will highlight the variation that may occur in the grid generation when subdividing the sections or sub-pipes. Two different cases of two-phase flow will also be presented: stratified flow on a downhill elbow simulated with both incompressible and compressible models, followed by a test-case of terrain-induced slugging in a v-section.

5.3 Single-phase flow: the Shallow-Water equations

The Shallow Water equations represent a free surface flow of incompressible water. They are based on conservation laws and provide a hyperbolic system. However, topography introduces some source term related to the unknown. The Shallow Water equations are obtained by depth averaging of the continuum mass and momentum balances given by the three-dimensional incompressible Navier-Stokes equations. They describe the evolution of an incompressible fluid in response to gravitational accelerations.

The one-dimensional shallow-water equations may be written as follows [26]

$$\frac{\partial w}{\partial t} + \frac{\partial F(w)}{\partial x} = R(x,w) \tag{5.1}$$

where

$$w(x,t) = \begin{pmatrix} h \\ uh \end{pmatrix}, F(w) = \begin{pmatrix} uh \\ hu^2 + \frac{1}{2}gh^2 \end{pmatrix} \tag{5.2}$$

and

$$R(x,w) = \begin{pmatrix} 0 \\ ghH'(x) \end{pmatrix} = \begin{pmatrix} 0 \\ -ghB'(x) \end{pmatrix}, \tag{5.3}$$

and represent a wave motion in shallow water (Fig. 5.3). The $h(x,t)$ represents the height of a free water surface in a stream with a velocity $u(x,t)$ and g is the gravitational acceleration constant.

The physical properties of flow are related to the mathematical properties of the model. The two characteristic velocities of the system can be evaluated by calculating the eigenvalues $\lambda_{1,2}$ of the Jacobian A of F.

$$A(w) = \frac{\partial F}{\partial w} \tag{5.4}$$

We set $w = \begin{pmatrix} h \\ \phi \end{pmatrix}$, with h and ϕ independent variables, and then $F = \begin{pmatrix} \phi \\ \frac{\phi^2}{h} + \frac{gh^2}{2} \end{pmatrix} = \begin{pmatrix} F_1 \\ F_2 \end{pmatrix}$, then

$$A(w) = \begin{pmatrix} \frac{\partial F_1}{\partial h} & \frac{\partial F_1}{\partial \phi} \\ \frac{\partial F_2}{\partial h} & \frac{\partial F_2}{\partial \phi} \end{pmatrix} = \begin{pmatrix} 0 & 1 \\ \frac{-\phi^2}{h^2} + gh & \frac{2\phi}{h} \end{pmatrix} = \begin{pmatrix} 0 & 1 \\ -u^2 + gh & 2u \end{pmatrix}. \tag{5.5}$$

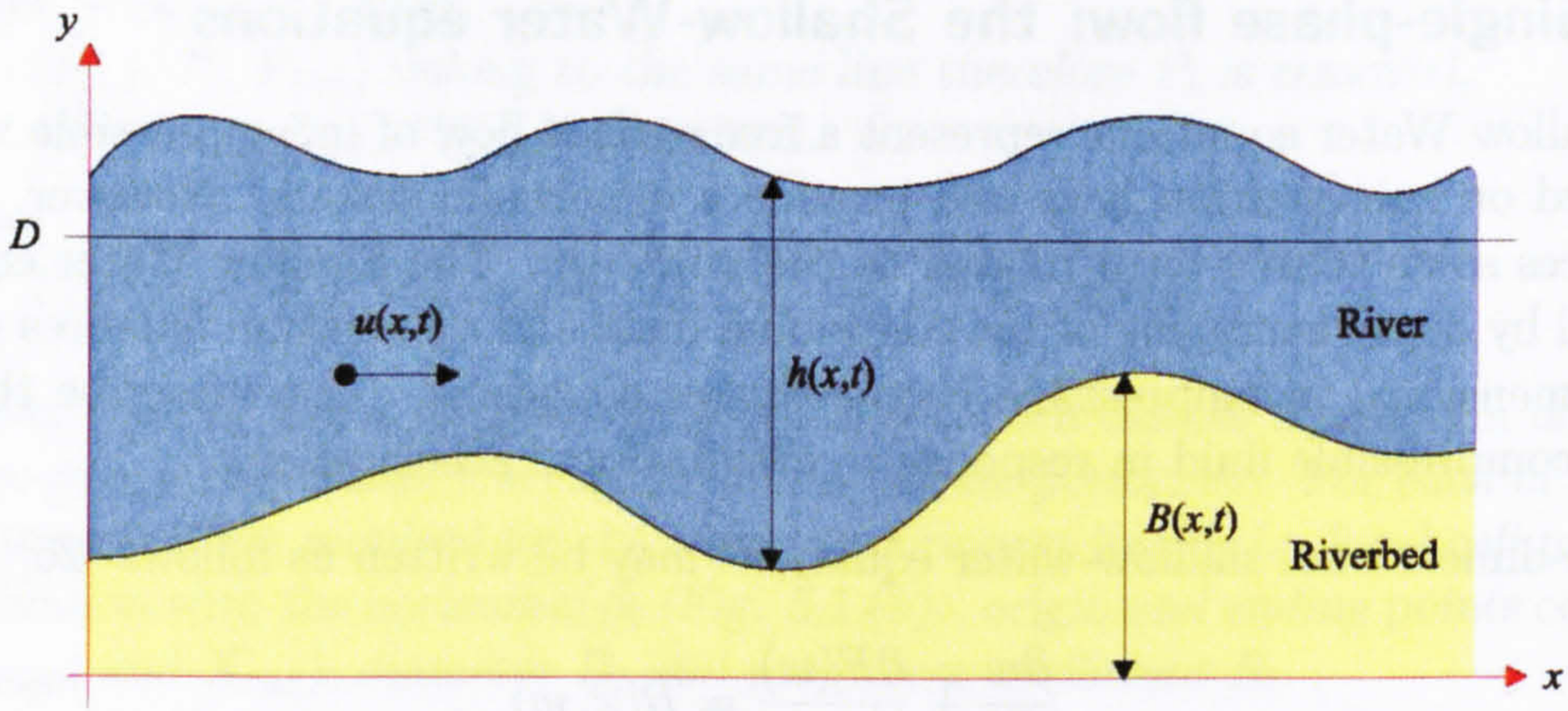

Figure 5.3 : *The Shallow Water Variables.*

Hence, the eigenvalues are :

$$\lambda_1 = u + \sqrt{gh} \quad \text{and} \quad \lambda_2 = u - \sqrt{gh} \tag{5.6}$$

These two velocities represent the speed of propagation of the two fronts of the wave.

5.3.1 Analytical solution (Dam Break problem)

The Dam Break test simulates the rupture of a barrier placed across a channel. The initial conditions for this problem are:

$$h(x,0) = \begin{cases} h_L & x < 0 \\ h_R & x > 0 \end{cases} \quad \text{and} \quad u(x,0) = 0 \tag{5.7}$$

The analytical solution for this problem was proposed in [26], for the case $R(x,w) = 0$, as:

$$h(x,t) = \begin{cases} h_L & \text{if} \quad \frac{x}{t} \leq -\sqrt{gh_L} \\ \frac{1}{9g}\left(2\sqrt{gh_L} - \frac{x}{t}\right)^2 & \text{if} \quad -\sqrt{gh_L} \leq \frac{x}{t} \leq \left(u_m - \sqrt{gh_m}\right) \\ h_m & \text{if} \quad \left(u_m - \sqrt{gh_m}\right) \leq \frac{x}{t} \leq s \\ h_R & \text{if} \quad s \leq \frac{x}{t} \leq \infty \end{cases} \tag{5.8}$$

and

$$u(x,t) = \begin{cases} 0 & \text{if} \quad \frac{x}{t} \leq -\sqrt{gh_L} \\ \frac{2}{3}\left(\sqrt{gh_L} + \frac{x}{t}\right) & \text{if} \quad -\sqrt{gh_L} \leq \frac{x}{t} \leq \left(u_m - \sqrt{gh_m}\right) \\ u_m & \text{if} \quad \left(u_m - \sqrt{gh_m}\right) \leq \frac{x}{t} \leq s \\ 0 & \text{if} \quad s \leq \frac{x}{t} \leq \infty \end{cases} \tag{5.9}$$

where the terms h_m and u_m are defined as function of the wave propagation velocity s as:

$$h_m = \frac{1}{2}\left(\sqrt{1 + \frac{8s^2}{gh_R}} - 1\right) h_R, \tag{5.10}$$

$$u_m = s - \frac{gh_R}{4s}\left(1 + \sqrt{1 + \frac{8s^2}{gh_R}}\right) \tag{5.11}$$

with s the positive real solution of the following equation

$$u_m + 2\sqrt{gh_m} - 2\sqrt{gh_L} = 0. \tag{5.12}$$

To solve this equation, an iterative scheme such as dichotomy can be used. However the exact solution was provided by the authors of the paper [26].

5.3.1.1 Numerical results - flat channel

The initial heights for the test simulated were $h_L = 0.1$ and $h_R = 0.5$ with a discontinuity located at $0.5\ m$. The total distance is $1\ m$. Simulations have been run on 2 different riverbeds. The first one is a flat channel; the second is the same channel divided into three parts. The purpose of this comparison is to check the integrity of the process at the pipe junctions.

Fig. 5.4 show the height and velocity profiles obtained with the Shallow Water model at 0.1 second when using the central and upwind schemes described in the previous chapter.

All the simulations presented in Fig. 5.4 use a CFL value of 0.2 to calculate the time step. Although not providing the most accurate results for the test in hand, this value was selected, firstly, because it highlights a bit better the differences between the numerical schemes evaluated, and secondly, because it is the CFL value generally used for two-phase flow simulations presented later in this thesis.

In general, the characteristic-based schemes are less diffusive and more accurate than

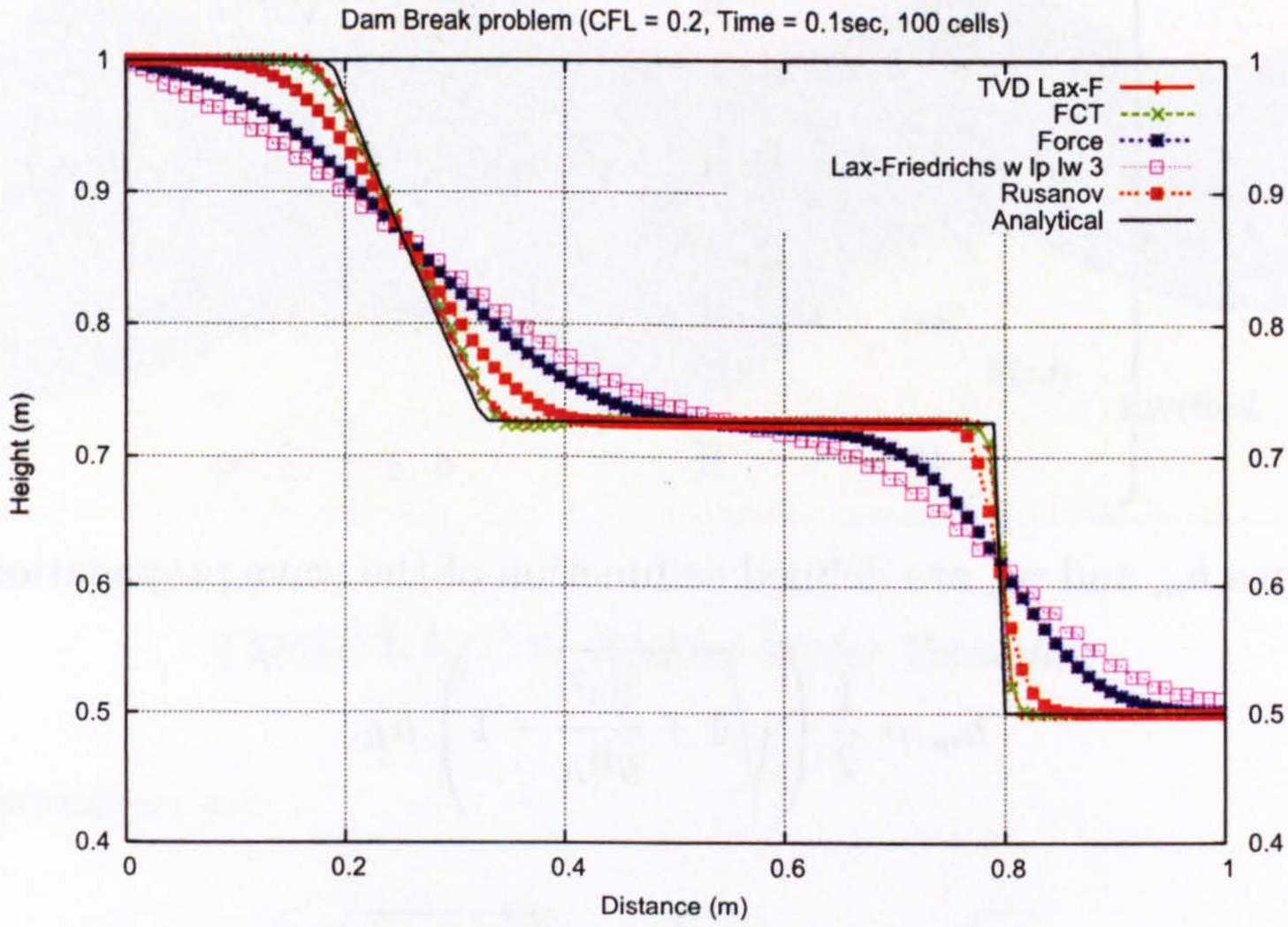

(a)

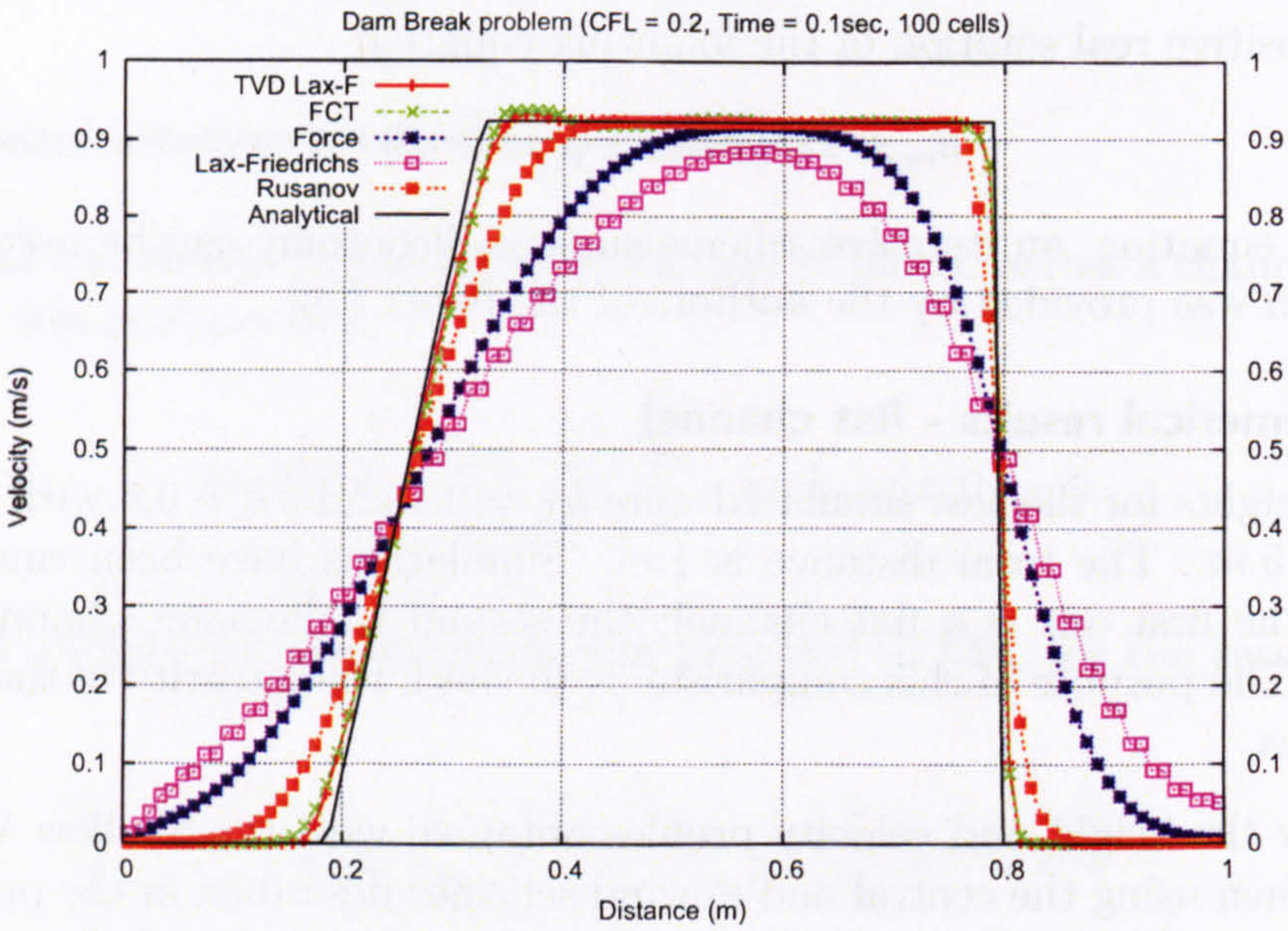

(b)

Figure 5.4 : *Shallow Water (Dam Break). Height and velocity profiles at $t = 0.1$ s for central and upwind schemes. Conclusion can be drawn that FCT and TVD Lax-Friedrichs schemes give the best answers. The Rusanov scheme is also very satisfying.*

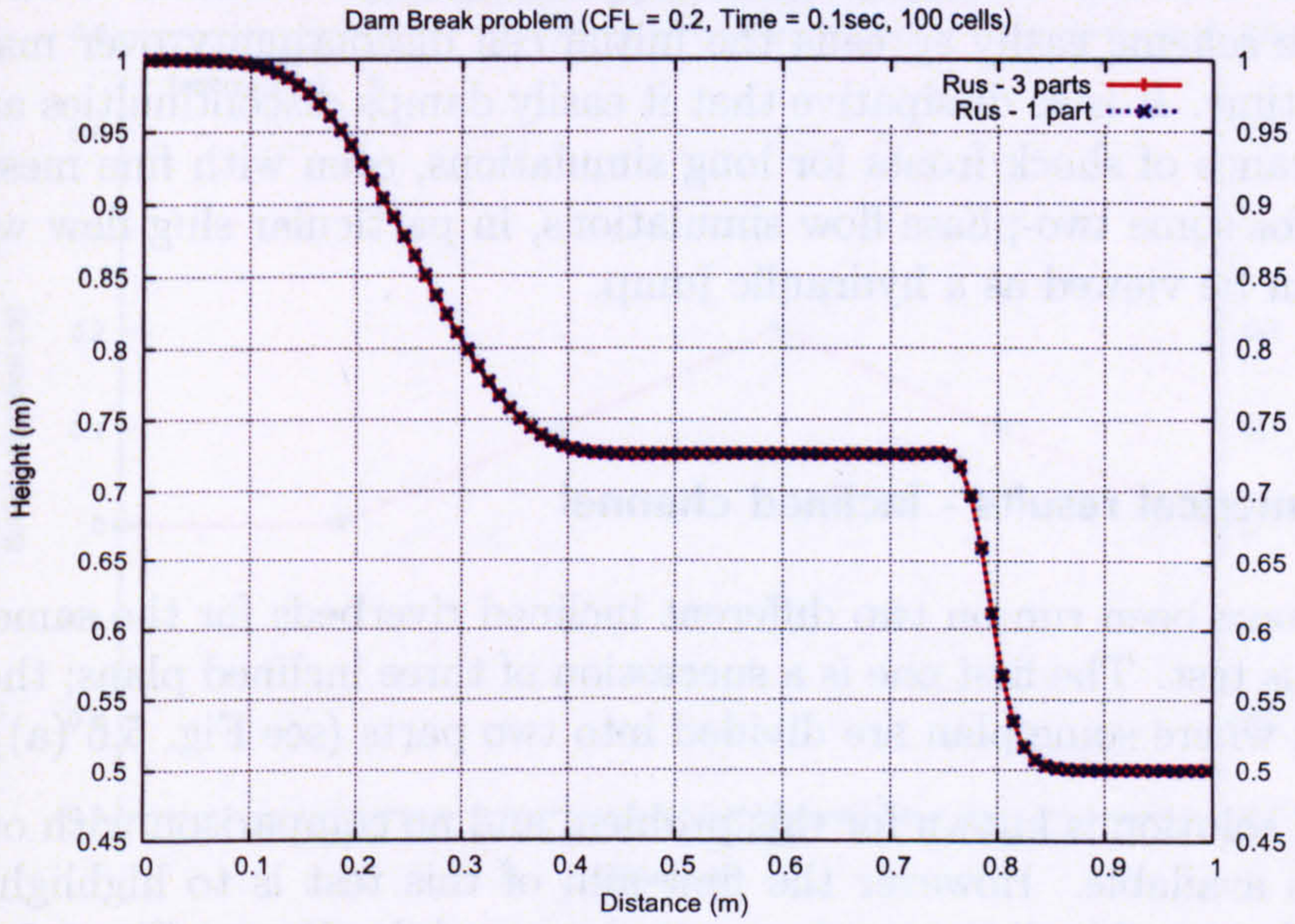

(a)

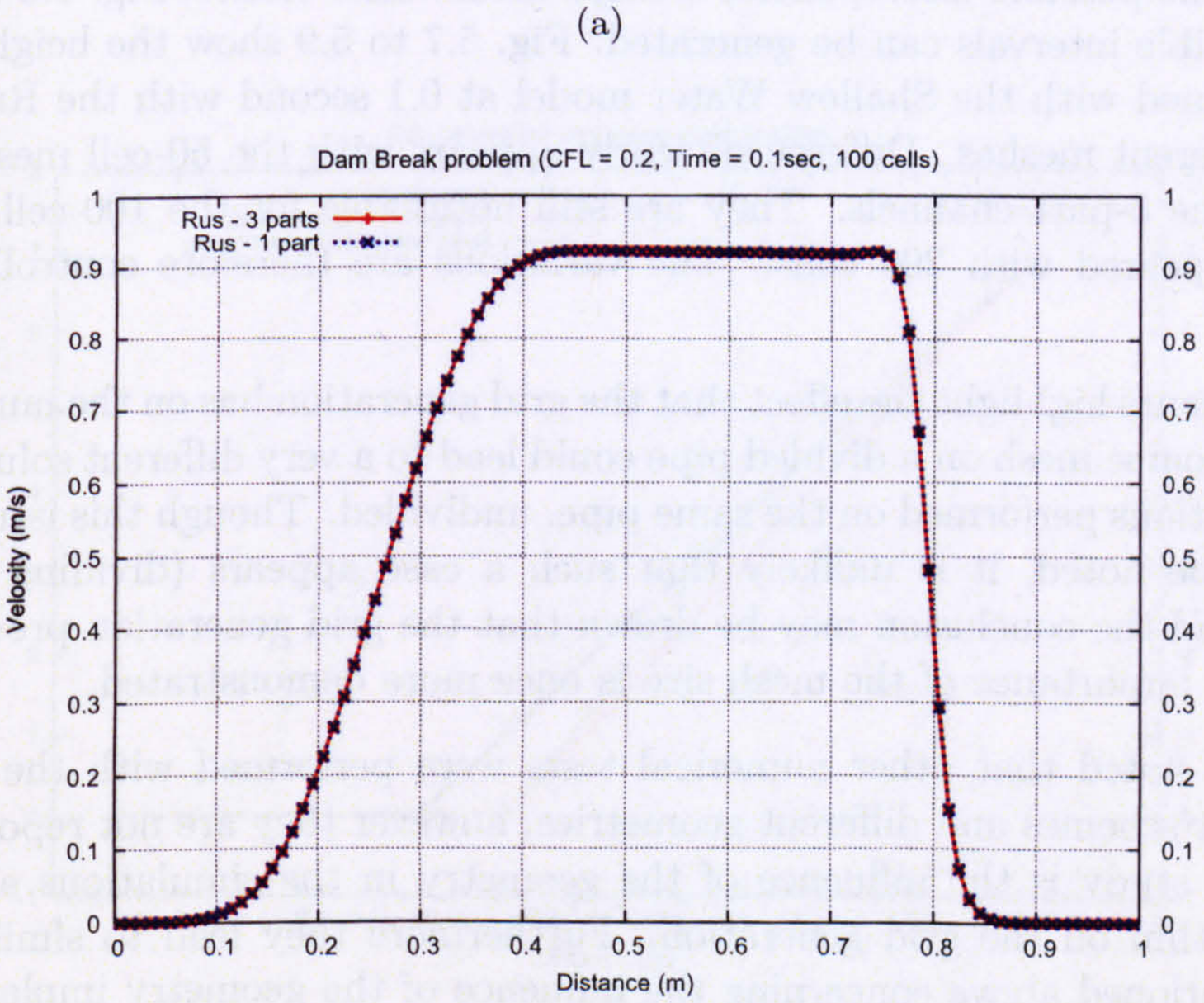

(b)

Figure 5.5 : *Shallow Water (Dam Break). Height and velocity profiles at $t = 0.1\,s$ comparison between single channel and three-part channel.*

the central ones. But for the Shallow-water problem, the FCT scheme is found to be the most accurate, followed closely by the TVD Lax-Friedrichs scheme, then the Rusanov and Force schemes. The Lax-Friedrichs results appear the least accurate of all the numerical results, as the scheme easily spreads the initial cell discontinuity over many cells while advancing in time. It is so dissipative that it easily damps discontinuities and can lead to the disappearance of shock fronts for long simulations, even with fine meshes. This fact is undesired for some two-phase flow simulations, in particular slug flow where the front of the slug can be viewed as a hydraulic jump.

5.3.1.2 Numerical results - inclined channel

Simulations have been run on two different inclined riverbeds for the same conditions as in the previous test. The first one is a succession of three inclined plans; the second is the same channel where some plan are divided into two parts (see Fig. 5.6 (a)).

No analytical solution is known for this problem and no comparison with other numerical predictions is available. However the first aim of this test is to highlight the gridding process and the possible discrepancies created meanwhile. Hence, Fig. 5.6 (b) exemplifies how the possible intervals can be generated. Fig. 5.7 to 5.9 show the height and velocity profiles obtained with the Shallow Water model at 0.1 second with the Rusanov scheme for three different meshes. Difference clearly appears with the 50-cell mesh between the 3-part and the 5-part channels. They are still noticeable for the 100-cell mesh and are almost disappeared with 200 cells. The variations are therefore controlled with mesh refinement.

The above results highlight the effect that the grid generation has on the numerical results. Using a too coarse mesh on a divided pipe could lead to a very different solution compared to the simulations performed on the same pipe, undivided. Though this issue is important and should be noted, it is unlikely that such a case appears (dividing a single pipe-section) [1], and the conclusion may be drawn that the grid generation process is reliable, although the importance of the mesh size is once more demonstrated.

It should be noted that other numerical tests were performed with the geometry [25] with different schemes and different geometries, however they are not reported here. The focus of this study is the influence of the geometry in the simulations and the impact of the algorithm on the grid generation. Furthermore they lead to similar conclusions to those mentioned above concerning the influence of the geometry implementation into the computations and regarding the numerical schemes accuracy and robustness already described in Chapter 4.

[1] In the case of Adaptive Mesh Refinement (AMR), a single pipe would be divided. However, the AMR process will refine the existing mesh when needed without modifying the pipe length, therefore eliminating the geometric anomaly creation.

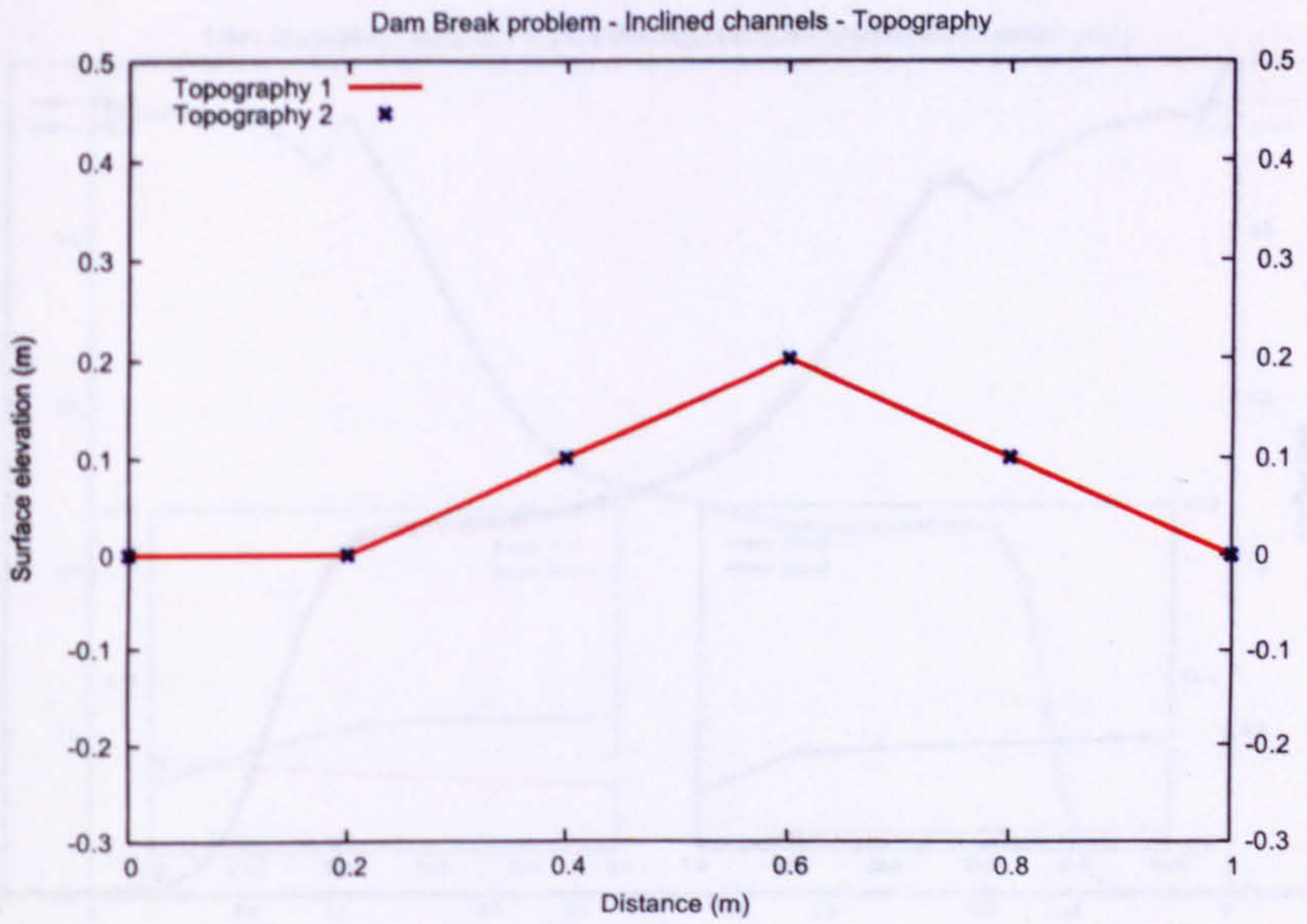

(a)

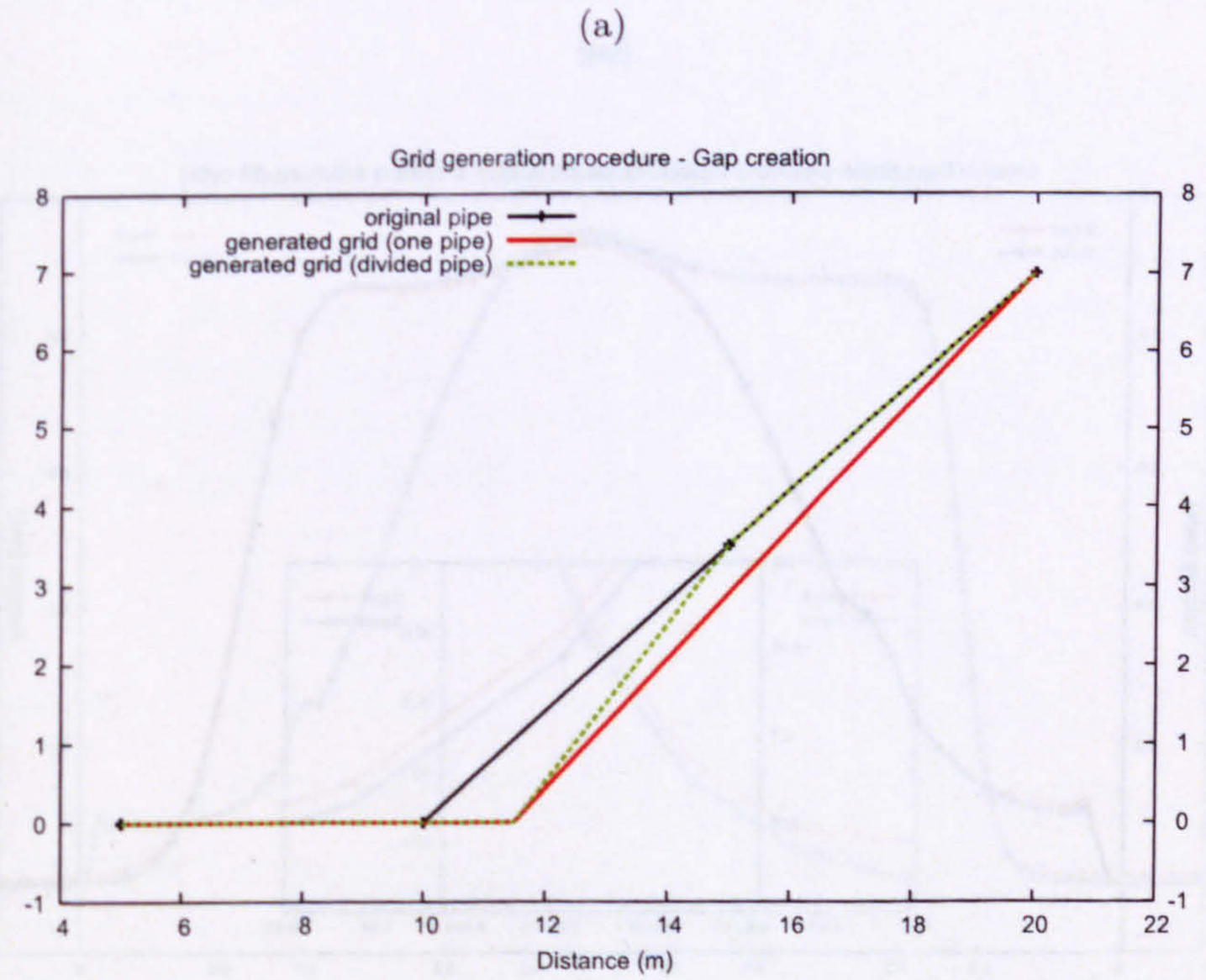

(b)

Figure 5.6 : *(a) Shallow Water - Inclined channel topographies. (b) Interpolation between divided pipe and non-divided pipe. The figure is deliberately zoomed in to highlight the geometric anomaly creation.*

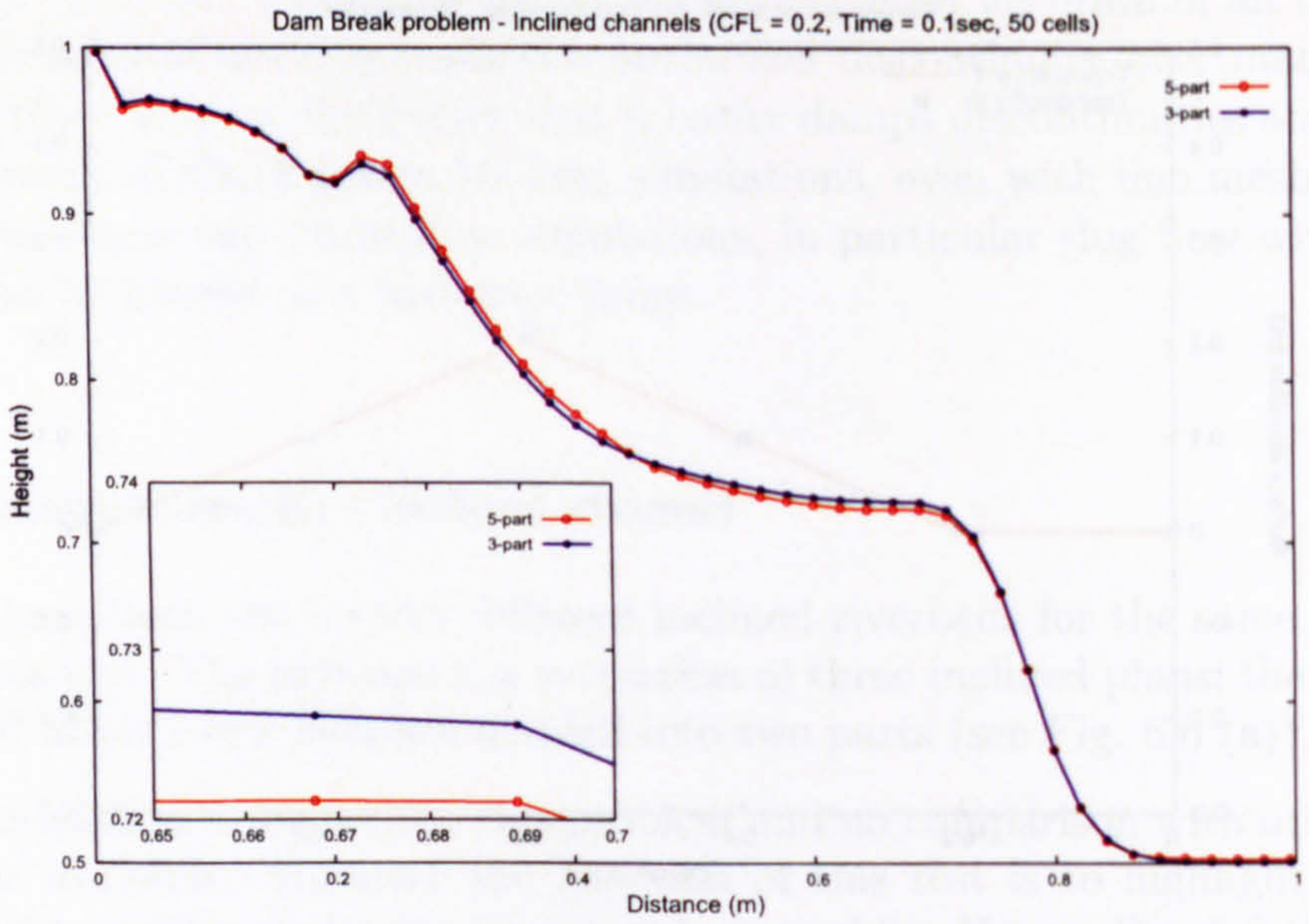

(a)

(b)

Figure 5.7 : *Shallow-Water problem - Inclined channels. Influence of the gridding process on the predictions (creation of discrepancies) with 50 cells.*

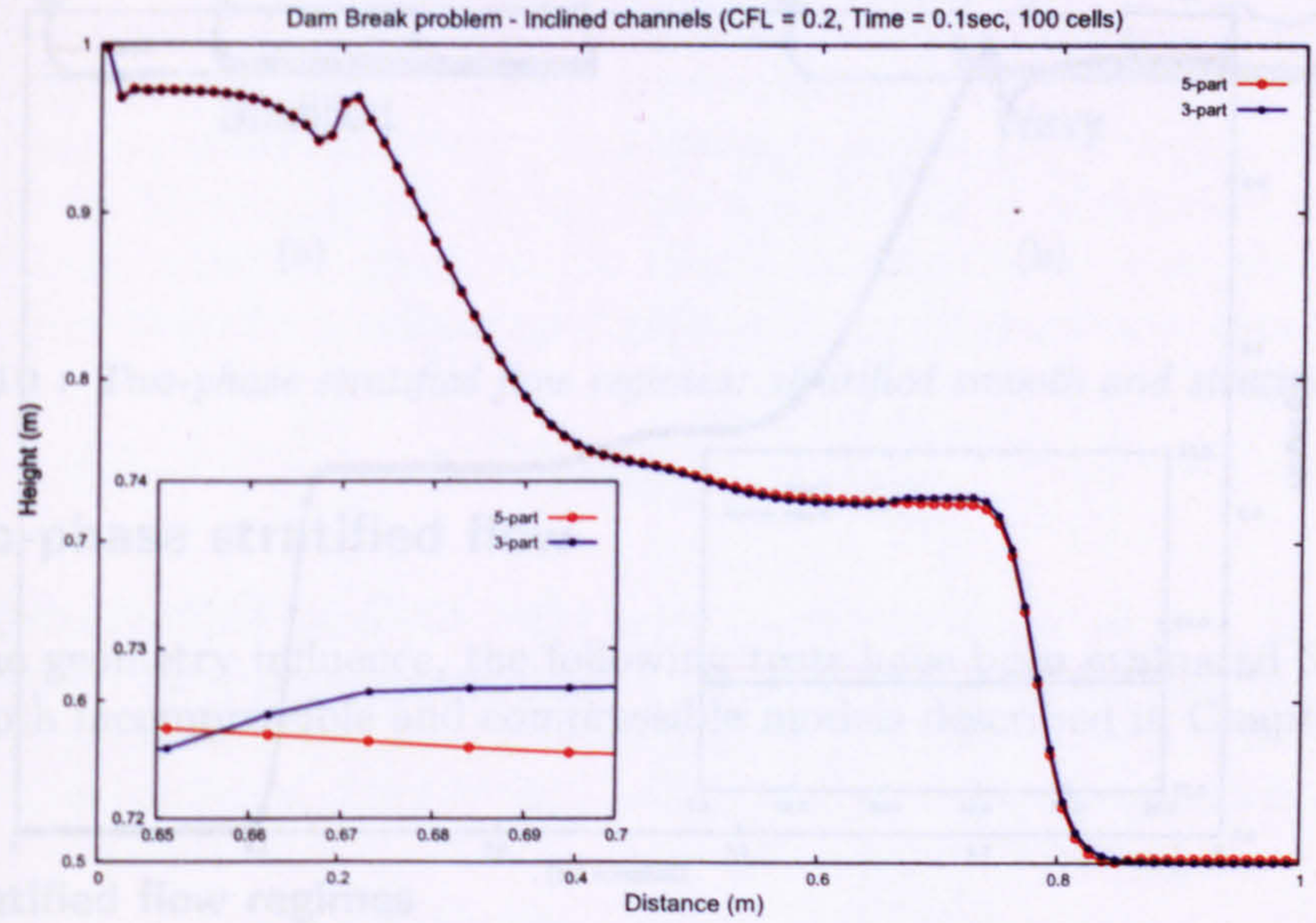

(a)

(b)

Figure 5.8 : *Shallow-Water problem - Inclined channels. Influence of the gridding process on the predictions (creation of discrepancies) with 100 cells.*

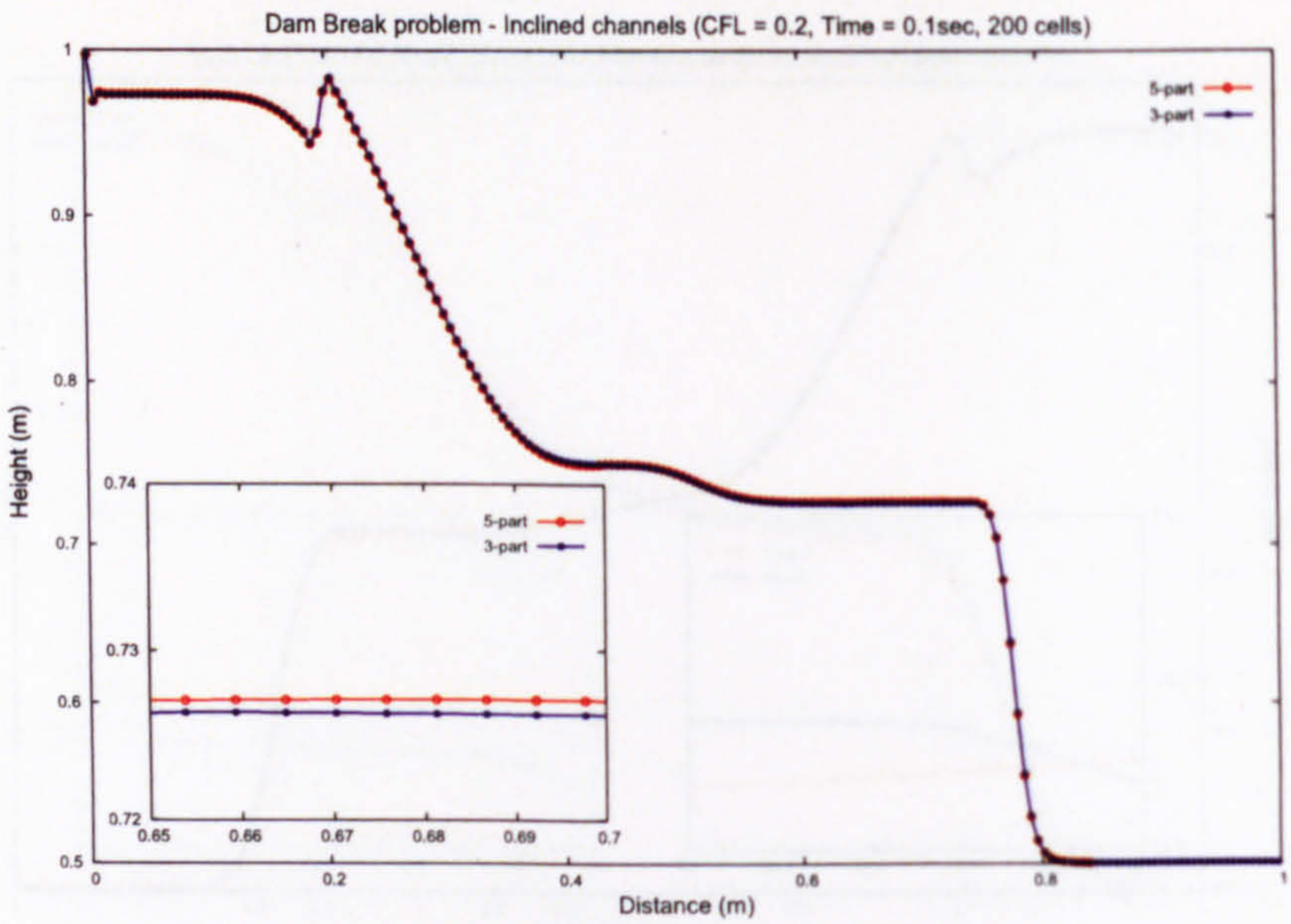

(a)

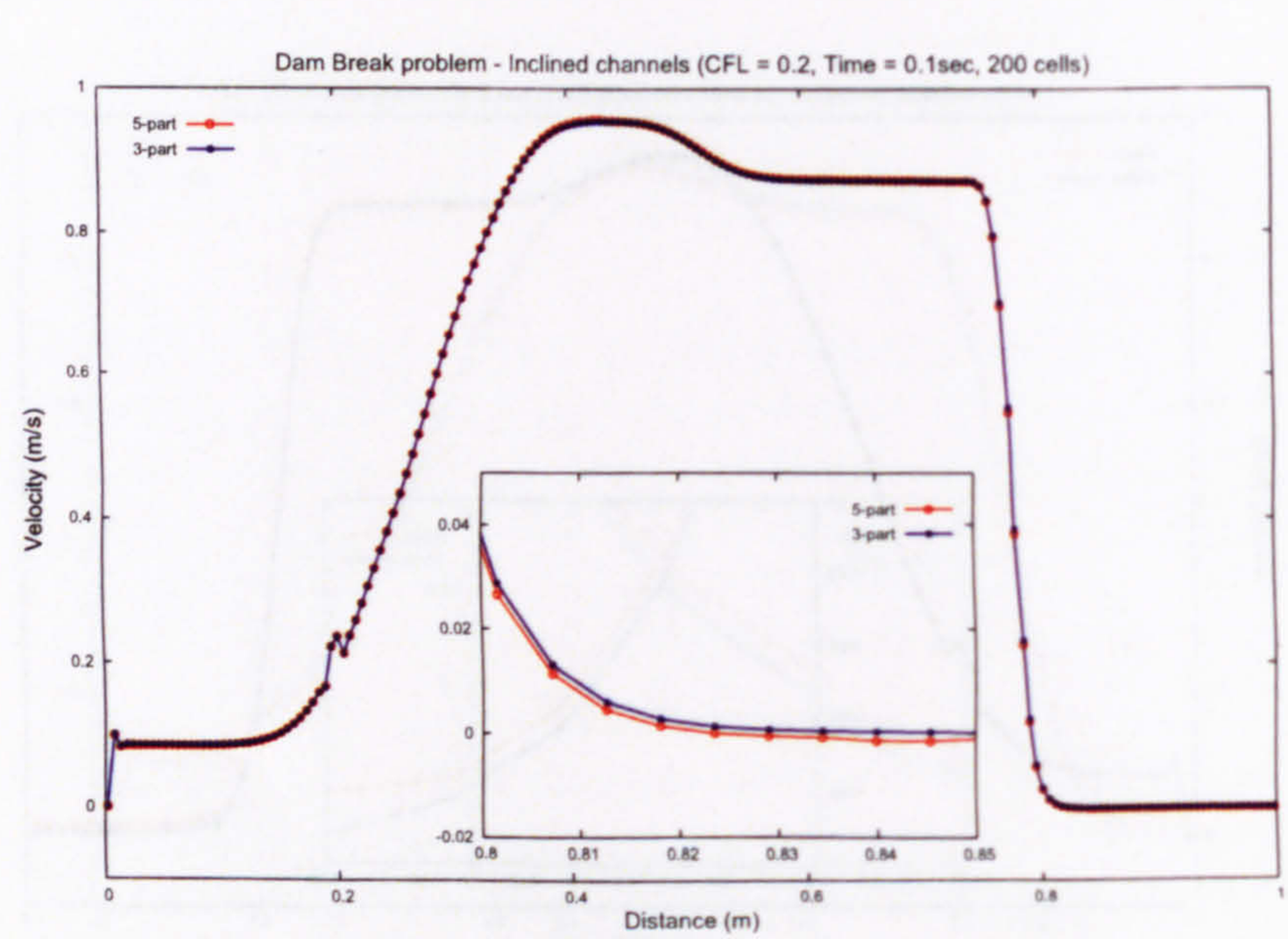

(b)

Figure 5.9 : *Shallow-Water problem - Inclined channels. Influence of the gridding process on the predictions (creation of discrepancies) with 200 cells. The differences created by the algorithm are controlled with fine meshes.*

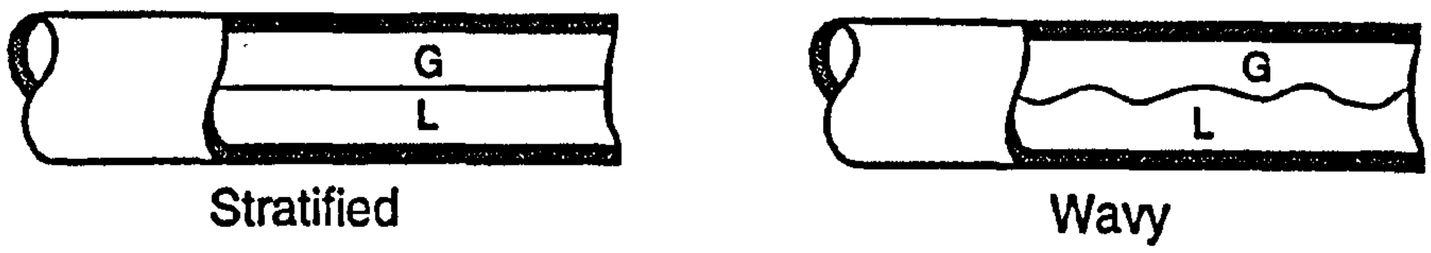

(a) (b)

Figure 5.10 : *Two-phase stratified flow regimes: stratified smooth and stratified wavy flow.*

5.4 Two-phase stratified flow

To assess the geometry influence, the following tests have been evaluated for a stratified case with both incompressible and compressible models described in Chapter 3.

5.4.1 Stratified flow regimes

This flow pattern is characterized by the complete two phases separation from each other. The liquid whose density is the highest flows down the pipe whereas the gas flows above the liquid. The two phases are separated by a curved mean interface (concave towards the gas) in a straight pipe-section. Two different stratified flows occur depending on the interface (Fig. 5.10): the shear between the gas and the liquid leads to wave formation when the velocity difference is high, we talk about *stratified wavy*. At low gas velocities, the gas-liquid interface appears undisturbed or smooth, we talk about *stratified smooth* flow. Stratified flows happen in horizontal and nearly horizontal pipes but not in vertical flow.

5.4.2 Modelling

There are two important design parameters for petroleum engineers, the pressure drop and the liquid holdup, and many methods have been derived to predict them accurately. Although the primary goal of this study is to predict unsteady flows, an accurate estimation of these full developed parameters is often required as initial conditions for transient simulations. Additionally, for a rapid convergence of the mathematical models and numerical schemes, these two parameters have to be properly evaluated.

The correlations for pressure drop and liquid holdup used in the simulations are the only ones presented here. Detailed review of pressure drop and liquid holdup can be found in the following works [20, 35]. We also detail in this section the friction factors correlations used.

5.4.2.1 Pressure drop correlation

The pressure drop is defined as a combination of three terms, frictional, acceleration and gravitational:

$$\frac{dP}{dx} = \left(\frac{dP}{dx}\right)_f + \left(\frac{dP}{dx}\right)_{acc} + \left(\frac{dP}{dx}\right)_{grav} \tag{5.13}$$

The gravitational or hydrostatic pressure drop is given by:

$$\left(\frac{dP}{dx}\right)_{grav} = \rho_g g \Delta h \sin\beta \tag{5.14}$$

and is equal to zero for horizontal flow. Also when the total mass velocity is less than $2700 kg/(m^2/s)$, only the frictional term is of importance [13]. As most prediction methods are concerned with this case, we only define here the frictional term of the overall pressure drop. The frictional pressure drop formulation [32] we used, is defined as follows:

$$\left(\frac{dP}{dx}\right)_f = G(1-x_g)^{1/3} + bx_g^3 \tag{5.15}$$

with

$$G = \left(\frac{dP}{dx}\right)_{l0} + 2\left(\left(\frac{dP}{dx}\right)_{g0} - \left(\frac{dP}{dx}\right)_{l0}\right) x_g \tag{5.16}$$

$$\left(\frac{dP}{dx}\right)_{k0} = \frac{2 f_{k0}(G_g + G_l)^2}{D\rho_k} \tag{5.17}$$

$$f_{k0} = \max\left(\frac{16}{Re_{k0}}, \frac{0.046}{Re_{k0}^{0.2}}\right) \tag{5.18}$$

$$Re_{k0} = \frac{(G_g + G_l)D}{\mu_k} \tag{5.19}$$

$$x_g = \frac{G_g}{G_g + G_l} = \frac{\rho_g V_{sg}}{\rho_g V_{sg} + \rho_l V_{sl}} \tag{5.20}$$

V_{sg} and V_{sl} are respectively the gas and liquid superficial velocities.

5.4.2.2 Liquid holdup equilibrium value

The default value as initial liquid holdup is generally obtained with the semi-theoretical correlation developed by Taitel and Dukler [41]. They used a one-dimensional steady state separated flow model and proposed the first analytical solution for the liquid holdup value combining separate momentum balances for the gas and liquid by eliminating the pressure gradient terms. Assuming that the liquid layer is of constant height, with a smooth gas-liquid interface, and that the interfacial shear term is equal to the gas-wall shear term, they derived a non-dimensional form of this combined momentum balance as:

$$X^2 \left[(\tilde{V}_l \tilde{D}_l)^{-n} \tilde{V}_l^2 \frac{\tilde{S}_l}{\tilde{A}_l} \right] - \left[(\tilde{V}_g \tilde{D}_g)^{-m} \tilde{V}_g^2 \left(\frac{\tilde{S}_g}{\tilde{A}_g} + \frac{\tilde{S}_l}{\tilde{A}_l} + \frac{\tilde{S}_I}{\tilde{A}_g} \right) \right] - 4Y = 0 \tag{5.21}$$

The inclination parameter Y is defined as

$$Y = \frac{(\rho_l - \rho_g) g \sin\beta}{\left(\frac{dP}{dx}\right)_g} \tag{5.22}$$

where $\left(\frac{dP}{dx}\right)_g$ is the pressure drop correlation given in Eq. 5.15.

The Martinelli parameter X^2 is constant for given gas and liquid flowrates and fluid properties and is defined as:

$$X = \frac{\left(\frac{dP}{dx}\right)_l}{\left(\frac{dP}{dx}\right)_g} \tag{5.23}$$

with

$$\left(\frac{dP}{dx}\right)_k = \frac{2 f_k (\alpha_k \rho_k V_k)^2}{D \rho_k} \tag{5.24}$$

$$f_k = \max\left(\frac{16}{Re_k}, \frac{0.046}{Re_k^{0.2}}\right) \tag{5.25}$$

$$Re_k = \frac{\alpha_k \rho_k V_k D}{\mu_k} \tag{5.26}$$

The equilibrium equation Eq. 5.21 is an implicit function of the liquid height. It therefore requires an iterative root finding scheme (Newton's method) to solve it and provide an accurate estimate for the stratified liquid height and also for the equilibrium gas and liquid volume fractions and velocities.

5.4.2.3 Friction factors

As previously stated in Chapter 3, the closure equations for friction factors has to be treated with great care in the formulation of two-fluid models. Despite numerous theoretical [41] and experimental [4] investigations into gas liquid pipe flow, no general friction models are available to predict frictional pressure drop and liquid holdup for all horizontal flow situations. However, some validated models exist in the literature. The purpose of this section is not to review all of them but for more details, we recommend the following thesis [20, 35].

We present here the correlations used for the stratified cases which are the correlation from Taitel and Dukler [41] for the gas-wall and the gas-liquid interfaces, and the Hand correlation [21] for the liquid-wall interface:

$$f_g = \begin{cases} 0.046 Re_g^{-0.25} & \text{if } Re_g < 2100 \\ \dfrac{16}{Re_g} & \text{if } Re_g \geq 2100 \end{cases} \tag{5.27}$$

$$f_l = \begin{cases} \dfrac{24}{Re_l} & \text{if } Re_l < 2100 \\ 0.0262(\alpha_l Re_{sl})^{-0.139} & \text{if } Re_l \geq 2100 \end{cases} \tag{5.28}$$

$$f_i = f_g \tag{5.29}$$

with $Re_{sl} = \dfrac{V_{sl} D}{\mu_l}$.

This association of friction factor correlations has been chosen for their simplicity and their ability to reproduce stratified flow simulations. It is however known that this choice of interfacial friction factor may overestimate the liquid holdup value in horizontal part. Another expression such as the one proposed by Andritsos and Hanratty [4] might give more accurate results in the purpose of simulating stratified flow as suggested in [35]. However our first motivation, here, is to validate the geometry influence and not the investigation of interface drag law for stratified flow regimes.

5.4.3 Problem summary

The test case consists of a downhill elbow where the fluid mixture travel under stratified flow conditions. The downhill section is inclined at 1.5^o with respect to the horizontal. It is illustrated schematically in Fig. 5.11 and the specifications of the problem are given as:

- Pipeline length: $20m$ (section 1: $10m$ - section 2: $10m$)
- Diameter: $78mm$
- Operating fluids: air and water ($\rho_g = 1.16\, kg/m^3$, $\rho_l = 1000\, kg/m^3$)

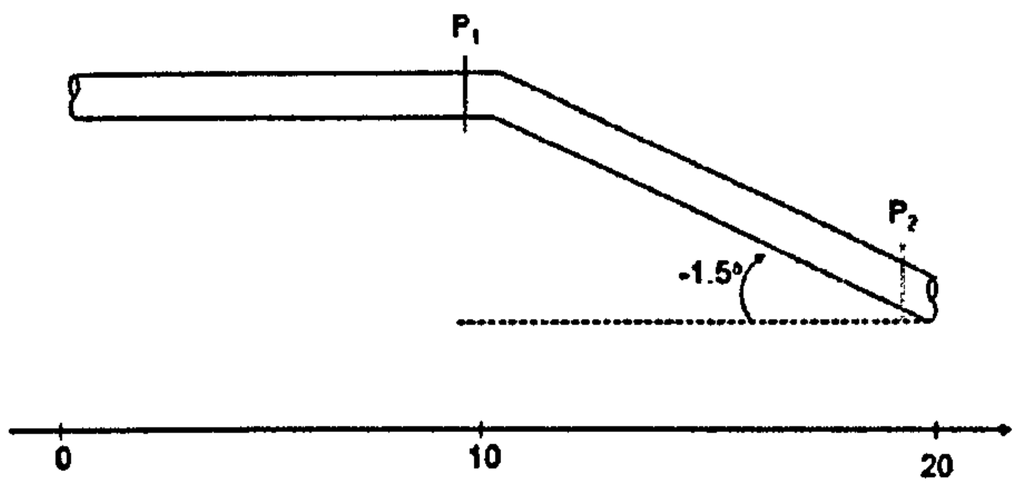

Figure 5.11 : *Stratified simulation: test pipe section. Data are collected at probes P_1 and P_2.*

- Flow temperature: $T = 296\,K$
- Outlet flow pressure: $10^5\,Pa$.

The objective of the problem is to test the interaction of the geometry in the momentum formulation.

Initially ($t = 0\,s$), the tube is filled with a uniform mixture of air and water with different velocities, such that the gas volume fraction is 0.5. The thermodynamic properties of the system at the initial state are assumed constant at values appropriate for air-water mixture and read 296 K for the temperature and 1 bar for the pressure. The boundary conditions at the inlet of the tube are similar to the initial input data, and are given as:

$$\begin{cases} V_{sg} = 2.0\,ms^{-1} \\ V_{sl} = 0.1\,ms^{-1} \\ \alpha_l^0 = 0.5 \end{cases} \tag{5.30}$$

The outlet is considered as an open boundary for the conservative variables except for the pressure which is fixed constant to atmospheric pressure (1 bar). However, when we use the incompressible two-fluid model to simulate this problem, we do not enforce explicitly this condition but consider the end of the tube as an open boundary for the conservative variables used by the model.

5.4.4 Numerical results

Various numerical effects are presented in this section for the stratified test case. The computational results for fluid volume fractions and velocities presented here are at different time steps and various grid meshes, and were all performed with a CFL condition of 0.2.

Taitel and Dukler [41] have given a formula to obtain the analytical value of the volume

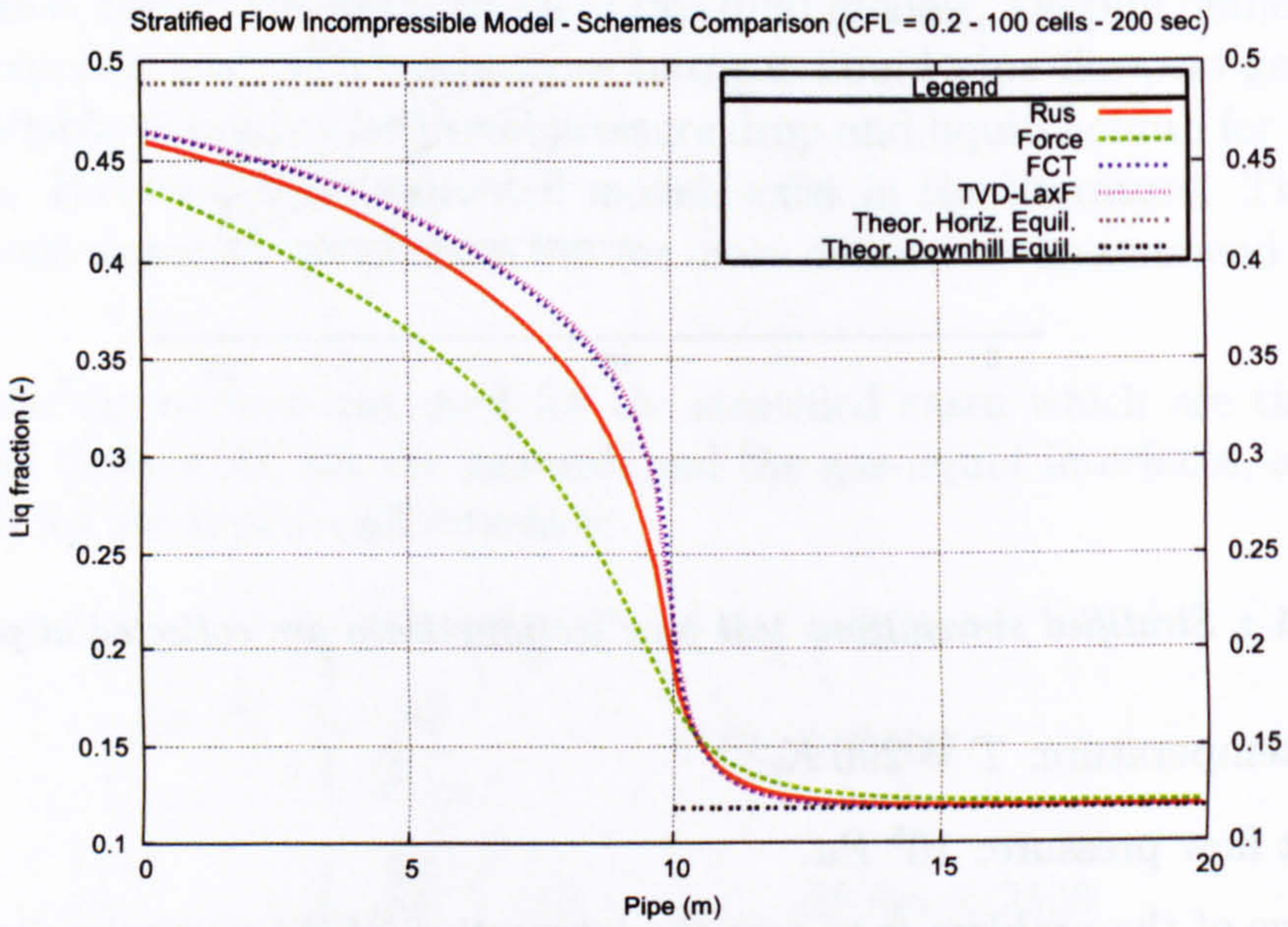

(a) Incompressible model

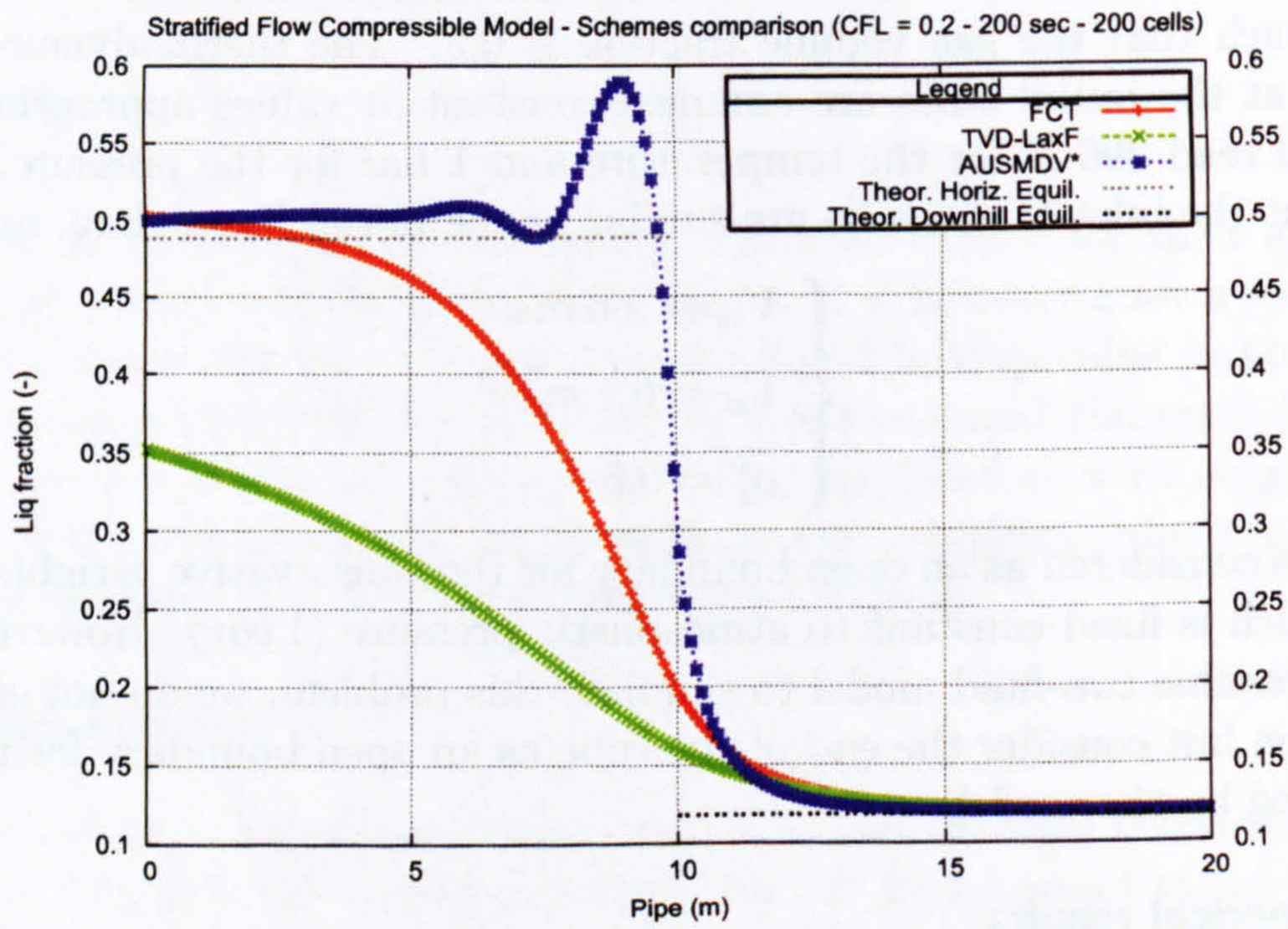

(b) Compressible model

Figure 5.12 : *Stratified horizontal-downward test - Liquid holdup profile for different schemes for both compressible and incompressible models.*

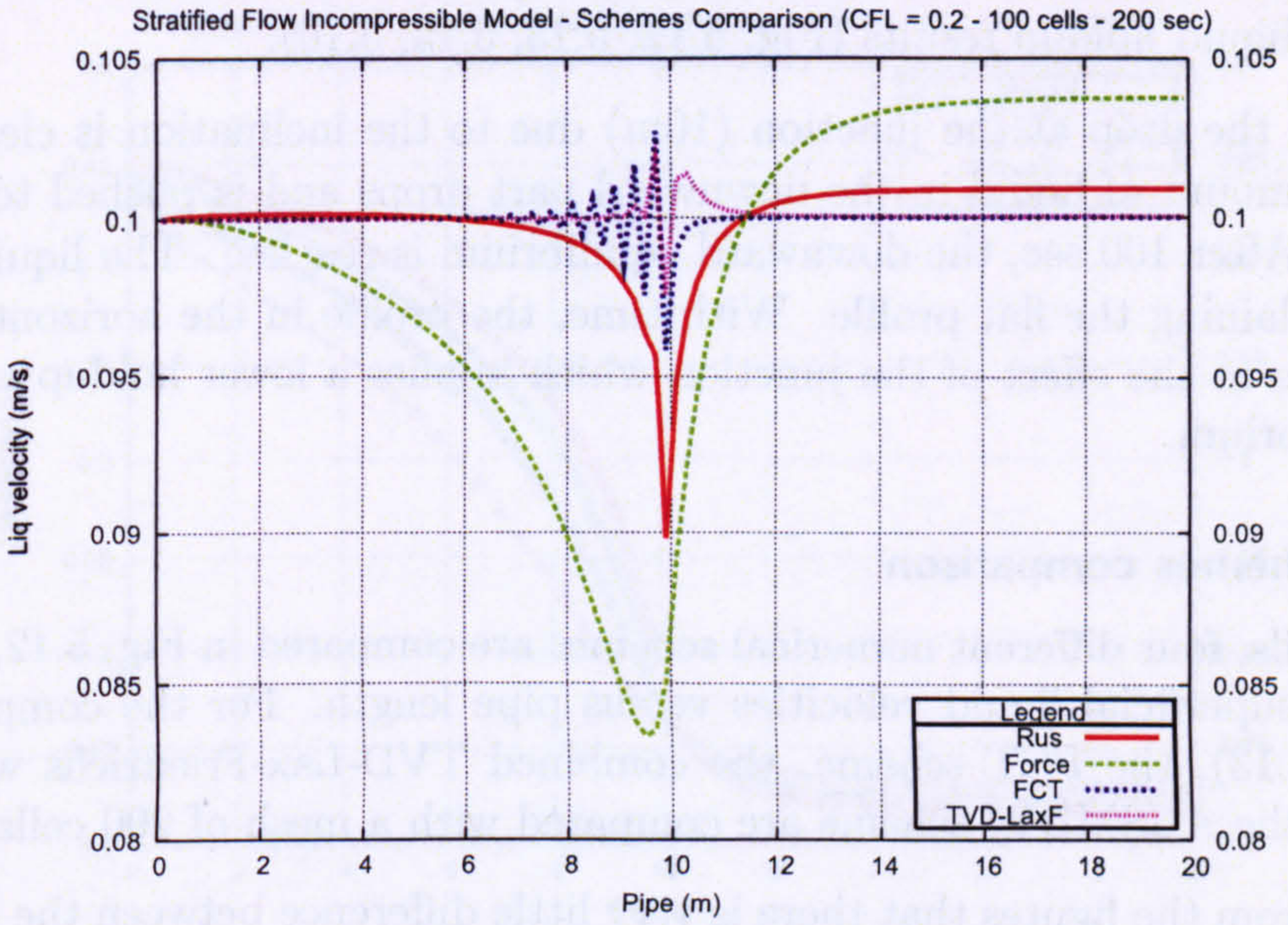

(a) Incompressible model

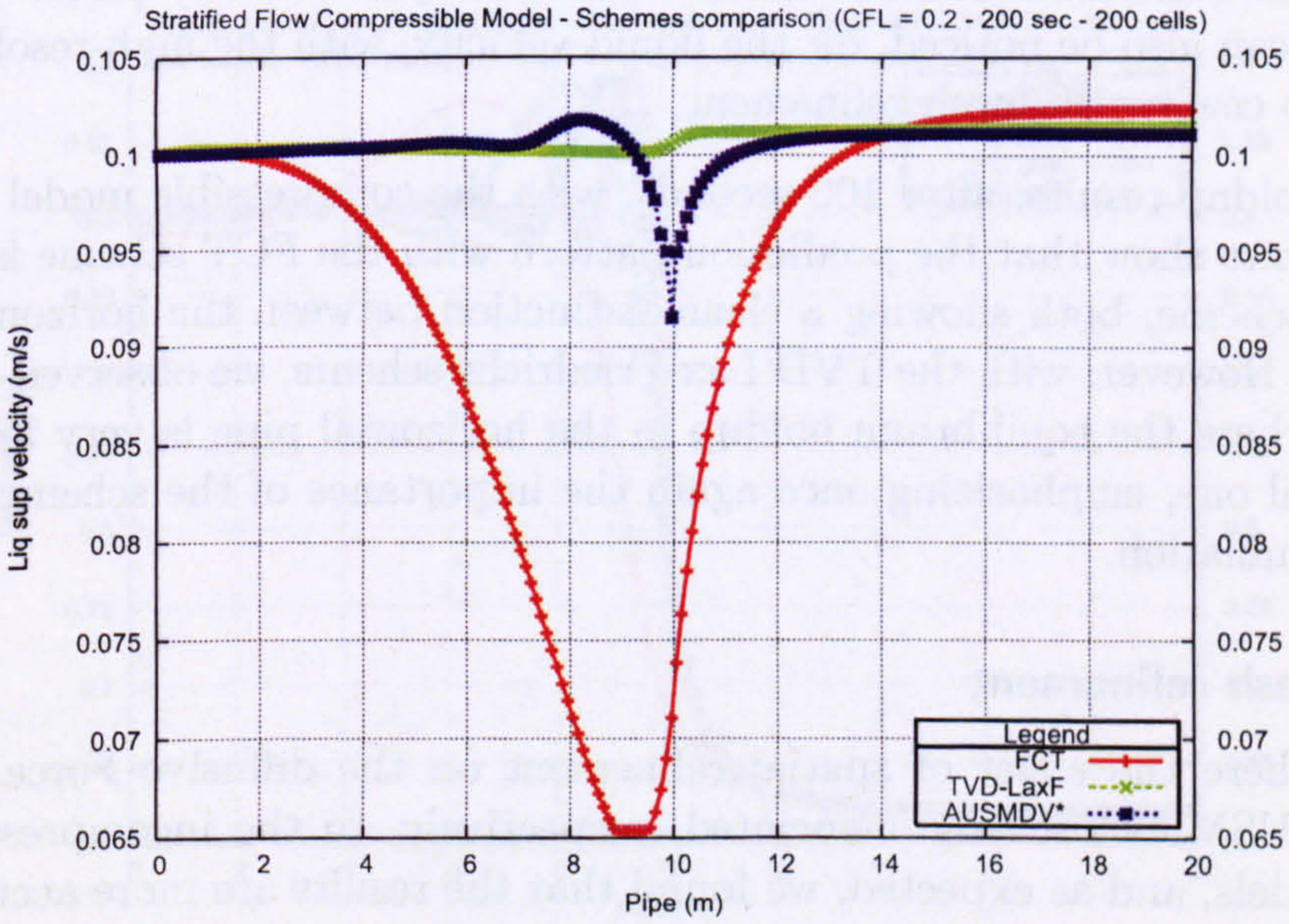

(b) Compressible model

Figure 5.13 : *Stratified horizontal-downward test - Superficial liquid velocity profile for different schemes for both compressible and incompressible models.*

fraction in steady-state cases, in any inclined single pipe. The two values of the liquid holdup concerned in our example are found 0.488 in the horizontal part, and 0.118 in the downward part. These two critical values are represented in dashed lines in the graphs showing the liquid holdup results (Fig. 5.12, 5.13, 5.15, 5.16).

After 10 sec, the drop at the junction ($10m$) due to the inclination is clearly identified. The initial amount of liquid in the downward part drops and is pushed towards the end of the pipe. After 100 sec, the downward equilibrium is reached. The liquid height never changes, explaining the flat profile. With time, the profile in the horizontal branch gets smoother due to the effect of the junction which implies a lower holdup value compared to the equilibrium.

5.4.4.1 Schemes comparison

Using 100 cells, four different numerical schemes are compared in Fig. 5.12, 5.13 for liquid holdup and superficial liquid velocities versus pipe length. For the compressible model (Fig. 5.12, 5.13), the FCT scheme, the combined TVD-Lax-Friedrichs with Minmod-2 scheme and the AUSMDV* scheme are compared with a mesh of 200 cells.

We can see from the figures that there is very little difference between the high-resolution schemes (FCT and TVD-Lax-Friedrichs) for the liquid holdup with the incompressible model. The difference is clearly visible with the basic Force scheme and with the Rusanov scheme. Same conclusion can be drawn from the liquid velocity plots. Oscillations at the junction can also be noticed, for the liquid velocity, with the high-resolution schemes. They tend to cease with mesh refinement.

The liquid holdup results, after 100 seconds, with the compressible model for various numerical schemes show that the prediction pattern with the FCT scheme is similar to the AUSMDV* scheme, both showing a clear distinction between the horizontal and the inclined pipes. However, with the TVD Lax-Friedrichs scheme, we observed a very diffusive behaviour, where the equilibrium holdup in the horizontal pipe is very low compared to the analytical one, emphasizing once again the importance of the scheme selection for a particular simulation.

5.4.4.2 Mesh refinement

We present here the effect of spatial refinement on the diffusive Force and the high-resolution AUSMDV* scheme associated, respectively, to the incompressible and compressible models, and as expected, we found that the results are more accurate with finer meshes.

Fig. 5.14 (a) summarises the behaviour of the liquid holdup profile obtained using the combined incompressible model and Force scheme with different grid sizes. The results show to be diffusive in the horizontal part. In Fig. 5.14 (b), we present the grid size effect on the liquid holdup predictions for the compressible model. The scheme is the AUSMDV*. Oscillations are created at $10m$ and decreased in amplitude with mesh re-

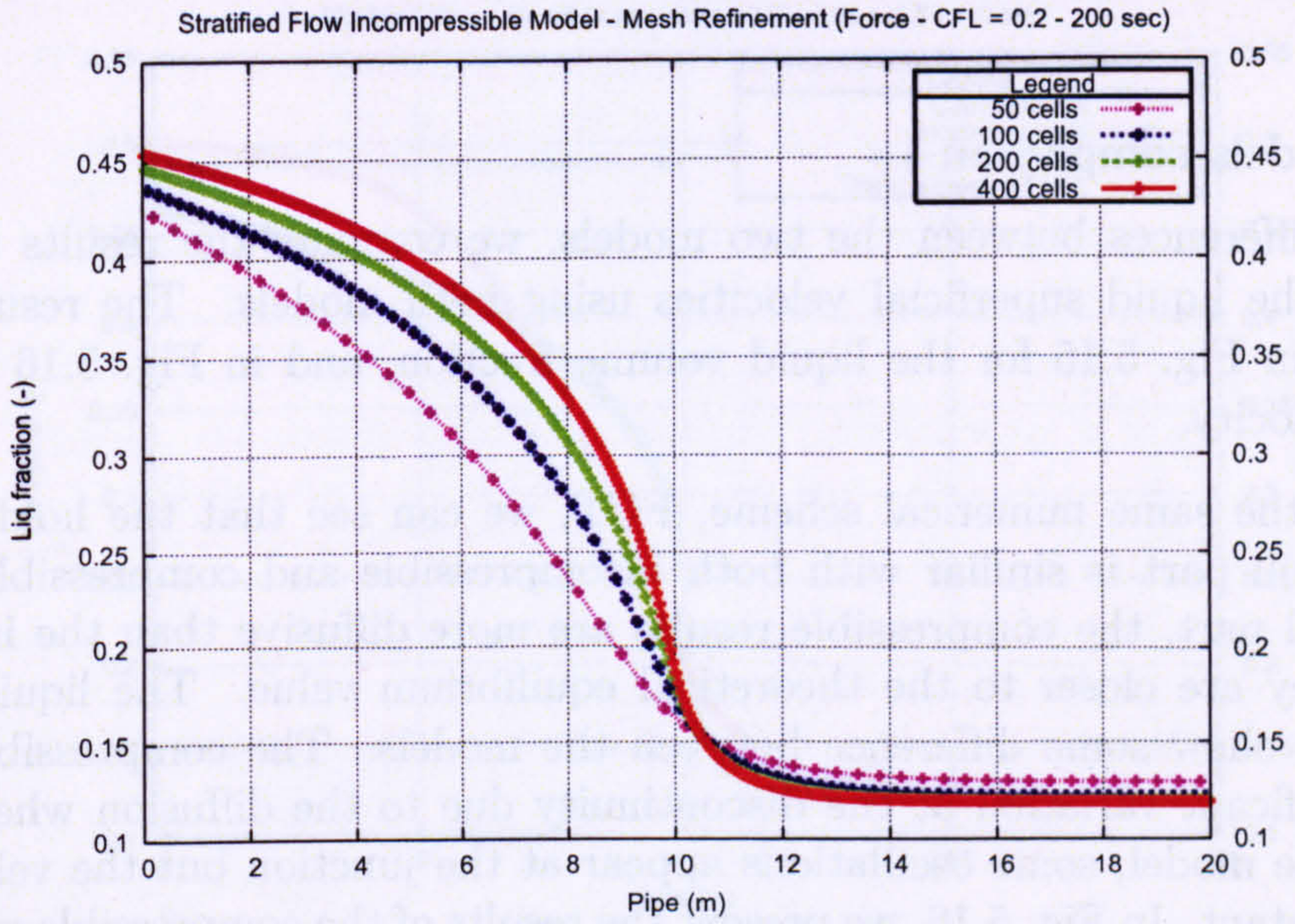

(a)

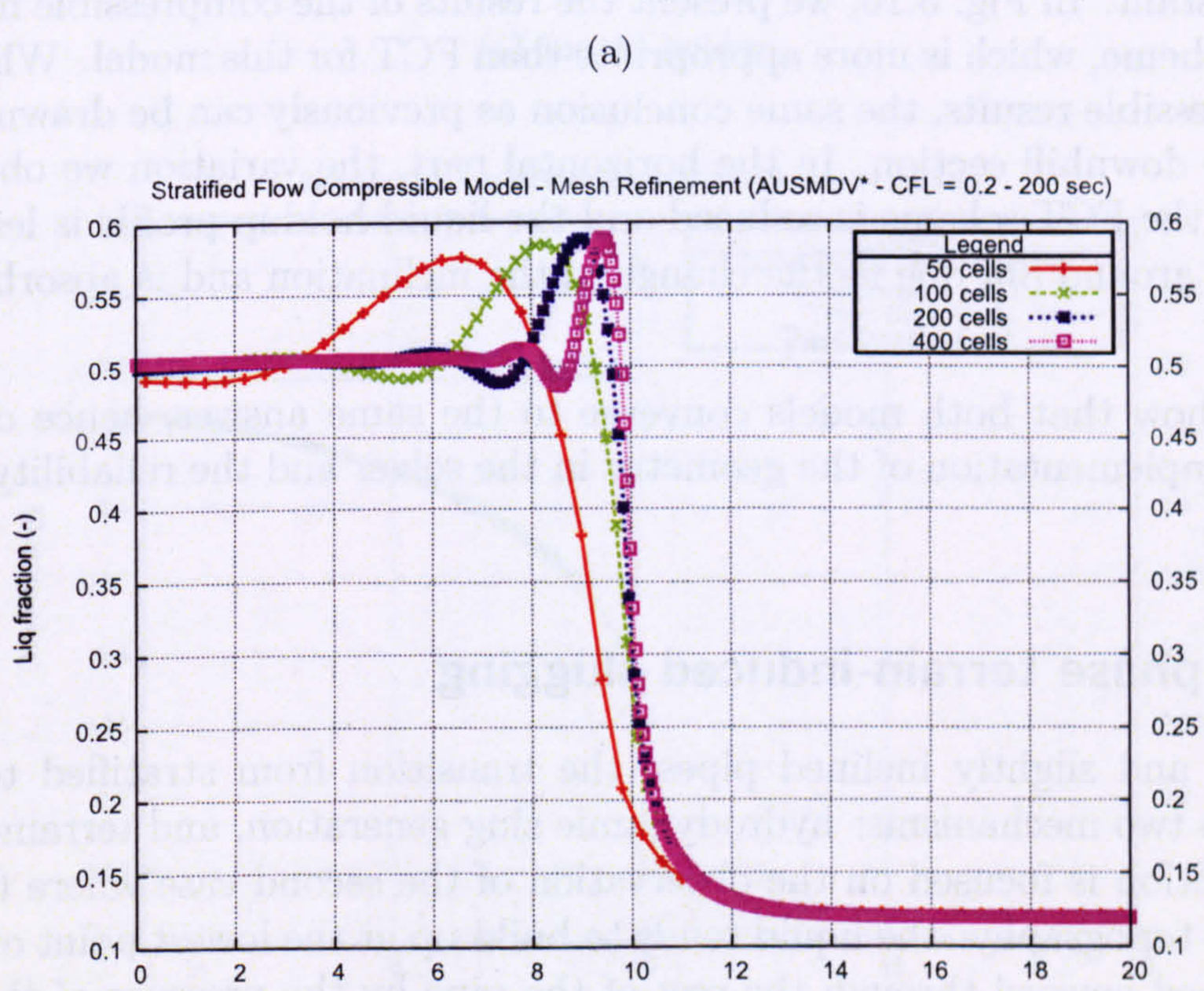

(b)

Figure 5.14 : *Stratified horizontal-downward test - Mesh refinement for the liquid holdup at* $100sec$ *and* $CFL = 0.2$.

finement. We also note that the effect of the bend is sharper with this model and this scheme, and gets more accentuated with mesh refinement. The finer the mesh size is, the more accurate is the solution of the two-fluid model, evidence of a well-behaved numerical method.

5.4.4.3 Models comparison

To see the differences between the two models, we compare the results for the liquid holdup and the liquid superficial velocities using both models. The results are given, respectively, in Fig. 5.15 for the liquid volume fraction, and in Fig. 5.16 for the liquid superficial velocity.

When using the same numerical scheme, FCT, we can see that the holdup prediction in the downhill part is similar with both incompressible and compressible models. In the horizontal part, the compressible results are more diffusive than the incompressible ones, but they are closer to the theoretical equilibrium value. The liquid velocity results however show some difference between the models. The compressible predictions define a significant variation at the discontinuity due to the diffusion whereas with the incompressible model, some oscillations appear at the junction but the velocity remains somehow constant. In Fig. 5.16, we present the results of the compressible model with the AUSMDV* scheme, which is more appropriate than FCT for this model. When comparing with incompressible results, the same conclusion as previously can be drawn for the liquid holdup in the downhill section. In the horizontal part, the variation we obtained for the velocity with the FCT scheme is reduced and the liquid holdup profile is less diffusive. A wave appears around $8m$ due to the change in the inclination and is absorbed with mesh refinement.

The results show that both models converge to the same answer, hence confirming the satisfactory implementation of the geometry in the solver and the reliability of the procedure.

5.5 Two-phase terrain-induced slugging

In horizontal and slightly inclined pipes, the transition from stratified to slug flow is mainly due to two mechanisms: hydrodynamic slug generation, and terrain-induced slugging. This section is focused on the observation of the second case where the slugging is caused by the topography: the liquid tends to build up at the lowest point of the v-section until it is forced onward through the rest of the pipe by the pressure of the gas trapped behind. Comparisons between the code and another numerical code predictions for a test of terrain-induced slugging on a v-section are presented. The geometry influence will thereby be validated into the computations.

The objective is to look for reliable simulations of volume fractions and velocities as well as the slug frequency and the slug length for slugging induced by terrain effects. Several mathematical and numerical challenges arise when predicting slug flow such as

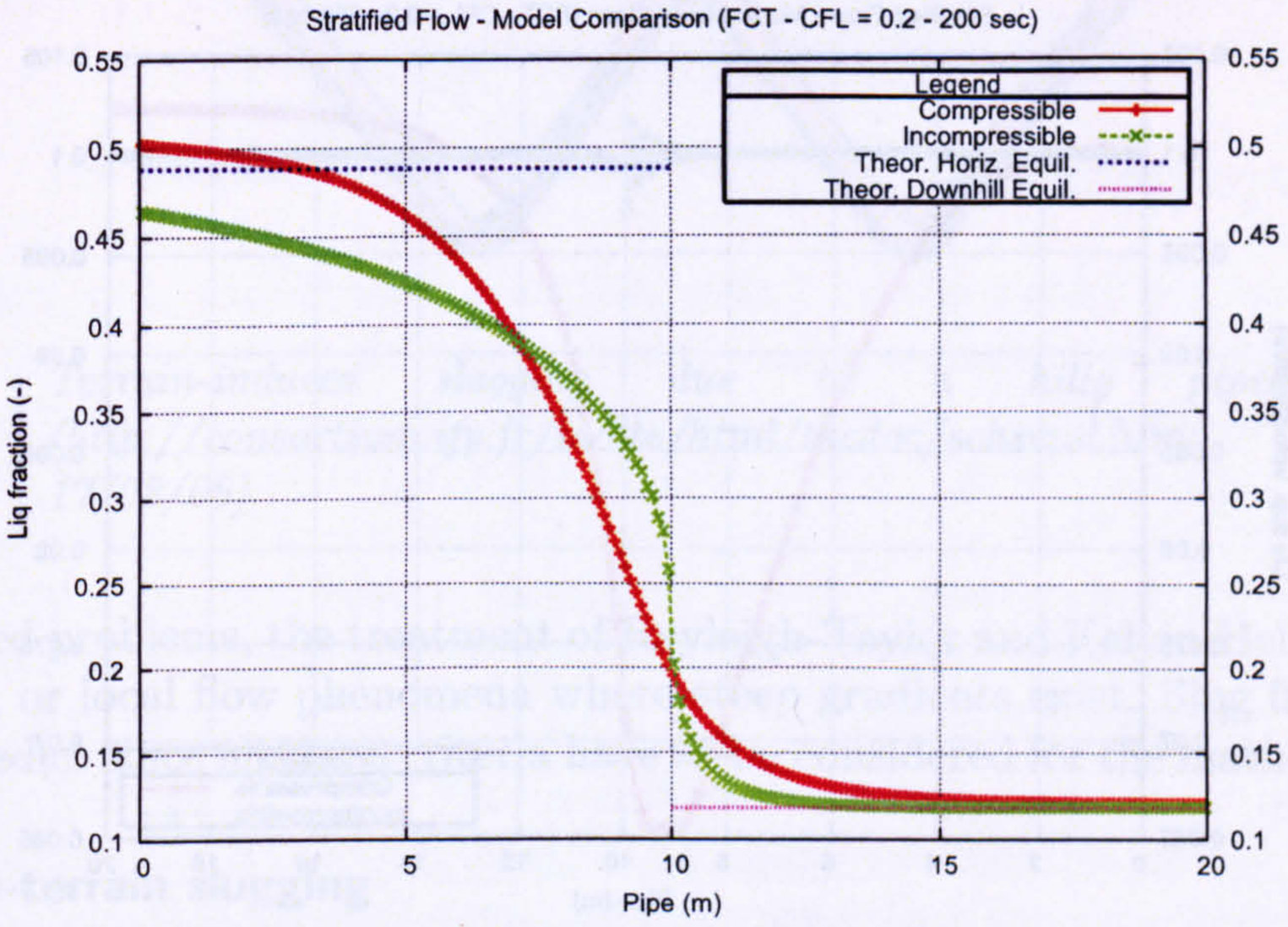

(a) Liquid holdup

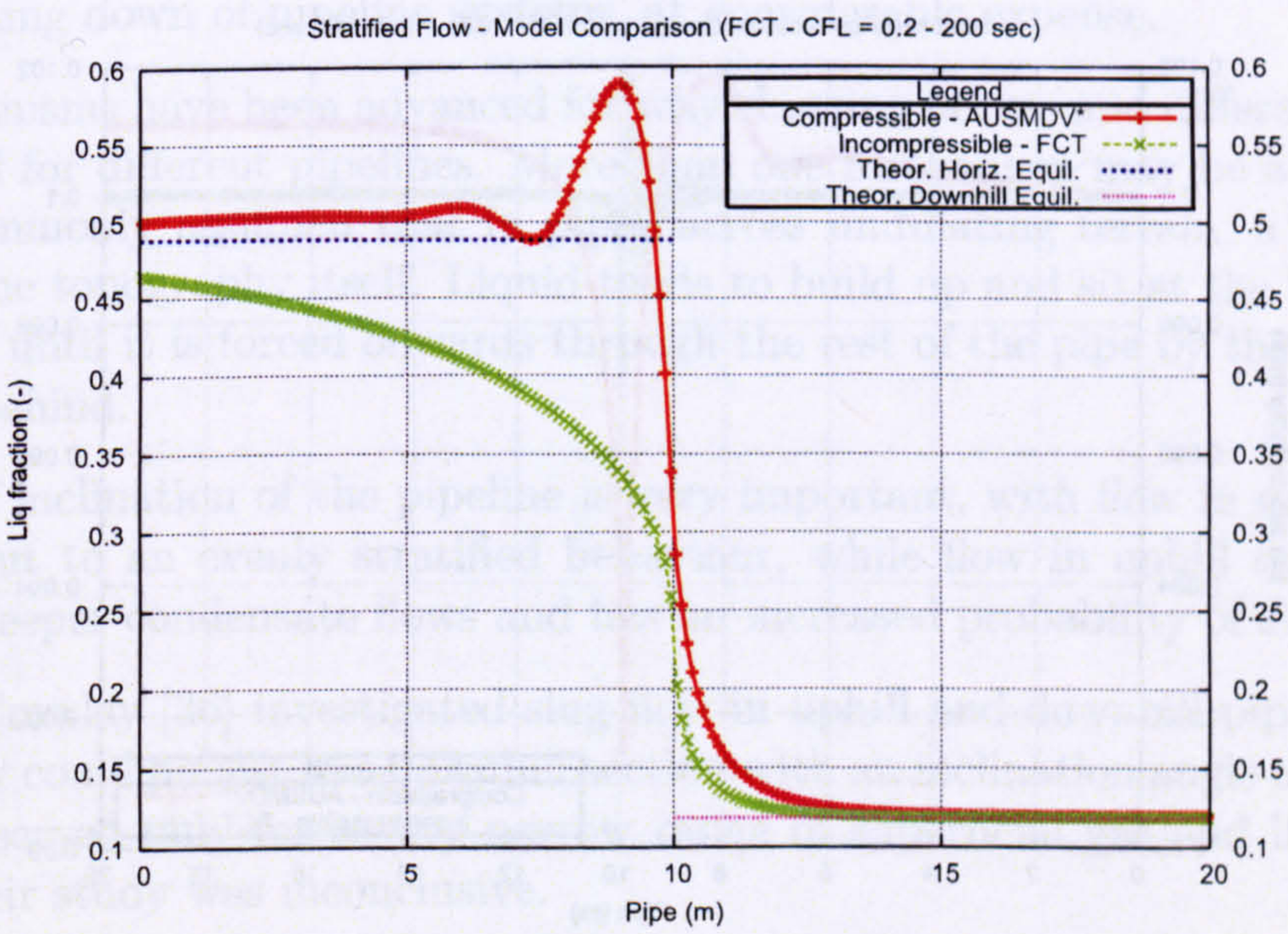

(b) Liquid superficial velocity

Figure 5.15 : *Stratified horizontal-downward test - Liquid holdup profiles for both models after* $200sec$, $CFL = 0.2$.

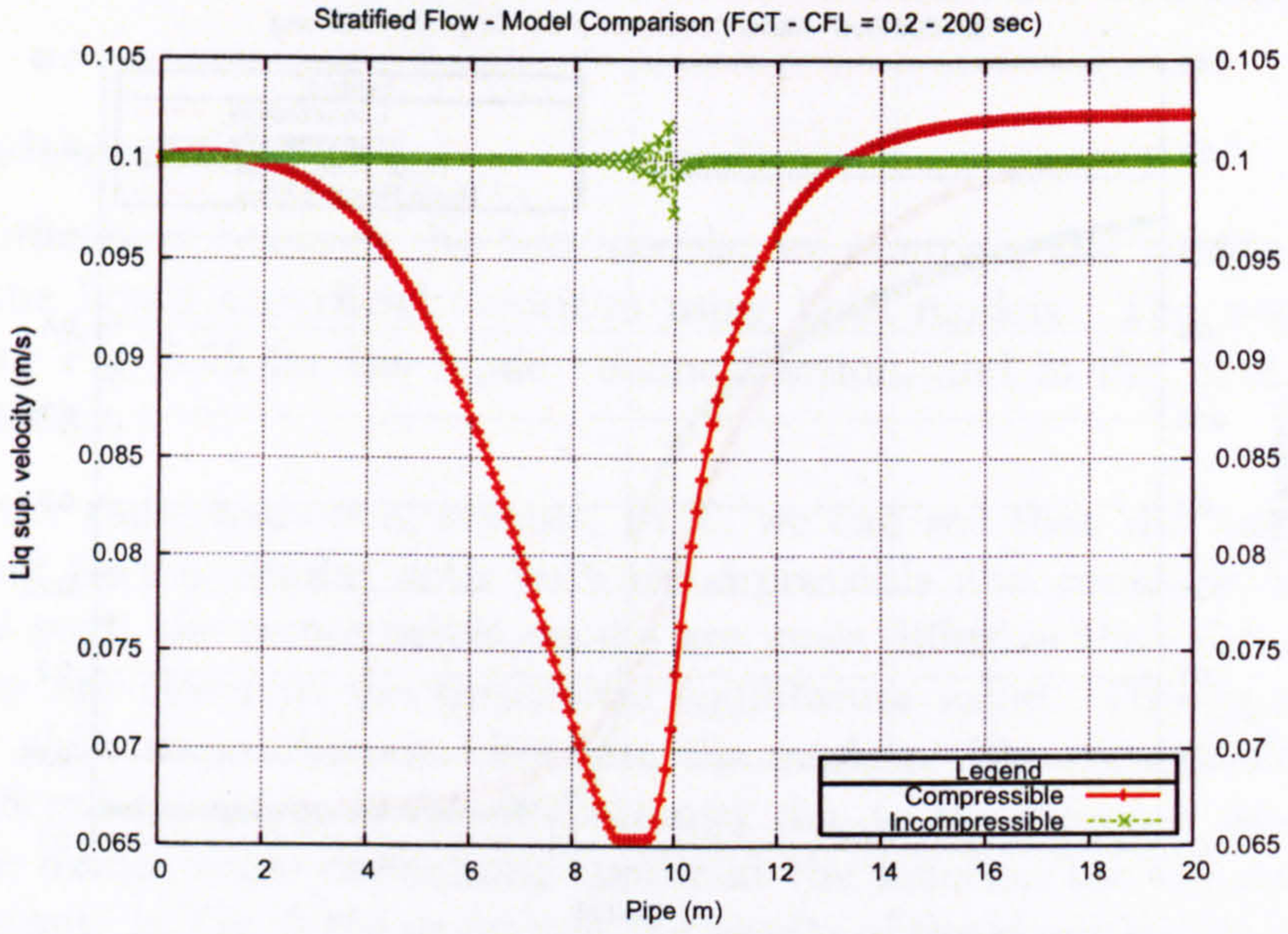

(a) Liquid holdup

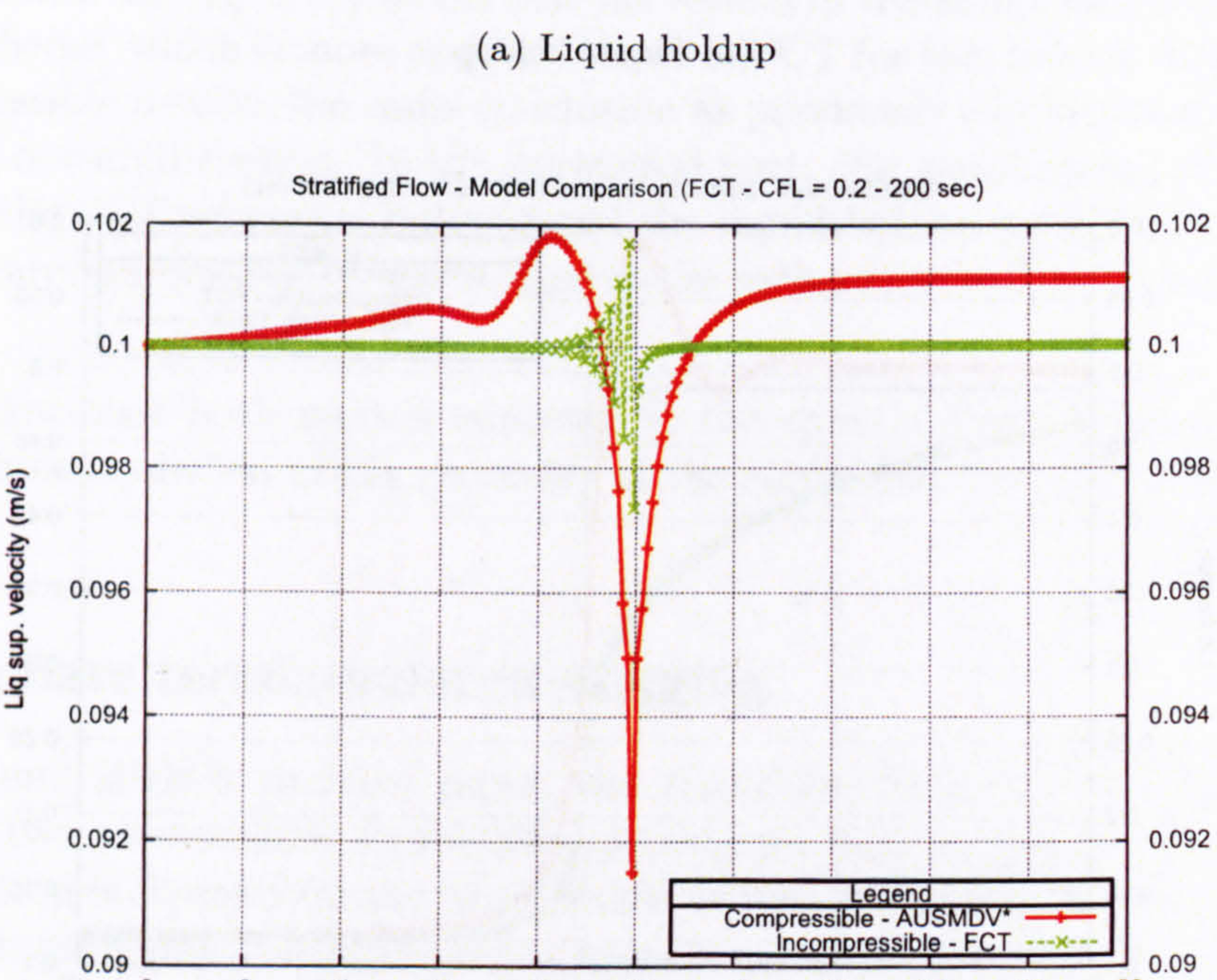

(b) Liquid superficial velocity

Figure 5.16 : *Stratified horizontal-downward test - liquid superficial velocity profiles for both models after* $200sec$, $CFL = 0.2$.

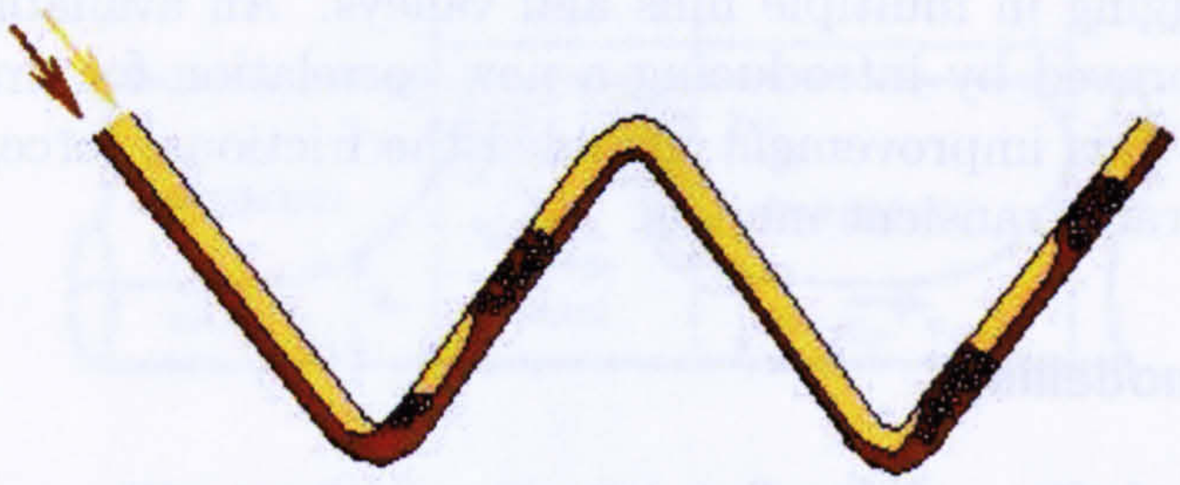

Figure 5.17 : *Terrain-induced slugging due to a hilly pipeline topography (http://consortium.ifp.fr/tacite/html/tacdoc/schsevsl.htm; last visited 17/03/06)*

ill-conditioned problems, the treatment of Rayleigh-Taylor and Kelvin-Helmholtz instabilities [29, 41], or local flow phenomena where steep gradients exist. Slug flow is a difficult regime to predict since all these criteria have to be considered for the mathematical model.

5.5.1 Hilly-terrain slugging

Slugging is a worldwide problem in pipelines carrying both liquid and gas, and is a particular problem in offshore wells. It makes control of flows at the outlet difficult, and may lead to shutting down of pipeline systems, at considerable expense.

Many mechanisms have been advanced for why slugging occurs and different explanations may be valid for different pipelines. More than one mechanism may be acting at a time. But it is commonly assumed that in pipes across undulating terrain, a major cause of slugging is the topography itself. Liquid tends to build up and sit at the lowest points of the pipeline, until it is forced onwards through the rest of the pipe by the pressure of the gas caught behind.

The angle of inclination of the pipeline is very important, with flow in downhill sections smoothing out to an evenly stratified behaviour, while flow in uphill sections develops slower and deeper condensate flows and has an increased probability of slugs forming.

Rothe and Crowley [36] investigated slug flow in uphill and downhill pipes. They found that slug flow could persist in a downhill section with an inclination angle of -15^o to -20^o. This was observed only for a very narrow range of superficial gas and liquid velocities. However, their study was inconclusive.

In studies by Zheng et al. [46, 45] and Zheng [44], the effects of a hilly-terrain pipeline configuration on flow characteristics were clearly demonstrated. Zheng et al. [46] proposed a simple slug-tracking model that follows the behavior of all individual slugs for a rather simple geometry consisting of a single hilly-terrain unit (one upward and one downward inclined section).

De Henau and Raithby [8] conducted an experimental study and model validation on

induced terrain slugging in multiple hills and valleys. An available transient two-phase flow model was improved by introducing a new correlation for drag coefficient and the virtual mass force. This improvement included the frictional force, which was neglected in previous hilly-terrain transient models.

5.5.2 Slug flow modelling

The most distinctive feature of slug flow is its intermittent nature. Any attempt to model the flow by a standard time-averaging procedure would therefore be extremely restrictive. Instead, a much more detailed analysis is required which takes account of the inherent intermittency and distinguishes between the liquid slug region, possibly containing dispersed gas bubbles, and the large gas bubble region that follows. This means the phenomenological model of slug flow must in effect use characteristics from both the dispersed and stratified flow models while still accounting for the exchange of fluid between each region.

The easiest, and therefore the most popular, approach is to reduce the intermittency to periodicity and to assume fully developed flow so that the complex structure can be simplified to an "equivalent cell" consisting of a liquid slug and a long bubble (Fig. 5.18). The balance equations can then be written in a frame of reference moving with the cell so that the flow appears steady with mass and momentum conserved across the boundary between the liquid slug and the long gas bubble region.

Early studies of two-phase flow, such as those by Lockhart and Martinelli [24], concentrated on obtaining overall pressure drop and holdup correlations encompassing all flow regimes. However, this approach results in poor predictions when the correlations are applied to systems other than those used in their development. Therefore a phenomenological approach was adopted, in which the main characteristics of individual flow types are modelled. This has progressively led to slug flow models able to simulate "steady-state" behaviour well enough to calculate pressure drop and other slug flow parameters with a relatively high degree of confidence and generality (Greskovich and Shrier [18]; Dukler and Hubbard [10]; Nicholson et al. [33]).

In all these models, a solution of the "steady-state" mass and momentum balances is not possible when only the values of the system parameters are specified. Additional information must be provided in the form of auxiliary relations, such as the dispersed bubble translational velocity, the elongated bubble translational velocity, the slug body liquid holdup and either slug length or slug frequency. In what follows, we will only discuss slug length, slug frequency and friction factors.

5.5.2.1 Slug length

The liquid slug length and the slug frequency are closely related properties that are often used interchangeably. In vertical pipes of small diameter (25 to 50mm) the slug lengths are observed to be approximately 8 to $25D$ (Table 5.1). For horizontal pipes of similar diameter, Dukler and Hubbard [10] and later Dukler *et al.* [11] found that the mean length

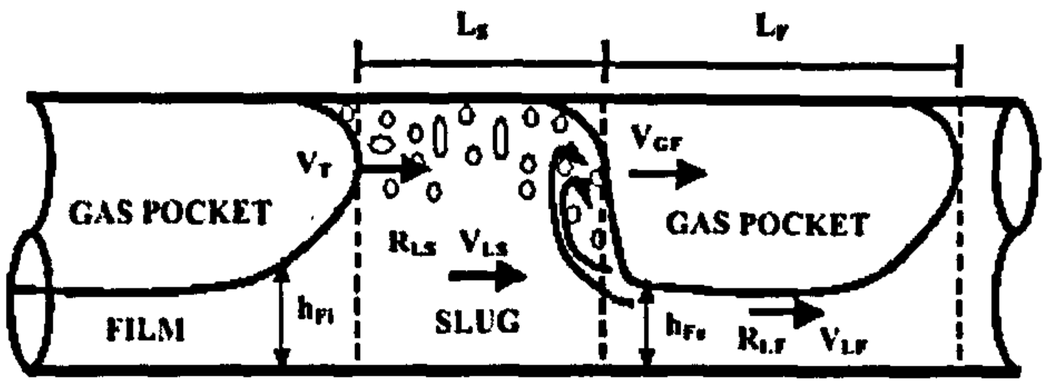

Figure 5.18 : *The "equivalent slug unit"*

is approximately 12 to $30D$. Other researchers have confirmed the same observations as indicated in Table 5.2. In both cases, the slug length appears to be relatively insensitive to gas and liquid flowrates. Hence constant values are generally used for the mean slug length in slug flow models. Although these models provide reasonable estimated in pipes of small diameter, they greatly under-predict typical values encountered in large diameter pipes (400 to 500mm). In absence of any theory to predict this parameter satisfactorily, some logarithmic expressions have been suggested.

Brill et al. [7] developed a correlation to predict the mean slug length in horizontal pipelines, assuming the slug length follows a Log-normal distribution. This correlation is in terms of mixture velocity and pipe diameter:

$$\ln(L_S) = -3.851 + 0.059 \ln\left(\frac{V_m}{0.3048}\right) + 5.445 \left(\ln\left(\frac{D}{0.0254}\right)\right)^{0.5} \tag{5.31}$$

This correlation was modified and using the entire expanded data set, Scott et al. [39] developed an even better correlation that also considered slug growth:

$$\ln(L_S) = -26.6 + 28.495 \left(\ln\left(\frac{D}{0.0254}\right)\right)^{0.1} \tag{5.32}$$

Scott and Kouba [38] studied the changes in slug flow characteristics in hilly-terrain pipelines. They proposed a model for slug length change, assuming no change in the liquid holdup in the slug and an equilibrium film thickness. However, they did not consider slug initiation or dissipation in their model.

Gopal [15] developed a mechanistic model to predict the mean slug length and investigated the effect of liquid phase properties on the mean slug length. The mechanistic model uses the Froude number of both the liquid film and the slug body. He found that the Froude number for the liquid film is always greater than unity. It decreases in the slug-mixing zone and tends to increase toward the tail of the slug where it reaches unity.

In an experimental study, Nydal et al. [34] investigated mean slug characteristics length, holdup and velocity and their statistical distributions. They found that the mean slug length is insensitive to phases flow rates.

Dhulesia et al. [9] developed a probabilistic correlation to determine the mean slug length

Correlation	System	Mean slug length
Moissis and Griffith [31]	Air-water $D = 19mm - 51mm$	6D-8D
Schmidt [37]	Air-kerosene $D = 51mm$	30D-48D
Fernandes *et al.* [14]	Air-water $D = 51mm$	21.7D
Barnea and Brauner [5]	Theory	16D
Dukler *et al.* [11]	Theory	16D-24D

Table 5.1 : *Mean slug lengths in vertical pipes.*

and the entire distribution. They also found that the Inverse Gaussian distribution fits the slug length distribution the best when compared with Gamma or Log-normal distributions. However, the Inverse Gaussian distribution fails to fit the slug length distribution generated by terrain slugging. Furthermore, statistically Log-normal and Inverse Gaussian distributions are hard to distinguish without a very large data set.

To summarise, in horizontal and nearly horizontal slug flow, many researchers [10, 12] found that the slug body length is dependent only on the pipe diameter D (and not on physical properties or inlet velocities):

$$L_S \approx 12D - 30D \tag{5.33}$$

and this simple correlation is the one used to compare the code predictions.

5.5.2.2 Slug frequency

Due to the intermittent nature of the slug flow regime, the slug frequency is an important parameter when modelling this flow pattern. The slug frequency varies whether the flow is developing or fully developed. The majority of the correlations found in the literature are empirical correlations that provide predictions for downstream fully developed slugs. Very few phenomenological models have been proposed for slug frequency obtained near the pipe entrance.

Based on measured values for the carbon dioxide-water system in a $19\,mm$ diameter pipe, Gregory and Scott [17] proposed one of the first slug correlations, given as:

$$\omega_s = 0.0226 \left(\frac{V_{sl}}{gD} \left(\frac{19.75}{V_m} + V_m \right) \right)^{1.2} \tag{5.34}$$

Correlation	System	Mean slug length
Dukler and Hubbard [10]	Air-water $D = 38mm$	12D-30D
Nicholson *et al.* [33]	Air-light oil $D = 25mm - 51mm$	$\sim$ 30D
Gregory *et al.* [16]	Air-light oil $D = 25mm - 51mm$	$\sim 30D$ (NB: some slugs reached $375D$)
Barnea and Brauner [5]	Theory	32D
Andreussi *et al.* [2]	Air-water $D = 50mm$	22D
Nydal *et al.* [34]	Air-water $D = 53mm - 90mm$	$15 - 20D$ $(53mm)$ $12D - 16D$ $(90mm)$

Table 5.2 : *Mean slug lengths in horizontal pipes.*

Greskovich and Shrier [18] subsequently re-arranged this expression using the Froude number and obtained:

$$\omega_s = 0.0226 \left(\lambda_l \left(\frac{2.02}{D} + Fr_m^2 \right) \right)^{1.2} \tag{5.35}$$

where λ_l is the no-slip liquid holdup and Fr_m is the Froude number based on the mixture velocity V_m. However, based on data collected from a $45\,mm$ internal diameter line, they suggested that the diameter effect is not properly taken into account by this expression. Therefore, to overcome this deficiency, they recommended to use their graphical correlation instead for cases involving large diameters.

Using the gamma densitometer for air-water flow in a $42\,mm$ diameter pipe, Heywood and Richardson [22] determined the probability density function and the power spectral densities of the holdup. From these functions they estimated the average slug frequency. By subsequently using a similar expression to Greskovich and Shrier [18], they proposed that the slug frequency may be obtained by:

$$\omega_s = 0.0434 \left(\lambda_l \left(\frac{2.02}{D} + Fr_m^2 \right) \right)^{1.02} \tag{5.36}$$

Conducting a large number of experiments on a $78\,mm$ diameter pipe for both air-water and air-oil data at various system pressures, Manolis et al. [28] proposed the following expression, described with only five dimensionless numbers:

$$\omega_s = \left(\frac{V_{sg}}{D} \left(0.0363 \frac{Fr_l}{\hat{F}r_g} \frac{Z_l}{Eo^{0.2}} \right) \right)^n \tag{5.37}$$

where n is a function of the viscosity number and is given by:

$$n = \frac{N_f}{260 + 0.85N_f} \tag{5.38}$$

The Eotvös number is defined as:

$$Eo = gD^2 \frac{|\rho_g - \rho_l|}{\sigma} \tag{5.39}$$

while the viscosity number is expressed as:

$$N_f = \frac{D^{1.5}\sqrt{\rho_l|\rho_g - \rho_l|g}}{\mu_l} \tag{5.40}$$

The liquid Froude number Fr_l and the modified gas Froude number $\hat{Fr}_g$ are given by:

$$Fr_l = \frac{V_{sl}}{\sqrt{gD}}, \qquad \hat{Fr}_g = \frac{V_{sg}}{\sqrt{gD(\rho_l/|\rho_g - \rho_l|)}} \tag{5.41}$$

The parameter Z_l is a combination of two numbers X and Y used by Manolis [28], and is defined as the ratio of the liquid inertia to the liquid pressure drop. Its expression is:

$$Z_l = \left[\frac{\frac{\rho_l V_{sl}^2}{2D}}{\left(\frac{dP}{dx}\right)_l}\right]^{0.5} = \left[\frac{1}{4C_f Re_{sl}^{-m}}\right] \tag{5.42}$$

The liquid Reynolds number is based on the liquid superficial velocity. C_f and m are respectively the friction factor constant coefficient and the exponent; they depend on the nature of the flow, laminar or turbulent. Hence, they are defined as:

$$\begin{cases} C_f = 0.046, & m = 0.2, & \text{if } Re_l < 2000, \\ C_f = 16, & m = 1, & \text{otherwise.} \end{cases} \tag{5.43}$$

Tronconi [43] proposed a semi-theoretical model which assumes that slug frequency is half the frequency of the unstable wave precursors. Using a non-linear analysis of inviscid two-dimensional flow in a rectangular channel, similar to that of Mishima and Ishii [30], to obtain the precursor wave frequency he suggested the slug frequency as:

$$\omega_s = 0.61 \frac{\rho_g}{\rho_l} \frac{V_{ge}}{h_{ge}} \tag{5.44}$$

where V_{ge} and h_{ge} are respectively the equilibrium gas velocity and height obtained by using the data of Taitel and Dukler [41] type of momentum balance.

Adopting a different approach, Taitel and Dukler [42] considered slug frequency to be an entrance phenomenon and assumed that the frequency is given by the inverse of the time taken for the film to rebuild its level and form a slug. They then solved one-dimensional mass and momentum relations using the shallow channel approximation to calculate the characteristic time for this process. Comparison of their results with those of Gregory and Scott [17] they reported satisfactory agreement, although a general validation of the model is still lacking.

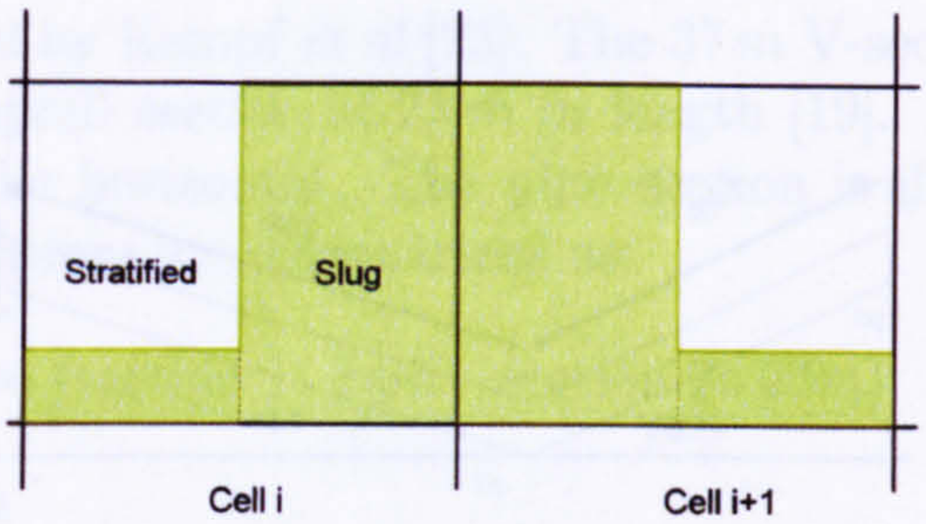

Figure 5.19 : *Description of slug cells.*

5.5.2.3 Friction factors

As already mentioned, the intermittent nature of slug flow requires to account the liquid slug and the stratified regions separately. Following this idea, we use a combined correlation for the liquid wall friction. Each cell is seen as a combination of slug flow and stratified film flow (Fig. 5.19). Therefore the liquid wall friction can be estimated as a linear combination of stratified wall friction and slug wall friction and is given as:

$$\tau_{wl} = \beta T_l^{slug} + (1-\beta) T_l^{film} \tag{5.45}$$

where β is the no-slip coefficient:

$$\beta = \lambda_{noslip} = \frac{V_{sl}}{V_{sg} + V_{sl}} \tag{5.46}$$

The correlation used for the film friction factor is given by Taitel and Dukler [41]. In the slug region, we choose the modified correlation from Andreussi [1]:

$$f_l^{slug} = \phi^{malnes} \times f_l^{strat} \tag{5.47}$$

where f_l^{strat} is the correlation developed by Hand [21], described in Chapter 3, and ϕ^{malnes} is the dispersed bubble correction factor formulated by Malnes [27] for liquid wall frictions:

$$\phi^{malnes} = \frac{1}{\alpha_l}\left(1 - 15.3\frac{\alpha_g V_D}{\sqrt{\alpha_l V_m}}\right) \tag{5.48}$$

and

$$V_D = 1.18\left[\frac{g\sigma|\rho_g - \rho_l|}{\rho_l^2}\right]^{0.25} \tag{5.49}$$

Hence the shear stresses T_l^{film} and T_l^{slug} can be defined as:

$$T_l^{film} = \frac{1}{2} f_l^{strat} \rho_l V_l |V_l| \frac{S_l}{A} \tag{5.50}$$

$$T_l^{slug} = \frac{1}{2} f_l^{slug} \rho_l V_l |V_l| \frac{S_l^{slug}}{A} = \frac{2}{D} f_l^{slug} \rho_l V_l |V_l| \tag{5.51}$$

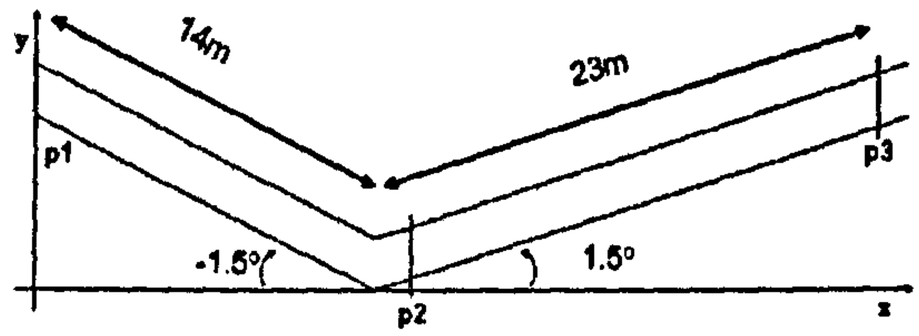

Figure 5.20 : *Terrain-induced slugging pipe V-section.*

since $S_l^{slug} = \pi D$, and the liquid wall friction factor is thus defined.

The gas wall shear stress follows the formulation given by:

$$\tau_{wg} = \frac{1}{2} f_g \rho_g V_g |V_g| \frac{S_g}{A} \tag{5.52}$$

where the friction factor f_g is given by Taitel and Dukler [41].

The gas-liquid interfacial friction factor, used for slug flow, has been developed by Andreussi and Persen [3]:

$$\begin{cases} f_i = f_g & \text{if } Fr_g \leq 0.36 \\ f_i = f_g \left(1 + 29.7(Fr_g - 0.36)^{0.67} \left(\frac{h_l}{D}\right)^{0.2}\right) & \text{otherwise} \end{cases} \tag{5.53}$$

with the gas Froude number Fr_g defined as:

$$Fr_g = V_g \sqrt{\left[\frac{\rho_g}{\rho_l - \rho_g} \frac{dA_l/dh_l}{A_g} \frac{1}{g \cos\beta}\right]}. \tag{5.54}$$

All closure laws required for slug flow are then formulated.

5.5.3 Simulations

In this section we study the validity of the compressible two-fluid model (TPM5), presented in Chapter 3, for a slug flow test on a V-section pipeline. The correlations (Eq. 5.45 and Eq. 5.52) presented in the previous section are used for the gas and liquid wall friction factors, and the stratified-smooth relation of Taitel and Dukler [41] for the interfacial friction factor.

The two-phase flow of water and air in a V-section is simulated using the compressible model with the friction factors described earlier (Eq. 5.45), and then compared against the

numerical results obtained by Kempf *et al* [23]. The $37\,m$ V-section consists of a downhill section of $14\,m$ and an uphill section of $23\,m$ in length [19]. Both sections are inclined at 1.5^o with respect to the horizontal. The pipe section is illustrated schematically in Fig. 5.20 and the specifications are summarised as:

- Pipeline length: $37m$ (section 1: $14m$ - section 2: $23m$)
- Diameter: $77.92mm$
- Operating fluids: air and water ($\rho_g = 1.16\,kg/m^3$, $\rho_l = 1000\,kg/m^3$)
- Flow temperature: $T = 296\,K$
- Outlet flow pressure: $10^5\,Pa$.

The atmospheric properties of air and water are used (the outlet pressure is fixed to atmospheric). The initial conditions correspond to a uniform stratified flow, and the boundary conditions at the tube inlet are similar to the initial input data, and are given as:

$$\begin{cases} V_{sg} = 6.0\,ms^{-1} \\ V_{sl} = 0.6\,ms^{-1} \\ \alpha_l^0 = 0.4 \end{cases} \tag{5.55}$$

As in the stratified problem, the only outflow boundary condition at the end of the tube is constant atmospheric pressure ($1bar$). The rest of the conservative variables are considered as an open boundary.

5.5.3.1 Numerical results

In what follows, the numerical liquid holdup traces, obtained with the compressible model, will be shown at different times in the simulations, and comparisons with experimental and numerical results from Imperial College for global holdup, slug frequency and slug length will be made.

The liquid holdup traces over the pipe length are shown in Fig. 5.21 and 5.24 for different times. As Fig. 5.21 indicates, the onset of slugging occurs in the dip region, located at $14\,m$: wave initiation and wave growth start in the first two seconds. The flow in the downward section is stratified. At around $18\,m$ from the pipe inlet, slugs initiate and it is remarkable that slug flow generates in the upward section of the pipe straight from stratified flow. No transition from stratified smooth to wavy is observed. The first slug is generated after around $3s$, and grows in length. The slugs that are generated next are smaller.

Slugs are generated at the entrance section of the upward pipe. Usually, however, the frequency of generation of slugs is relatively high. As a result, a series of short slugs

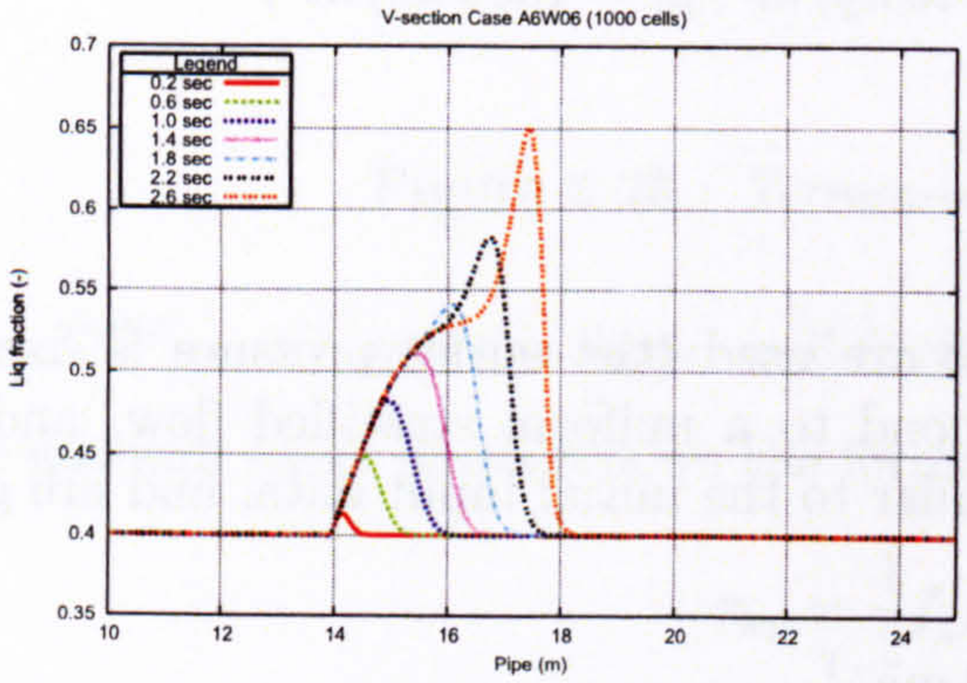

(a)

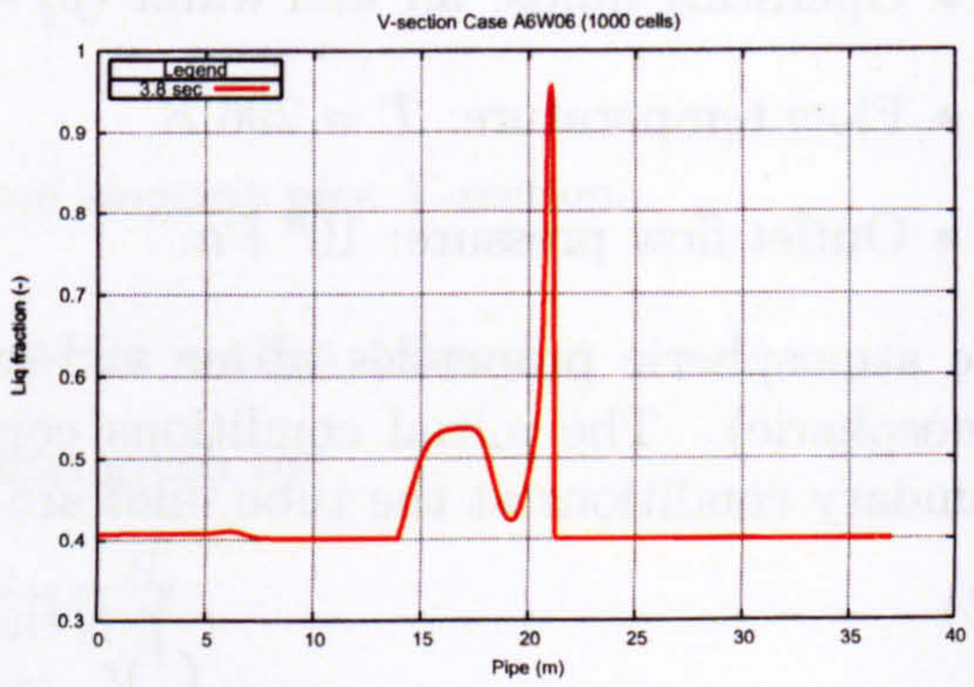

(b)

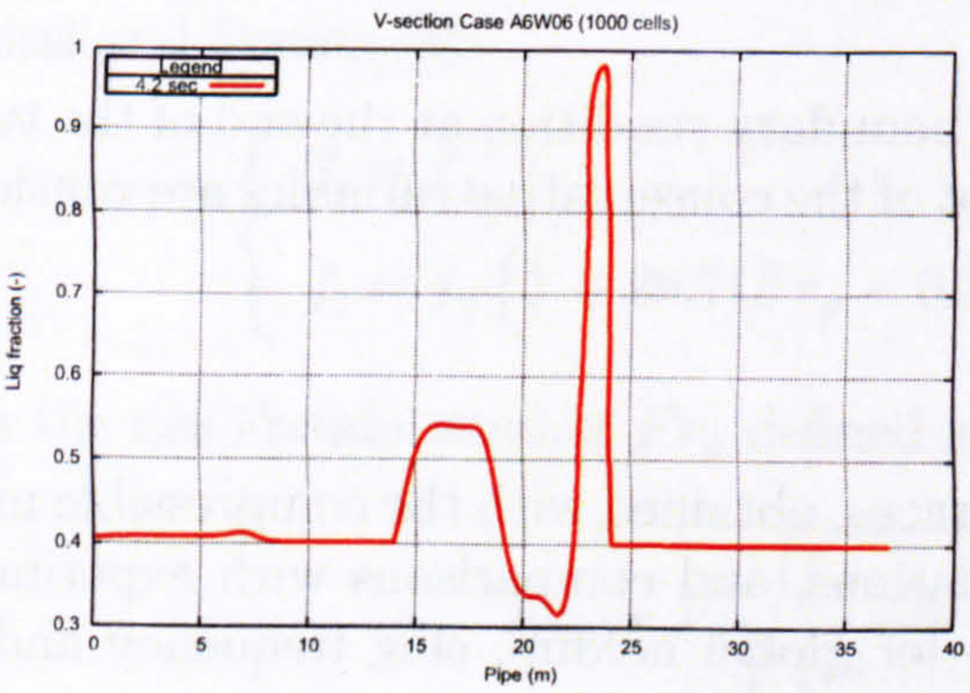

(c)

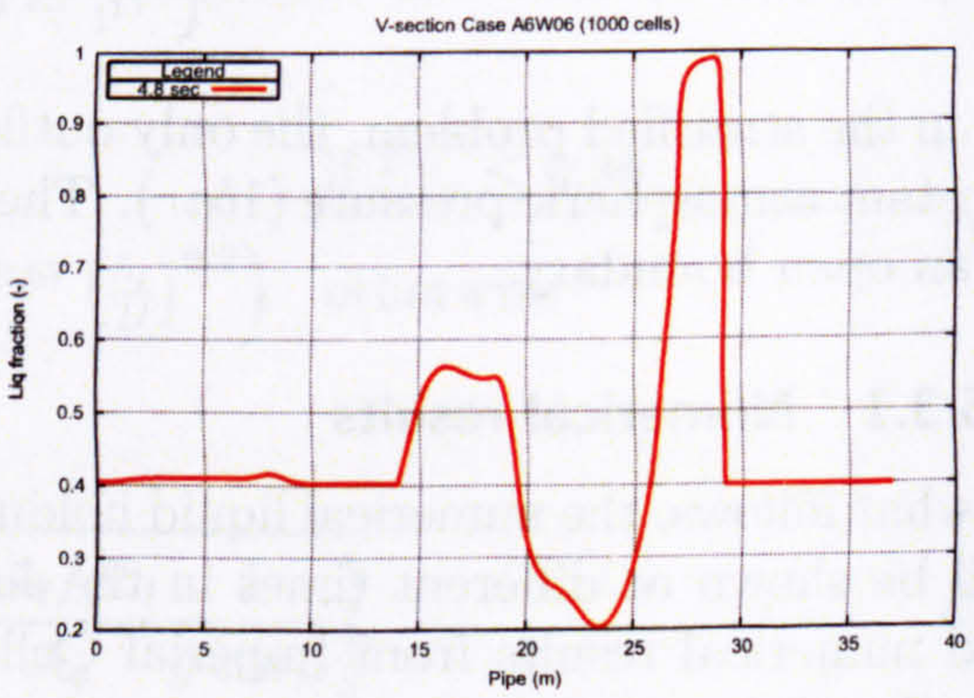

(d)

Figure 5.21 : *Slug wave initiation, growth and pipe bridging - Liquid holdup profiles.*

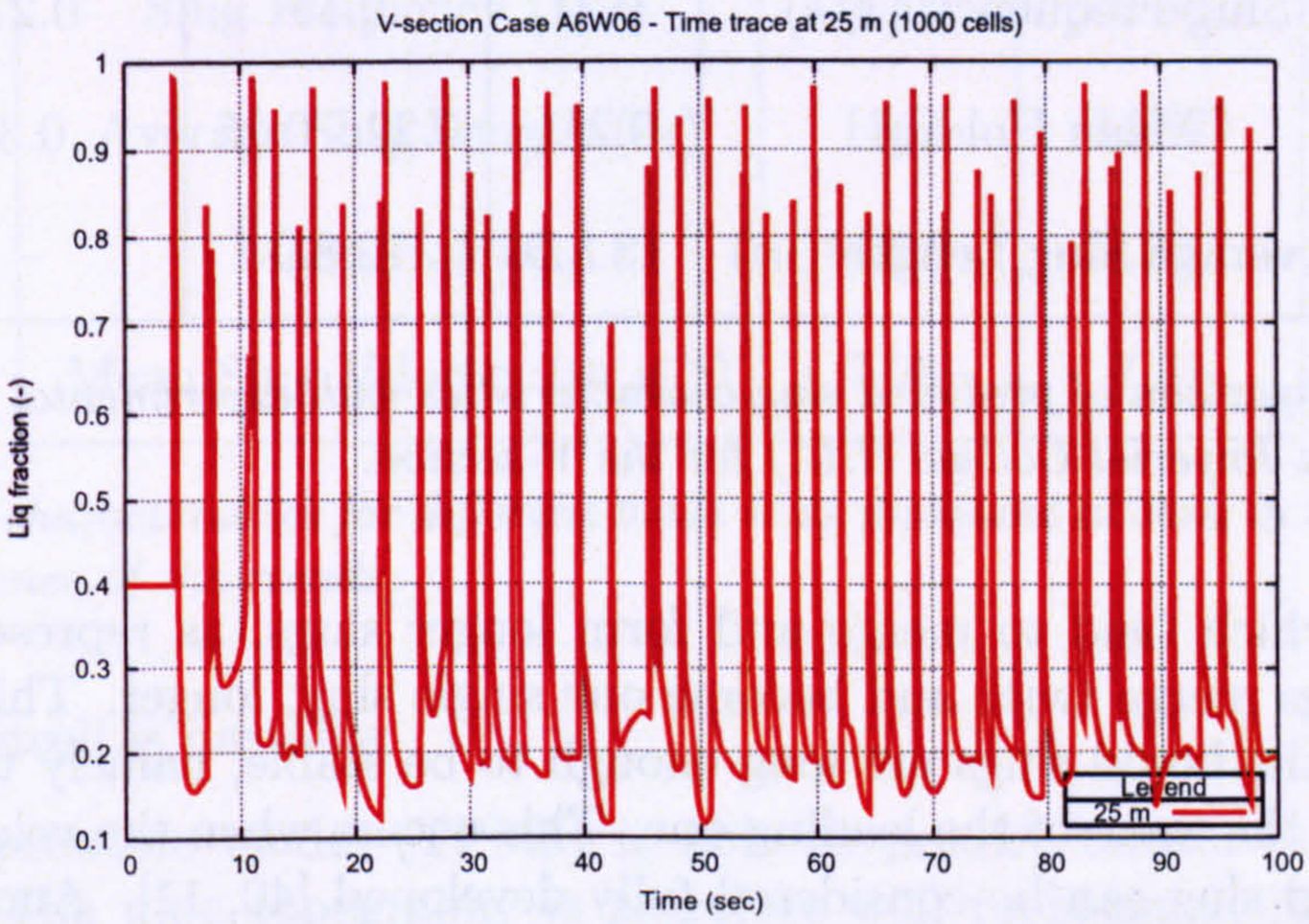

Figure 5.22 : *Time trace of the liquid holdup at 25 m. Slug frequency can be obtained from there.*

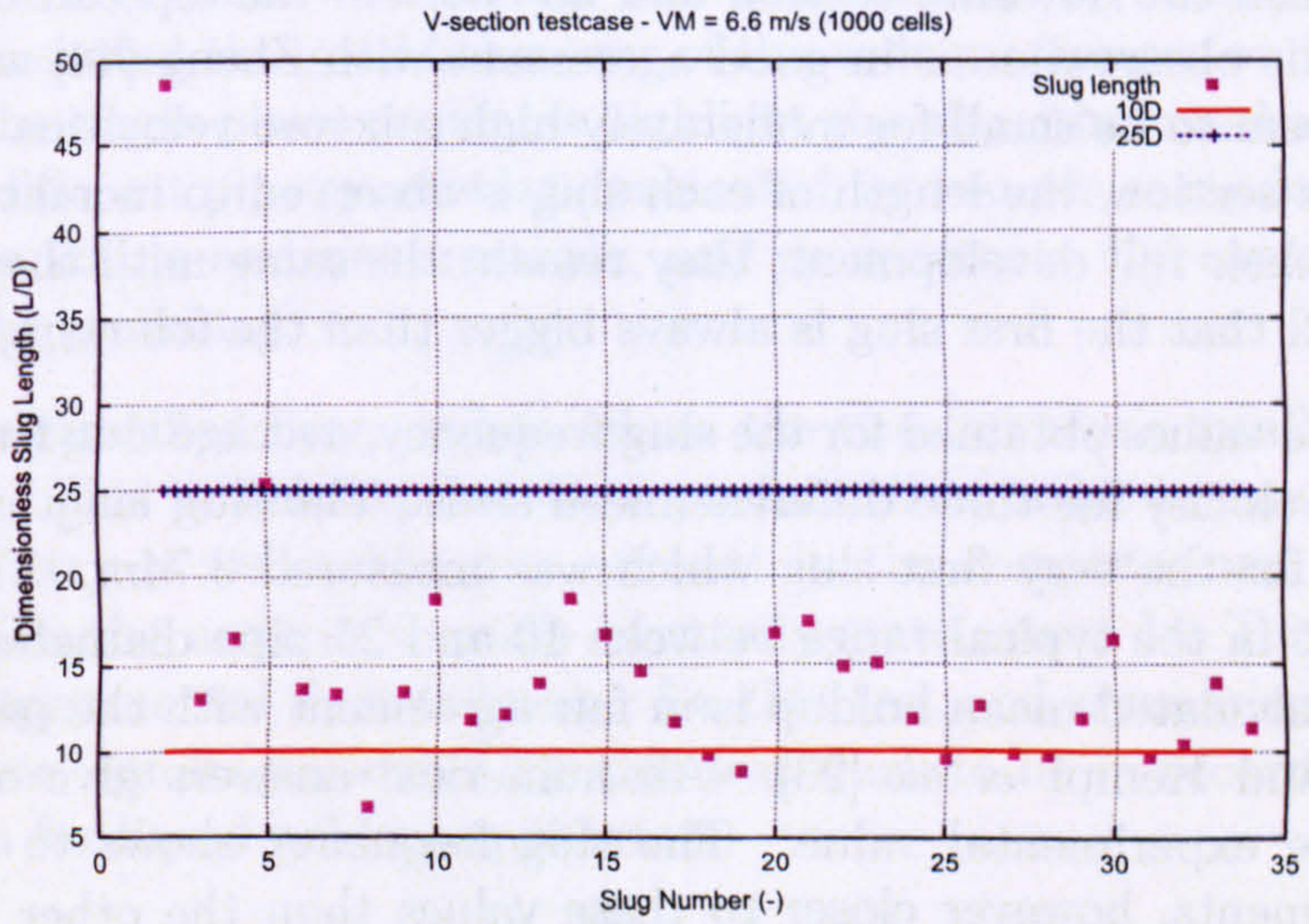

Figure 5.23 : *Slug length measured at 34 m in the V-section. Apart from the first one which is always bigger than the following ones, the length of the slugs obtained falls within the experimental range.*

Characteristic	TPM5	I.C.	Exp. Data
Slug Frequency $(1/s)$	0.31	0.15	0.27
Mean Holdup	0.211	0.22 - 0.25	0.3
Average Slug Length (m)	$13.5D$	$12.8D$	–

Table 5.3 : *Comparison of predicted slug characteristics with experimental and numerical data from Imperial College (I.C.) for the V-section.*

are generated which tend to merge and form longer slugs, as represented in Fig. 5.24 where three slugs merge twice and become one single slug, longer. This merging process continues until the liquid slugs are long enough to be stable, namely the trailing bubble is unaffected by the wake of the leading one. This occurs when the velocity profile at the rear of the liquid slug can be considered fully developed [40, 11]. Another problem also related to the slug length is the change of slug length as it travels in a hilly terrain pipeline with upward and downward sections. Slug length tends to increase as it moves from a horizontal or downward section into an uphill section, as a result of liquid accumulating in the low elbow and being picked up by the approaching slugs [38]. In addition, new slugs can be generated in low elbows. These slugs usually are short and therefore unstable and tend to dissipate. With the present mixture velocity, no slug is generated in the downhill part of the V-section. Slugging starts from the dip onwards. For higher mixture velocities, slugs are formed in the downhill section and no effect of the dip can be detected after a few seconds. This observation is in good agreement with Zheng [44] who found that the terrain effects seem to be small for moderately high mixture velocities. Also, for the case presented in this section, the length of each slug is observed to increase until $30m$ where the slugs reach their full development; they remain the same until they exit the pipe. It is noticed as well that the first slug is always bigger than the following ones.

Table 5.4 lists the values obtained for the slug frequency, average slug length, mean holdup and mean slug velocity for three different mesh sizes. The slug lengths range is 0.546 to $1.989m$, except for the very first slug which was measured $3.74m$. The calculated slug body lengths are in the typical range between 10 and 25 pipe diameters, as presented in Fig. 5.23. The calculated mean holdup is in fair agreement with the predictions obtained by Bonizzi [6] and Kempf *et al.* [23]. All numerical answers give a lower estimation compared to the experimental value. The slug frequency shows to be slightly higher than the experiments, however closer to these values than the other numerical results. Furthermore, when compared with the correlations provided in the sub-section 5.5.2.2, our predictions are within the range.

For all slug parameters that have been studied, the mesh refinement analysis summarised in Table 5.4 demonstrates the convergence of the problem to a single solution and this is evidence that the system of equations is well-posed for the given flow conditions, even

Characteristic	750 cells	1500 cells
Slug Frequency $(1/s)$	0.31	0.30
Average Slug Length (m)	$15D$	$14.6D$
Mean Holdup	0.212	0.201
Mean Slug Velocity $(m.s^{-1})$	7.03	7.41

Table 5.4 : *Slug characteristics for different mesh sizes measured at 34m in the v-section. Convergence of the results.*

though the flow itself is unstable.

Hence, the compressible model (TPM5) is able to predict terrain-slugging in slightly inclined pipes. The pipe topography is therefore well represented in the calculations validating the algorithm proposed in Section 5.2.

5.6 Summary

The present chapter illustrates the pipeline topography and the algorithm developed and embedded in the EMAPS framework to take it into account in the computations. We have validated the algorithm with several numerical examples (on single- and two-phase flows) and demonstrated the good behaviour of the code predictions on inclined pipelines. More precisely, the single-phase problems highlight the algorithm mechanism and its limitations; the two different pipe geometries, presented for two-phase models, induce distinct flow regimes, one stable and one unstable, and demonstrate the capability of the code enhanced with the geometry.

We first simulate stratified flow, regime where the two fluids are totally separated, on a downward elbow. This initial step has been performed in order to ensure that the effect of the pipe geometry is well taken into account in the computations. The simulations are compared with the analytical result of steady-state, given by Taitel and Dukler in 1976 [41]. No experimental data is known for this test and comparisons are difficult to establish. However, results presented for this test show to be in accordance with theoretical values given for liquid holdup equilibrium.

The second geometry is composed of a V-section where slugs form mostly because of terrain-induced effects. The literature review on hilly-terrain studies confirms the significant impact of hilly-terrain pipeline geometry on slug flow characteristics. We therefore investigated various slug flow parameters, such as slug frequency, slug body length, mean holdup and slug velocity, and compared them with experiments performed by different workers [6, 23]. The V-section predictions have shown that the code with the geometry

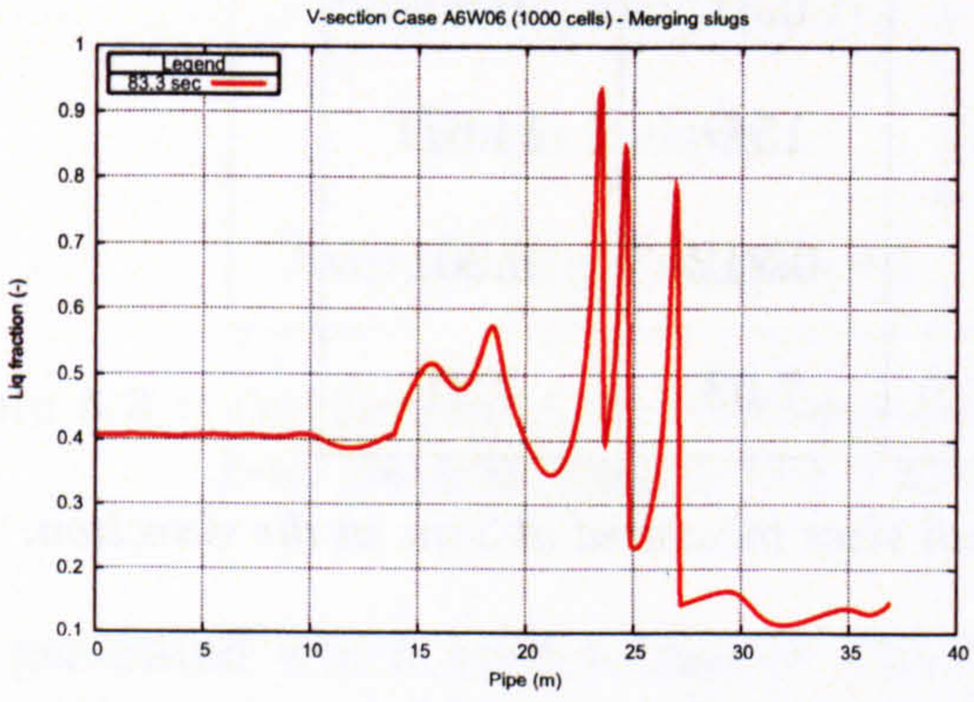

(a) 83.3 sec

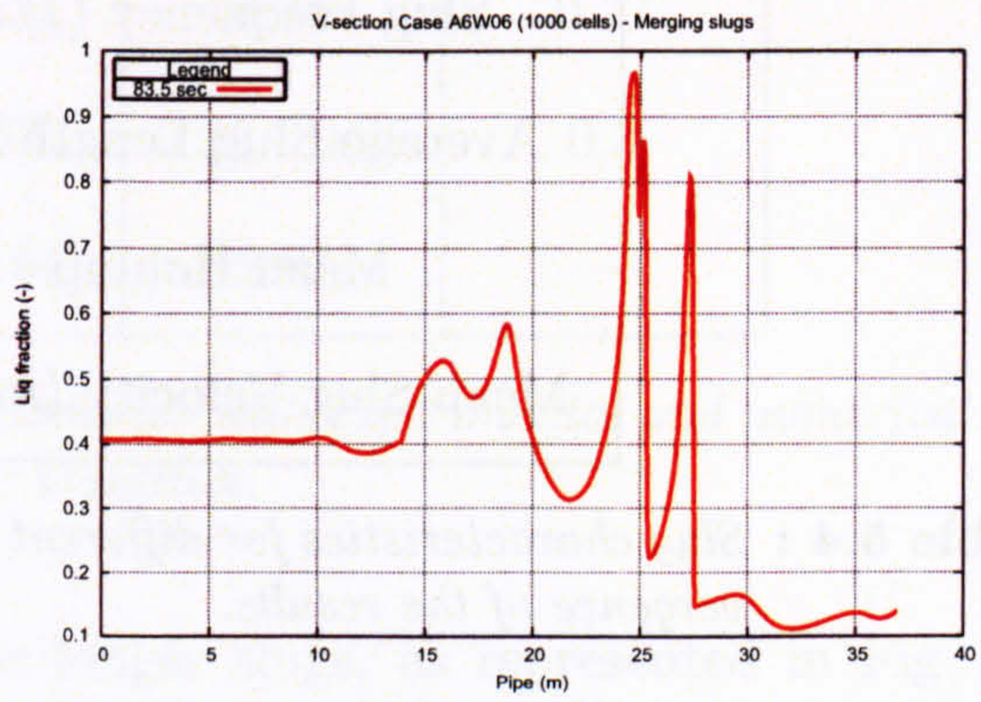

(b) 83.5 sec

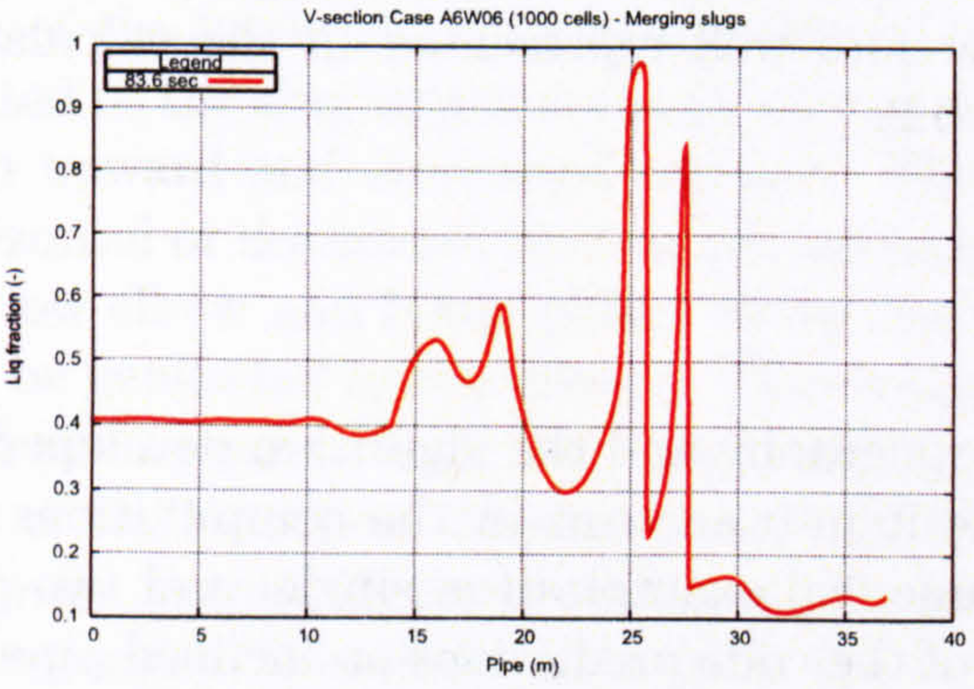

(c) 83.6 sec

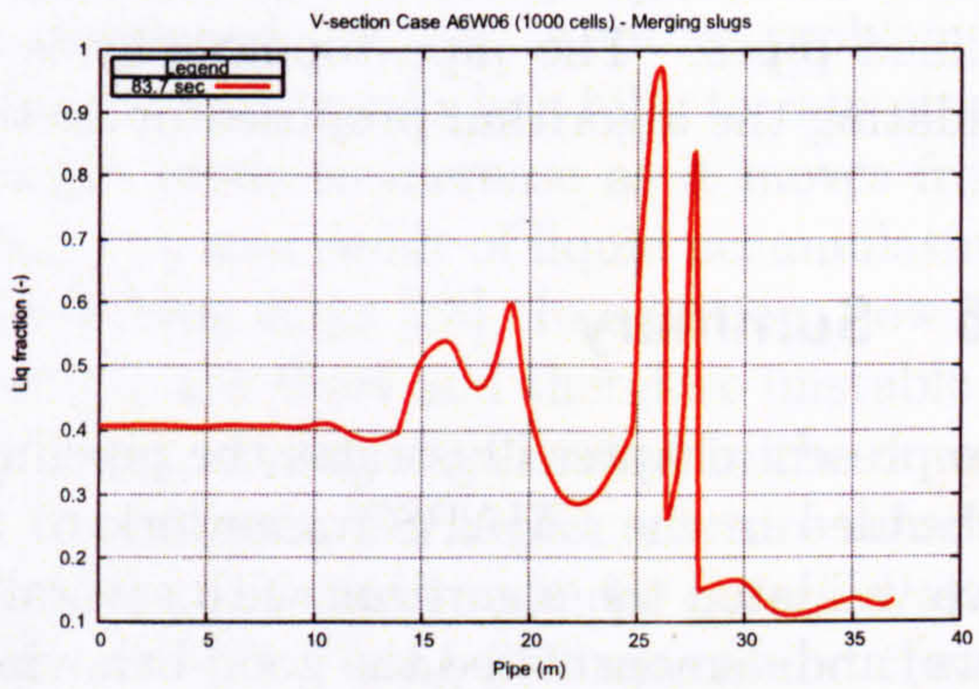

(d) 83.7 sec

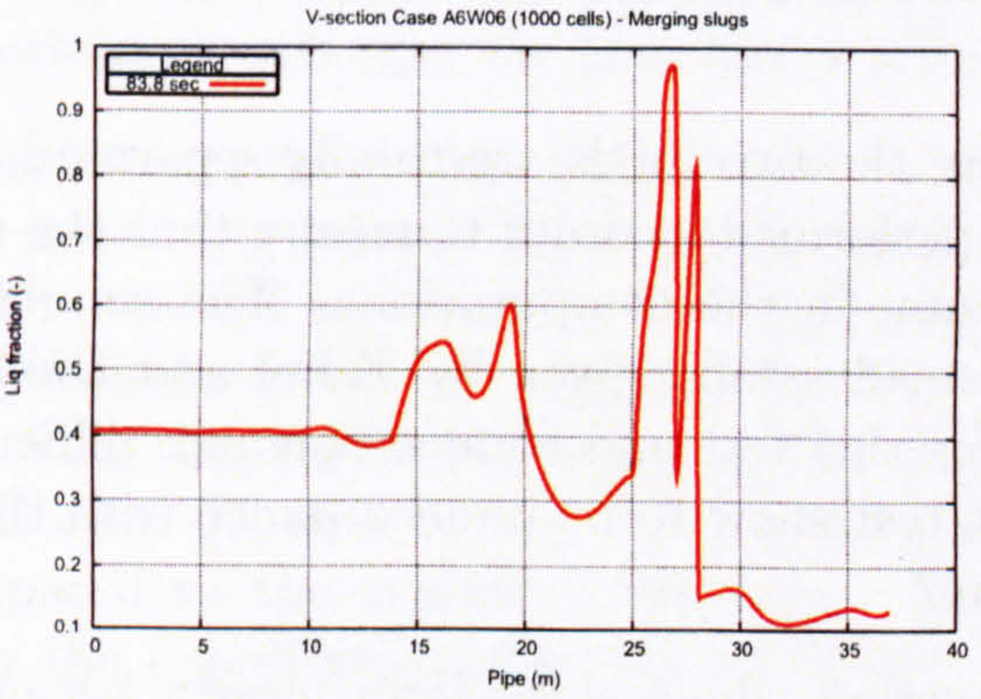

(e) 83.8 sec

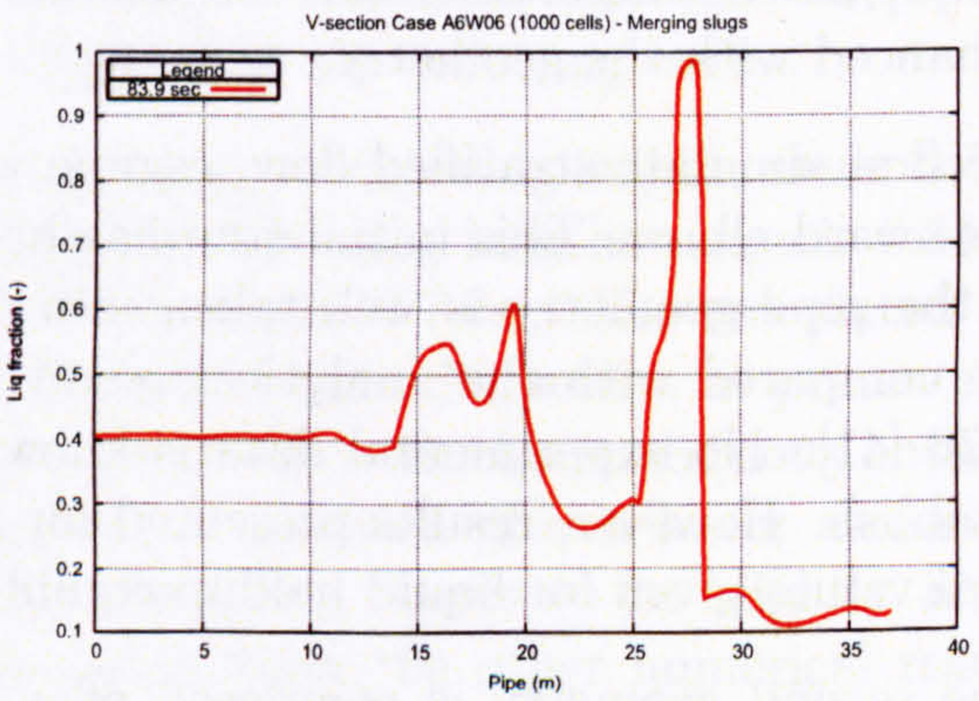

(f) 83.9 sec

Figure 5.24 : *Snapshots of liquid holdup profiles illustrating merging slugs.*

can simulate two-phase slug flow in slightly inclined pipes. It should be noted that there are some areas where our terrain-induced slugging model still needs research and improvement. Considering that the best set of shear stresses is still an important open question in slug flow, the use of new friction factors combination needs to be developed further, as well as the validation of new models for slug flow, for instance using complex mechanisms such as gas entrainment which are not naturally included in a classic two-fluid model and which can be modelled by an additional transport equation for the dispersed gas bubbles [6].

In the end, we succeeded in implementing a robust and efficient algorithm to take into account pipelines topography for one-dimensional models in the EMAPS framework, which proved itself in execution. However, using a non-uniform grid would be an asset and should be one of the areas of future research. In that respect, the mesh creation process has been developed keeping this feature in mind: each sub-pipe can be seen as a patch where refinement technique, such as Adaptive Mesh Refinement [35, Chapter 4] already embedded within the EMAPS framework, can be performed.

References - 5

[1] ANDREUSSI, P. BENDIKSEN, K., AND NYDAL, O. J. Void distribution in slug flow. *Int. J. Multiphase Flow 19*, 5 (1993), 817–828.

[2] ANDREUSSI, P., PAGLIANTI, A., VATISTAS, N., MINERVINI, A., AND BENDIKSEN, K. Analysis of slug flow in near horizontal and horizontal pipes. In *European Two-Phase Flow Group Meeting* (30 May to 1 June 1988), no. Paper B2. Brussels, Belgium.

[3] ANDREUSSI, P., AND PERSEN, L. N. Stratified gas-liquid flow in downwardly inclined pipes. *Int. J. Multiphase Flow 13*, 5 (1987), 565–575.

[4] ANDRITSOS, N., AND HANRATTY, T. Influence of interfacial waves in stratified gas-liquid flows. *AIChE Journal 33*, 3 (1987), 444–454.

[5] BARNEA, D., AND BRAUNER, N. Holdup of the liquid slug in two-phase intermittent flow. *Int. J. Multiphase Flow 11*, 1 (1985), 43–49.

[6] BONIZZI, M. *Transient one-dimensional modelling of multi-phase slug flows.* Ph.D. thesis, Imperial College, University of London, UK., 2002.

[7] BRILL, J., SCHMIDT, Z., COBERLY, W., HERRING, J., AND MOORE, D. Analysis of two-phase tests in large-diameter flow lines in prudhoe bay field. *SPE Journal* (June 1981), 363–378.

[8] DE HENAU, V., AND RAITHBY, G. A study of terrain-induced slugging in two-phase flow pipelines. *Int. J. Multiphase flow 21*, 3 (1995), 365–379.

[9] DHULESIA, H., BERNICOT, M., AND DEHEUVELS, P. Y. Statistical analysis and modeling of slug lengths. In *BHRG Multiphase 1991 proceedings* (1991). Cannes, France.

[10] DUKLER, A., AND HUBBARD, M. G. A model for gas-liquid slug flow in horizontal and near horizontal tubes. *Ind. Eng. Chem. Fundam. 14*, 4 (1975), 337–347.

[11] DUKLER, A., MOALEM-MARON, D., AND BRAUNER, N. A physical model for predicting the minimum stable slug length. *Chem. Eng. Sci. 40* (1985), 1379–1385.

[12] FABRE, J., AND LINÉ, A. Modelling of two-phase slug flow. *Annual Rev. Fluid Mech. 24* (1992), 21–46.

[13] FERGUSON, M., AND SPEDDING, P. Measurement and predication of pressure drop in two-phase flow. *J. Chem. Technol. Biotechnol. 62* (1995), 262–278.

[14] FERNANDES, R., SEMIAT, R., AND DUKLER, A. Hydrodynamic model for gas-liquid slug flow in vertical tubes. *AIChE Journal 29*, 6 (1983), 981–989.

[15] GOPAL, M. Development of a mechanistic model for the prediction of slug length in horizontal multiphase flow. In *BHRG Multiphase 1998 proceedings* (1998). Banff, Canada.

[16] GREGORY, G., NICHOLSON, M., AND AZIZ, K. Correlation of the liquid volume fraction in the slug for horizontal gas-liquid slug flow. *Int. J. Multiphase Flow 4* (1978), 33–39.

[17] GREGORY, G., AND SCOTT, D. Correlation of liquid slug velocity and frequency in horizontal cocurrent gas-liquid slug flow. *AIChE Journal 15* (1969), 307–320.

[18] GRESKOVICH, E. J., AND SHRIER, A. L. Pressure drop and holdup in horizontal slug flow. *AIChE Journal 17*, 5 (1972), 1214–1219.

[19] HALE, C. Slug flow in a v-section. Private communication, Chemical Engineering department, Imperial College, 1999.

[20] HALE, C. *Slug formation, growth and decay in gas-liquid flows.* Ph.D. thesis, Department of Chemical Engineering, Imperial College, London, UK., 2000.

[21] HAND, N. P. *Gas-liquid co-current flow in a horizontal pipe.* Ph.D. thesis, Queen's University Belfast, Northern Ireland, 1991.

[22] HEYWOOD, N. I., AND F., R. J. Slug flow of air-water mixtures in a horizontal pipe: determination of liquid holdup by g-ray absorption. *Chem. Eng. Sci. 34* (1979), 17–30.

[23] KEMPF, M. Simulation of a slug flow in a "v"-section. Tech. rep., Imperial College, August 1999. Interim Report on work conducted within Project 3 of the Transient Multiphase Flow Programme.

[24] LOCKART, R., AND MARTINELLI, R. Proposed correlation of data for isothermal two-phase, two component flow in pipes. *Chem. Eng. Prog. 1* (1949), 39–48.

[25] LOILIER, P. *Numerical approach of modelling a multiphase flow problem in a complex geometry.* MSc thesis, Applied Mathematics & Computing, Cranfield University, 2002.

[26] LOUAKED, M., AND HANICH, L. Tvd scheme for the shallow water equations. *Journal of Hydraulic Research 36*, 3 (1998).

[27] MALNES, D. Slug flow in vertical, horizontal and inclined pipes. Tech. rep., Report IFE/KR/E-83/002,V. Inst. for Energy technology, Kjeller, Norway, 1982.

[28] MANOLIS, I. *High Pressure Gas-Liquid Slug Flow.* Ph.D. thesis, Department of Chemical Engineering and Chemical Technology, Imperial College of Science, Technology and Medicine, UK., 1995.

[29] MILNE-THOMSON, L. *Theoretical Hydrodynamics*, 5th ed. The MacMillan Press, London, 1968.

[30] MISHIMA, K., AND ISHII, M. Theoretical prediction of onset of horizontal slug flow. *Journal of Fluids Engineering 102* (1980), 441–444.

[31] MOISSIS, R., AND GRIFFITH, P. Entrance effects in a two-phase slug flow. *AIChE Journal of Heat Transfer, Trans. ASME 84* (1962), 29–39.

[32] MÜLLER-STEINHAGEN, H., AND HECK, K. A simple friction pressure drop correlation for two-phase flow in pipes. *Chem. Eng. Proc. 20*, 6 (1986), 297–308.

[33] NICHOLSON, M., AZIZ, K., AND GREGORY, G. Intermittent two-phase flow in horizontal pipes: Predictive models. *Can. J. Chem. Eng. 56* (1978), 653–663.

[34] NYDAL, O., PINTUS, S., AND ANDREUSSI, P. Statistical characterization of slug flow in horizontal pipes. *Int. J. Multiphase Flow 18*, 3 (1992), 439–455.

[35] OMGBA-ESSAMA, C. *Numerical modelling of transient gas-liquid flows (application to stratified and slug flow regimes).* Ph.D. thesis, Cranfield University, Applied Mathematics & Computing group, 2004.

[36] ROTHE, P., AND CROWLEY, C. InsigniïñĄcant terrain effects in multiphase pipelines. *AGA Catalog No. L15526* (1986).

[37] SCHMIDT, Z. *Experimental study of two-phase slug flow in a pipeline-riser pipe system.* Ph.D. dissertation, University of Tulsa, 1977.

[38] SCOTT, S., AND KOUBA, G. Advances in slug flow characterization for horizontal and slightly inclined pipelines. In *SPE 20628* (1990), pp. 39–48. New Orleans, LA.

[39] SCOTT, S., SHOHAM, O., AND BRILL, J. Prediction of slug length in horizontal, large-diameter pipes. *SPE Prod. Facil. 4* (1989), 335–340.

[40] TAITEL, Y., BARNEA, D., AND DUKLER, A. Modelling flow pattern transitions for stratified flow in vertical tubes. *AIChE Journal 26*, 3 (1980), 345–354.

[41] TAITEL, Y., AND DUKLER, A. A model for predicting flow regime transitions in horizontal and near horizontal gas-liquid flow. *AIChE Journal 22*, 1 (1976), 47–55.

[42] TAITEL, Y., AND DUKLER, A. E. A model for slug frequency during gas-liquid flow in horizontal and near horizontal pipes. *Int. J. Multiphase Flow 3*, 6 (1977), 585–596.

[43] TRONCONI, E. Prediction of slug frequency in horizontal two-phase flow. *AIChE Journal 36*, 5 (1990), 701–709.

[44] ZHENG, G. *Two-phase slug flow in hilly-terrain pipelines.* Ph.D. dissertation, The University of Tulsa, Tulsa, OK, 1991.

[45] ZHENG, G., BRILL, J., AND SHOHAM, O. An experimental study of two-phase slug flow in hilly-terrain pipelines. *SPE J. Prod. Fac.* (1995).

[46] ZHENG, G., BRILL, J., AND TAITEL, Y. Slug flow behavior in a hilly-terrain pipeline. *Int. J. Multiphase Flow 20*, 1 (1994), 63–79.

6 Bubbly flows

6.1 Overview

Chapter 3 demonstrated that the one-dimensional compressible model associated to the AUSM method is capable of dealing with extreme flow conditions, as established by the benchmarks simulations; it also gave the formulation of the specific model developed for bubbly flows. The present chapter will now focus on the description, and subsequent validation of this mathematical model to simulate vertical two-phase bubbly flows against experimental data.

After an overview, in the next section, of the numerical experiments presented in this work, Section 6.3 will be the subject of simulations of two-phase air-water flows in a $70\,mm$ diameter pipe; a description of the problem and comparisons between the model and experimental predictions are detailed.

Section 6.4 will show numerical simulations carried out for naphtha-nitrogen mixtures in large vertical pipe, and operating at high pressures. A grid size and time step sensitivity analysis is performed, and discussions on results of void fraction, velocities and pressure are presented too. We also investigate, throughout the section, the effect of the extra buoyancy term introduced in the model.

6.2 Presentations of the simulations

The present study aims to provide predictions of two-phase flow in vertical risers. A first stage is to study vertical bubbly flow regime.

This section presents the validation of our model by comparing the numerical predictions with the experimental data for bubbly flow configurations. Our test-cases cover a wide range of pipe configurations: $70\,mm$ and $189\,mm$ pipe diameters with operating pressure of $1\,bar$, $20\,bar$ and $90\,bar$.

The predicted gas fractions and pressure are compared to the experimental data for the $189mm$ pipe with the naphtha-nitrogen mixture at pressure of $20bar$ and $90bar$ and for the $70mm$ pipe with the air-water mixture at atmospheric pressure. The comparisons between

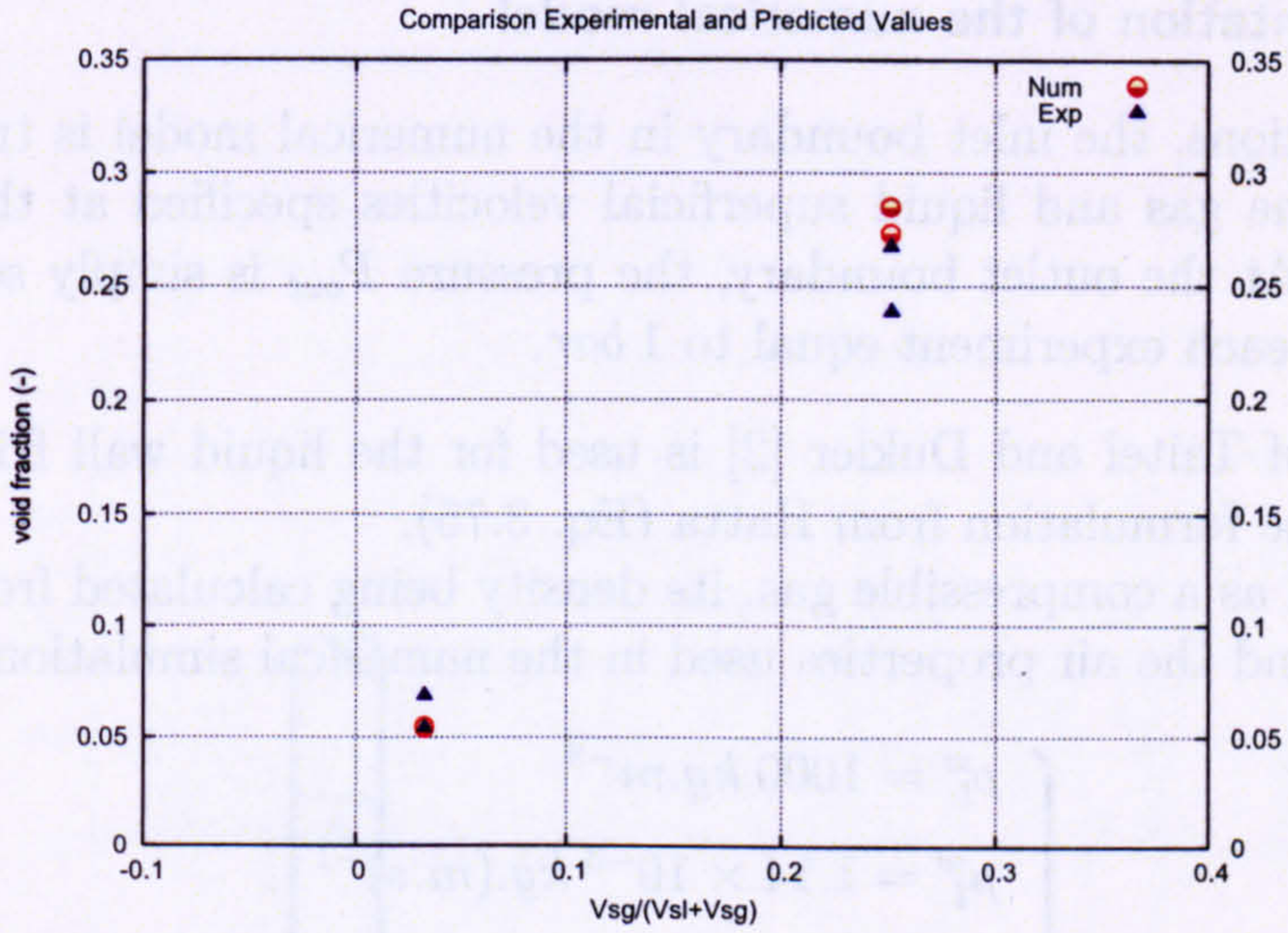

Figure 6.1 : *Average gas fraction for air-water bubbly flow in a vertical pipe. Comparison between numerical and experimental data. Values are collected at both probes located along the pipe.*

the predicted and the experimental values are illustrated for each test-case. Different probes are located along the pipes (Fig. 6.2 and Fig. 6.6) to collect the informations.

6.3 Air-water simulations

6.3.1 Description of the experiments

The experiments run by Nottingham University were performed on a vertical riser $5.5m$ long with a diameter of $70mm$, at atmospheric pressure ($1bar$). Because of space constraints, the length of the pipes used in the experimental setup is limited, which in turn narrows the range of flow conditions for which measurements are collected. Additionally the experimental setup is a T-junction (Fig. 6.2) whose T-arm was blocked off to avoid inducing voidage and making results senseless. Therefore it was possible to reproduce two-phase bubbly flow situations, yielding valuable data for the model validation.

Each experiment was run with air and water for 33.19 sec and corresponds to 2006 datapoints per instrument. Two probes collecting the void fraction are located along the pipe at 4.1m and at 5.3m (Fig. 6.2). Both test-cases with air-water have been run with the following initial gas velocities $0.218\,m.s^{-1}$ and $0.022\,m.s^{-1}$. The same initial liquid superficial velocity of $0.65\,m.s^{-1}$ is chosen for both cases.

Experimental data collected volume fractions and no data are available for pressure drop and velocities. Therefore comparisons on volume fractions are the only results presented hereafter.

6.3.2 Implementation of the numerical model

For the computations, the inlet boundary in the numerical model is treated as a source boundary with the gas and liquid superficial velocities specified at the inlet boundary control volume. At the outlet boundary, the pressure P_{out} is simply set to the pressure measured during each experiment equal to 1 bar.

The correlation of Taitel and Dukler [2] is used for the liquid wall friction while C_D is evaluated with the formulation from Hatta (Eq. 3.75).
The air is treated as a compressible gas, its density being calculated from the perfect gas law. The water and the air properties used in the numerical simulations are given by:

$$\begin{cases} \rho_l^w = 1000\, kg.m^{-3} \\ \mu_l^w = 1.14 \times 10^{-3}\, kg.(m.s)^{-1} \\ \rho_g^w = 1.16\, kg.m^{-3} \\ \mu_g = 1.46 \times 10^{-5} \\ \sigma = 0.0717\, N.m^{-1} \end{cases} \tag{6.1}$$

where the surface tension σ is estimated by empirical correlation.

	u93	u96
V_{sg}	$0.218\, m.s^{-1}$	$0.022\, m.s^{-1}$
V_{sl}	$0.65\, m.s^{-1}$	$0.65\, m.s^{-1}$
P^{out}	1 bar	1 bar
T^{in}	293 K	293 K

Table 6.1 : *Air-water test-cases conditions.*

6.3.3 Comparisons between the experimental results and the model predictions

The comparisons between the experimental results and the two-fluid model predictions for the time evolution of the gas fractions for cases with various inlet gas mass flow rates are shown in Fig. 6.3 to 6.5.

Generally, a good agreement between experimental and numerical data is reached. The best agreement between computed results and the experimental data is obtained for the higher gas rates as the u96-case illustrates in Fig. 6.1. The measured variables shown in Fig. 6.3 to 6.5 exhibit oscillations associated with the experiments measurement apparatus. Because the present model treats the flow by averaging the velocities and volume fractions over control volumes, it is not able to predict all the oscillations but only average

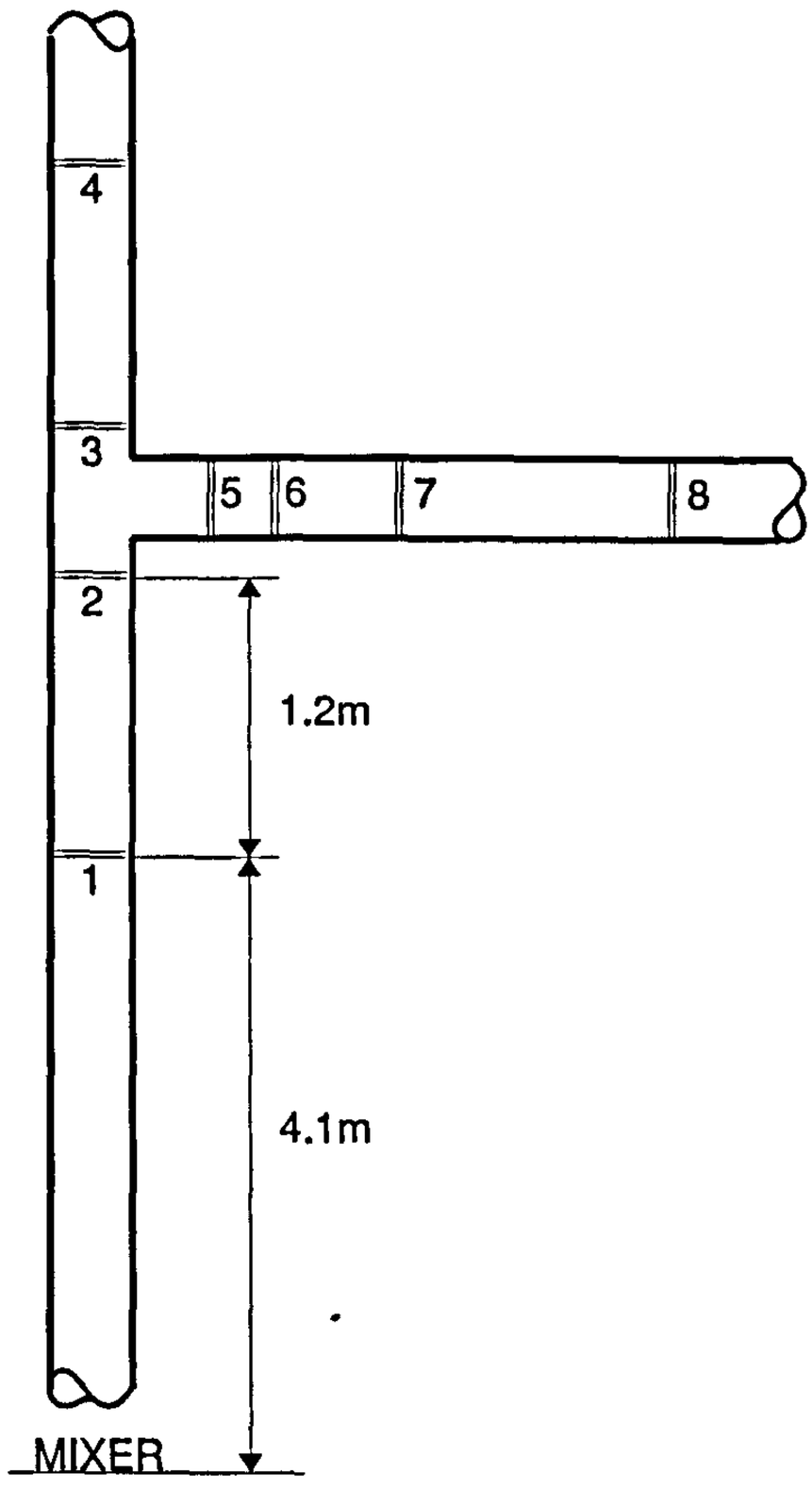

Figure 6.2 : *Nottingham 70mm Vertical T-junction – Identification of probe location.*

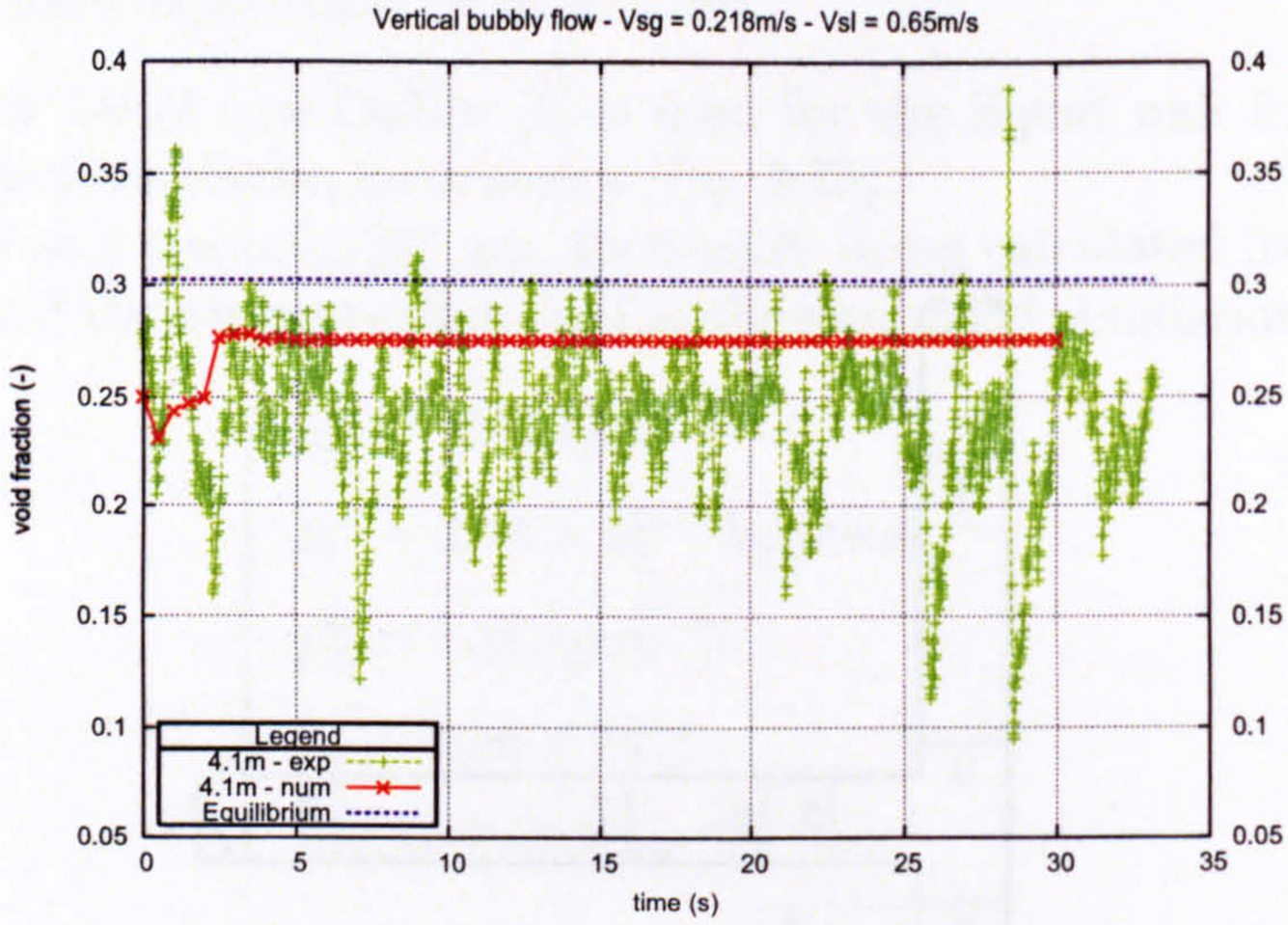

(a) 4.1m

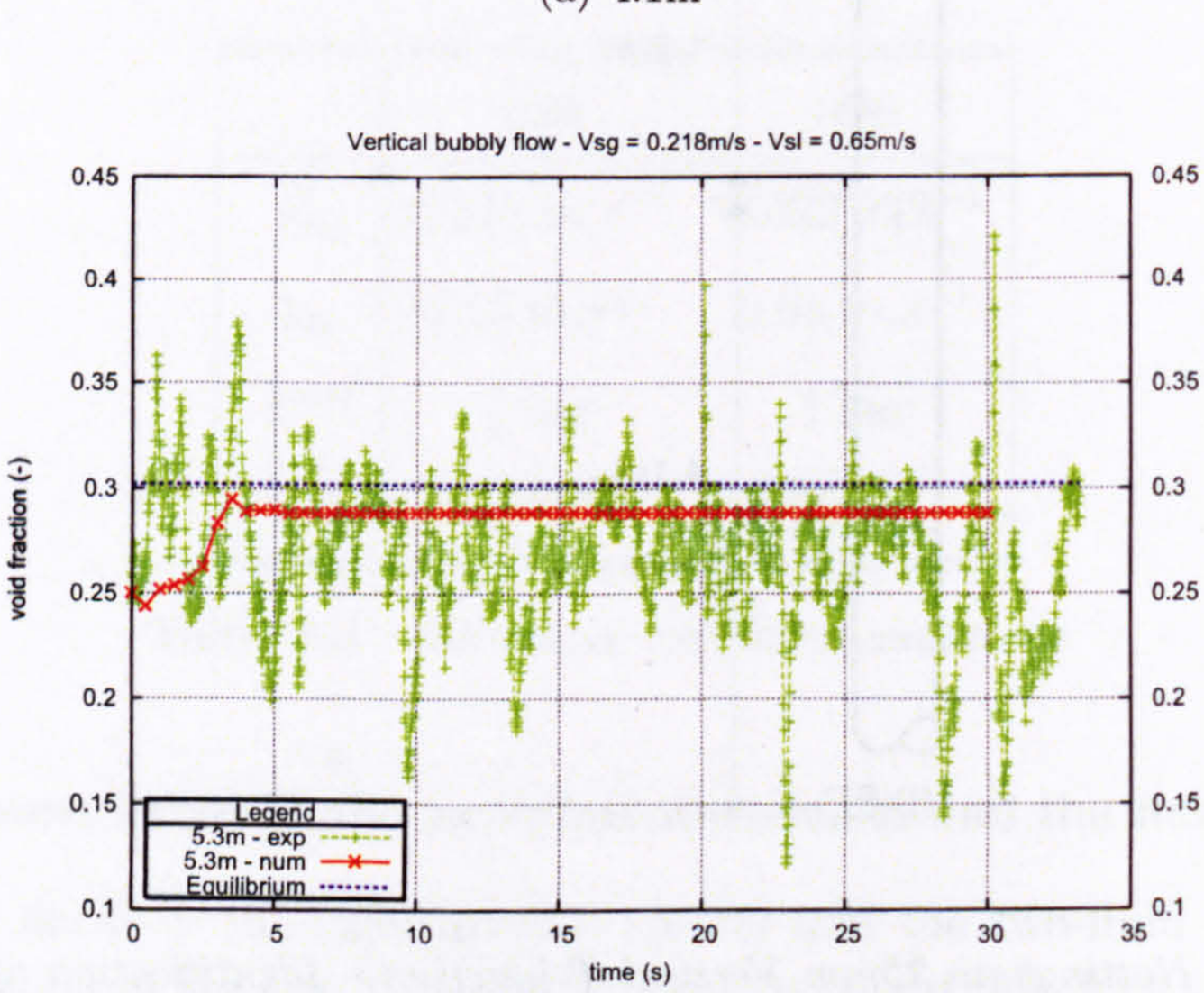

(b) 5.5m

Figure 6.3 : *Nottingham u93 test-case - Void fraction time profile.*

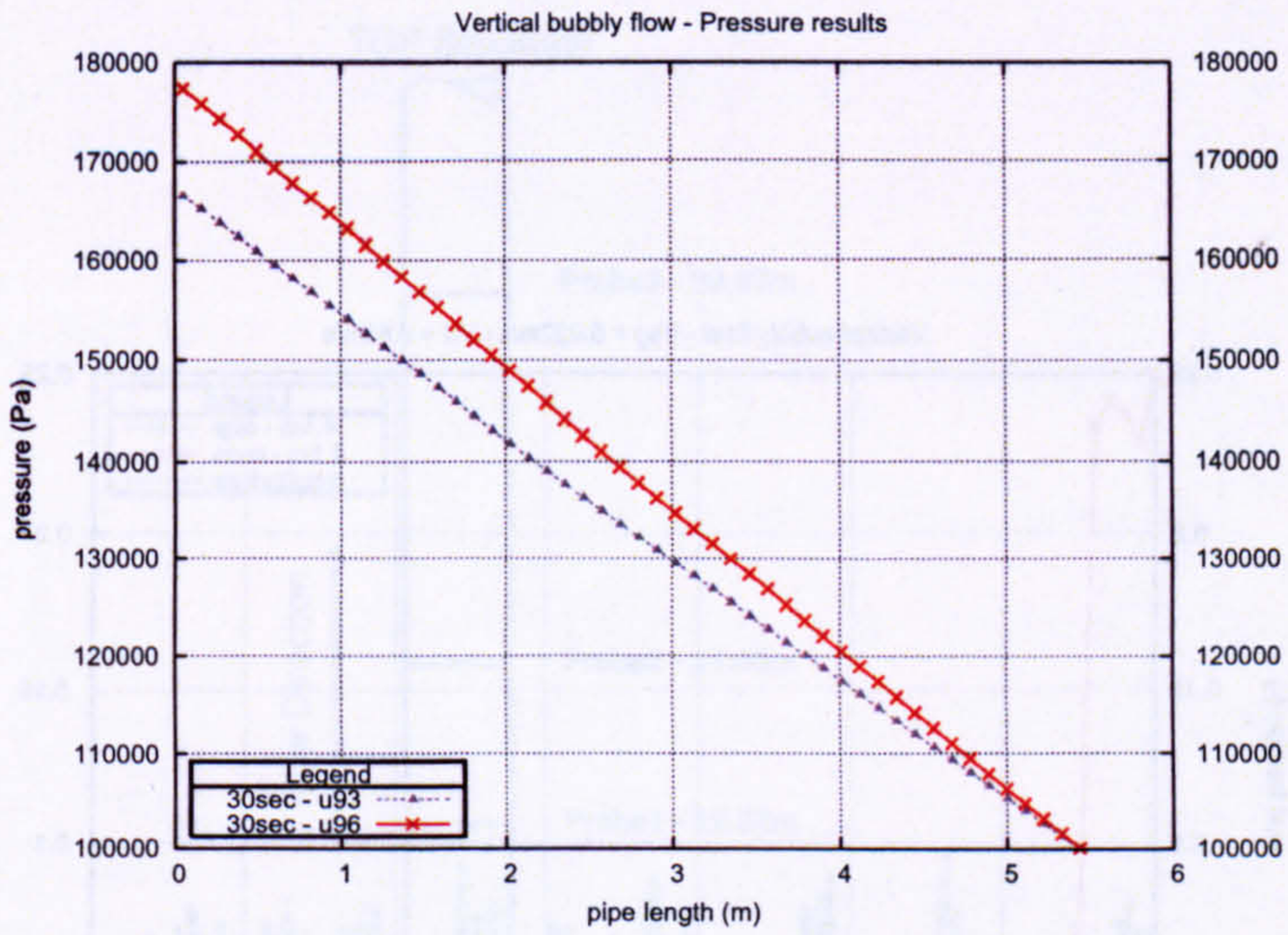

Figure 6.4 : *Pressure results - Comparison of both test-cases.*

mass flow rates.

The case is particularly interesting because the gas superficial velocity is very low and leads to a low experimental gas holdup (around 5×10^{-2}). We start the simulation with a holdup of 0.25 to investigate the behaviour of the code in such situation and the required time to converge to the experimental value. In Fig. 6.5, one may notice that the code goes quickly towards the equilibrium value and agree with the measured value.

The numerical results agree well with the experimental data. The comparison between the predicted and the experimental gas fractions is illustrated in Fig. 6.1. The calculated gas fractions are within 20% of the measured values, with the best comparison for the smaller gas velocities where the computed gas fractions fall within 0.6% of the data.

It has to be noted that since only volume fractions are known for the air-water test-cases, the code predictions for α_g only are compared to the experimental values. However pressure predictions in Fig. 6.4 can also be discussed. From the graph, the pressure drop can be evaluated: its value is higher with the case where the gas velocity is the lowest and where the liquid holdup is the highest. The hydrostatic pressure head component does not vary for these cases. Only the frictional pressure drop does, with the mixture velocity and the friction factor via the Reynold number, which is also a function of the mixture velocity. As the gas velocity decreases, the mixture velocity does as well and the frictional pressure drop increases. This confirms the increase in amplitude for the pressure drop.

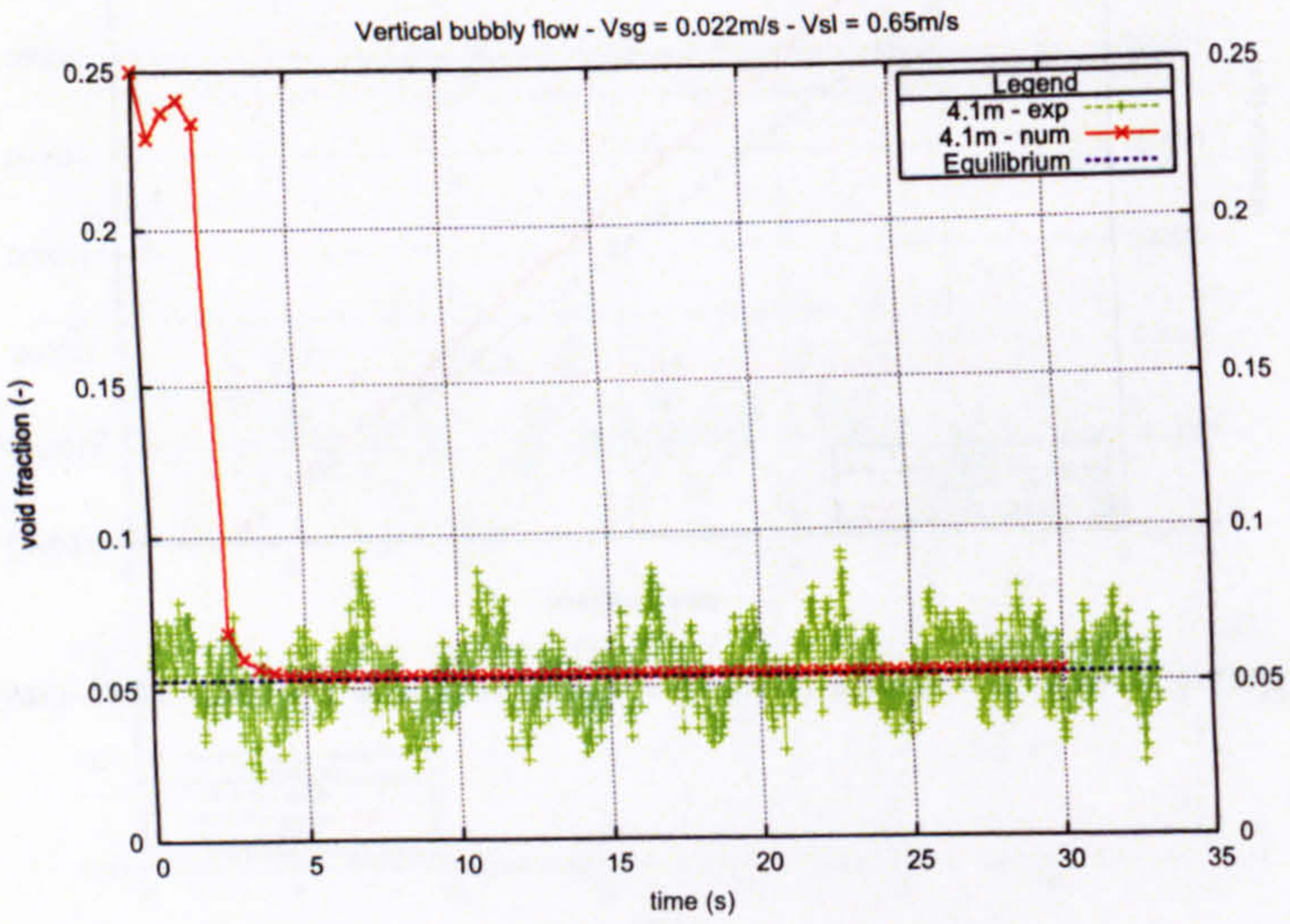

(a)

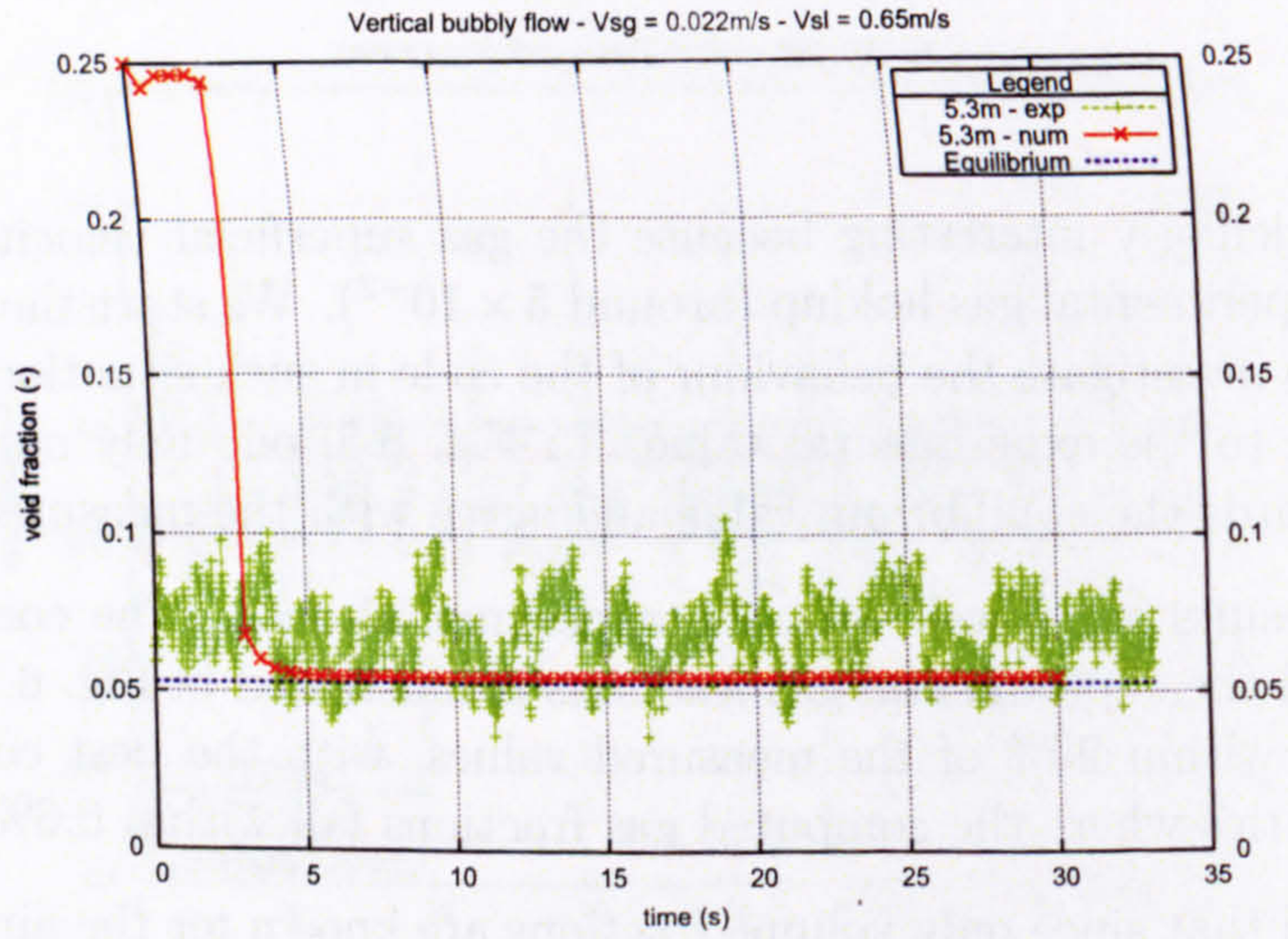

(b)

Figure 6.5 : *Nottingham u96 test-case - Void fraction time profile showing the time the code needs to equilibrate.*

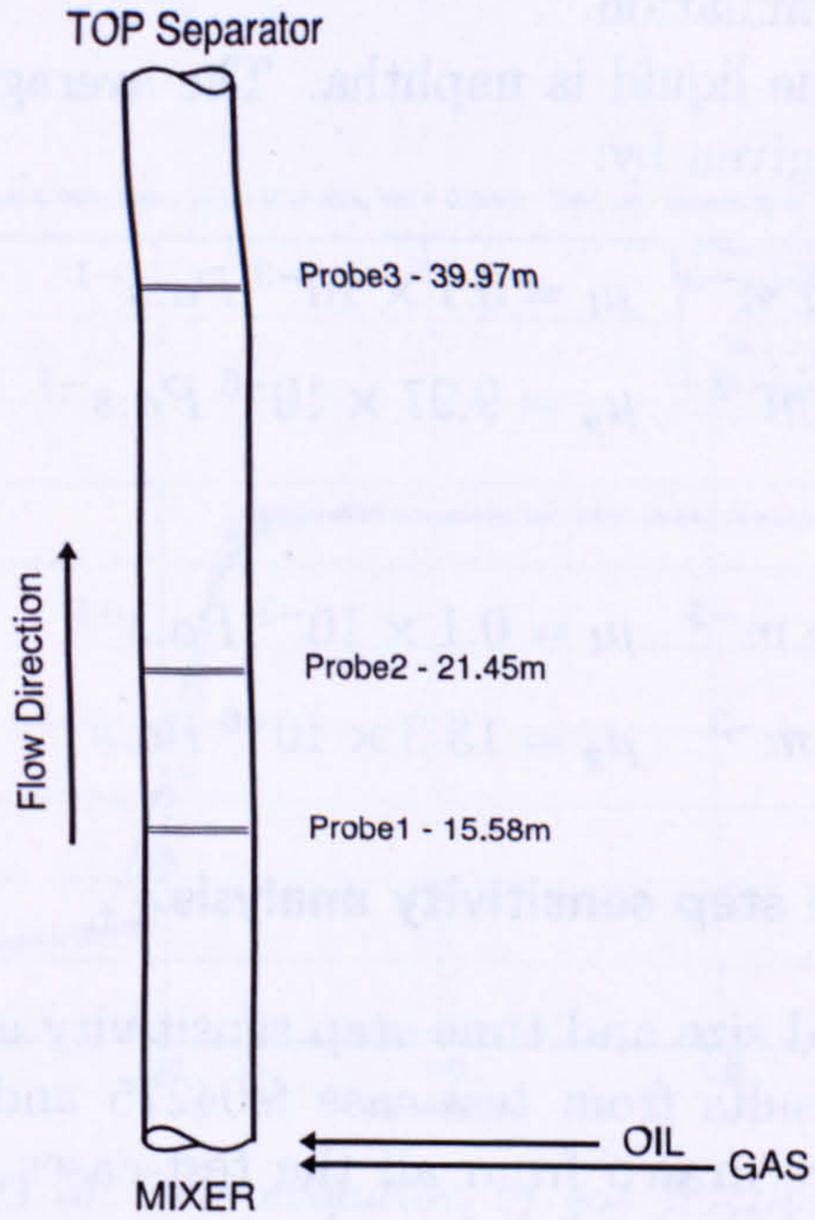

Figure 6.6 : *Trondheim 189mm vertical system - Identification of probe location.*

6.4 Naphtha-nitrogen simulations

6.4.1 Description of the experiments

In order to simulate vertical two-phase flow in wide pipes, a large scale experimental apparatus was designed and built in Trondheim with the purpose of simulating such flows in a laboratory using nitrogen and naphtha as the working fluids.

Experiments are conducted with the pipeline system simplified, described with simplifications in Fig. 6.6. The superficial velocity for the liquid phase is set constant for all test-cases to $V_{sl} = 0.5\,m.s^{-1}$ and is varied for the gas phase from $V_{sg} = 0.09$ to $0.35\,m.s^{-1}$. All the time, the temperature is set constant and is equal to $T = 303\,K$. Table 6.2 lists the conditions of the test-cases presented in this chapter.

6.4.2 Implementation of the numerical model

For the computations, as for the air-water cases, the inlet boundary in the numerical model is treated as a source boundary with the air and oil superficial velocities specified at the inlet control volume. At the outlet boundary, the pressure P_{out} is set to the pressure measured during each experiment and varies from 18.8 *bar* and 89 *bar* depending on the test-case.

The correlation of Taitel and Dukler [2] is used for the liquid wall frictions while C_D is

estimated with Hatta's formulation.
The gas is nitrogen and the liquid is naphtha. The average fluid properties used in the numerical simulations are given by:

$$20\ bar: \begin{cases} \rho_l = 672.6\ kg.m^{-3} & \mu_l = 0.1 \times 10^{-3}\ Pa.s^{-1} \\ \rho_g = 22.0\ kg.m^{-3} & \mu_g = 9.97 \times 10^{-6}\ Pa.s^{-1} \end{cases} \quad \sigma = 14.1 \times 10^{-3}\ N.m^{-1}$$

$$90\ bar: \begin{cases} \rho_l = 674.6\ kg.m^{-3} & \mu_l = 0.1 \times 10^{-3}\ Pa.s^{-1} \\ \rho_g = 99.5\ kg.m^{-3} & \mu_g = 13.3 \times 10^{-6}\ Pa.s^{-1} \end{cases} \quad \sigma = 10.5 \times 10^{-3}\ N.m^{-1}$$

6.4.3 Grid size and time step sensitivity analysis

For the present work, a grid size and time step sensitivity analysis is performed for each of the cases. Only the results from test-case fe04275 and fe04086 are presented here as the same conclusions are drawn from all the test-cases. Calculations are performed with different grid sizes and time steps in order to ensure that predictions used for the comparisons with the experimental data are grid size and time step independent. A constant ratio $CFL = 0.1$ is chosen with grid sizes of 0.125, 0.25, 0.5 and $1\,m$ respectively.

The predicted time evolution of the gas fraction α_g and pressure P for test-case fe04275 obtained with the $0.125\ m$, $0.25\ m$ and $0.5\ m$ grids are compared to the predictions for the $1\ m$ grid in Fig. 6.7 and 6.8. The pressure levels are not very much affected by the grid and time step changes. For $\Delta x \leq 0.25$, the effects of the grid size and time step on the gas fraction variation with time become negligible.

For the time-step study, a $\Delta x = 1\,m$ is chosen for Δt varying between $10^{-4}\ sec$, $10^{-5}\ sec$, $10^{-6}\ sec$.

In the comparisons between the experimental results and the numerical predictions, a grid size of $\Delta x = 1\,m$ and a ratio $CFL = 0.1$ are adopted.

	fe04084	fe04085	fe04086	fe04275	fe04276
V_{sg}	$0.09\ m.s^{-1}$	$0.18\ m.s^{-1}$	$0.36\ m.s^{-1}$	$0.19\ m.s^{-1}$	$0.35\ m.s^{-1}$
V_{sl}	$0.5\ m.s^{-1}$	$0.5\ m.s^{-1}$	$0.5\ m.s^{-1}$	$0.5\ m.s^{-1}$	$0.5\ m.s^{-1}$
P	20 bar	20 bar	20 bar	90 bar	90 bar
T	303 K	303 K	303 K	303 K	303 K

Table 6.2 : *Naphtha-nitrogen test-cases conditions.*

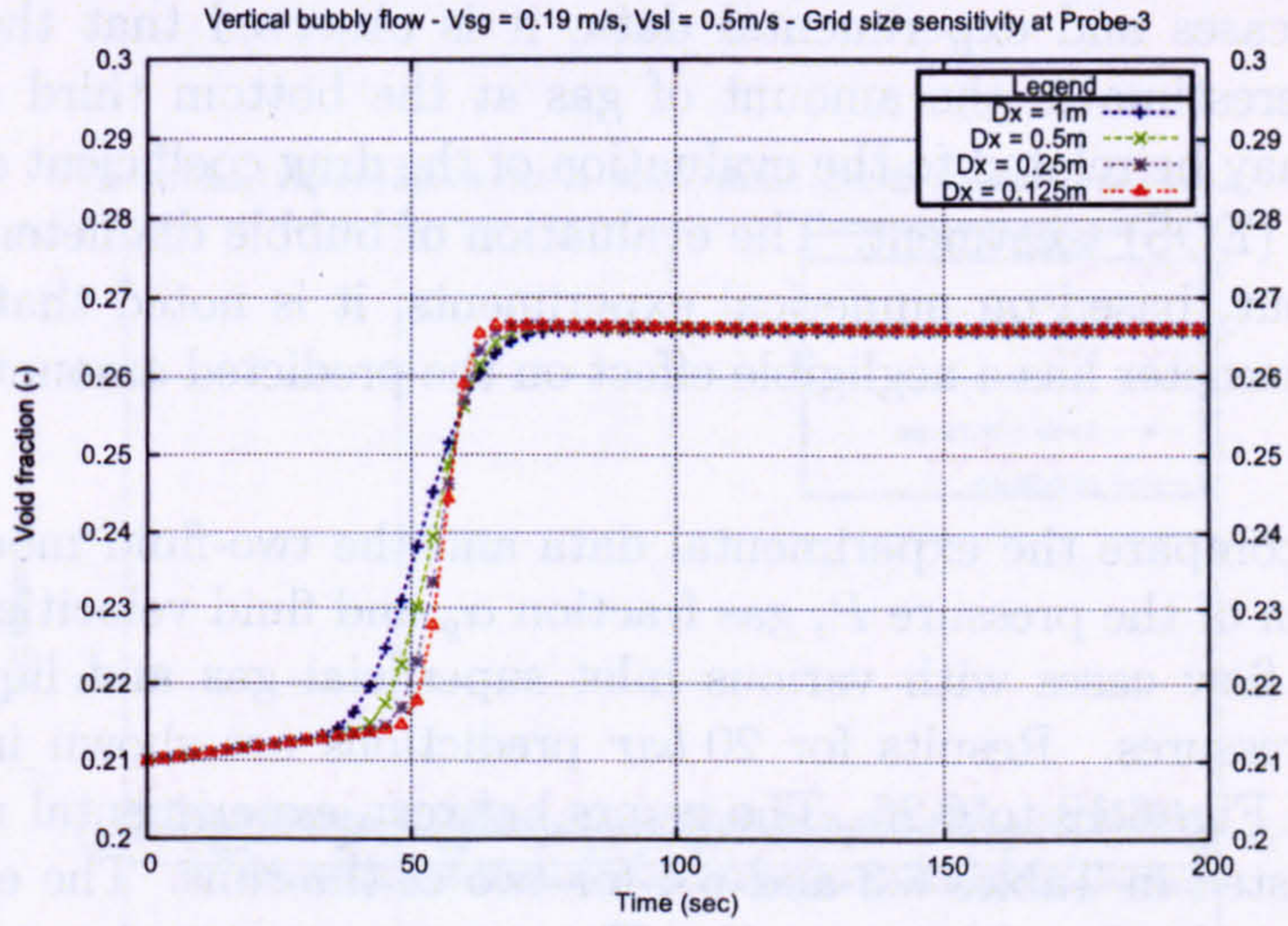

Figure 6.7 : *Grid size effects on time evolution of gas fraction - Test-case fe04275 -* $\Delta x = 0.125m$ *to* $\Delta x = 1m$.

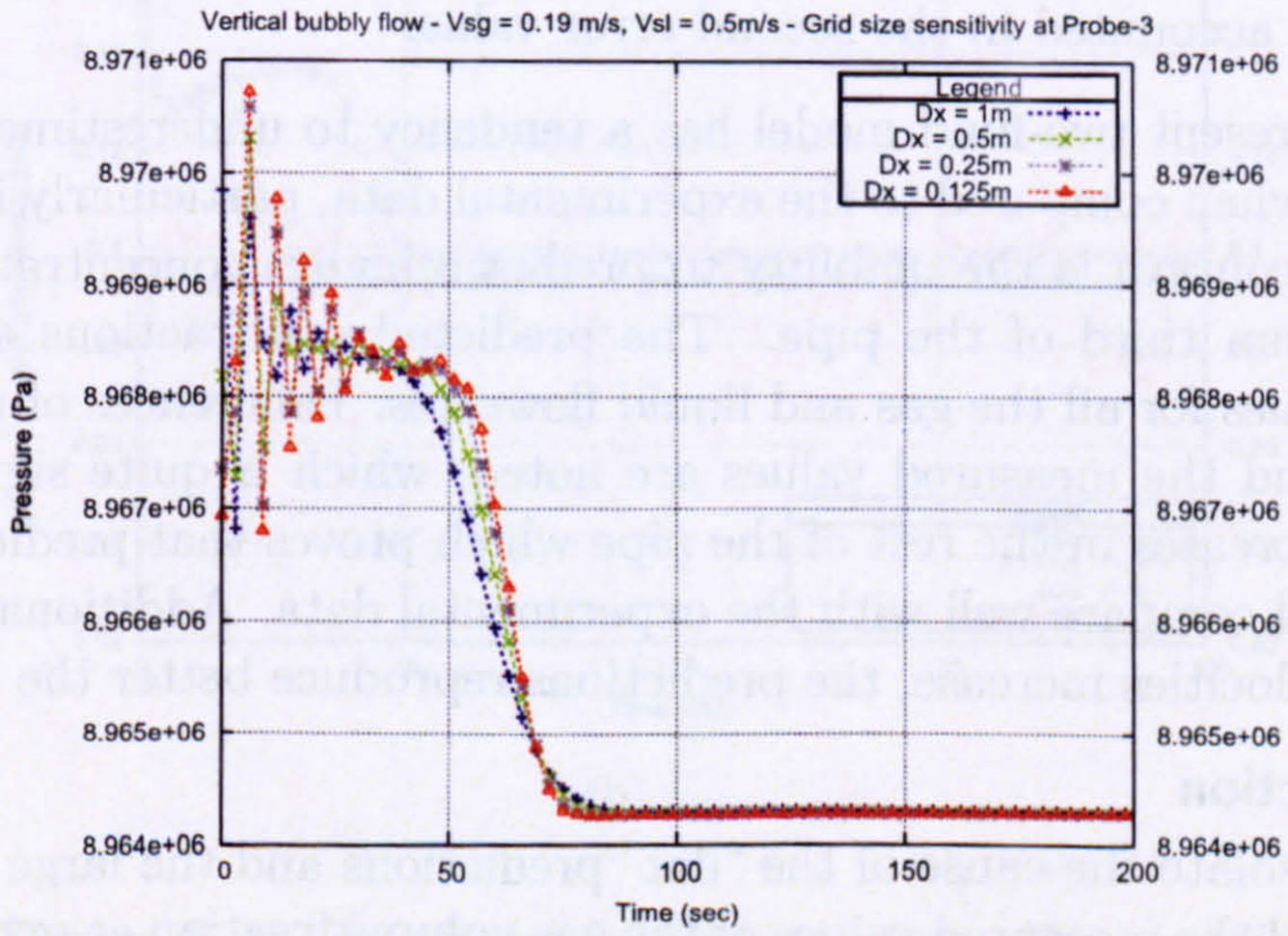

Figure 6.8 : *Grid size effects on time evolution of pressure - Test-case fe04275 -* $\Delta x = 0.125m$ *to* $\Delta x = 1m$.

6.4.4 Comparisons between the experimental results and the model predictions

Following the comparisons (not all shown in the thesis) between several numerical solutions for bubbly flow cases and experimental data, it is observed that the two-fluid model consistently underestimates the amount of gas at the bottom third of the pipe. The reasons for this may be related to the evaluation of the drag coefficient or thermodynamic equation of state (EOS) treatment. The evaluation of bubble diameter is another source of uncertainty; but, based on numerical experiments, it is noted that accounting for a varying bubble diameter has a negligible effect on the predicted amount of gas in the first third of the pipe.

Fig. 6.9 to 6.26 compare the experimental data and the two-fluid model predictions for the time evolution of the pressure P, gas fraction α_g and fluid velocities for the naphtha-nitrogen bubbly flow cases with various inlet superficial gas and liquid velocities and various outlet pressures. Results for 20 *bar* predictions are shown in Fig. 6.9 to 6.18 and for 90 *bar* in Fig. 6.19 to 6.26. The errors between experimental measurements and predictions are listed in Tables 6.3 and 6.4 for two of the runs. The error tables for the other test-cases can be found in appendix. The error percentage is evaluated as follows:

$$\text{error} = \frac{|x^{exp} - x^{num}|}{x^{exp}} \times 100 \tag{6.2}$$

where x is the time average of the variable for which the error is computed. The error is computed for the whole computational time. The error for the last $100 sec$ is also reported. The purpose of this is to compare the predictions once the code has reached a steady-state. The possible numerical instabilities occurring at the beginning of the simulations are therefore not accounted in the second error value.

In general, the present two-fluid model has a tendency to underestimate the average gas volume fraction when compared to the experimental data, particularly in the fe04084 test-case. The main concern is the inability to predict a higher concentration of gas bubbles in the first bottom third of the pipe. The predicted gas fractions are lower than the experimental values for all the gas and liquid flowrates. Differences of up to 65% between the calculated and the measured values are noted, which is quite significant. However, the difference decreases in the rest of the pipe which proves that predictions of outlet gas production would compare well with the experimental data. Additionally as pressure and superficial gas velocities increase, the predictions reproduce better the experimental data.

Gas volume fraction

It is difficult to isolate the cause of the "flat" predictions and the large difference between the numerical and the measured values of the gas volume fraction at probe 1. The problem seems to be the first 50 seconds of the simulations. Although several criteria have been investigated, none of them manages to improve this feature.

It is not believed that the drag force correlation for the interface is the main cause for the discrepancies between the present model predictions and the experimental data for

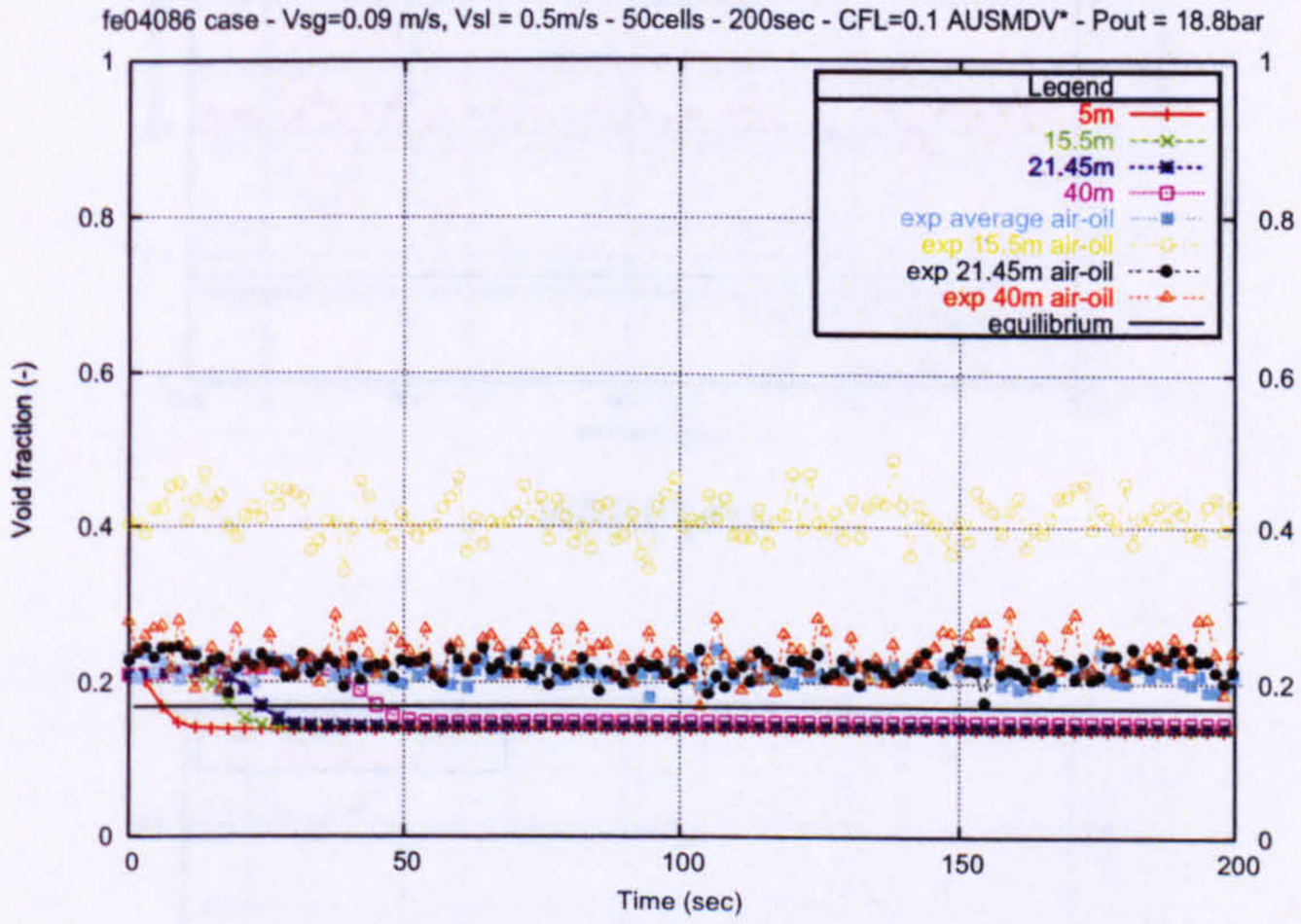

(a) all

(b) V_{sg}

Figure 6.9 : *Trondheim fe04084 test-case - Time profiles.*

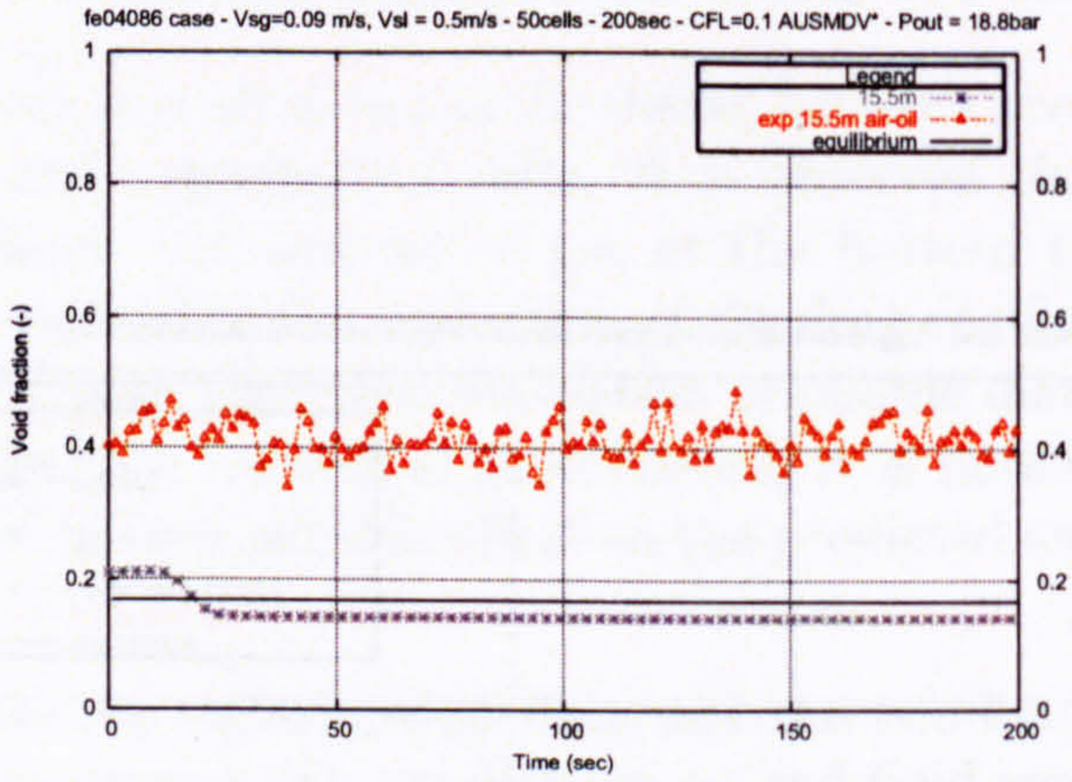

(a) 15.5m

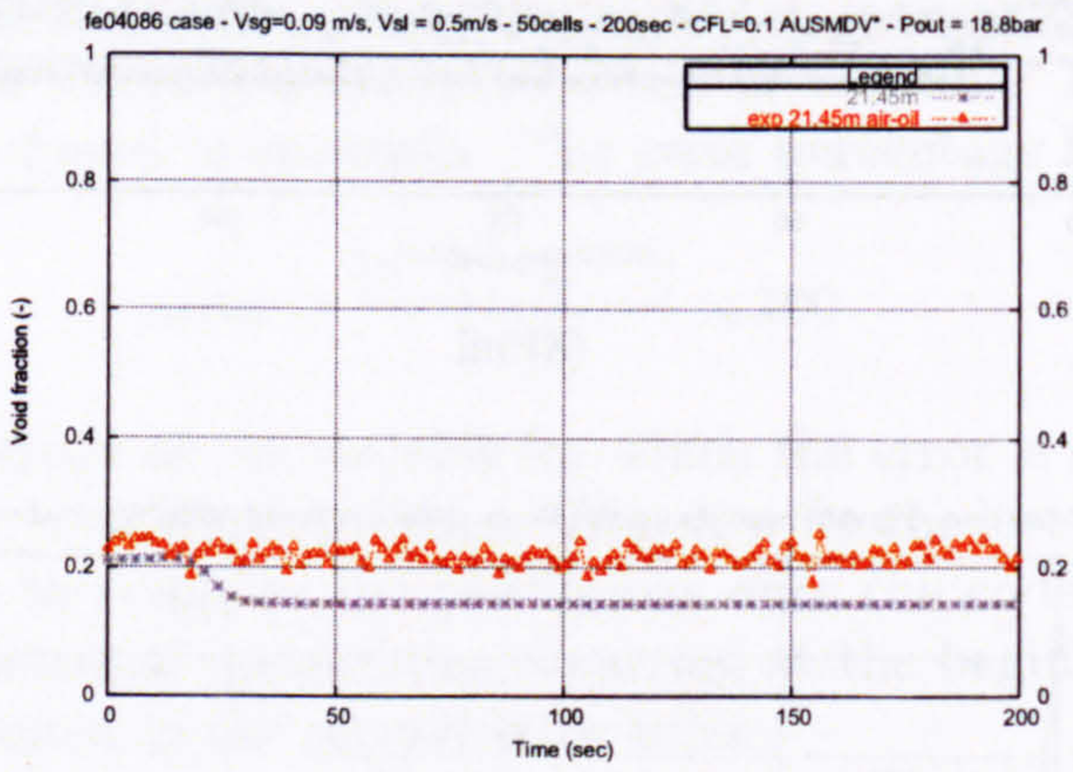

(b) 21.45m

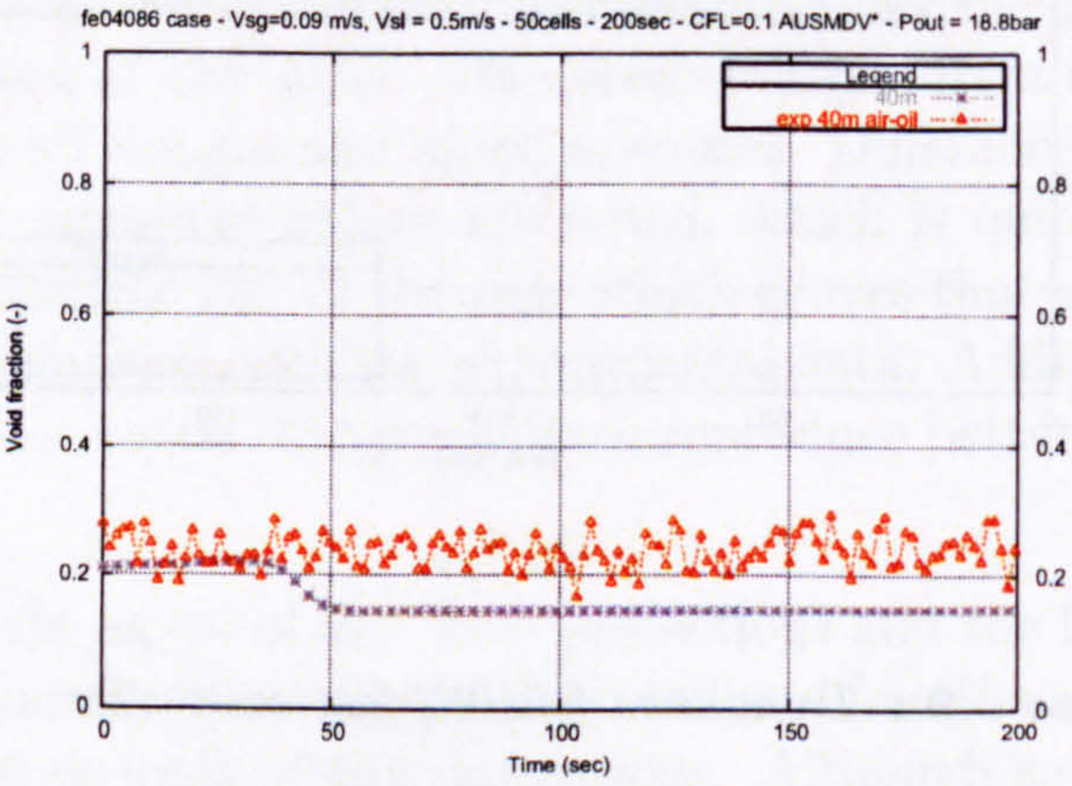

(c) 40m

Figure 6.10 : *Trondheim fe04084 test-case - Void fraction time profiles.*

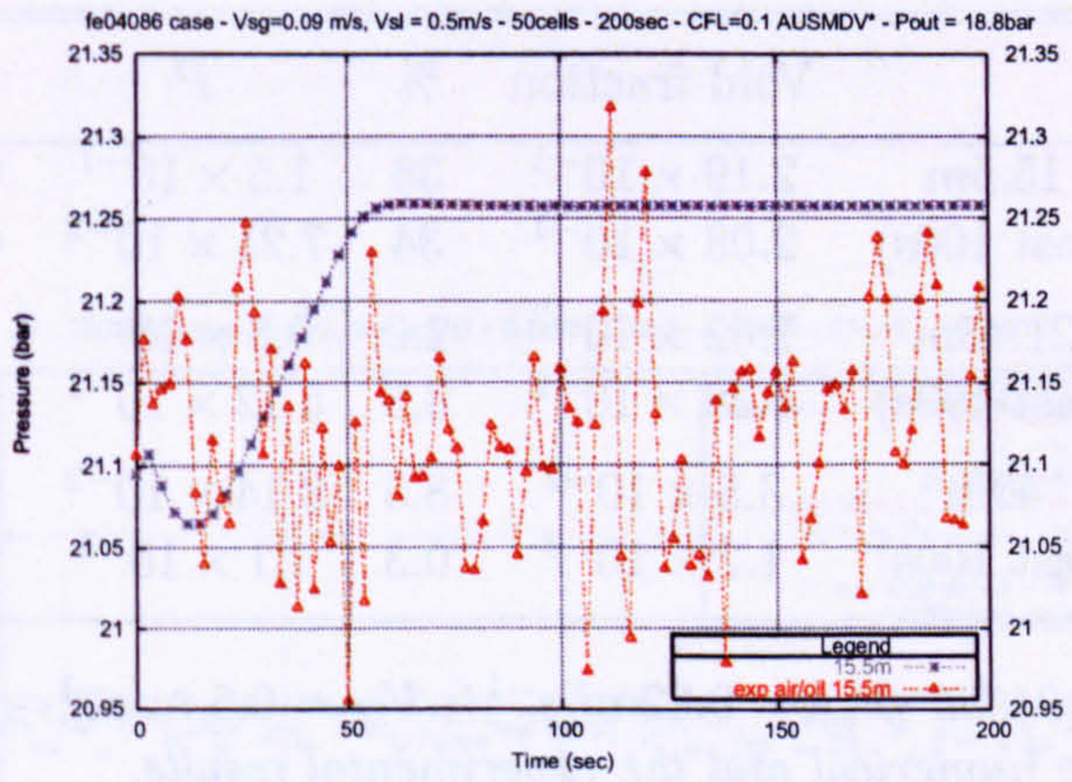

(a) 15.5m

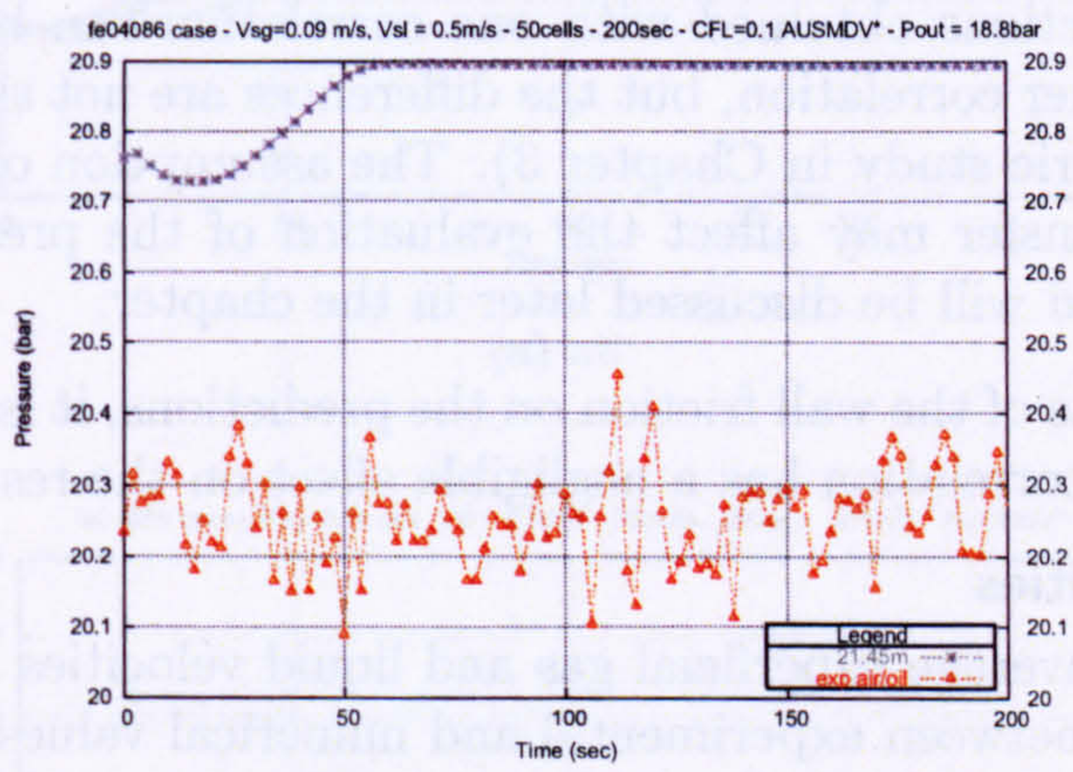

(b) 21.45m

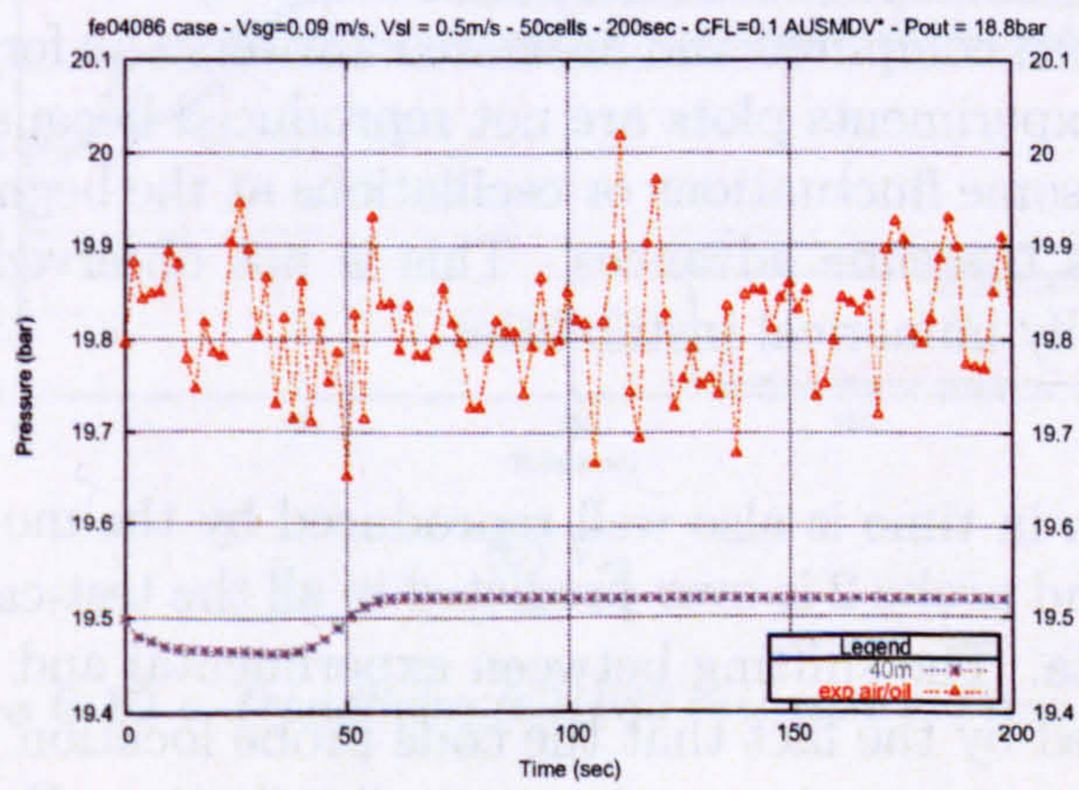

(c) 40m

Figure 6.11 : *Trondheim fe04084 test-case - Pressure time profiles.*

	Void fraction	%	P	%
$15.5m$	2.19×10^{-1}	36	1.5×10^{-1}	0.7
(last 100s)	2.08×10^{-1}	34	7.21×10^{-2}	0.4
$21.45m$	7.62×10^{-3}	2.0	5.8×10^{-1}	3
(last 100s)	1.28×10^{-2}	3.3	5.12×10^{-1}	2.6
$40m$	3.5×10^{-2}	8.5	8.14×10^{-2}	0.4
(last 100s)	1.2×10^{-3}	0.3	1.1×10^{-1}	0.5

Table 6.3 : *Testcase fe04086 ($V_{sg} = 0.32\, m.s^{-1}$ - $V_{sl} = 0.5\, m.s^{-1}$ - $P_{out} = 18.8\, bar$) - Error between the numerical and the experimental results.*

gas volume fraction. Several drag correlations have been tested and this investigation indicates that gas fractions obtained with one correlation can be higher or lower than predictions with another correlation, but the differences are not significant (as previously stated by the parametric study in Chapter 3). The assumption of the effect of buoyancy in the momentum transfer may affect the evaluation of the pressure drop and volume fraction (Fig. 6.15) and will be discussed later in the chapter.

Regarding the influence of the wall friction on the predictions, it is observed that a change in liquid wall friction correlation has a negligible effect on the results.

a. Superficial velocities

For all the cases, the average superficial gas and liquid velocities are very well predicted. The computed errors between experimental and numerical values reveal that predictions of superficial gas and liquid velocities match experimental data. Less than 2%-difference is obtained for the liquid velocity (and even less than 1% over the last 100sec of computations when the steady-state is reached). The difference for the gas velocity falls within the same error percentage between computed and measured answers. As for the other variables, the oscillations from the experiments plots are not reproduced because of the code averaging process. There is also some fluctuations or oscillations at the beginning of the simulations which are flattened as the time advances. This is not observed experimentally and is believed to be caused by numerical instabilities.

b. Pressure

The pressure evolution in time is also well reproduced by the model. Although the pressure level at probe 1 and probe 2 is over-predicted in all the test-cases, the trends compare favorably with the data. The shifting between experimental and numerical values at the probes can be explained by the fact that the code probe location might be slightly different from the experimental ones due to the mesh distribution. However it is not believed that the slight variation that may occur could yield such result. It also has to be noticed that the equation of state (EOS) used in the present model to represent the fluid thermodynamic properties might not be as accurate as other EOS such as the van der Walls

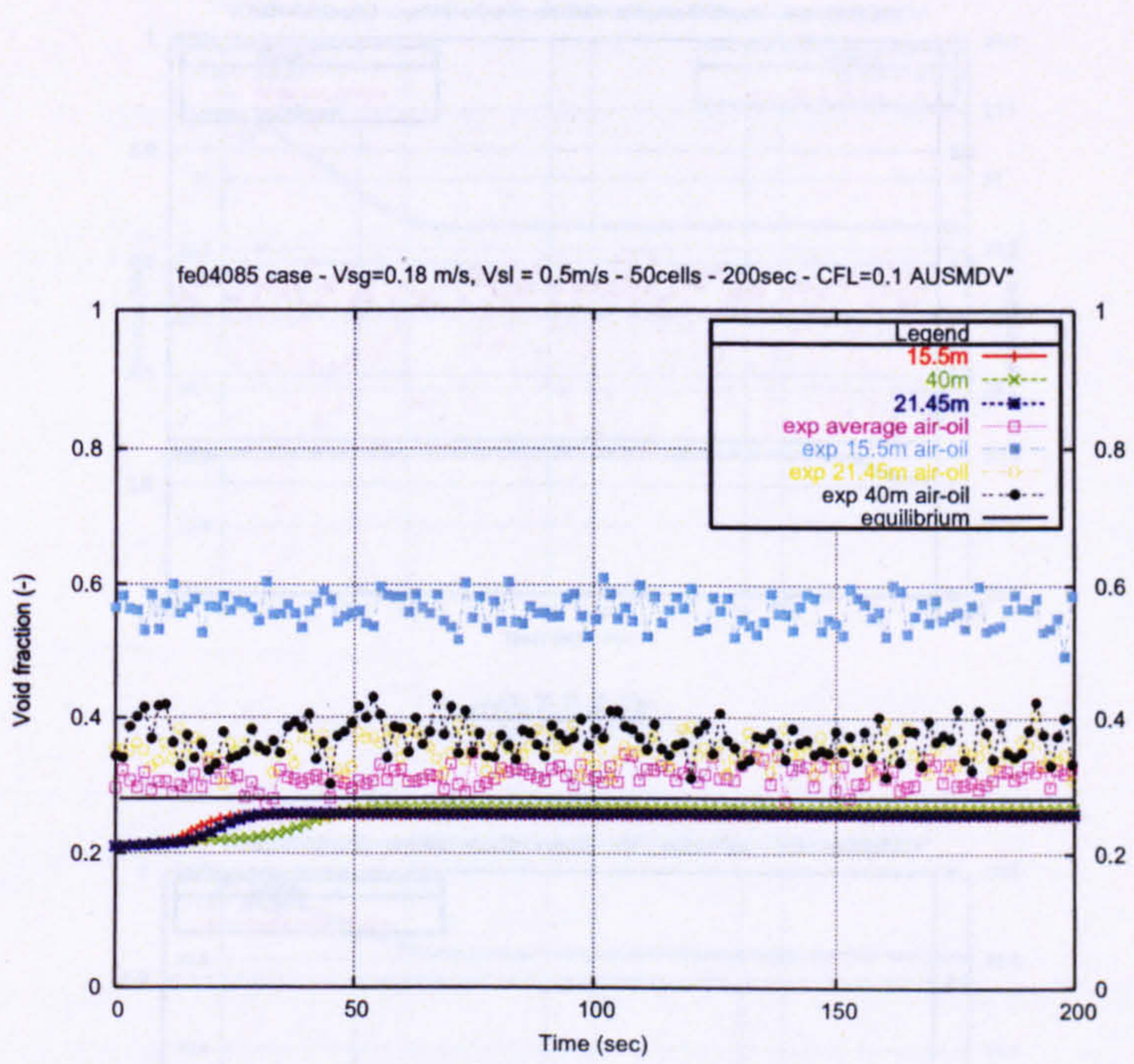

(a) all

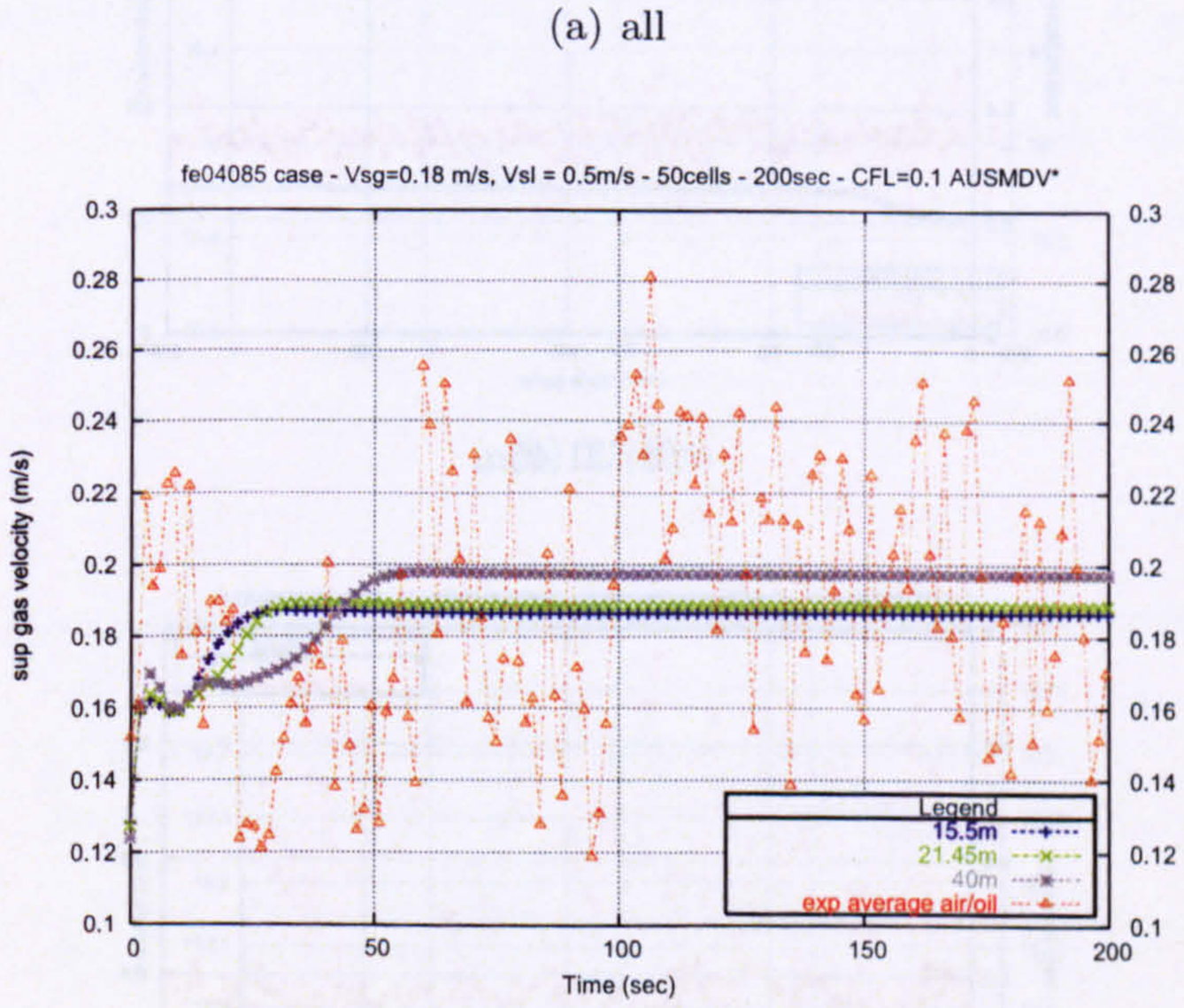

(b) V_{sg}

Figure 6.12 : *Trondheim fe04085 test-case - Time profiles.*

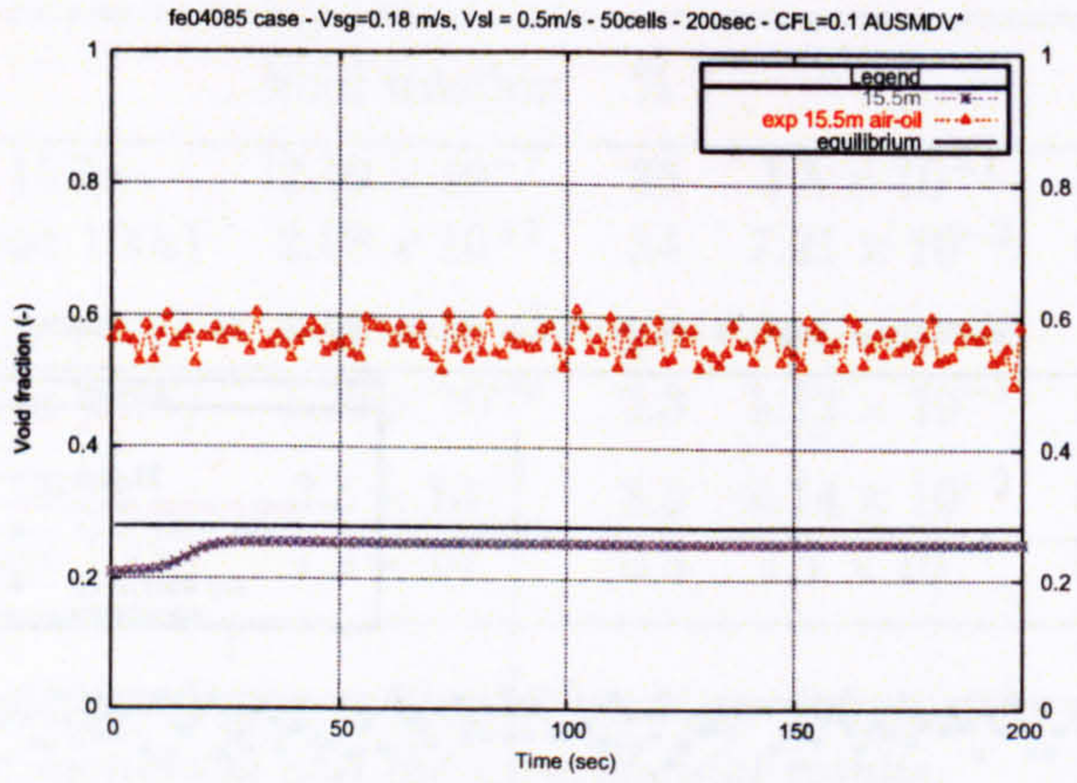

(a) 15.5m

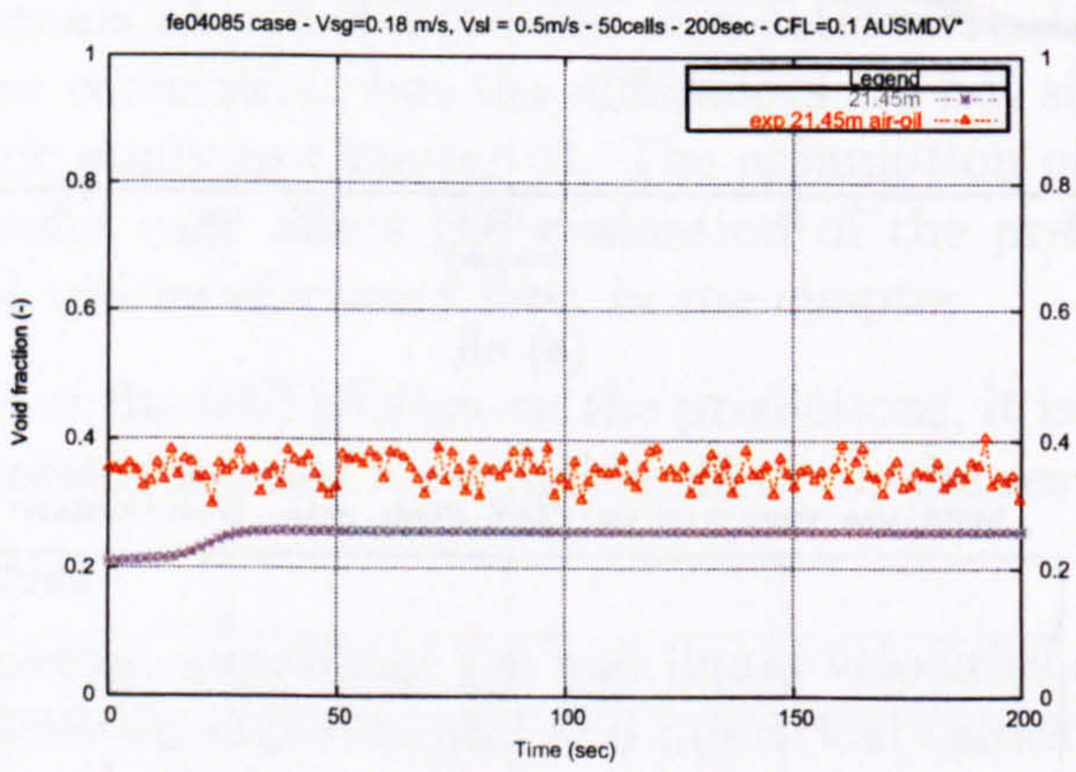

(b) 21.45m

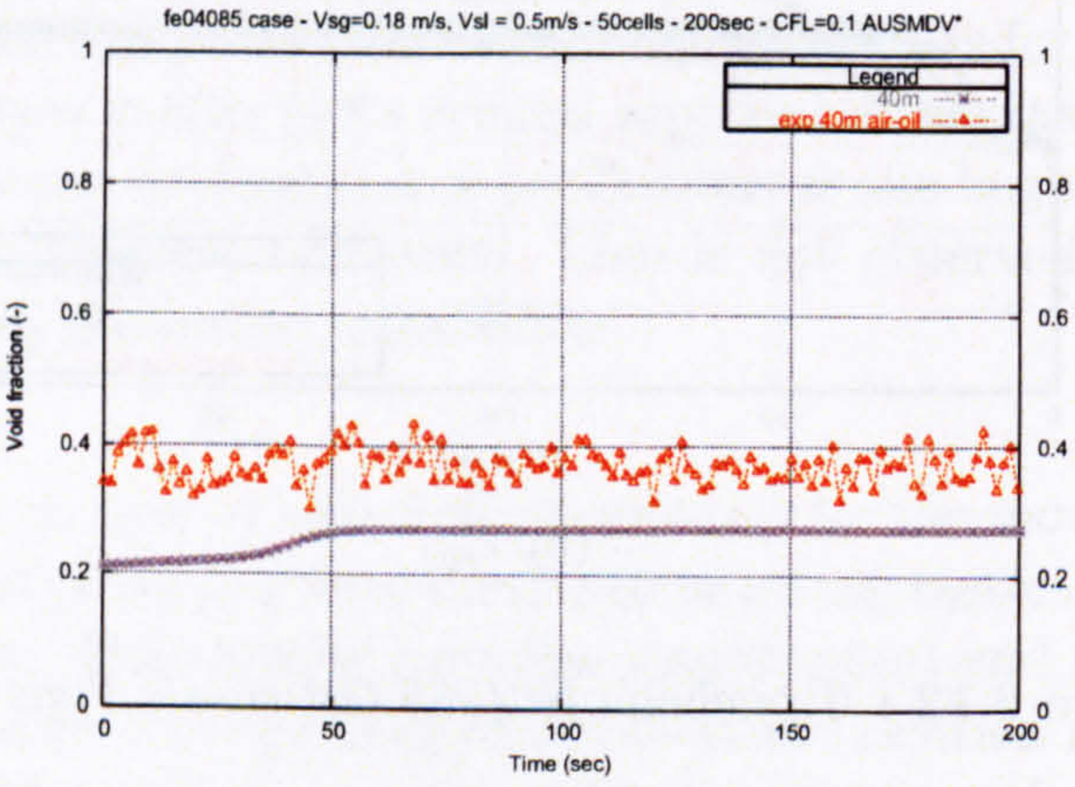

(c) 40m

Figure 6.13 : *Trondheim fe04085 test-case - Void fraction time profiles.*

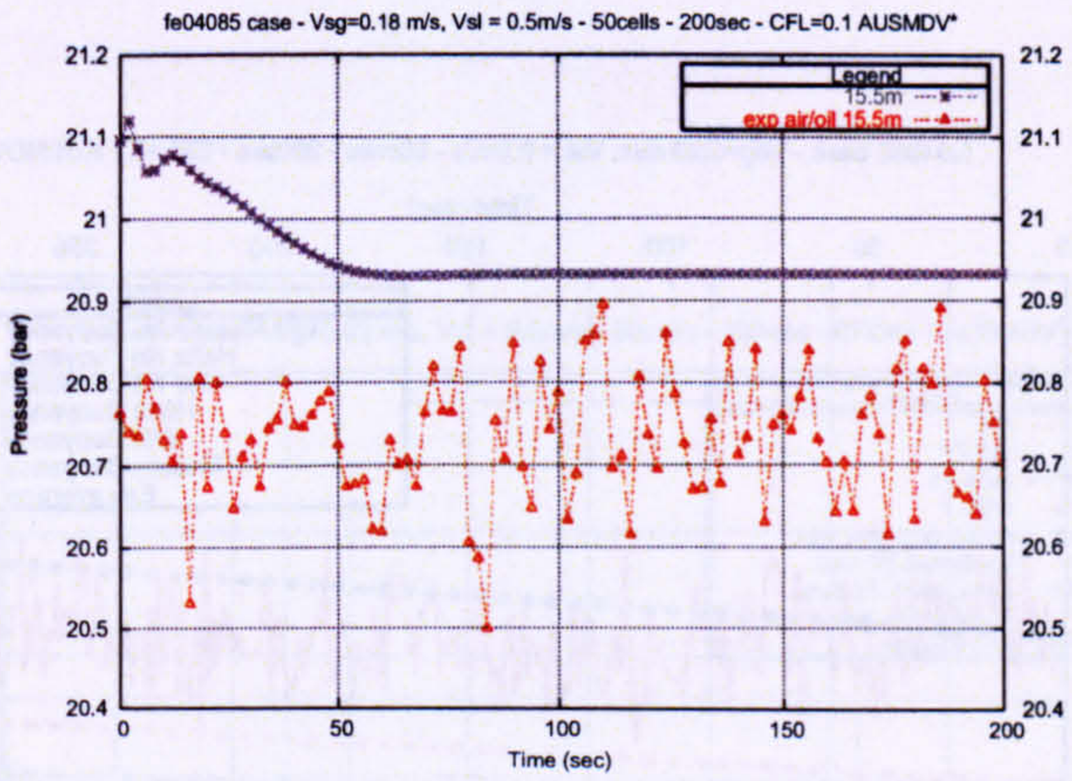

(a) 15.5m

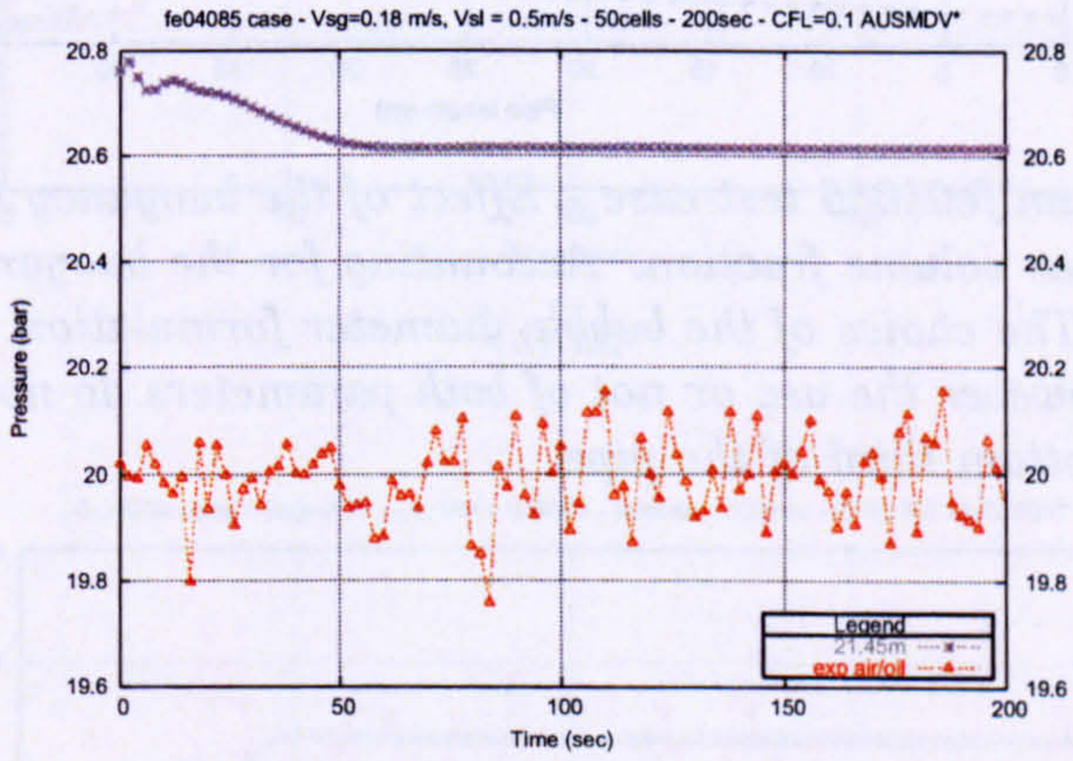

(b) 21.45m

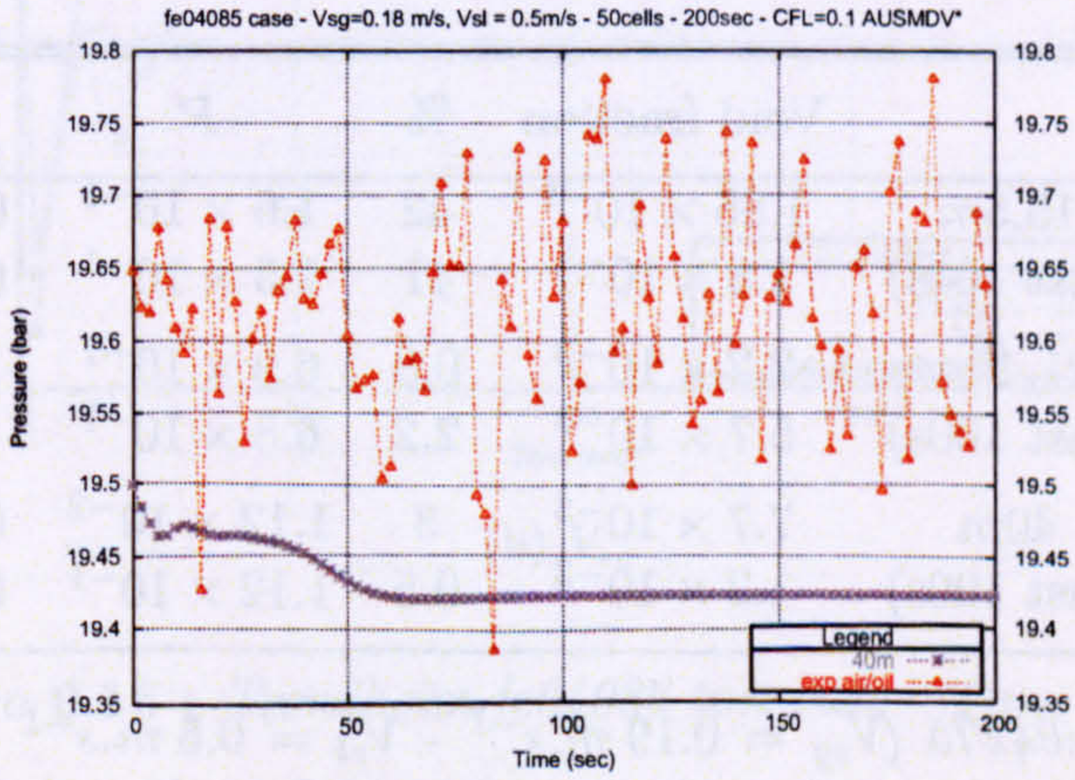

(c) 40m

Figure 6.14 : *Trondheim fe04085 test-case - Pressure time profiles.*

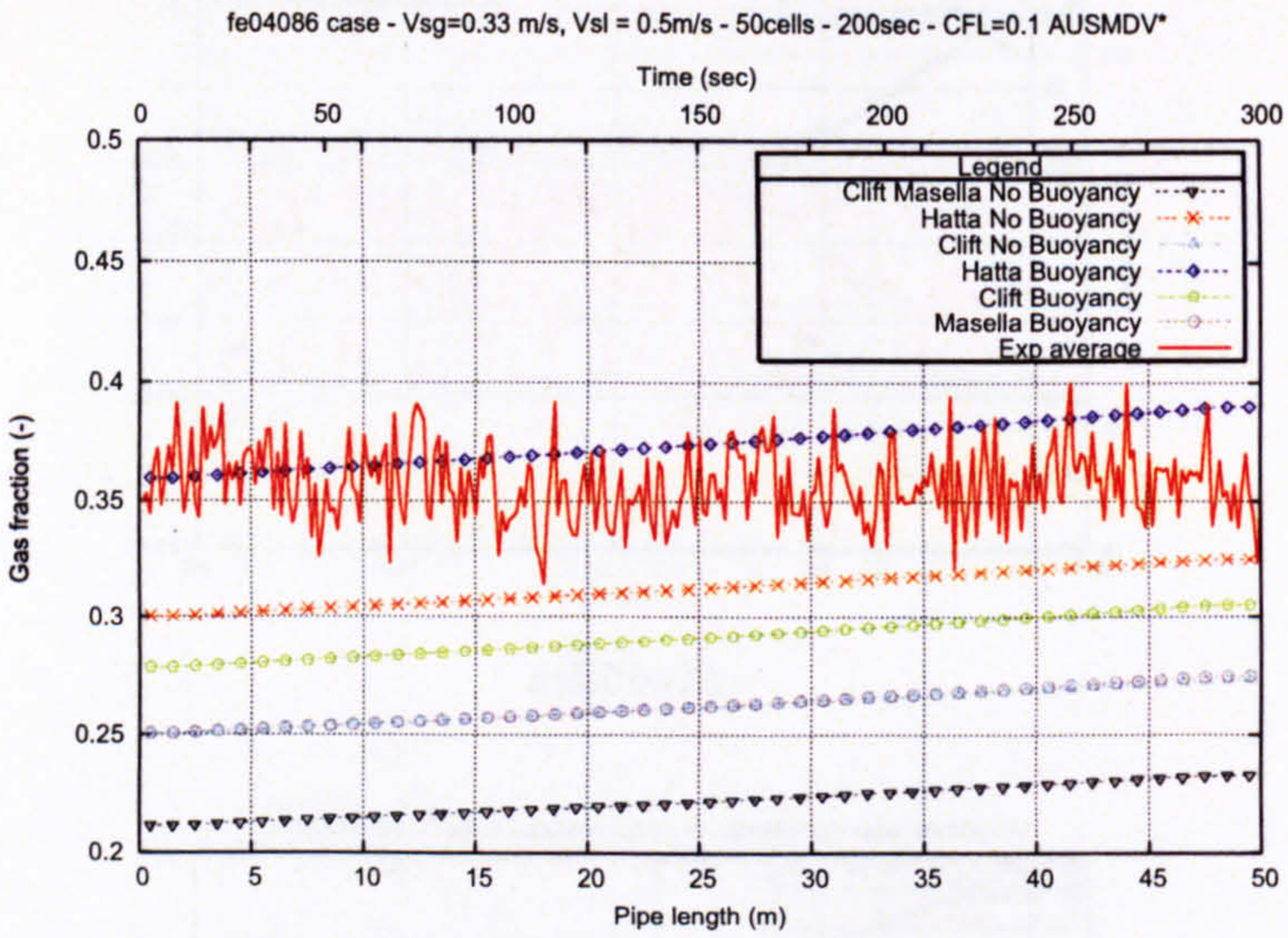

Figure 6.15 : *Trondheim fe04086 test-case - Effect of the buoyancy term and bubble diameter on the gas volume fraction. Accounting for the buoyancy lowers the predictions values. The choice of the bubble diameter formulation creates some variation as well. However the use or not of both parameters do not create the extra amount in the bottom third of the pipe.*

	Void fraction	%	P	%
$15.5m$	1.85×10^{-1}	42	1.6×10^{-1}	0.17
(last 100s)	1.8×10^{-1}	41	1.5×10^{-1}	0.16
$21.45m$	2.2×10^{-3}	0.8	6.9×10^{-1}	0.7
(last 100s)	5.7×10^{-3}	2.2	6.8×10^{-1}	0.7
$40m$	7.7×10^{-3}	3	1.12×10^{-2}	0.12
(last 100s)	1.2×10^{-3}	0.5	1.12×10^{-1}	0.12

Table 6.4 : *Testcase fe04275 ($V_{sg} = 0.19\ m.s^{-1}$ - $V_{sl} = 0.5\ m.s^{-1}$ - $P_{out} = 89\ bar$) - Error between the numerical and the experimental results.*

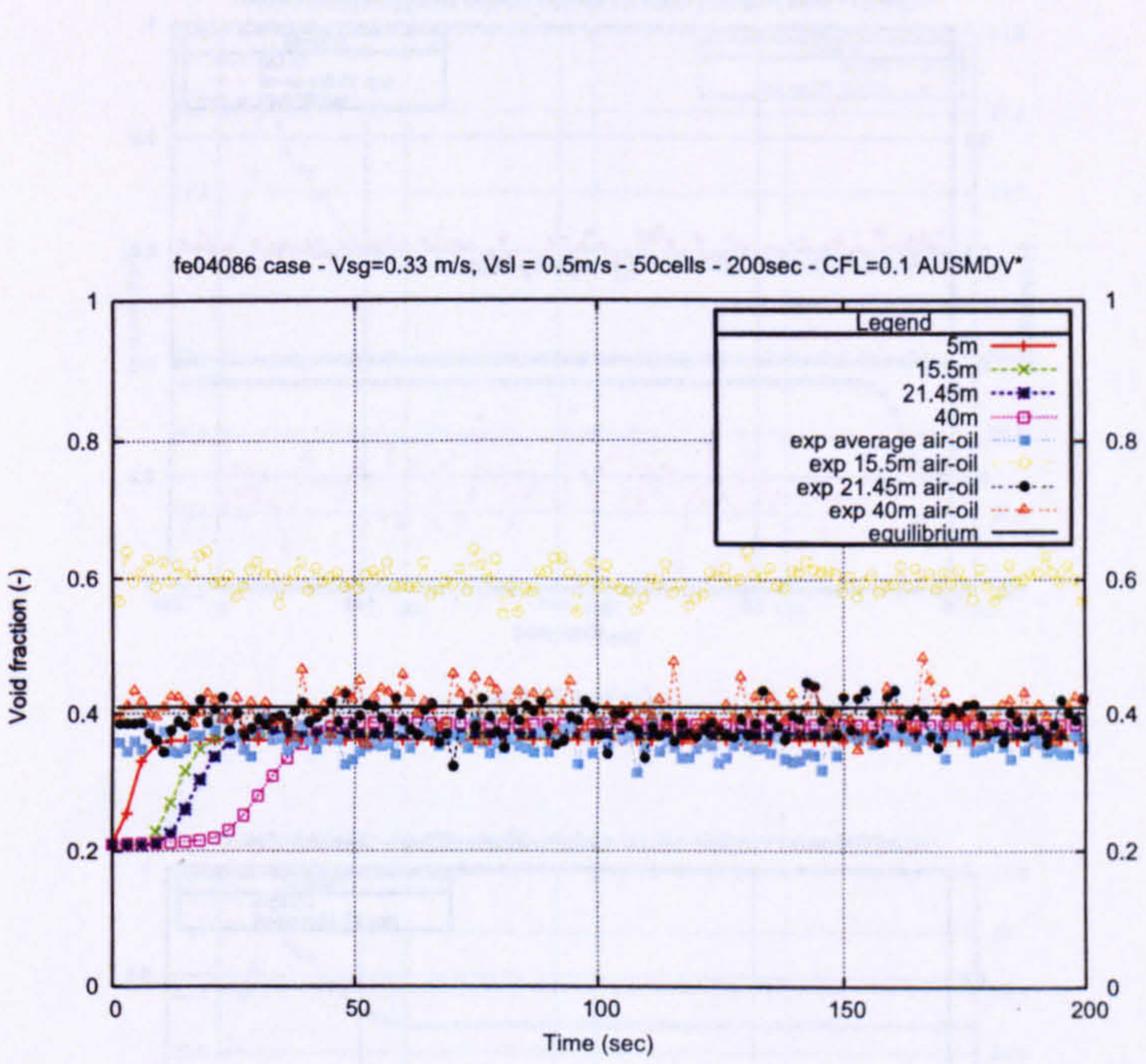

(a) all

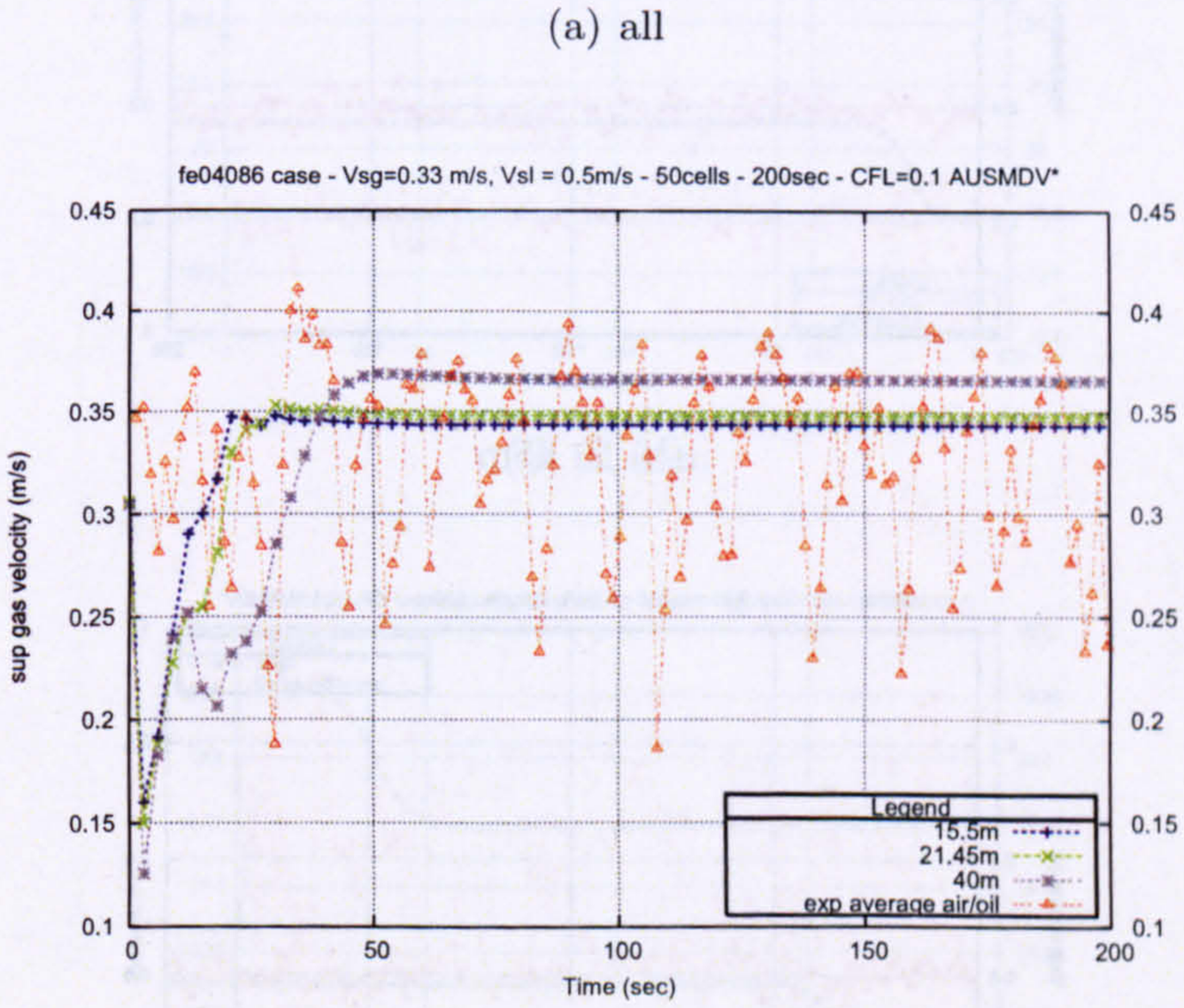

(b) V_{sg}

Figure 6.16 : *Trondheim fe04086 test-case - Time profiles.*

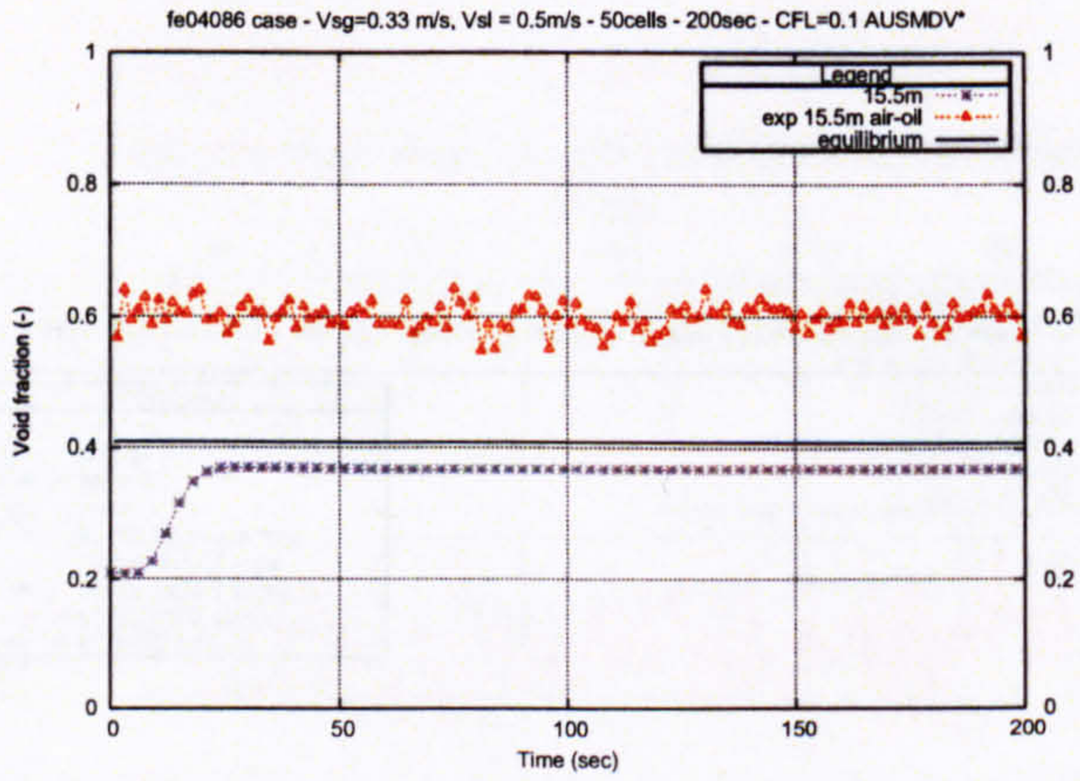

(a) 15.5m

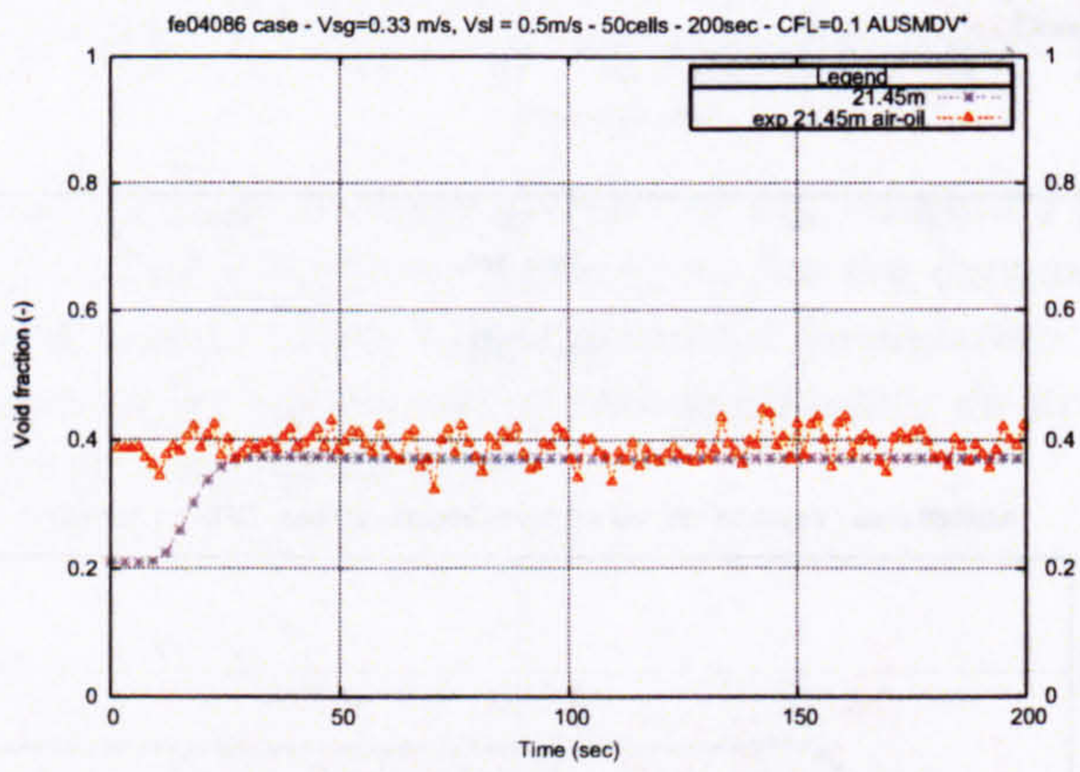

(b) 21.45m

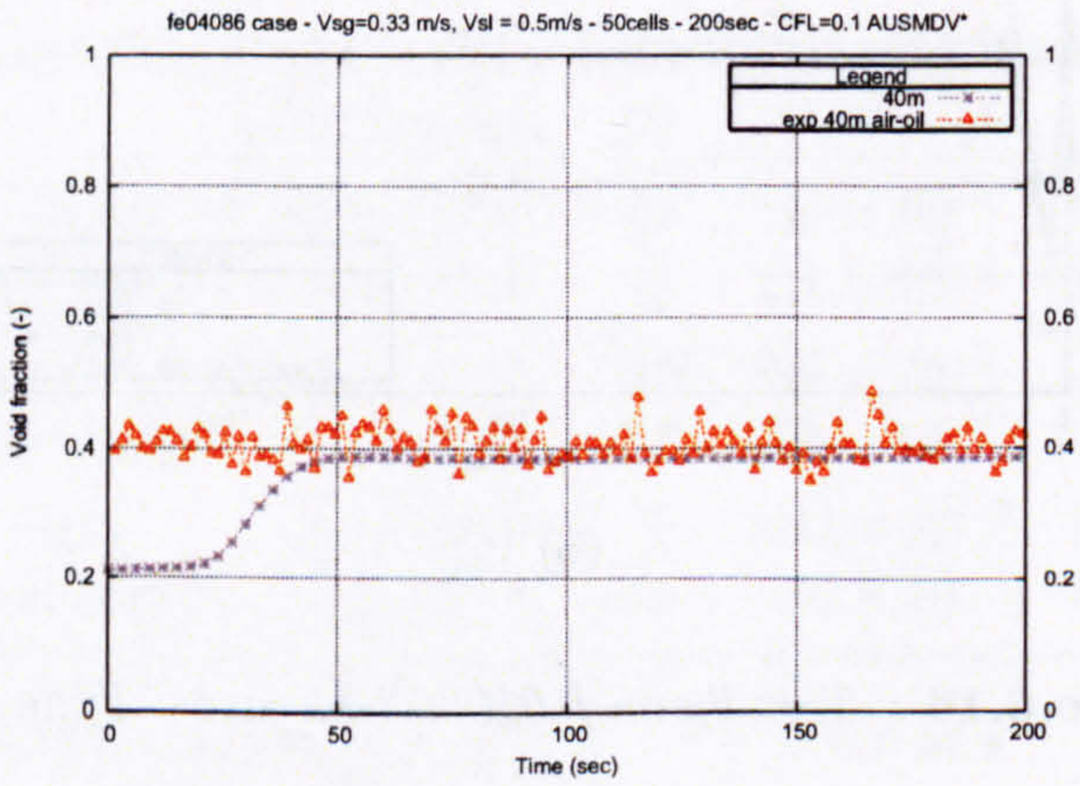

(c) 40m

Figure 6.17 : *Trondheim fe04086 test-case - Void fraction time profiles.*

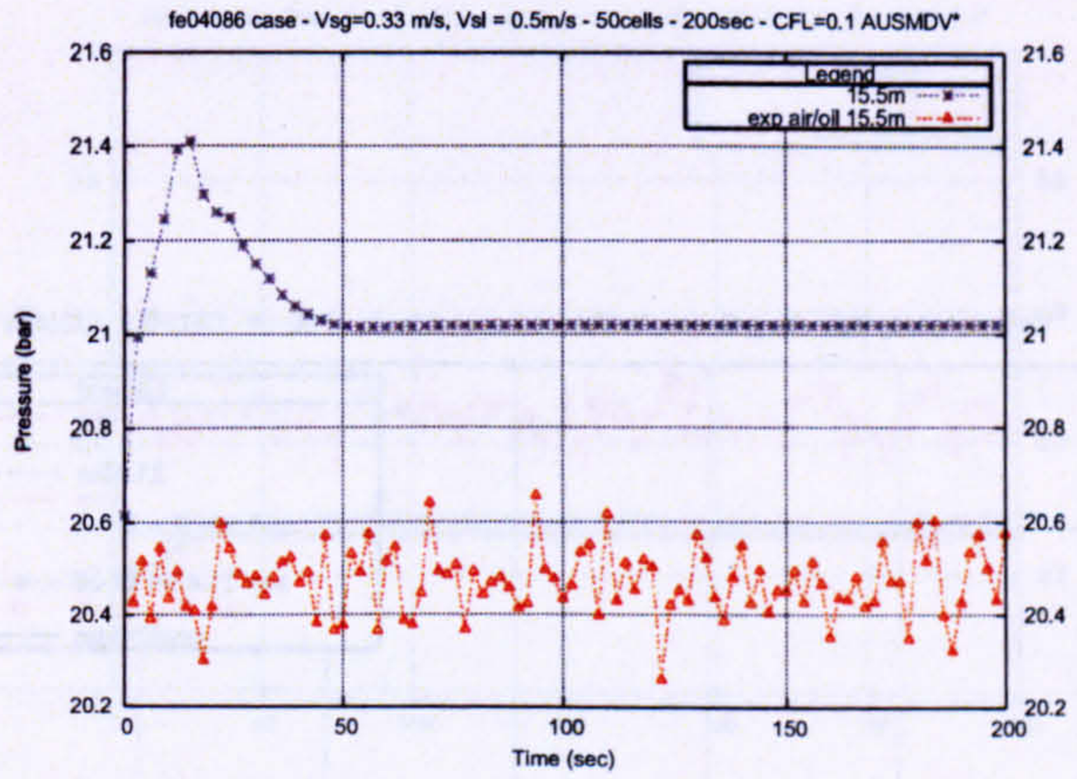

(a) 15.5m

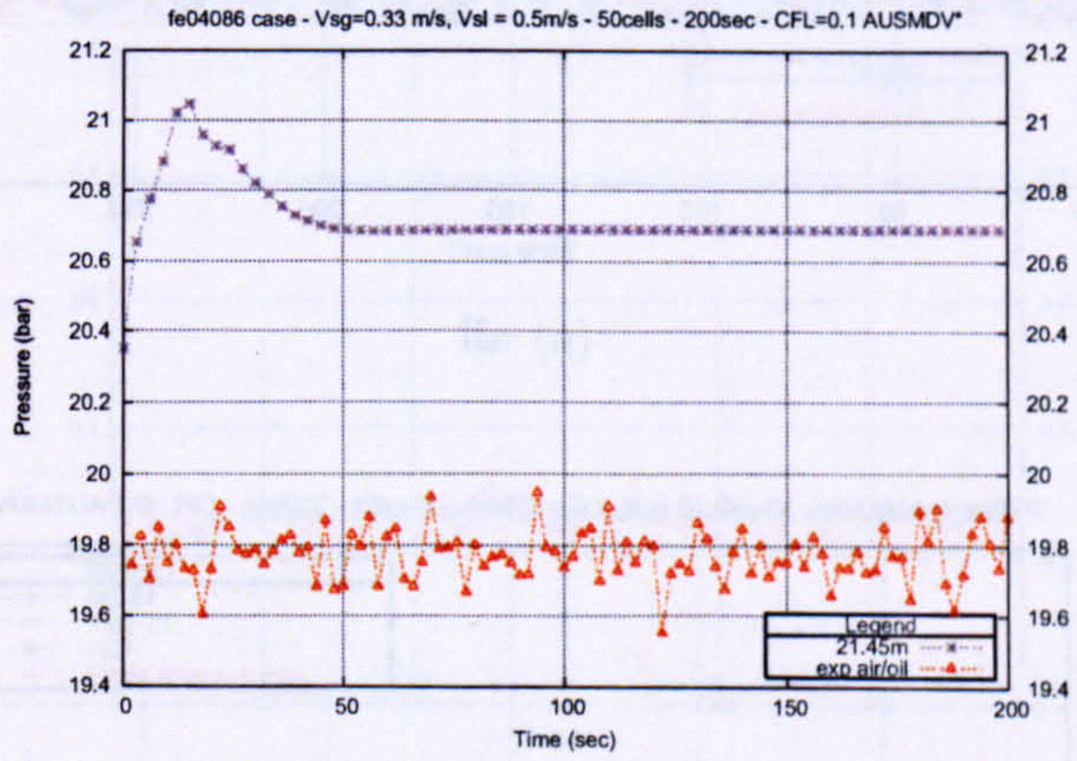

(b) 21.45m

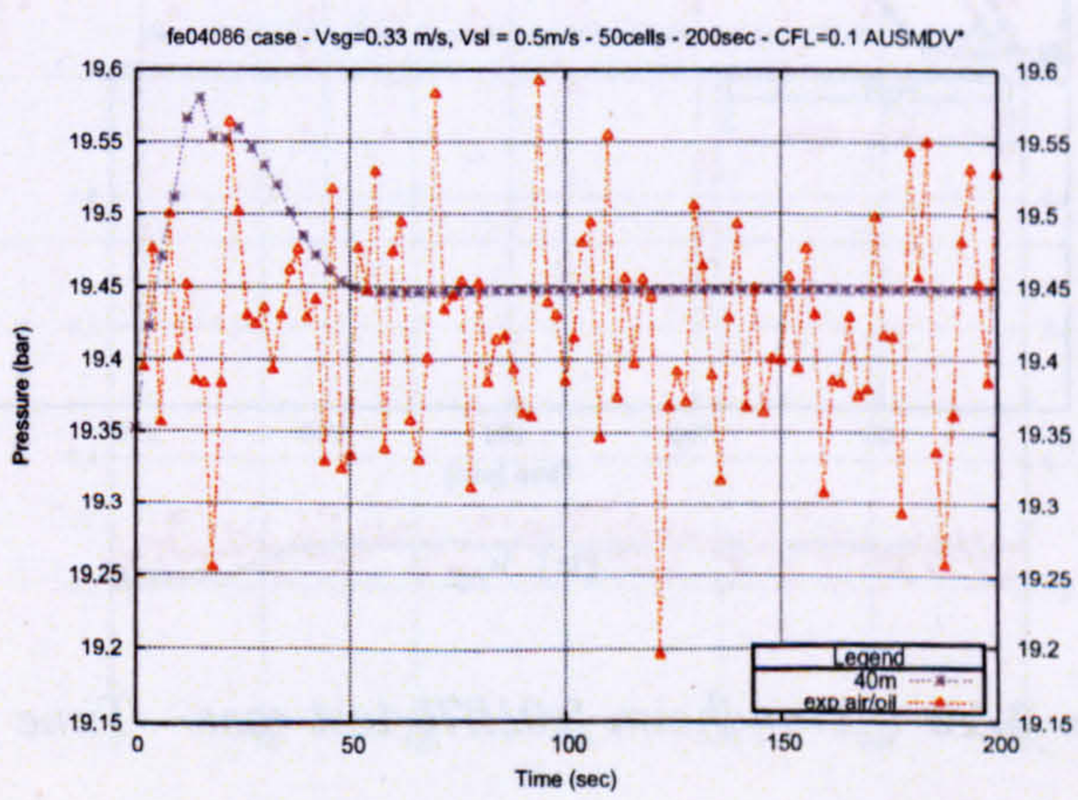

(c) 40m

Figure 6.18 : *Trondheim fe04086 test-case - Pressure time profiles.*

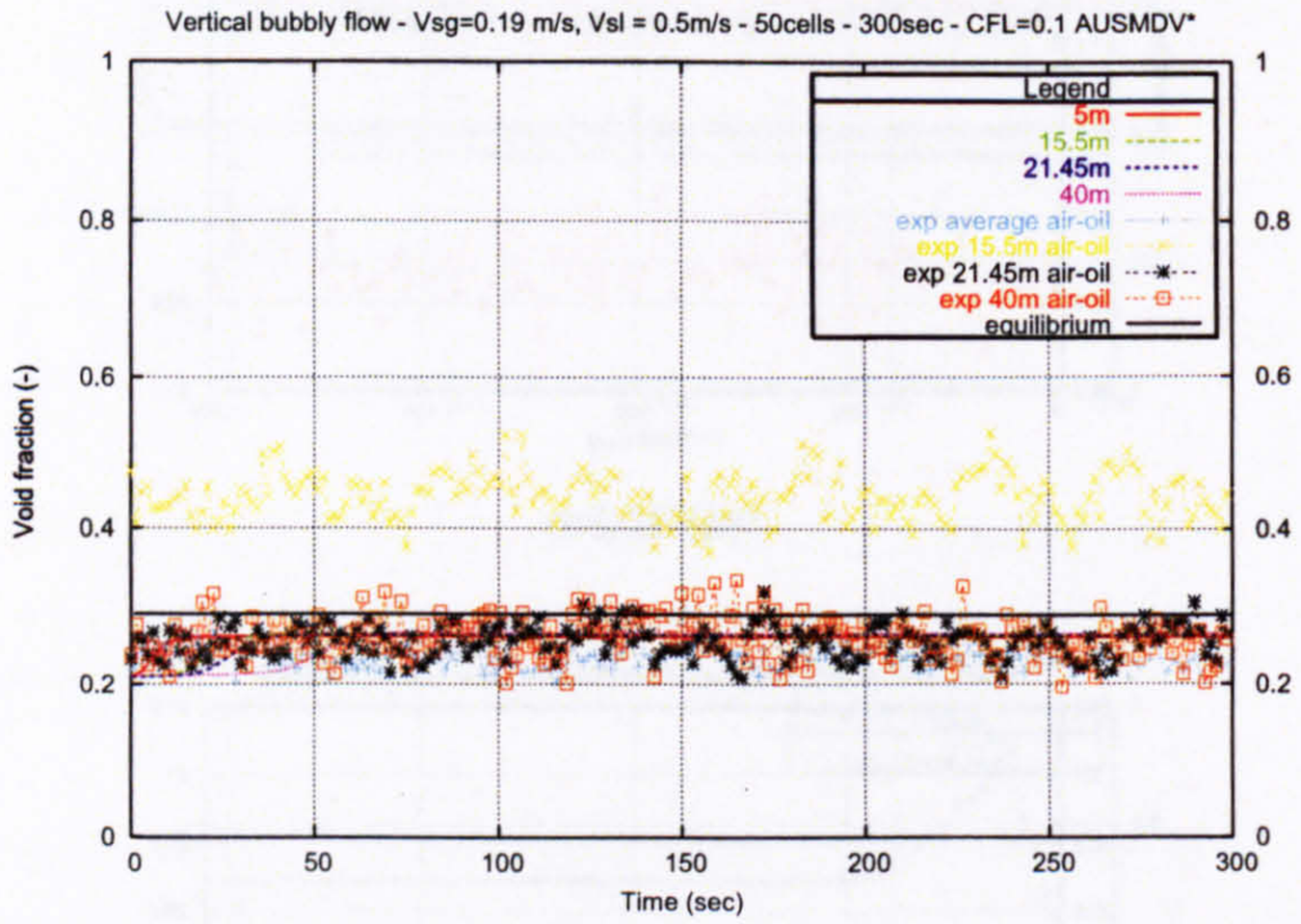

(a) all

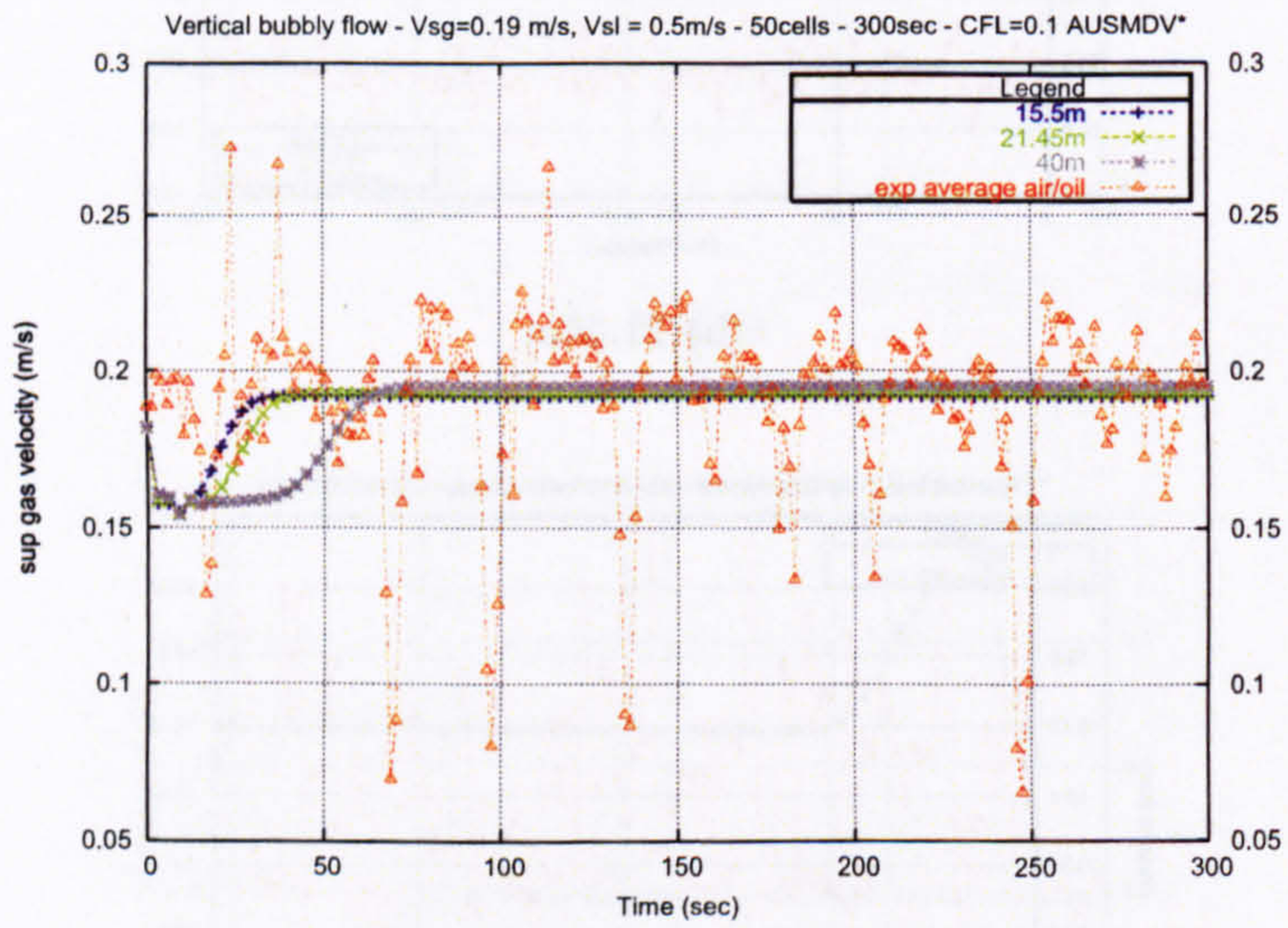

(b) V_{sg}

Figure 6.19 : *Trondheim fe04275 test-case - Time profiles.*

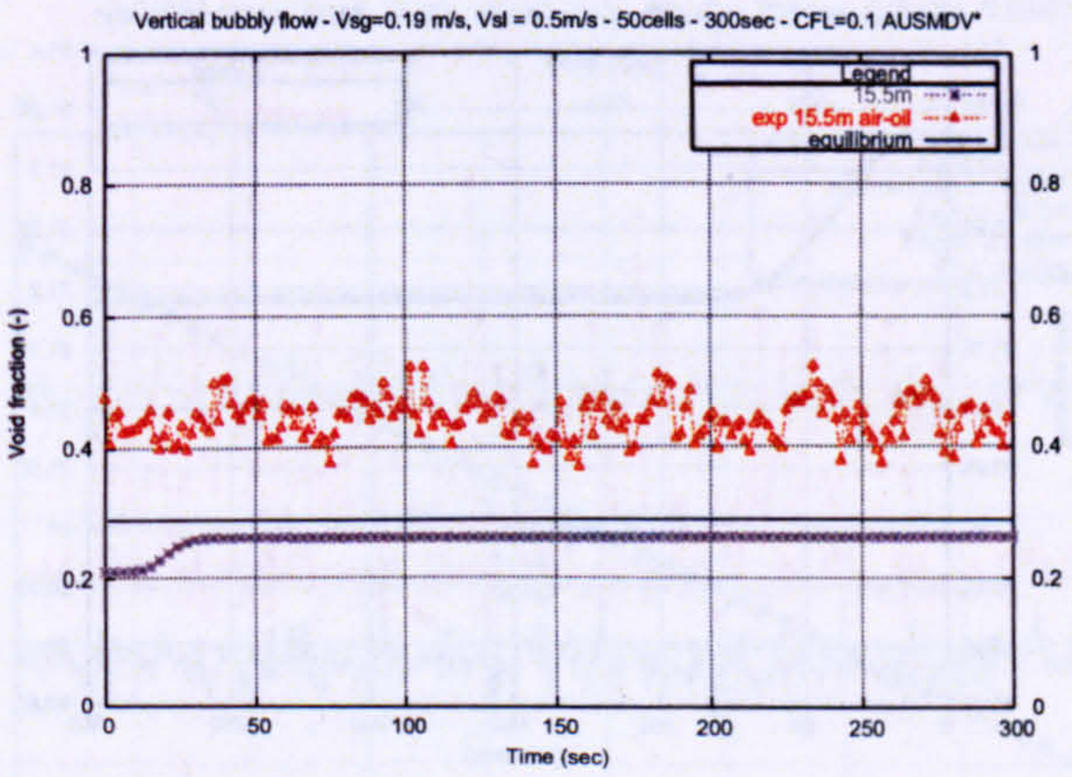

(a) 15.5m

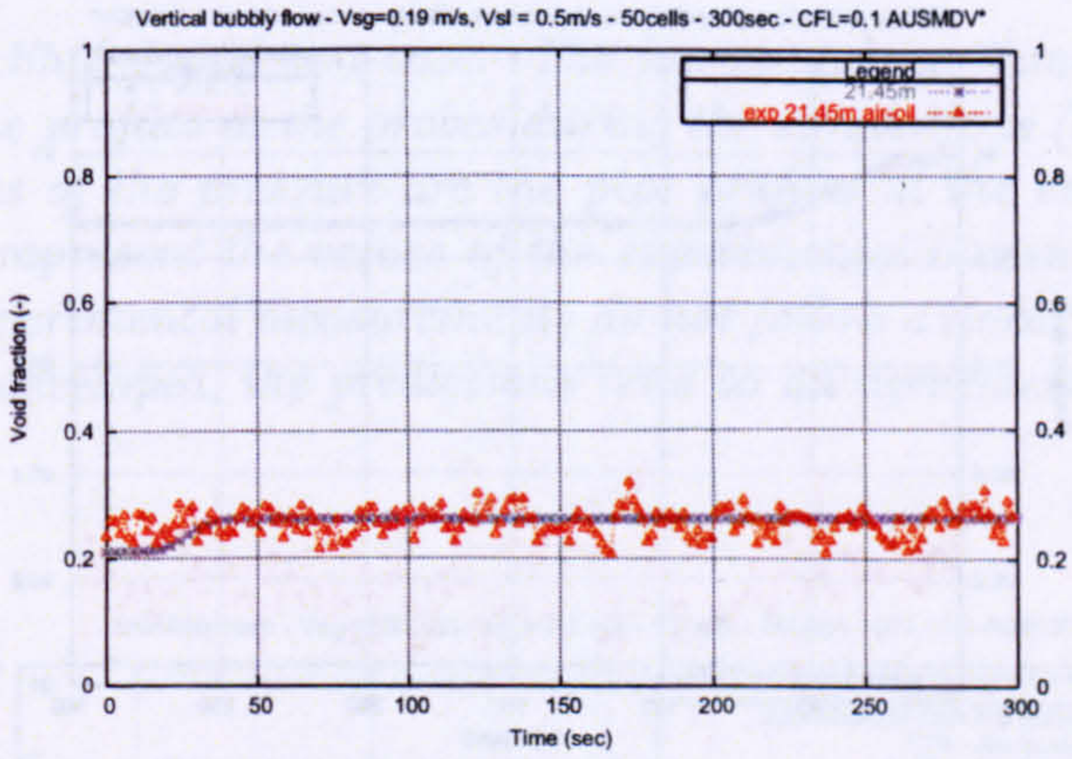

(b) 21.45m

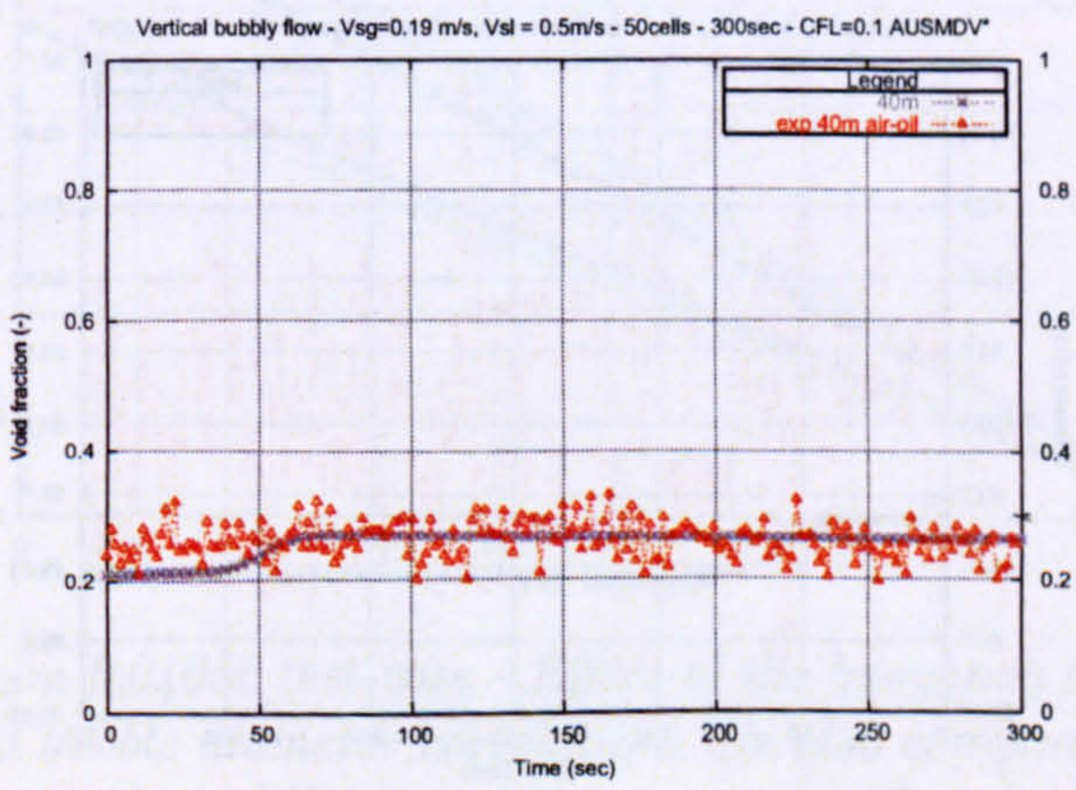

(c) 40m

Figure 6.20 : *Trondheim fe04275 test-case - Void fraction time profiles.*

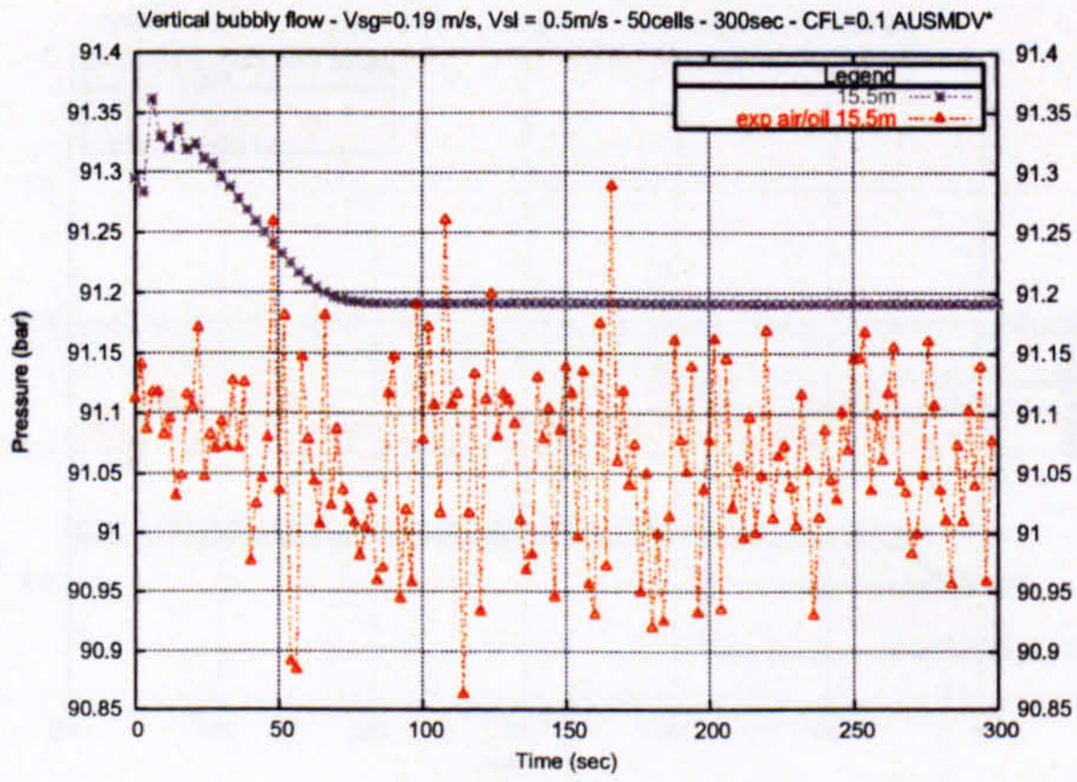

(a) 15.5m

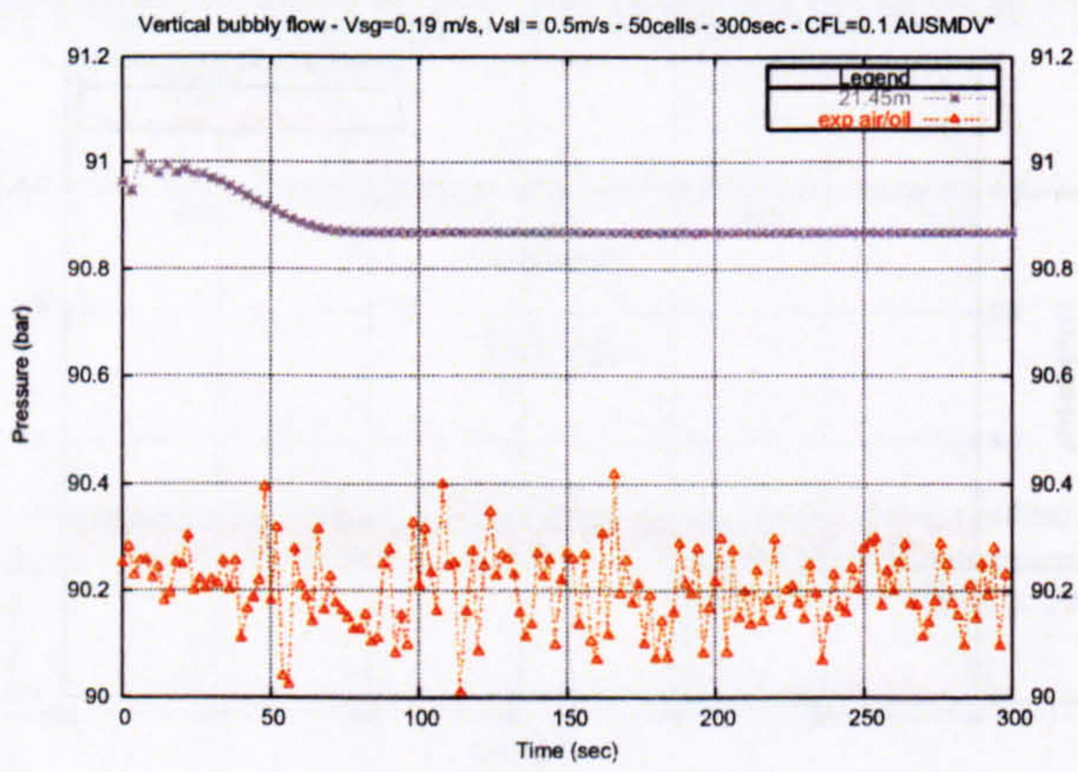

(b) 21.45m

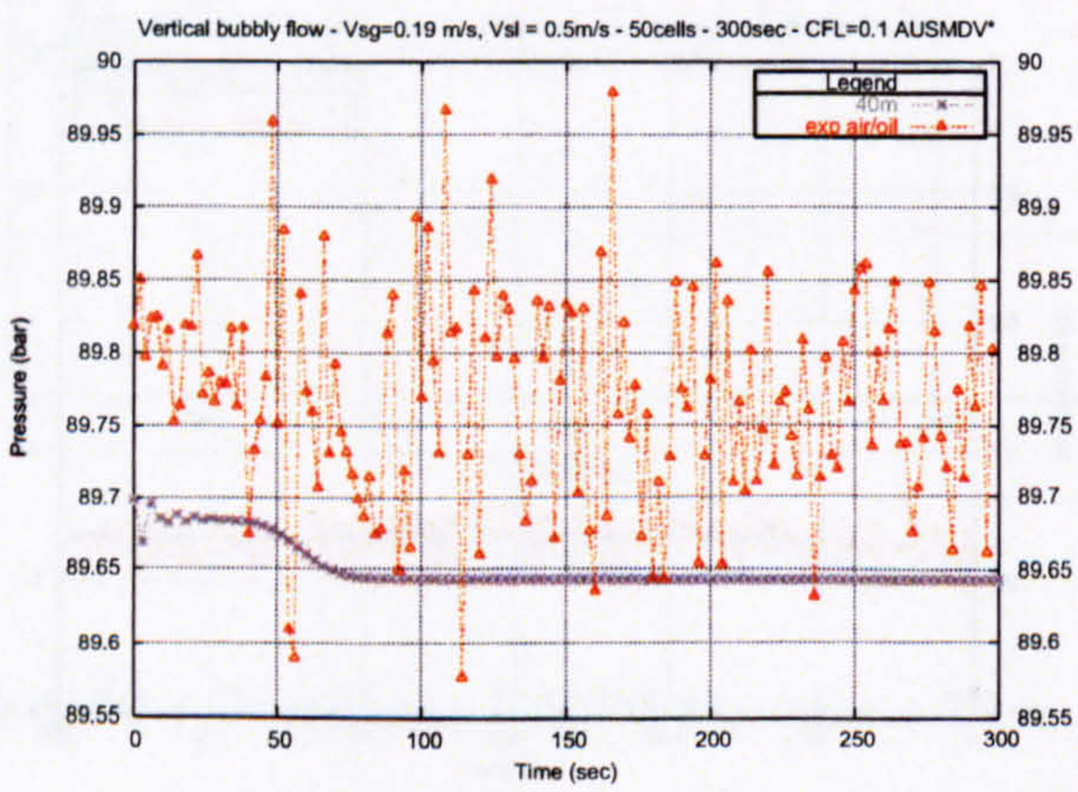

(c) 40m

Figure 6.21 : *Trondheim fe04275 test-case - Pressure time profiles.*

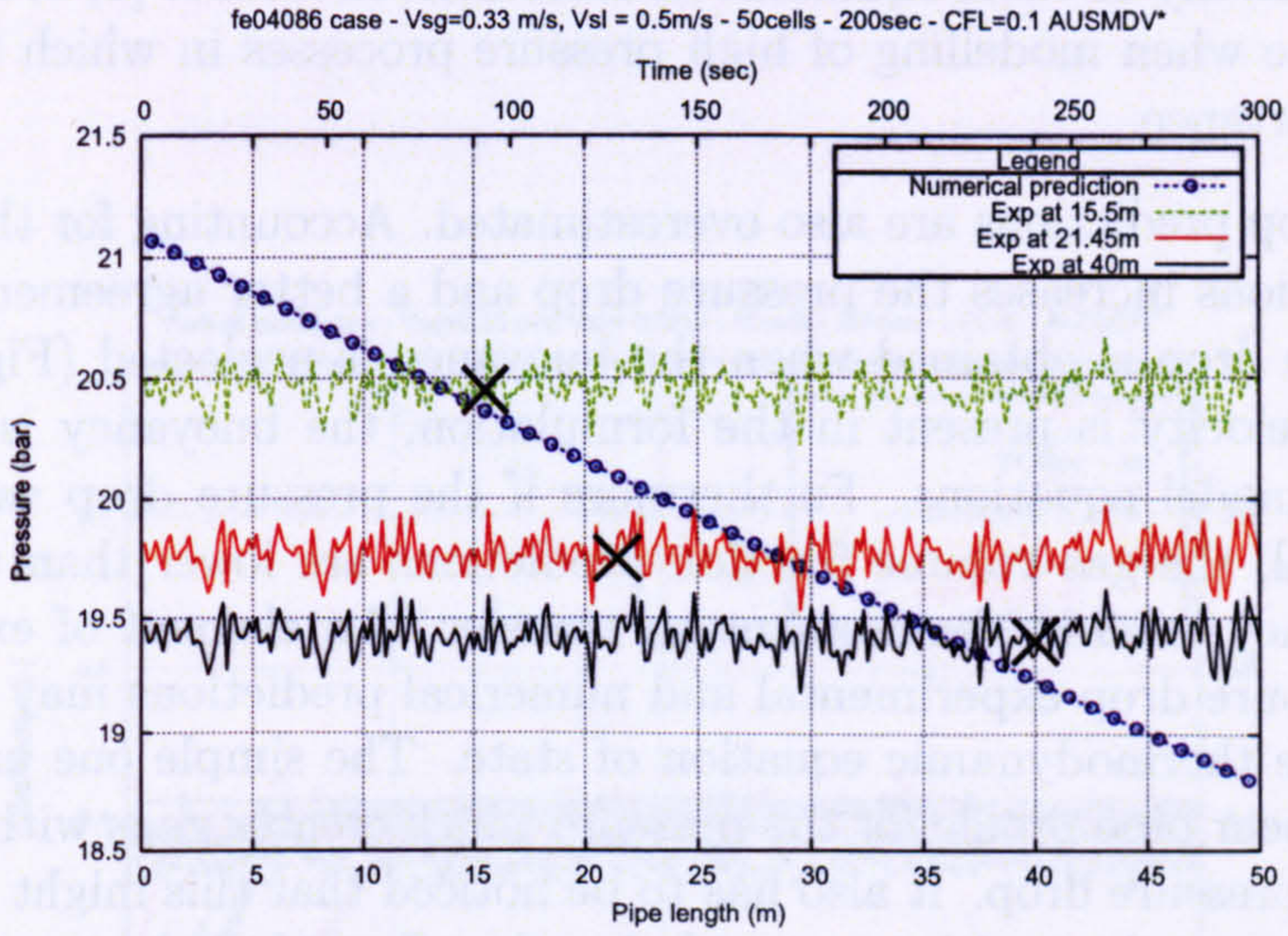

Figure 6.22 : *Trondheim fe04086 test-case. The horizontal experimental values are the pressure time profiles at the probes during the simulations (top x-axis). The predicted measures of the pressure are the pipe profiles at the end of the simulation. The crosses represent the values of the experimental measurements at the probe location: experimental measurements do not follow a linear evolution. When the flow is fully developed, the predictions tend to an agreement with the measurements.*

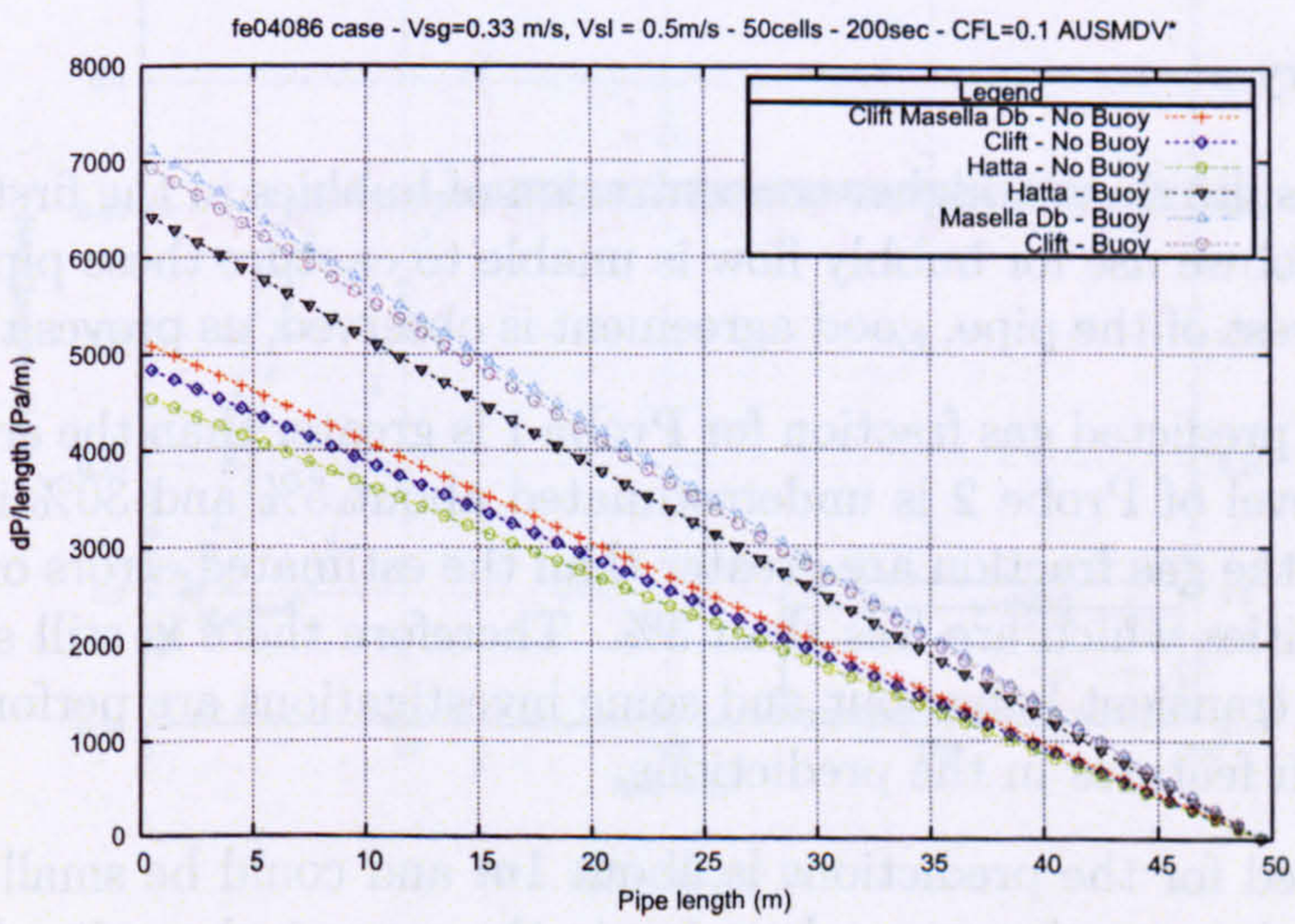

Figure 6.23 : *Trondheim fe04086 test-case - Effect of the buoyancy term on the pressure drop. Different bubble diameter correlations are also compared. The effect of the buoyancy does make a difference and is more significant than the choice of the bubble diameter formulation. But this significance is relative to the pressure, and volume fraction results do not allow to draw the same conclusions.*

equation or the family of cubic equations of state derived from it [3, 4, 1] which proved to be more accurate when modelling of high pressure processes in which the density of the liquid is of importance.

The pressure drop predictions are also overestimated. Accounting for the buoyancy effect in the computations increases the pressure drop and a better agreement with the experimental pressure drop is obtained when the buoyancy is neglected (Fig. 6.22). However as the bubble velocity is present in the formulation, the buoyancy is to be taken into account in the model equations. Furthermore if the pressure drop values are closer to the experimental, the gas volume fraction predictions are lower than the ones obtained with the buoyancy term in the momentum transfer. An element of explanation for the variance of pressure drop experimental and numerical predictions may again be found in the choice of the thermodynamic equation of state. The simple one used in the present model gives a linear pipe profile for the pressure which creates gaps with the experimental answers for the pressure drop. It also has to be noticed that this might explain the better prediction of pressure drop without considering the effect of the buoyancy only because of the linearity of the pressure trend. It therefore yields to some restrictions in the pressure drop estimation with difference of up to 49% (Fig. 6.23). The addition of the buoyancy term in the equations is therefore subject to interpretation. If it does improve the volume fraction predictions by Fig. 6.15, the pressure predictions are less accurate with its account than without. Therefore its presence in the results is interesting but its introduction in the model is not primordial. We conserve it for the simulations presented in the thesis, bearing in mind its behaviour in the prediction of both volume fraction and pressure.

6.4.5 Summary

Experimental results show a higher concentration of bubbles in the first third of the pipe. The simple model we use for bubbly flow is unable to capture these pipe entrance effects. However in the rest of the pipe, good agreement is observed, as proves the error Table 6.3.

The error in the predicted gas fraction for Probe 1 is greater than the error in Probe 2 and Probe 3. The level of Probe 2 is underestimated about 5% and 30% in the worst cases. These errors on the gas fraction are greater than the estimated errors on the pressure and superficial velocities which are less than 3%. Therefore there is still some improvement to make for the transient behaviour and some investigations are performed to determine the cause of such features in the predictions.

The grid size used for the predictions is about $1m$ and could be small enough to resolve the interface motion, causing some damping in the numerical results. However computations done with finer meshes and smaller time steps also lead to the same answers in the pressure and void fraction profiles.

The influence of the interfacial shear stress has been investigated. Various variations on the interfacial drag coefficients have been examined. As one may expect, when dividing the actual interfacial coefficient by ten, less drag force implies for the bubbles to travel

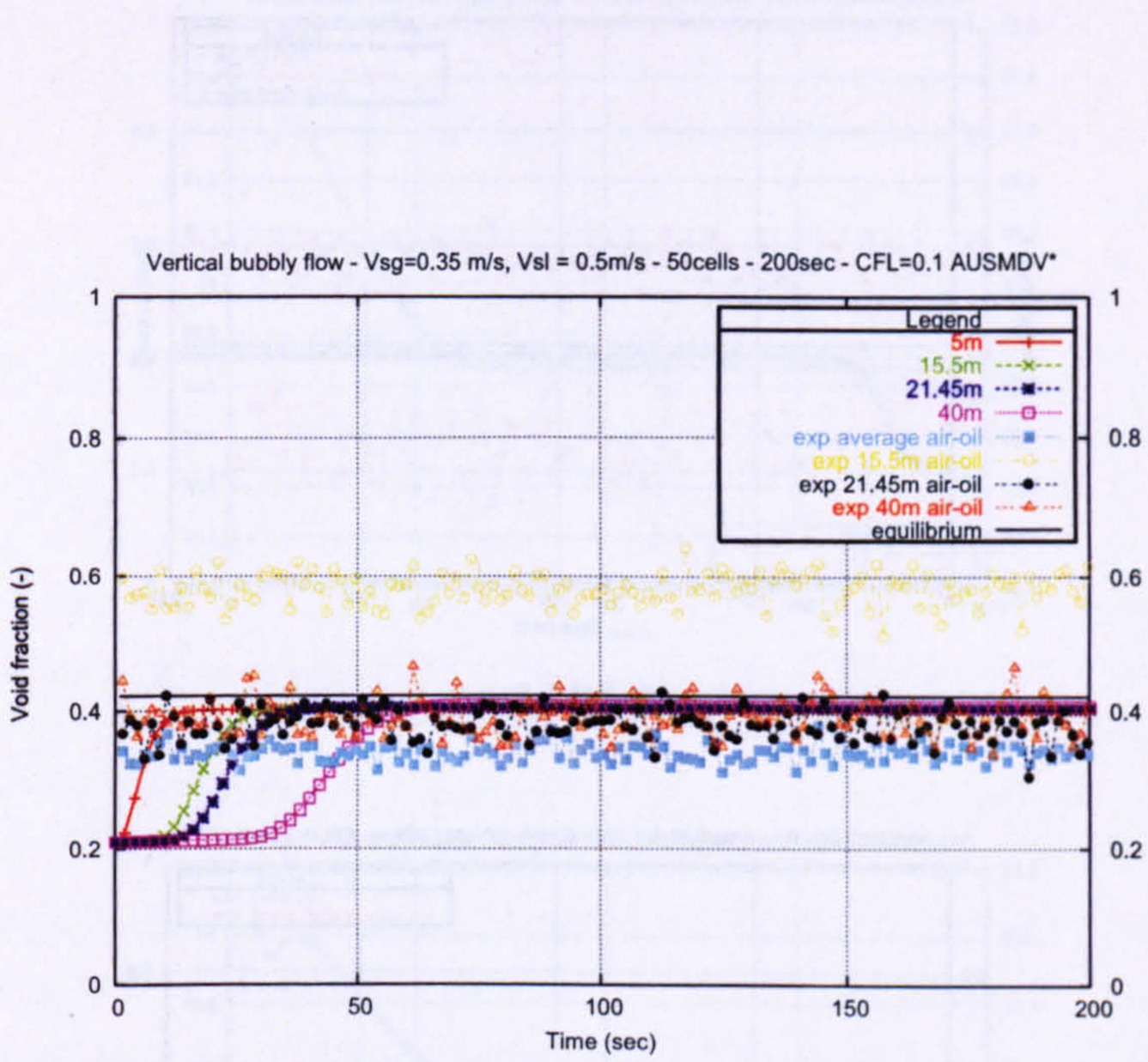

(a) all

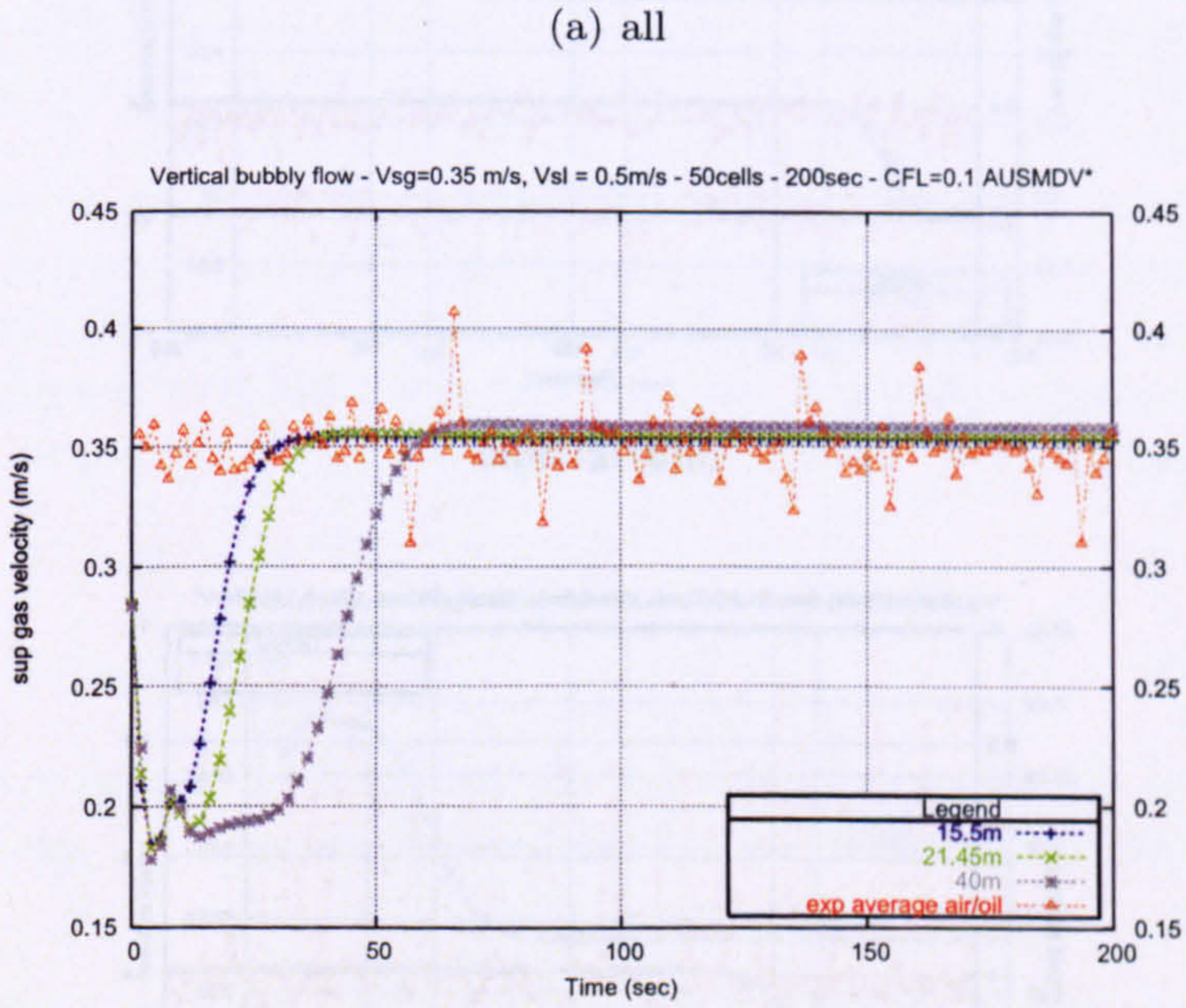

(b) V_{sg}

Figure 6.24 : *Trondheim fe04276 test-case - Time profiles.*

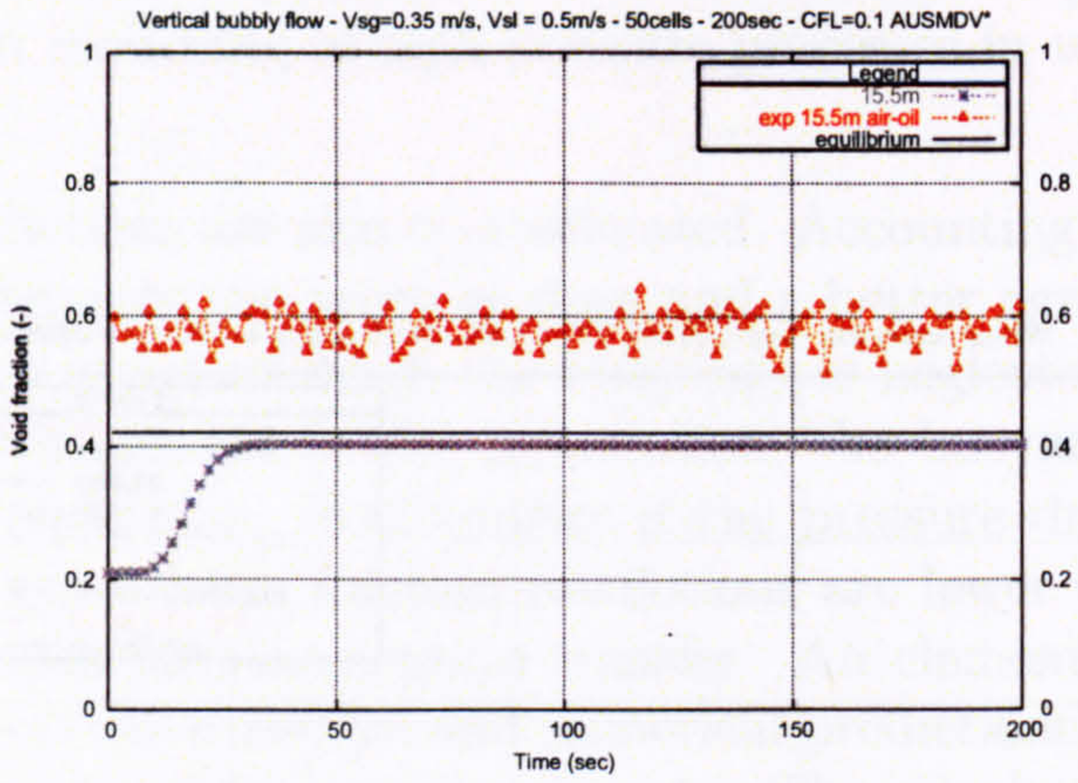

(a) 15.5m

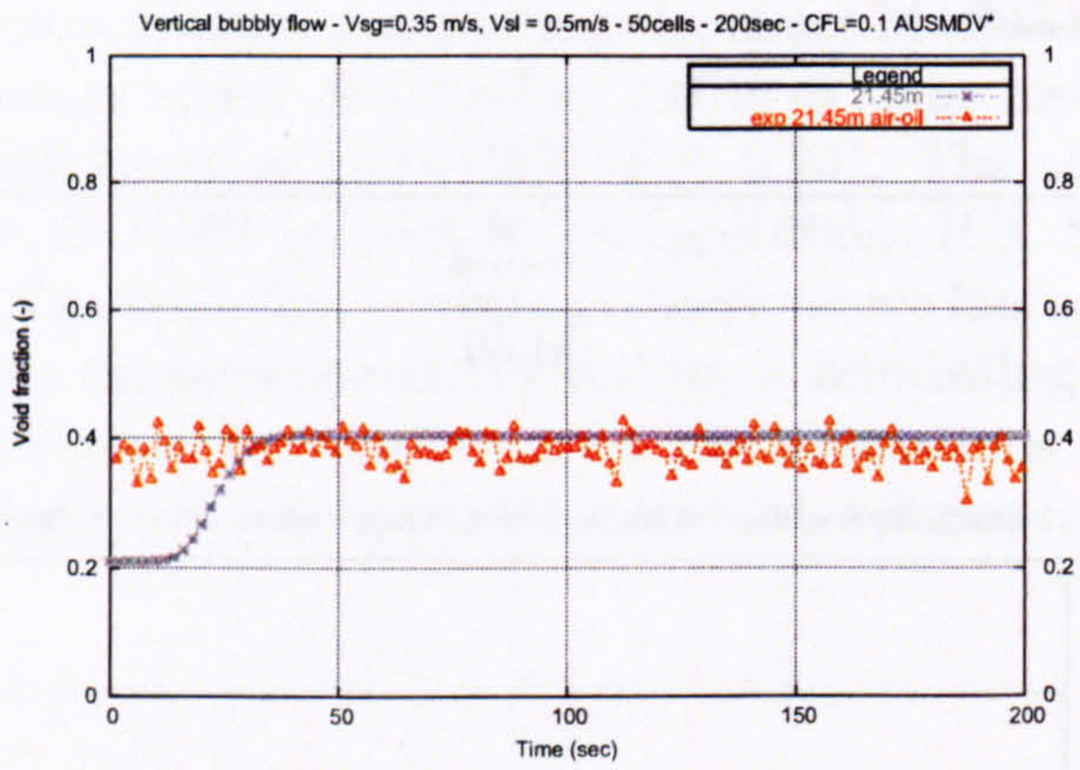

(b) 21.45m

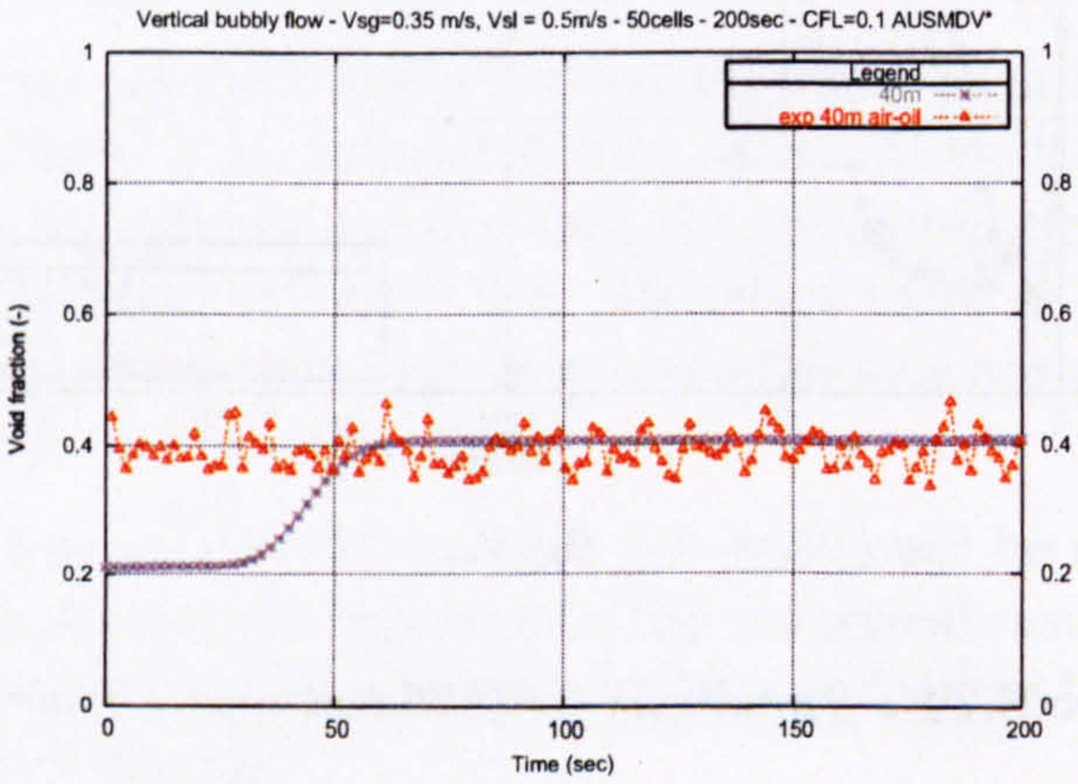

(c) 40m

Figure 6.25 : *Trondheim fe04276 test-case - Void fraction time profiles.*

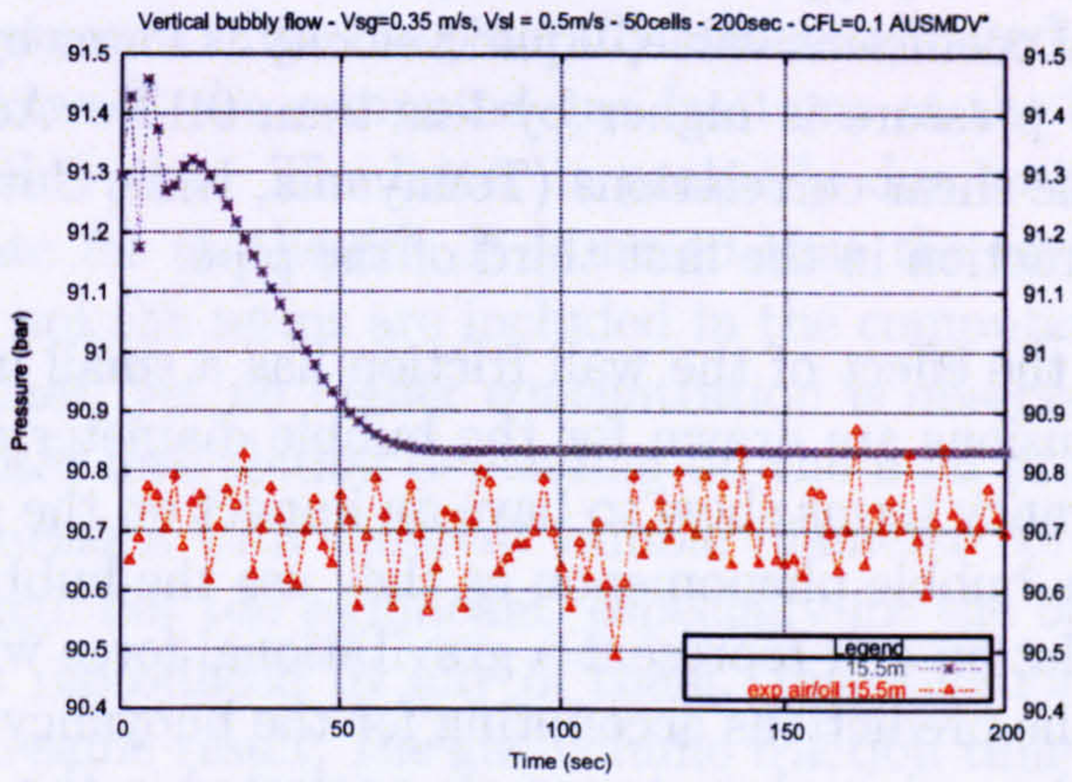

(a) 15.5m

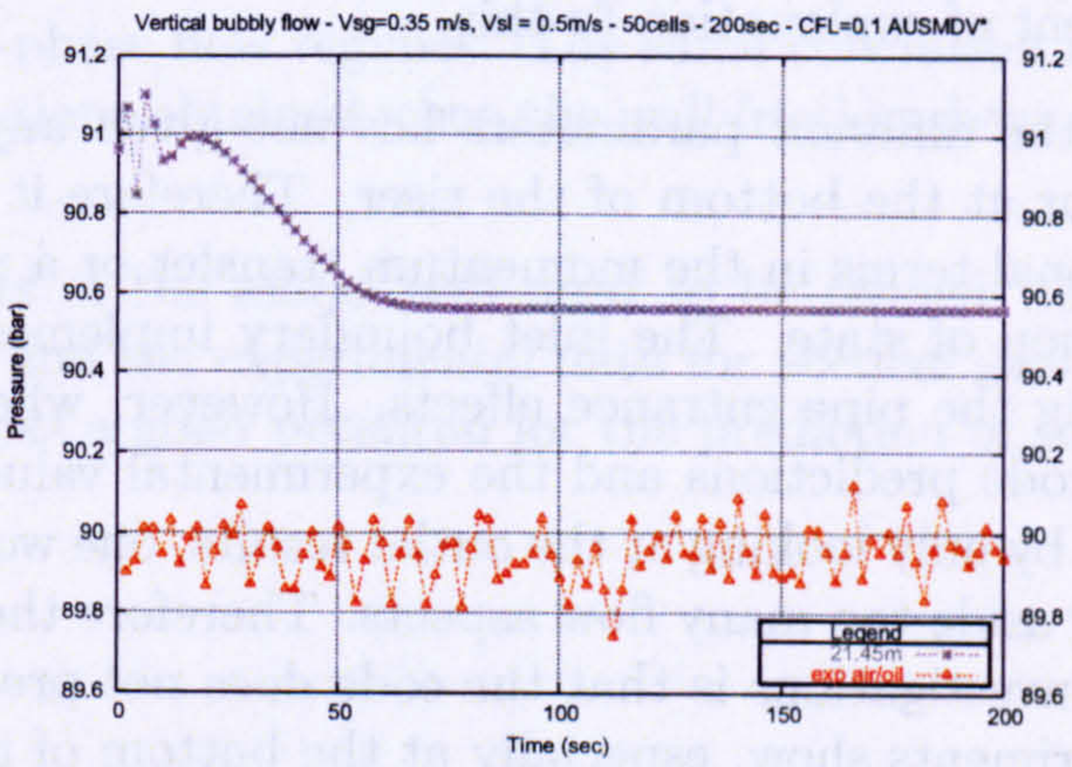

(b) 21.45m

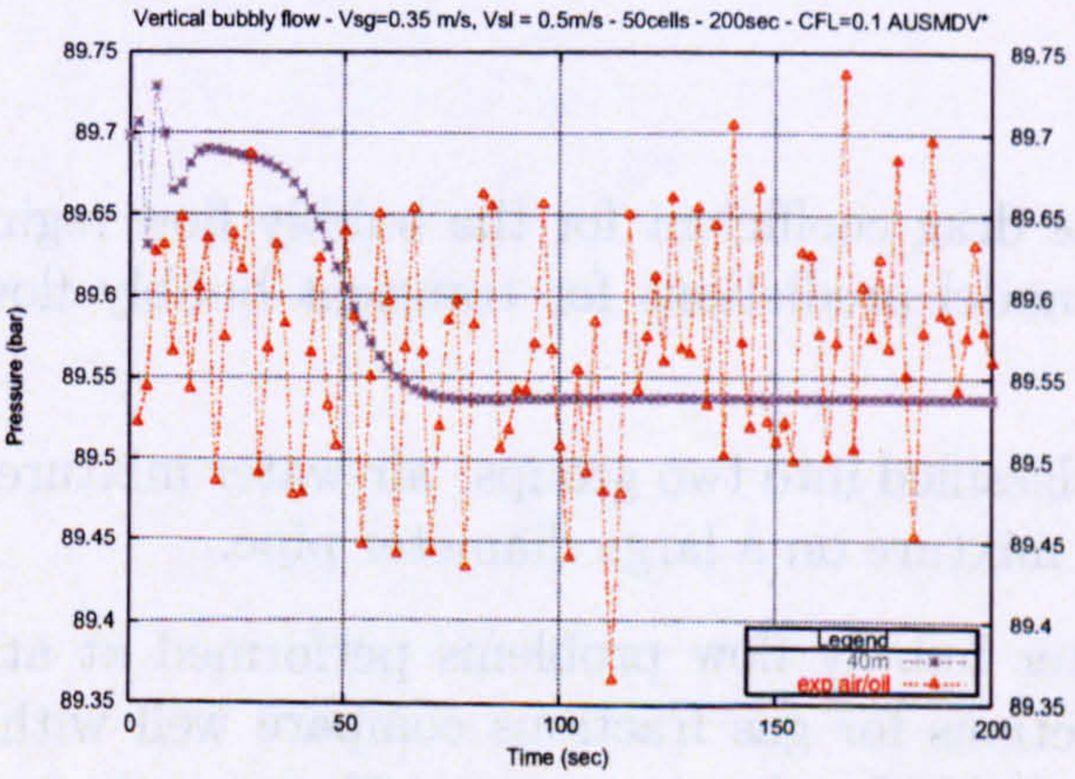

(c) 40m

Figure 6.26 : *Trondheim fe04276 test-case - Pressure time profiles.*

faster. However the difference appears to be very little. Indeed void fraction is lower than with original interfacial coefficient value, liquid velocity is lower by 2.8% and gas velocity is higher by 7%. The pressure is higher by less than 0.1%. Additionally, it has been noticed that none of the shear correlations (Tomiyama, Ishii, Govier, Clift or Hatta) will produce a higher gas fraction in the first third of the pipe.

It is also noticed that the effect of the wall friction has a small impact on the computations. The same conclusions are drawn for the bubble diameter and the bubble velocity formulation. The buoyancy terms show to have an impact on the predictions. They bring more description of the bubble phenomenon as they use the bubble diameter and bubble velocity in their formulation and represent a gravitational force which does affect flows in vertical cases. Hence the predictions accounting for the buoyancy are much closer for the gas fractions answers than when these terms are neglected in the computations. However it is also to be noticed that pressure drop values are not as well predicted with the buoyancy terms, and as already mentioned, the choice of the thermodynamic equation of state might give some element of explanation to this.

This investigation of the different parameters has not given any solution to reproduce the transient behaviour at the bottom of the riser. Therefore it might suggest that the model requires additional terms in the momentum transfer or a more adequate choice of thermodynamic equation of state. The inlet boundary implementation might also be a cause for not capturing the pipe entrance effects. However, when looking at the outlet production only, the code predictions and the experimental values provide a fairly good agreement. Of course, by only looking at the outlet results, one would restrict the problem and simplify it leaving aside too many flow aspects. Therefore the conclusion that can be drawn from all these investigations is that the code does not predict the whole transient behaviour as the experiments show, especially at the bottom of the pipe and the first 50 seconds, but happens to be a fairly good prediction tool for the second half of the pipe.

6.5 Summary

The formulation of the drag coefficient for the bubbly flow regime is evaluated by comparing the two-fluid model predictions for transient bubbly flow problems to available experimental data.

The experiments are classified into two groups: air-water mixture in a blocked T-junction and naphtha-nitrogen mixture on a large diameter pipe.

In the case of air-water bubbly flow problems performed at atmospheric pressure, the two-fluid model predictions for gas fractions compare well with the experimental data. No other data were available for these test-cases. However the two test-cases measure the ability of the code prediction for air-water mixtures, especially for the second one where the gas fractions are very low.
For two-phase naphtha-nitrogen flows, the predictions compare satisfactorily with the

data for the gas and liquid velocities, pressure and outlet gas fractions evolution in time. For all the cases, the amount of gas is generally underestimated by the model. Discrepancies are observed between the computed gas fractions at the bottom of the pipe and pressure drop across the pipe. The latter is probably due to the choice of thermodynamic equation of state for the liquid. It is noted that the results are sensitive to the buoyancy; whether or not the terms are included in the computations makes a difference in the gas fraction values, yet no higher concentration is observed in the bottom of the pipe. A bubble diameter formulation depending on the fluid properties is chosen in the computations. Comparisons with different bubble diameter correlations show that the effect is present although not too significant, especially for the bottom third of the pipe, a feature which is not reproduced by any of them. Investigations on interfacial friction factors have led to the same result: the gas volume fraction time profile is not related to the bubbly interfacial shear stress. The choice of the correlation affects the predictions in their amplitude, however the profile stays the same. The formulation used provides the best answers. Additionally the definition presents some facility to adapt it easily for the other vertical two-phase flow regimes. The same conclusion are drawn with the wall friction factors. Predictions obtained when the wall friction shear stress is varied are fairly identical.

Although some aspects of the model still need to be refined, the comparisons between the model predictions and the experimental data for vertical gas-liquid bubbly flow cases show that the model has a good potential for the prediction of such flows.

References - 6

[1] PENG, N., AND ROBINSON, D. A new two-constant equation of state. *Ind. Eng. Chem. Fundam. 15*, 1 (1976), 59–64.

[2] TAITEL, Y., AND DUKLER, A. A model for predicting flow regime transitions in horizontal and near horizontal gas-liquid flow. *AIChE Journal 22*, 1 (1976), 47–55.

[3] VALDERRAMA, J. A general patel-teja equation of state for polar and nonpolar fluids and mixtures. *J. Chem. Eng. Japan 23*, 1 (1990), 87–91.

[4] VALDERRAMA, J., AND ALFARO, M. Liquid volumes from generalized cubic equations of state: Take it with care. *Oil & Gas Science and Technology - Rev. IFP 55*, 5 (2000), 523–531.

7 Conclusion

7.1 Overview

The purpose of the present study was to develop a two-phase flow numerical model to predict vertical two-phase bubbly flows and terrain-induced slugging in two-phase flow pipelines made of several uphill and downhill sections. This chapter summarises the contributions achieved in this work. The main conclusions obtained are stated in this chapter and areas for further work are highlighted.

7.2 Conclusion

The present work has investigated, extended and developed capabilities based on a transient, one-dimensional, two-fluid model to capture vertical bubbly flow and terrain-slugging combining accuracy and efficiency. Detailed conclusions have been given in each relevant chapter. The main contributions are summarised as follows:

- Development of a working mathematical and numerical model for transient vertical two-phase bubbly flow and terrain-induced slugging in inclined pipes.

- Implementation of an advanced numerical method which provides high numerical accuracy.

- Design, development and implementation of an algorithm which enables simulations on pipelines made of several sections.

After reviewing the modelling approaches existing in the literature in the second chapter, we presented and, studied in detail, the mathematical properties of two specific transient, isothermal two-fluid models, which were developed based on the one-dimensional form of the mass and momentum conservation equations. The first model is the PFM (Pressure-Free Model), which assumes that both phases are incompressible. The second one which treats both phases as compressible fluids is referred to as the TPM5 (Two-Pressure Model). The wall fluid and interface interactions are accounted for by constitutive relations which are flow regime dependent. Relations used for each flow regime are therefore presented

throughout the chapters.

The two-fluid model transport equations are discretized using an explicit finite volume approach. The numerical schemes that we have investigated are described in detail in the fourth chapter. More focus has been given to the Advection Upwind Splitting Method (AUSM) approach and more precisely to the AUSMDV* scheme which is a hybrid of a flux-vector splitting (FVS) scheme and a flux-difference splitting (FDS) schemes. The hybrid flux-splitting scheme taking advantages of both FVS and FDS properties. We have shown that it can provide accurate and efficient solutions thereby offering a very attractive scheme. A number of two-fluid benchmark problems were successfully tested, showing the numerical accuracy of the method, and its ability to model flows over the whole range of void fractions and, in particular, stationary or moving interfaces. Additionally, the scheme is stable and possesses an inherent accuracy with a reduced computational cost compared to approximate Riemann solvers. It showed to be four times faster than the TVD-Lax-Friedrichs scheme, or twice as accurate as the Force scheme in some cases. Hence, as suggestions for future work, we advocate using the AUSMDV* scheme combined with the non-conservative Centred-S scheme for the compressible model (TPM5).

In offshore engineering, pipelines are often set across undulating terrain where the topography is an important issue. As the Finite Volume method discretises the domain over segments, in order to improve the capability of the solver, we therefore describe in the fifth chapter an algorithm which provides an efficient means of achieving simulations accounting for the effect of the topography.

To assess the validity of the proposed algorithm, simulations on the single-phase flow and two-phase flow problems are performed. Hence, with the Shallow-Water equations, we have shown the limitations of the process when the number of mesh cells is too small, and that the geometry can be well accounted for in the computations. In that chapter, we also present the first practical application for transient gas-liquid flow in pipelines. We studied the stratified flow pattern through a downward elbow pipe and compared predictions between incompressible and compressible models. Although both models give different answers, they follow the same trend and both are in accordance with the theoretical equilibrium value of each pipe given by Taitel and Dukler.

The second application is the simulation of terrain-induced slugging in a V-section with the compressible model developed in this work. The comparisons presented in Chapter 5 between numerical and experimental data show that the compressible model is able to accurately predict most of the features of this complex flow regime: physical observations such as wave formation at the interface, pipe bridging events, slug growth, slug propagation and merging slugs can be predicted qualitatively and critical flow characteristics such as slug frequency, slug length and slug velocity are fairly well determined too. These applications demonstrate both the good performance of the algorithm for the topography and the capability of our compressible model to predict stratified two-phase flows and

terrain-induced slugging in slightly inclined pipes.

In order to validate the various components of the two-fluid model for the bubbly flow regime reviewed in the second and third chapters, the model predictions for liquid (or gas) volume fractions, velocities and pressure gradients for transient vertical bubbly flow in pipes are compared to available experimental data in the penultimate chapter of the thesis.

In the case of two-phase air-water bubbly flows at atmospheric pressure in a vertical pipe having a diameter of $70\,mm$, the model predictions compare well with the experimental measurements. The calculated gas volume fractions fall within 20% of the measured values. For small mixture velocities where a very low gas volume fraction is expected, the model behaves well: it remains extremely stable despite the near-one phase configuration and the answers are in agreement with the measurements (within 1%).

The model predictions are also compared to experimental data for liquid volume fractions, velocities and pressure gradients in transient naphtha-nitrogen bubbly flows in a large pipe diameter of $189\,mm$ and $50\,m$-long, at high operating pressures of $20\,bar$ and $90\,bar$. These comparisons show that the present model consistently underestimates the average void fraction for all cases but achieves closer values to the measurements for the high pressure and high mixture velocities. It shows, for that particular case, predictions with less than 5% error when compared to the experimental measurements. The calculated pressures compare well with the data for vertical cases (constantly below 4% of error) but, overall, are lower than the measured pressure values, a consequence of the low gas volume fraction predictions. Disagreement is however observed in the bottom third of the pipe where an accumulation of gas bubbles is observed in the experimental data but are not represented in the numerical results of the void fraction. For that "region", the model used in the present study fails to predict the correct flow behaviour. Some of the discrepancies may result from the simplifying assumptions used in the model. A study of the influence of the closure laws correlations on the predictions shows no influence of the drag coefficient for this particular feature. The choice of the correlation plays a role in the steady-state value but the higher bubble concentration at the bottom of the pipe is never reproduced. This remains an open question for the author. However, a lack of an extra mechanism in the model, such as gas entrainment-type, and the inlet boundary conditions treatment might be part of the issue and investigations in that respect should be conducted in the future.

Although some aspects of the model need to be improved, the results of this research show the potential of the present approach to predict vertical bubbly flows and terrain-induced slugging in inclined pipes. Additionally, the simple model developed for vertical bubbly flows offers a good basis for future developements in vertical flow modelling; the interfacial drag correlation can easily be modified for the different flow regimes, and a flow transition mechanism can be implemented based on a simple switch of the interfacial friction.

7.3 Recommendation for future work

The assessment carried out for the compressible model has been mainly focused on slightly inclined pipes and vertical risers. It is appropriate now to extend the assessment to other pipe geometries. A first study will be the evaluation of the wall fluid correlations for terrain-slugging through a W-section, as performed by De Henau *et al.* [2, 3], where the inclinations ($\pm 15^o$) are higher than those used in the present study. It would also be advisable in the future to evaluate the TPM5 model for pipe-riser systems already studied by several authors in the literature [4, 9, 5, 10, 8] and to compare it against the available experimental and/or numerical data. It should be stressed that slug flow regimes operating in vertical pipes will be formed by Taylor bubbles where dispersed bubbles are entrained at the tail. Therefore we advise future researchers to include dispersed gas entrainment effects in subsequent models, such as suggested in Bonizzi [1] and hopefully, be able to predict this complex regime.

As for the bubbly flow simulations, the main issue concerns the lack of accuracy in the model predictions of liquid holdup at the bottom third of the pipe where experimental measurements reveal an accumulation of gas bubbles not reproduced by the compressible model. Here again, introducing a mechanism such as gas entrainment or volumetric interfacial area transport equation in the model should enhance the predictions, as it is suggested in the recent paper from Yao and Morel [11], and allow us to capture this particular feature.

We believe the compressible TPM5 model can be applied to various flow regimes regarding the use of the appropriate drag laws for each flow regime. Therefore, it would be interesting to consider the implementation of a flow transition mechanism, allowing us to switch from one regime to another. We recommend to investigate the model developed by Petalas and Aziz [7], which is applicable to a wide range of pipe inclinations. With this tool, we will hopefully be able to accurately predict the onset of two-phase flows in pipelines with any topography.

Another area for future research is the numerical method, and we present here two possible improvements to the computations speed (code efficiency). Considering that the best initial grid generation is still an open question, the use of implicit finite differences methods in the EMAPS solver needs to be developed further. Additionally, in the present work, we present calculations only on uniform grids, but the structure that accounts for the topography has been developed in such a way that it is valid for adaptive gridding such as the adaptive mesh refinement technique (AMR) presented in Chapter 4 of Omgba's thesis [6]. However, no validation tests for adaptive simulations on multiple pipes have been performed and that could be the subject for further research.

References - 7

[1] Bonizzi, M. *Transient one-dimensional modelling of multi-phase slug flows.* Ph.D. thesis, Imperial College, University of London, UK., 2002.

[2] De Henau, V., and Raithby, G. A study of terrain-induced slugging in two-phase flow pipelines. *Int. J. Multiphase Flow 21*, 3 (1995), 365–379.

[3] De Henau, V., and Raithby, G. A transient two-fluid model for the simulation of slug flow in pipelines - I. Theory. *Int. J. Multiphase Flow 21* (1995).

[4] Fabre, J., Peresson, L., Corteville, J., Odello, R., and Bourgeois, T. Severe slugging in pipeline/riser systems. *SPE Production Engineering* (August 1990), 299–305.

[5] Jansen, F. *Elimination of Severe slugging in a pipeline-riser system.* MSc thesis, Department of Petroleum Engineering, Tulsa University, 1990.

[6] Omgba-Essama, C. *Numerical modelling of transient gas-liquid flows (application to stratified and slug flow regimes).* Ph.D. thesis, Cranfield University, Applied Mathematics & Computing group, 2004.

[7] Petalas, N., and Aziz, K. A mechanistic model for multiphase flow in pipes. In *49th Annual Technical Meeting of the Petroleum Society of the Canadian Institute of Mining, Metallurgy and Petroleum* (8-10 June 1998). Calgary, Alberta, Canada.

[8] Sarica, C., and Shoham, O. A simpified transient model for pipeline/riser systems. *Chem. Eng. Sci. 46*, 9 (1991), 2167–2179.

[9] Taitel, Y., Vierkandt, S., Shoham, O., and Brill, J. Severe slugging in a riser system, experimental and modelling. *Int. J. Multiphase flow 16* (1990), 57–68.

[10] Vierkandt, S. J. *Severe slugging in a pipeline-riser system experiments and modeling.* MSc thesis, Department of Petroleum Engineering, Tulsa University, 1988.

[11] Yao, W., and Morel, C. Volumetric interfacial area prediction in upward bubbly two-phase flow. *Int. J. of Heat Mass Transfer 47* (2004), 307–328.

A EMAPS

The Eulerian Multiphase Adaptive Pipeline Solver (EMAPS) is the computational framework in which all the results presented in this thesis were simulated. It is a general-purpose one-dimensional fluid flow code that is capable of simulating single-phase, two-phase or three-phase flow problems encountered in the oil and gas industry. The general vector-matrix form of the set of partial differential equations (PDEs) solved by the numerical schemes implemented in EMAPS is given in Appendix, with three specific two-phase flow models.

The purpose of this appendix is not to describe all the modules implemented in the code but to give the reader a brief overview of the code main components; therefore we present in the next sections the general architecture of the code, and some of its main elements.

A.1 EMAPS Architecture

EMAPS is designed as a flexible collection of modules, and its complete structure involves three main parts:

a) The pre-processor for input text files (Pre-EMAPS)

b) The actual solver or processor (EMAPS)

c) The post-processor for analysing results of the simulation (Post-EMAPS)

The Figure A.1 shows a schematic diagram of the interaction between the three-parts.

A.2 The Pre-Processor

In its current version [2], the code requires five input and control data files to start a simulation. These input files are labelled:

a) Pipe.txt (for the pipe topography: length, diameter, inclination and mesh size,...)

b) Fluids.txt (for the physical properties of the fluids)

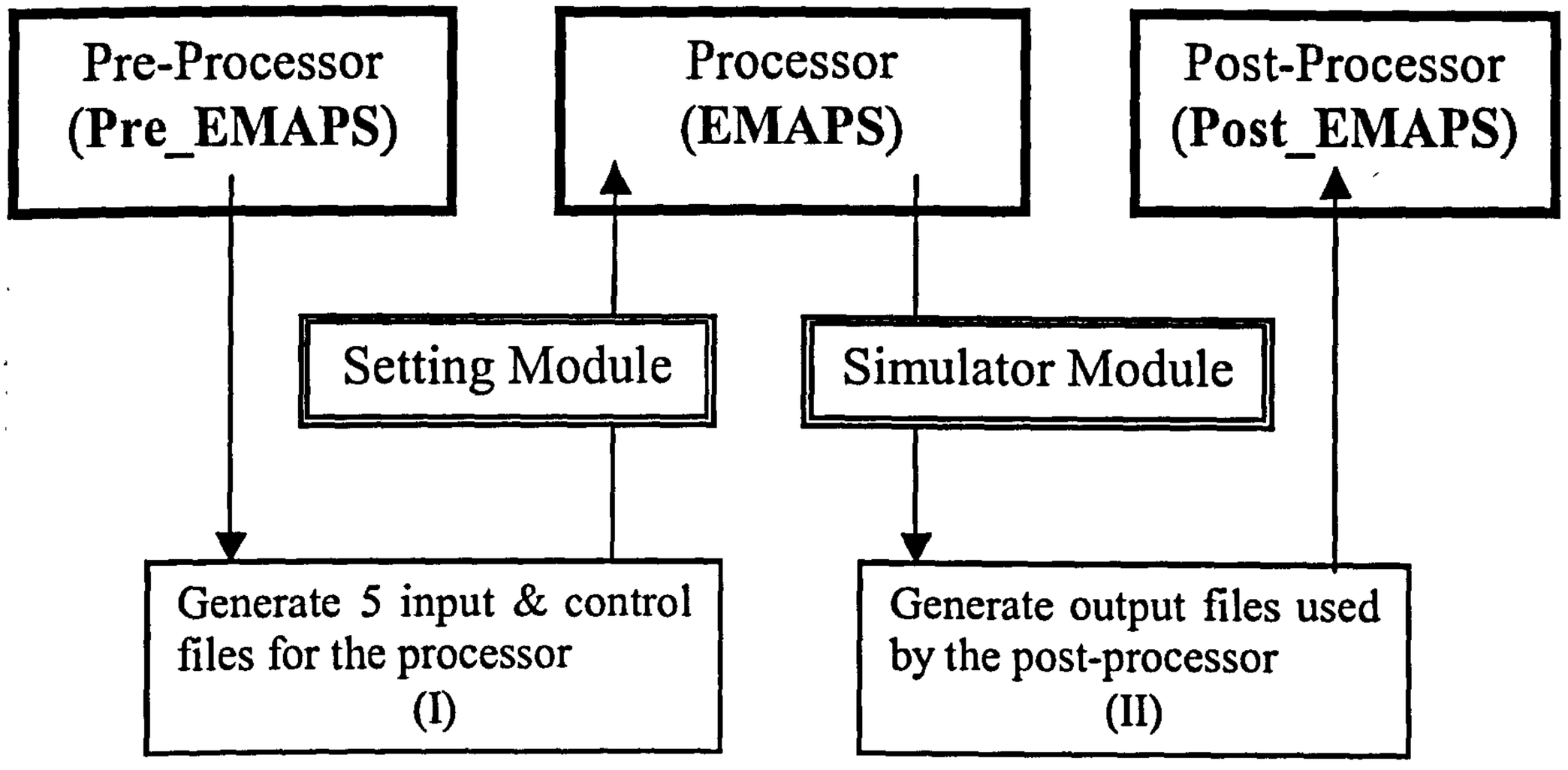

Figure A.1 : *Architecture of EMAPS.*

c) Control.txt (time step information, numerical schemes,...)

d) Problem.txt (test case name, initial and boundary condition data)

e) Model.txt (mathematical model, phase friction, interfacial pressure and velocity,...)

The five input files are generated either using a text-based pre-processor written in Fortran 90, or a graphical user interface [4] written in Java. A detailed description, of all the appropriate data in each of the above files, is given in the code user manual [2], and it is not repeated here.

A.3 The Processor

The processor read the input files generated by the pre-processor, via the module *setting* (file setting.f90). This module contains, therefore, many functions that check and read the control data, and initialises all the internal variables, which are necessary for successful start of a simulation.

The module *simulator* (simulator.f90) actually contains steady and transient solvers, which make use of the adaptive mesh refinement techniques described in [1, Chapter 4]. The processor runs the solver selected by the user, using the appropriate numerical schemes and write the solution vector in various output files described in the code user manual.

As already mentioned, the code is composed of many modules, which make it programmer-

friendly and also facilate its maintenance. The major modules that are present in the code are given in Fig. A.2. In addition to these major modules, many accessory modules were

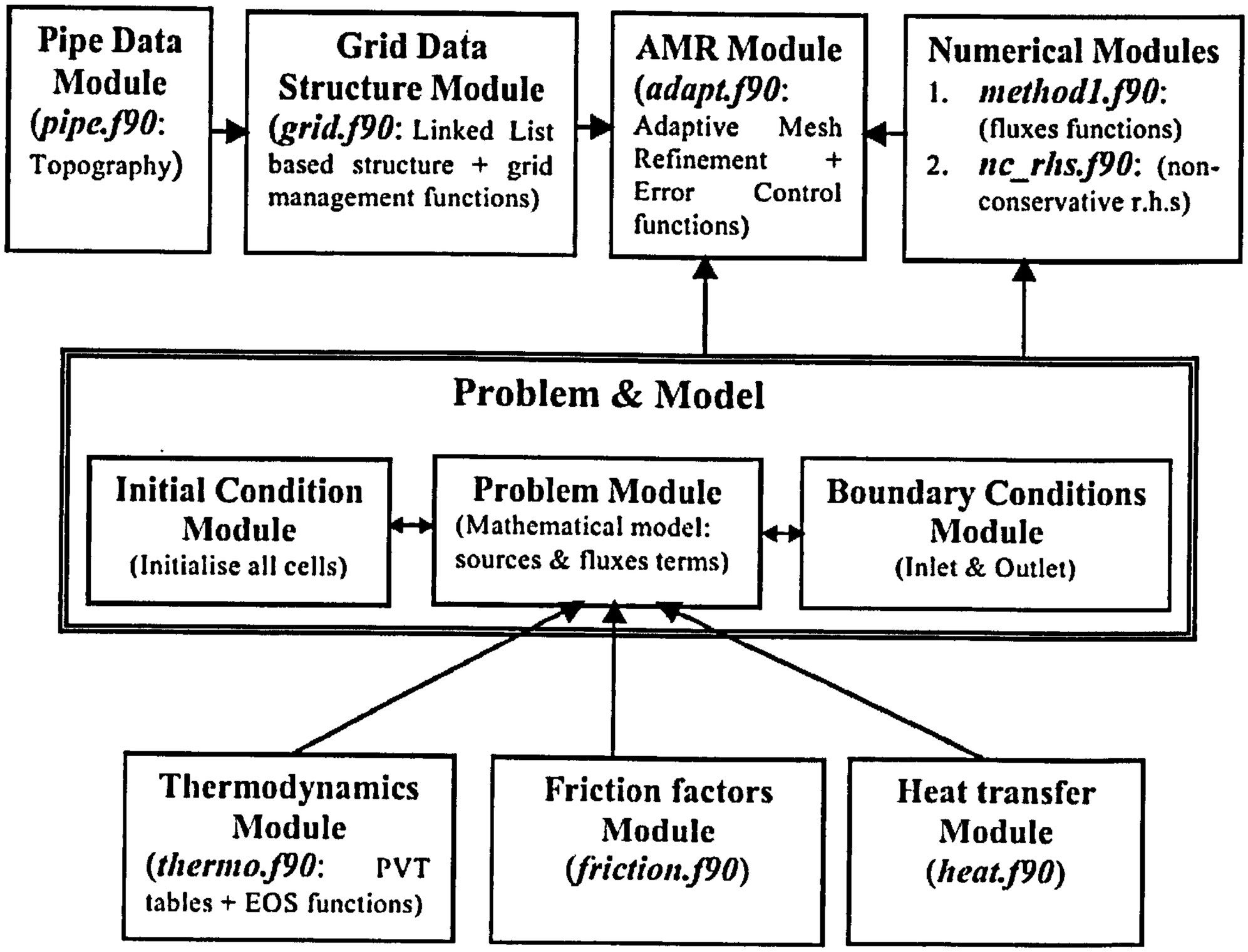

Figure A.2 : *Main modules of EMAPS.*

implemented such the error handling module (error.f90) or the file operations module (io_files.f90). All these files are fully described in the code technical manual.

The EMAPS files are identical for all the mathematical models simulated, except for the file or module implementing the vector-matrix formulation of the model. Hence, to run the code a specific executable must be created fore each of the mathematical models that the user is investigating.

A.4 The Post-Processor

In the current version of the code, there is no real Post-Processor which can automatically plot variables selected by the user. A graphical user interface [3] written in Java is still in development. Therefore to process the output files generated by the simulator and plot the required variables, we manually use a free software called GNUPLOT.

References - A

[1] OMGBA-ESSAMA, C. *Numerical modelling of transient gas-liquid flows (application to stratified and slug flow regimes).* Ph.D. thesis, Cranfield University, Applied Mathematics & Computing group, 2004.

[2] OMGBA-ESSAMA, C., HANICH, L., TENG, H., AND LOILIER, P. E.m.a.p.s.: Eulerian multiphase pipeline solver, user guide, version 3.50. Tech. rep., Applied Mathematics & Computing, Cranfield University, 2005.

[3] PINTO BASTO, A. *A graphical user interface (GUI) for EMAPS Post-Processor.* MSc thesis, Applied Mathematics & Computing, Cranfield University, 2004.

[4] VASSILAS, A. *Graphical User Interface for the EMAPS Code.* MSc thesis, Applied Mathematics & Computing, Cranfield University, 2002.

B Vector-matrix formulation

In this Appendix, the details of the formulation of the basic conservation equations for the one-dimensional two-fluid models presented in Chapter 3, into a vector-matrix form are given.

B.1 Vector-matrix formulation

For a successful implementation of a mathematical model in the EMAPS code, the model has to be written in the following vector-matrix formulation:

$$\frac{\partial U}{\partial t} + \frac{\partial F}{\partial x} = H\frac{\partial U}{\partial x} + S \tag{B.1}$$

where U is a vector of the conservative variables, F is a physical flux vector, H is a matrix containing non-conservative terms existing in the model, and S is a vector of algebraic source terms.

Hence, the two specific two-phase flow models described in Chapter 3, are explicitly re-written in the following sections.

B.2 PFM model

This incompressible two-fluid model is fully conservative, therefore the matrix H is set to zero, and from relations 3.3 and 3.4, the vectors U, F and S are given as:

$$U = \begin{pmatrix} \rho_l\alpha_l + \rho_g\alpha_g \\ \\ \rho_l\alpha_l - \rho_g\alpha_g \end{pmatrix} \qquad F = \begin{pmatrix} \rho_l\alpha_l V_l + \rho_g\alpha_g V_g \\ \\ \dfrac{\rho_l V_l^2 - \rho_g V_g^2}{2} + (\rho_l - \rho_g) g h_l \cos(\beta) \end{pmatrix} \tag{B.2}$$

$$S = \begin{pmatrix} 0 \\ \\ -(\rho_l - \rho_g) g \sin(\beta) + \tau_i S_i \left(\dfrac{1}{A_g} + \dfrac{1}{A_l}\right) + \dfrac{\tau_g S_g}{A_g} - \dfrac{\tau_l S_l}{A_l} \end{pmatrix} \tag{B.3}$$

B.3 TPM5 model

This two-fluid model contains non-conservative terms; hence to obtain the vector-matrix formulation, we transform the momentum expression from 3.19 as:

$$\frac{\partial}{\partial t}(\rho_g \alpha_g V_g) + \frac{\partial}{\partial x}(\alpha_g(\rho_g V_g^2 + P_g)) = P_i \frac{\partial}{\partial x}\alpha_g + F_{wg} + F_i + B_{fg} \tag{B.4}$$

$$\frac{\partial}{\partial t}(\rho_l \alpha_l V_l) + \frac{\partial}{\partial x}(\alpha_l(\rho_l V_l^2 + P_l)) = -P_i \frac{\partial}{\partial x}\alpha_g + F_{wl} - F_i + B_{fl} \tag{B.5}$$

Hence, from system 3.19 and Eq. B.5, the vectors U, F and S, and the matrix H are respectively given as:

$$U = \begin{pmatrix} \rho_g \alpha_g \\ \rho_l \alpha_l \\ \rho_g \alpha_g V_g \\ \rho_l \alpha_l V_l \\ \alpha_g \end{pmatrix} \qquad F = \begin{pmatrix} \rho_g \alpha_g V_g \\ \rho_l \alpha_l V_l \\ \rho_g \alpha_g V_g^2 + \alpha_g P_g \\ \rho_l \alpha_l V_l^2 + \alpha_l P_l \\ \alpha_g \end{pmatrix} \tag{B.6}$$

$$S = \begin{pmatrix} 0 \\ 0 \\ F_{wg} + F_i + B_{fg} \\ F_{wl} - F_i + B_{fl} \\ \mu(P_g - P_l) \end{pmatrix} \tag{B.7}$$

and

$$H = \begin{pmatrix} 0 & 0 & 0 & 0 & 0 \\ 0 & 0 & 0 & 0 & 0 \\ 0 & 0 & P_i & 0 & 0 \\ 0 & 0 & 0 & -P_i & 0 \\ 0 & 0 & 0 & 0 & -V_i \end{pmatrix} \tag{B.8}$$

From this last relation B.8, it appears that the non-conservative terms matrix H can be reduce into a vector, but EMAPS contains other mathematical models, such as three-phase flow ones, which require a matrix formulation for the non-conservative terms, and that is why a matrix form of these terms was selected as a default one.

C

Stability criteria: Stratified to slug transition

This Appendix describes the stability criteria between the stratified and slug flow regimes.

The transition from stratified to slug flow is a complex phenomenon that has been widely studied over the past thirty years. And besides the early empirical relations from Beggs and Brill, or Mandhane *et al.*, three theoretical relations have been often used to predict the transition criterion. These include the inviscid Kelvin-Helmholtz (IKH) theory, the viscous long waves (VLW) also known as viscous Kelvin-Helmholtz (VKH) theory and the slug stability theory.

However, early theoretical models from Taitel and Dukler, considered the process leading to the transition to be solely linked to the Kelvin-Helmholtz instability which occurs when the suction effect due to pressure variation over a wave overcomes the stabilising effect of gravity, enabling small interfacial disturbances to grow into waves that may be potentially large enough to bridge the pipe and form slugs. But nowadays, many researchers (Scott *et al.*, 1990, Bendiksen and Espedal, 1992; Woods and Hanratty, 1996) often used the stability of an existing slug to explain the transition from stratified flow.

It is still not clear which theoretical method is best as predictive tool for the transition from stratified flow, and we refer the reader to paper by Mata et al. (2002) which compared different stability limit methods, and the thesis by Hale (2000) which reviewed the various models dealing with the growth of disturbances into large amplitude waves and potentially slug flow. But, as a guide for selecting a transition mechanism, we advocate the recent article by Hurlburt and Hanratty (2002) who combined the use of the three existing theoretical methods depending on the gas superficial velocity. However, in this thesis, we only describe the Taitel and Dukler (1976) transition model, because it is most widely used in the literature.

Starting from a solitary wave of finite amplitude, Taitel and Duckler (1976) studied its growth on a smooth stratified layer in horizontal channel, and derived a stability criterion to pinpoint the transition between stratified and slug flow. Neglecting the wave motion, they wrote a balance equation between the pressure variation and the acceleration of the

gas phase. This results in a condition of instability for a rectangular channel, which was further modified for circular geometries as:

$$V_g > K\sqrt{\frac{(\rho_l - \rho_g)g\cos(\beta)}{\rho_g}\frac{A_g}{dA_l/dh_l}} \tag{C.1}$$

The coefficient K = 1 corresponds to a slightly modified version of the inviscid Kelvin-Helmholtz criteria given by Eq. 3.16. However, the authors realised that this IKH criteria over-predicted the transition limit, and recommended the following expression:

$$K = 1 - \frac{h_l}{D} \tag{C.2}$$

The Taitel and Dukler (1976) model (Eq. C.1 C.2) works reasonably well for horizontal pipes and its transition line is illustrated in Fig. C.1 for air-water flow at atmospheric conditions.

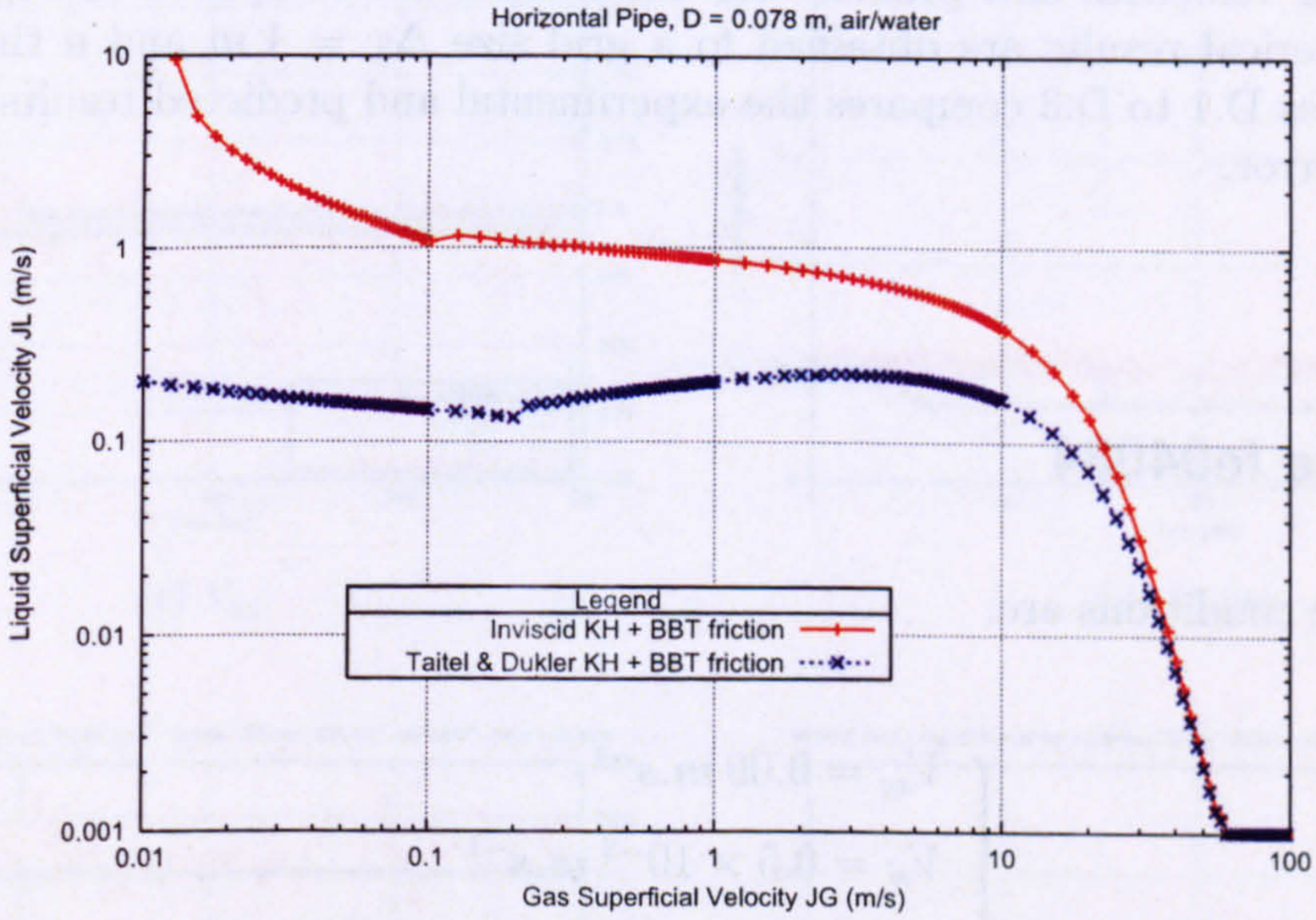

Figure C.1 : *Taitel and Dukler (1976), and Inviscid Kelvin-Helmholtz (IKH) transition lines from stratified flow.*

D

Vertical bubbly flow results

This Appendix contains additional numerical results for vertical naphtha-nitrogen bubbly cases described in Chapter 6, Section 6.4.

The experimental measurements and numerical predictions for the time evolution of volume fractions, velocities and pressure for three cases are compared in Fig. D.1 to D.6. All the numerical results are obtained fo a grid size $\Delta x = 1\,m$ and a time step $\Delta t = 10^{-5}\,s$. Tables D.1 to D.3 compares the experimental and predicted results and gives the percentage error.

D.1 Case fe04084

The testcase conditions are:

$$\begin{cases} V_{sg} = 0.09\,m.s^{-1} \\ V_{sl} = 0.5 \times 10^{-3}\,m.s^{-1} \\ P = 18.8\,bar \\ \rho_l^w = 672.6\,kg.m^{-3} \\ \mu_l^w = 0.3 \times 10^{-2}\,kg.(m.s)^{-1} \\ \rho_g^w = 22\,kg.m^{-3} \\ \mu_g = 0.997 \times 10^{-5} \\ \sigma = 0.0141\,N.m^{-1} \end{cases} \tag{D.1}$$

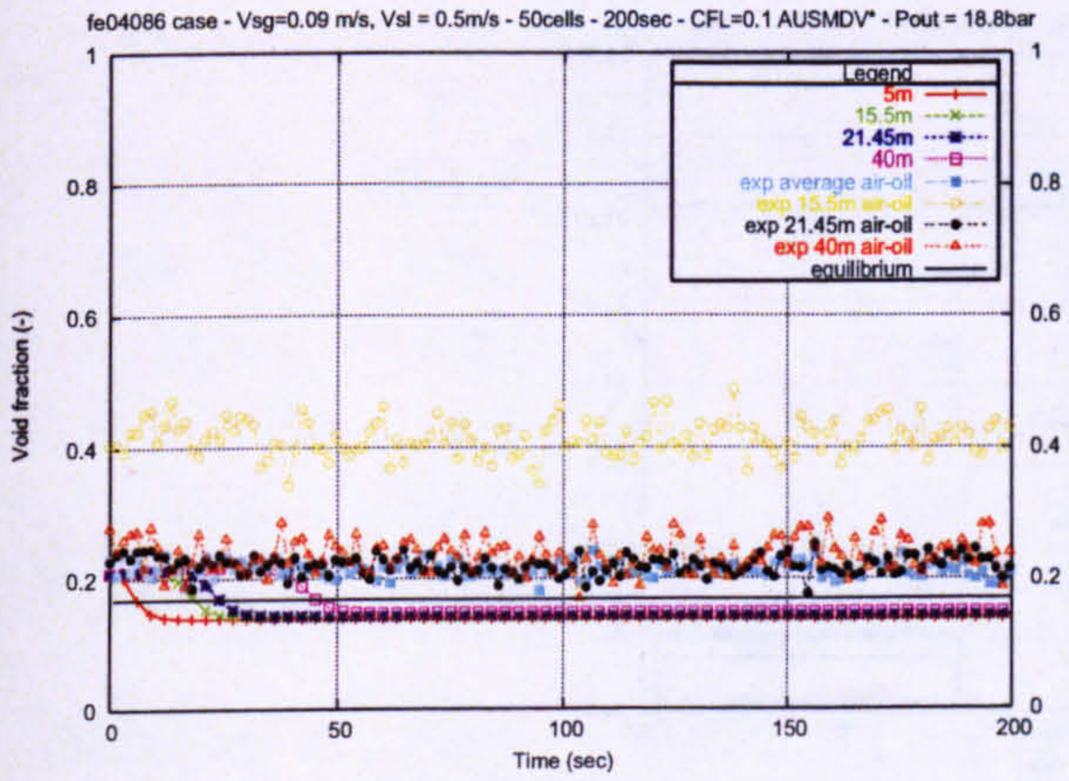

(a) all

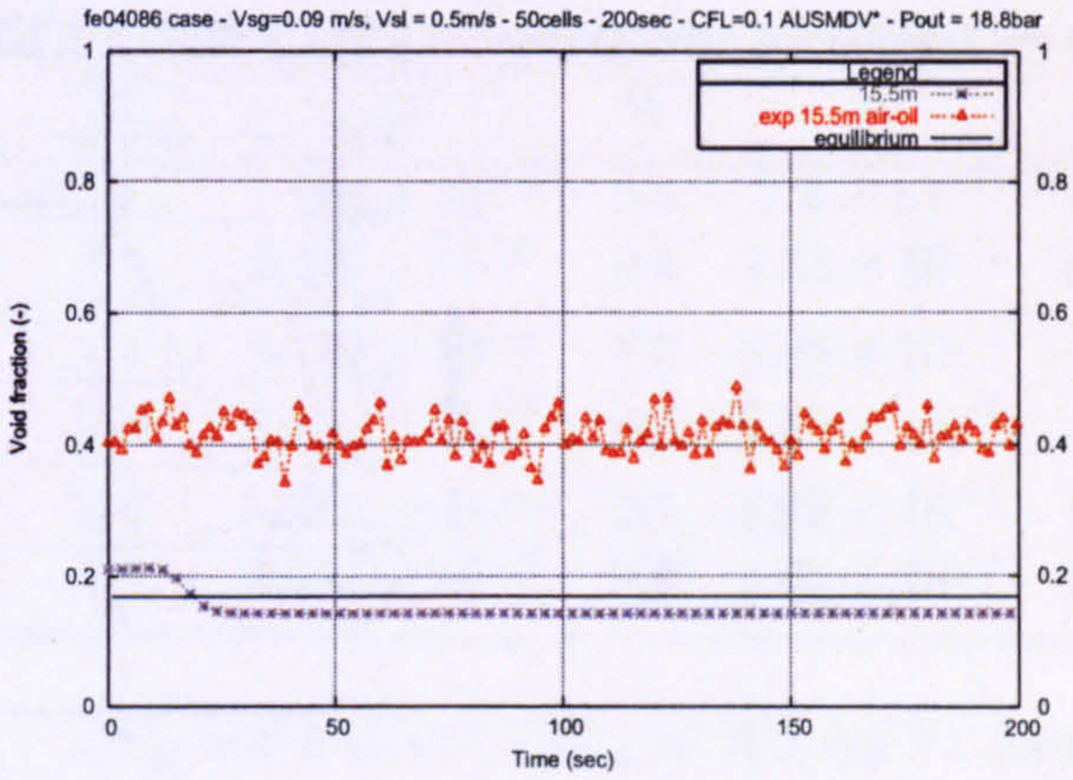

(b) 15.5m

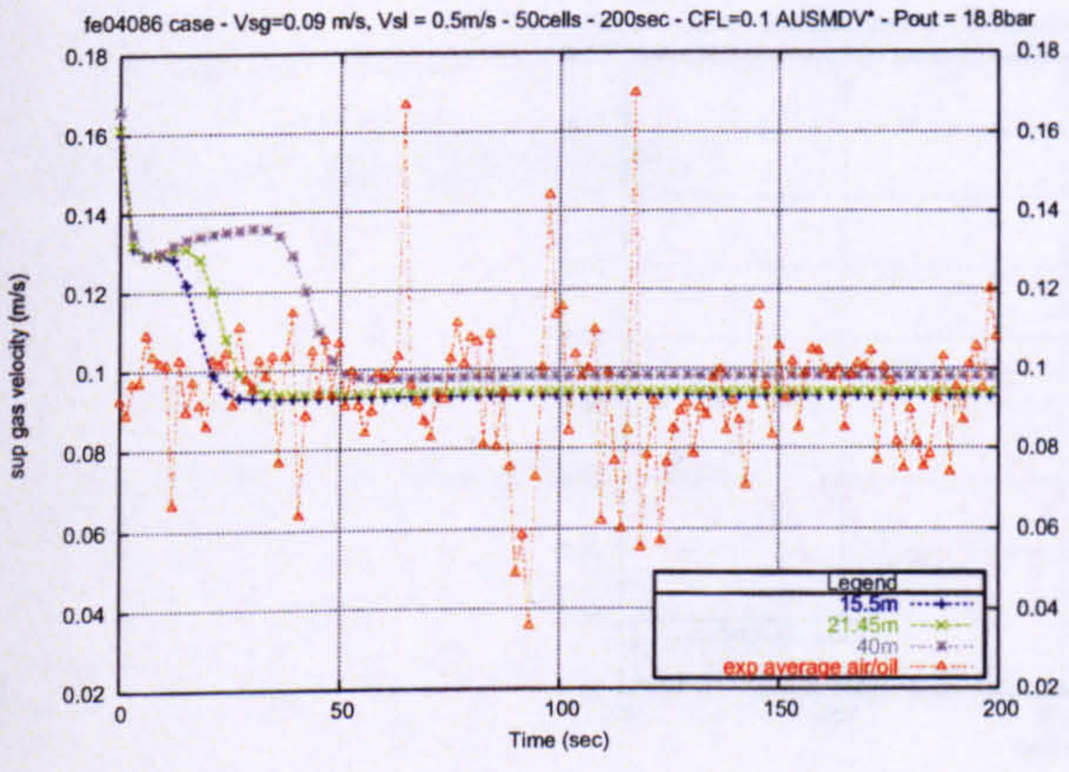

(c) V_{sg}

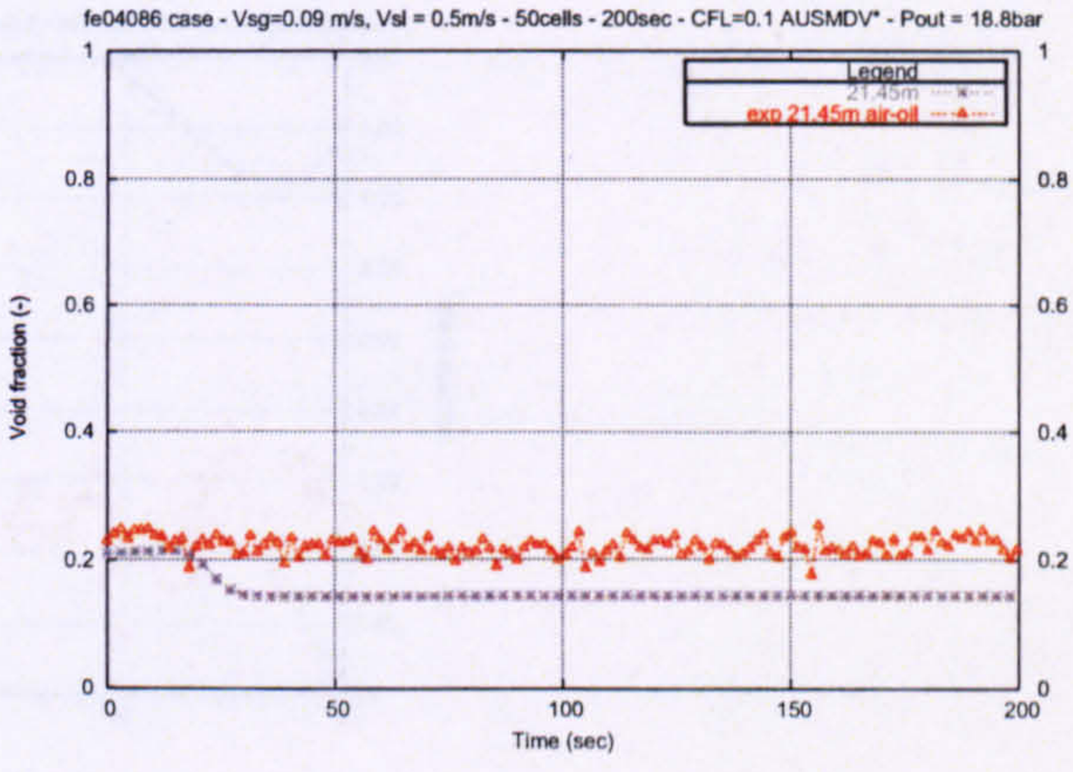

(d) 15.5m

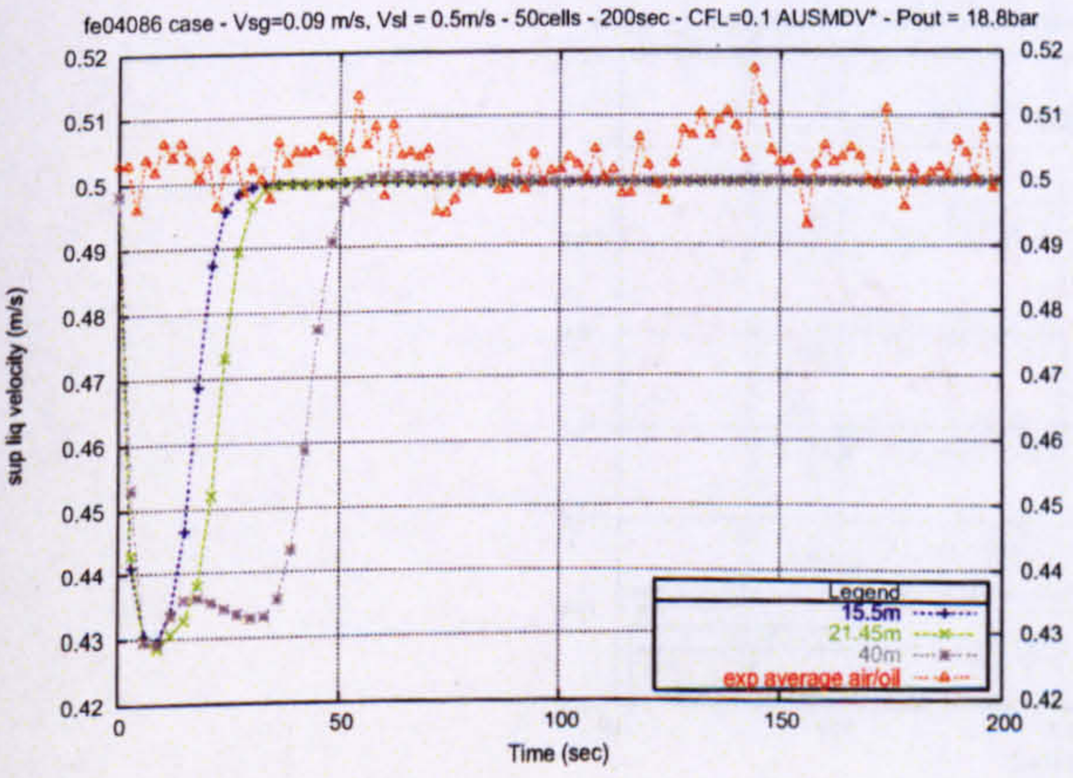

(e) V_{sl}

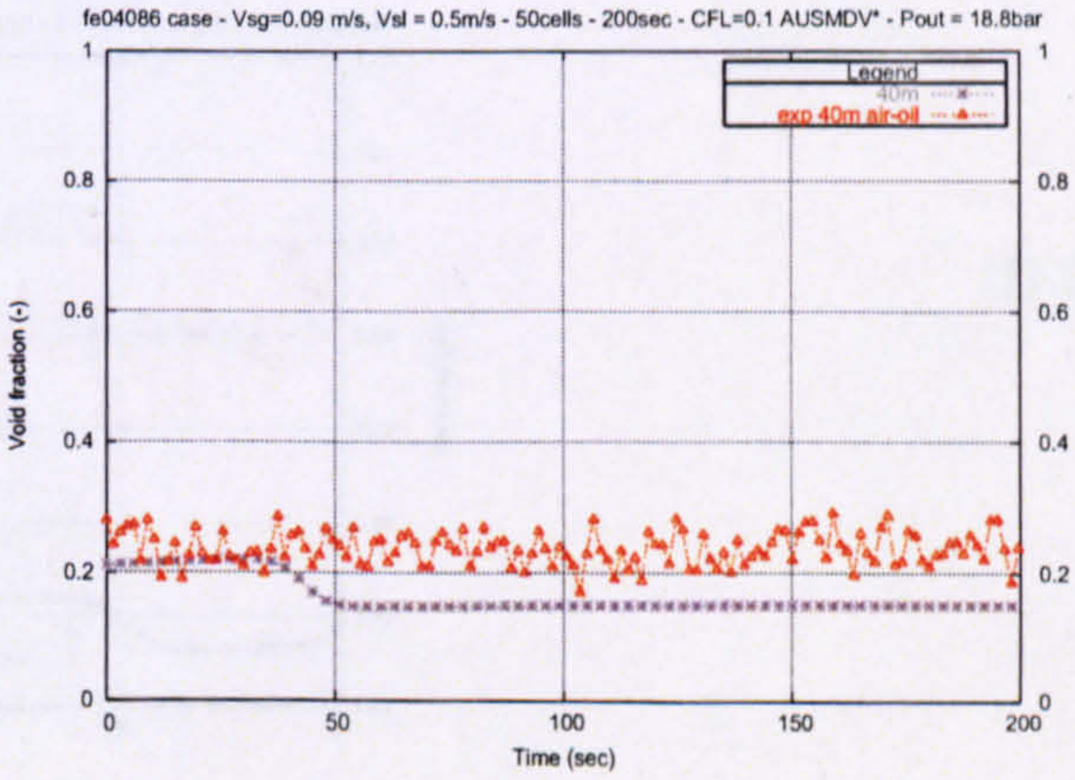

(f) 15.5m

Figure D.1 : *Trondheim fe04084 test-case - Time profiles.*

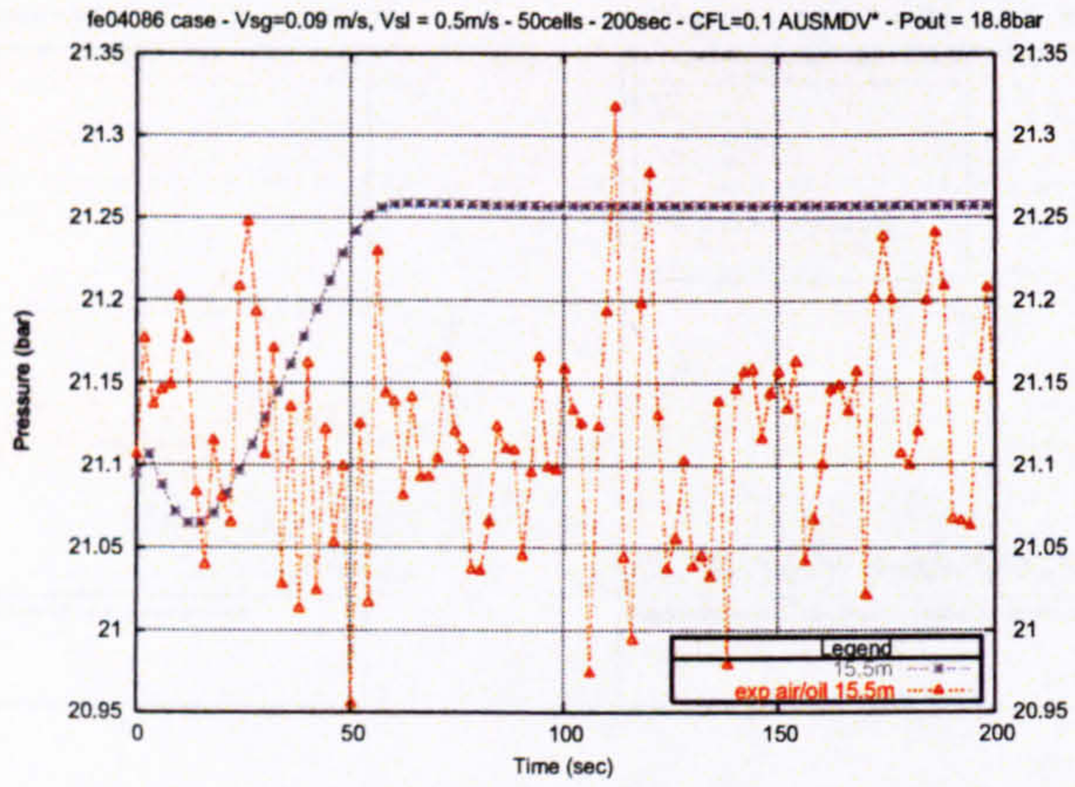

(a) 15.5m

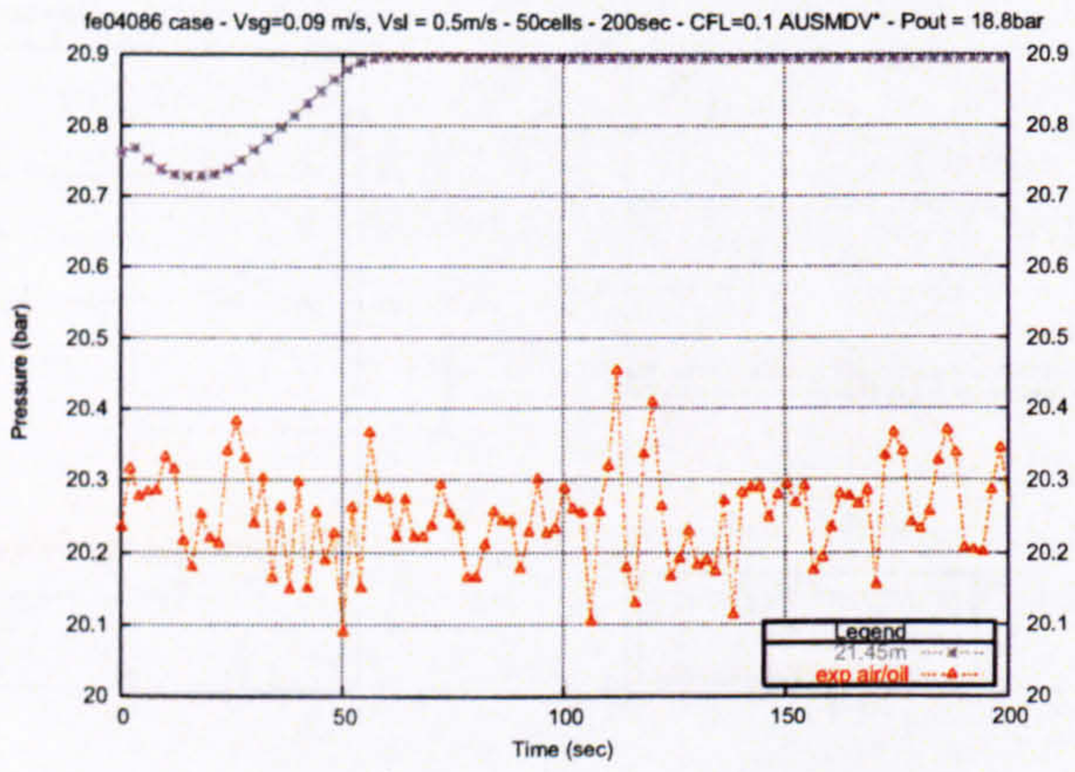

(b) 21.45m

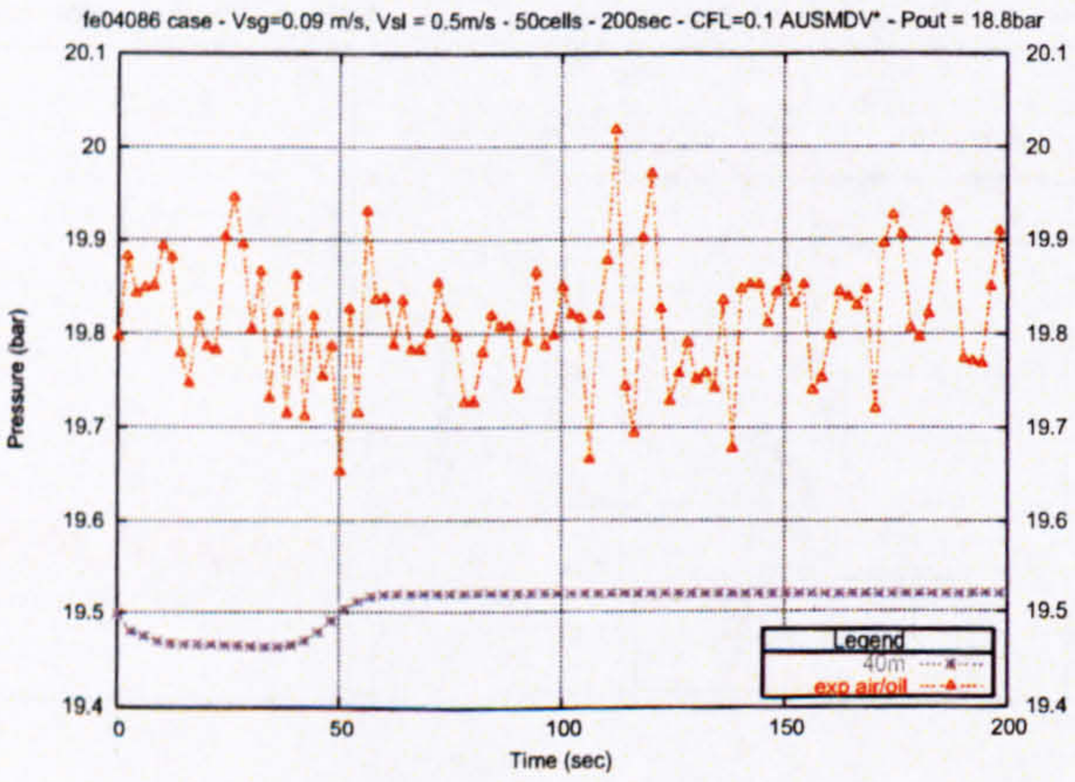

(c) 40m

Figure D.2 : *Trondheim fe04084 test-case - Pressure time profiles.*

	Void fraction	%	V_{sg}	%	V_{sl}	%	P	%
$15.5m$	2.6621×10^{-1}	64	5.8×10^{-5}	≤ 0.1	7.481×10^{-3}	1.5	1.2×10^{-1}	0.5
(last 100s)	2.7031×10^{-1}	65	1.35×10^{-3}	1.4	4.216×10^{-3}	0.8	1.33×10^{-1}	0.6
$21.45m$	7.054×10^{-2}	32	1.68×10^{-3}	1.7	8.632×10^{-3}	1.7	6.25×10^{-1}	3
(last 100s)	7.638×10^{-2}	34	3.5×10^{-4}	0.4	4.182×10^{-3}	0.8	6.36×10^{-1}	3
$40m$	8.068×10^{-2}	33	8.04×10^{-3}	8.4	1.2712×10^{-2}	2.5	3.02×10^{-1}	1.5
(last 100s)	8.873×10^{-2}	37	3.68×10^{-3}	3.8	4.053×10^{-3}	0.9	3.02×10^{-1}	1.5

Table D.1 : *Testcase fe04084 ($V_{sg} = 0.09\, m.s^{-1}$ - $V_{sl} = 0.5\, m.s^{-1}$ - $P_{out} = 18.8\, bar$) - Error between the numerical and the experimental results.*

D.2 Case fe04085

The testcase conditions are:

$$\begin{cases} V_{sg} = 0.18\, m.s^{-1} \\ V_{sl} = 0.5 \times 10^{-3}\, m.s^{-1} \\ P = 18.8\, bar \\ \rho_l^w = 672.6\, kg.m^{-3} \\ \mu_l^w = 0.3 \times 10^{-2}\, kg.(m.s)^{-1} \\ \rho_g^w = 22\, kg.m^{-3} \\ \mu_g = 0.997 \times 10^{-5} \\ \sigma = 0.0141\, N.m^{-1} \end{cases} \tag{D.2}$$

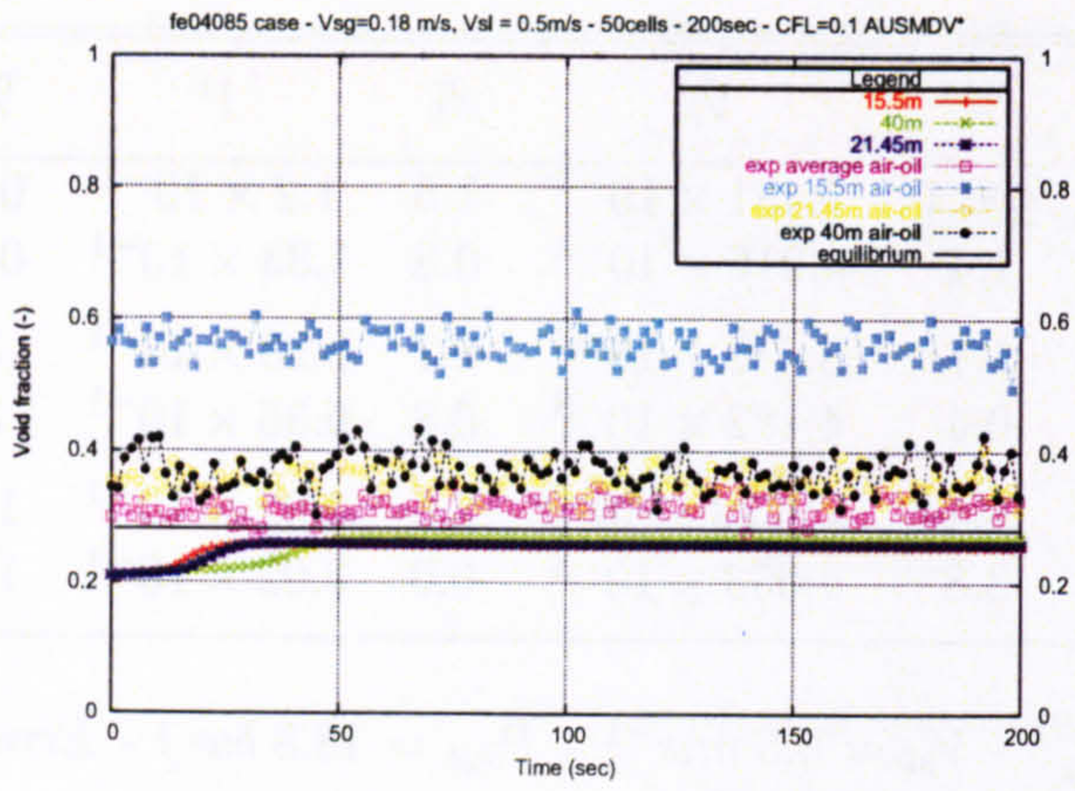

(a) all

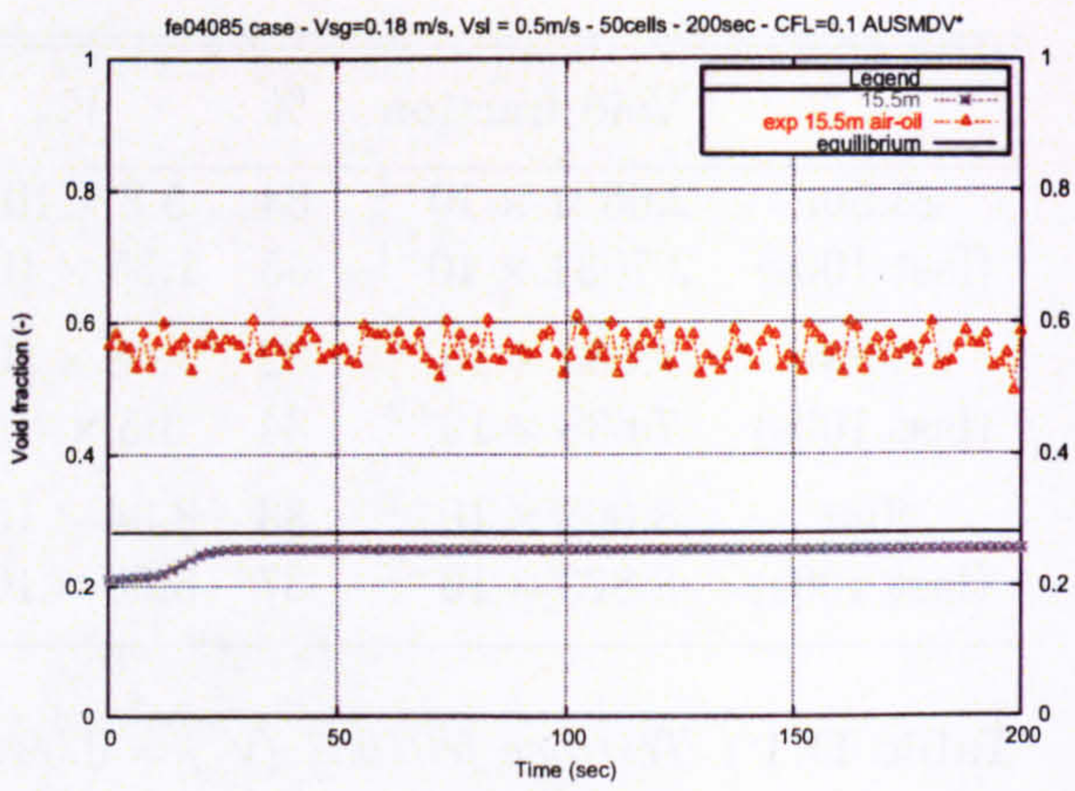

(b) 15.5m

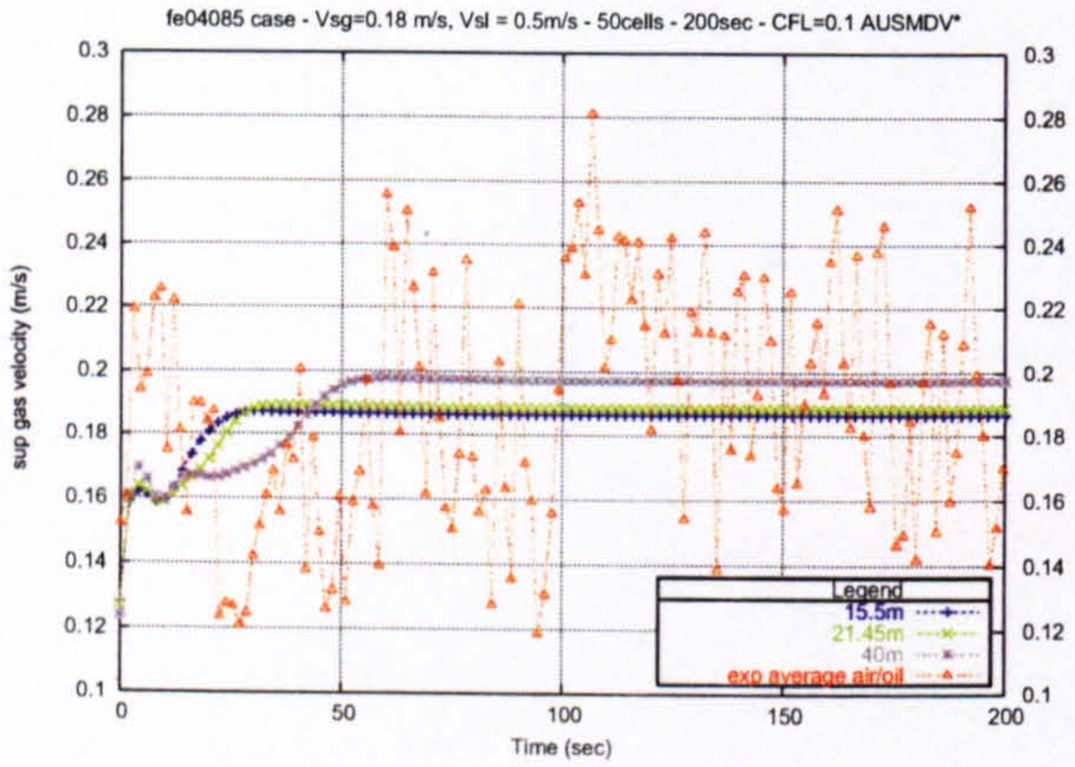

(c) V_{sg}

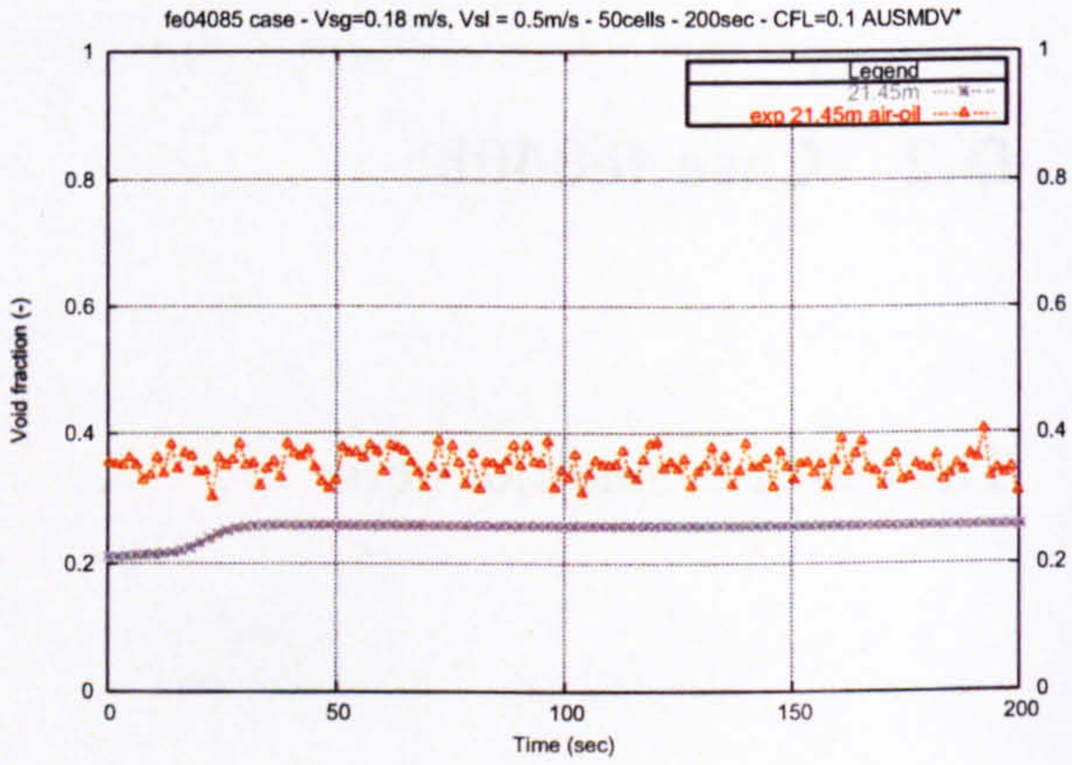

(d) 15.5m

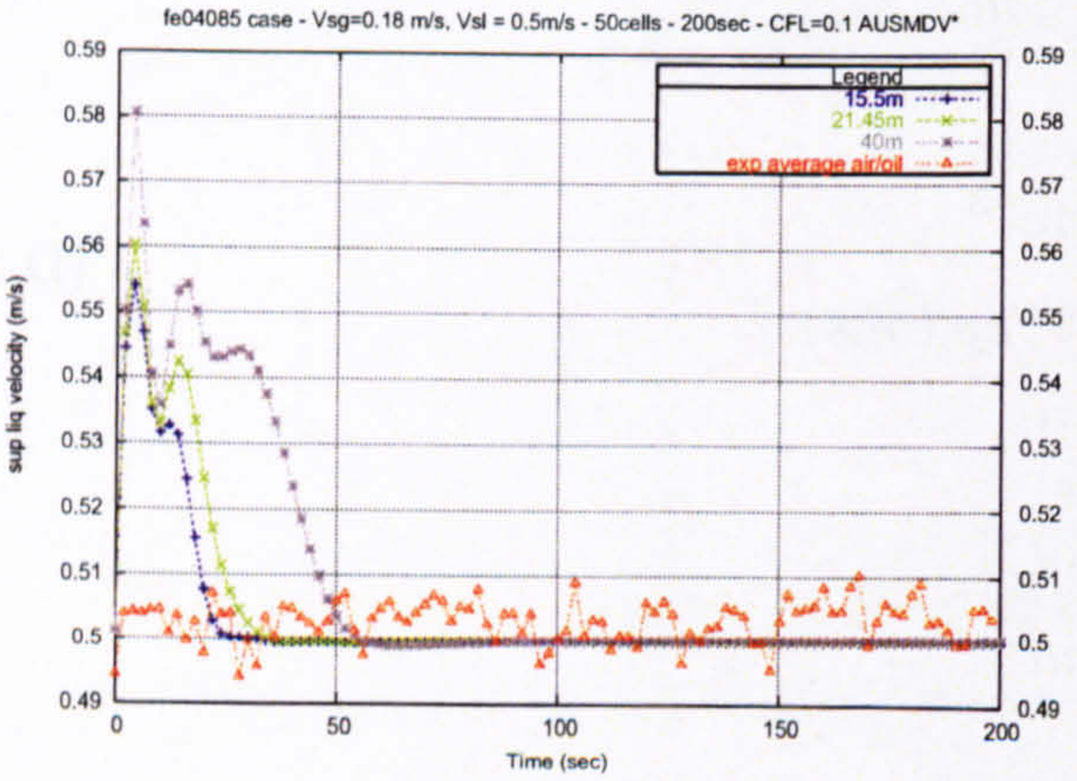

(e) V_{sl}

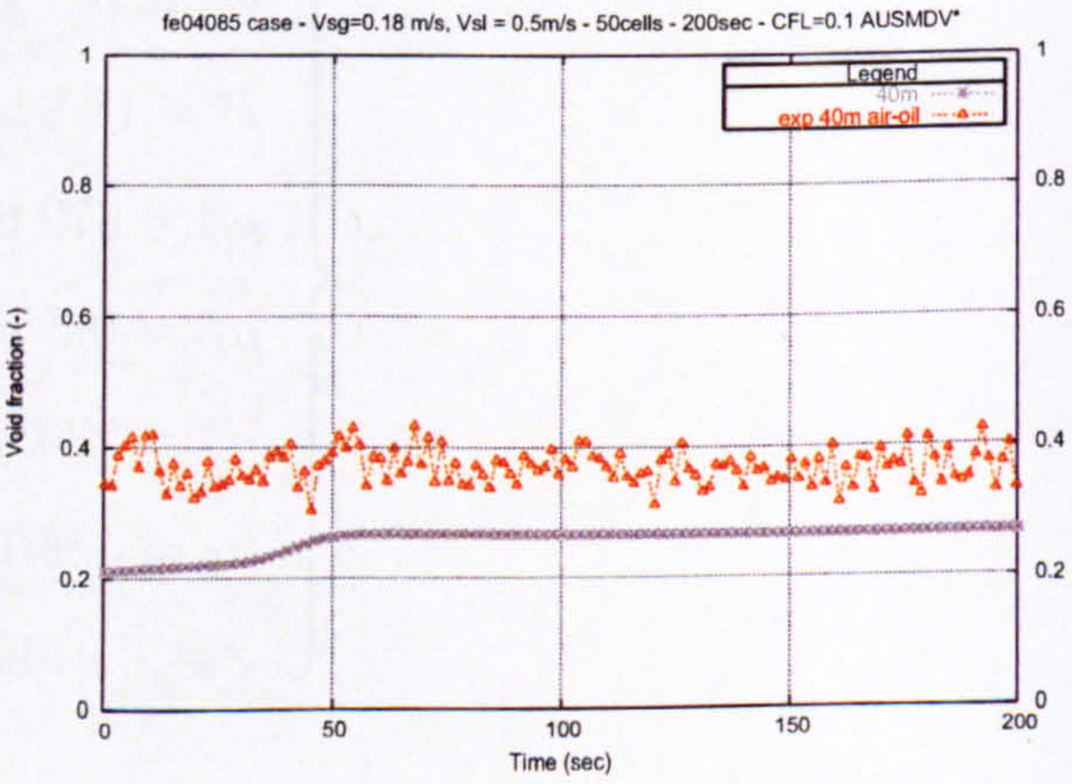

(f) 15.5m

Figure D.3 : *Trondheim fe04085 test-case - Time profiles.*

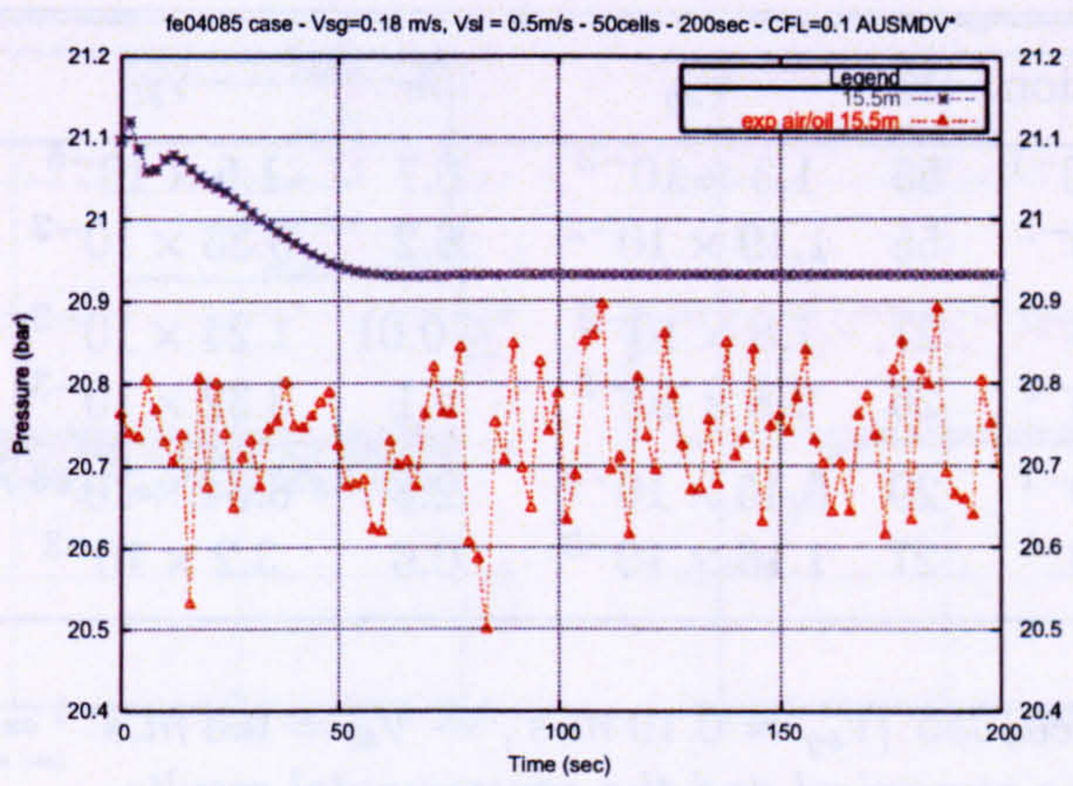

(a) 15.5m

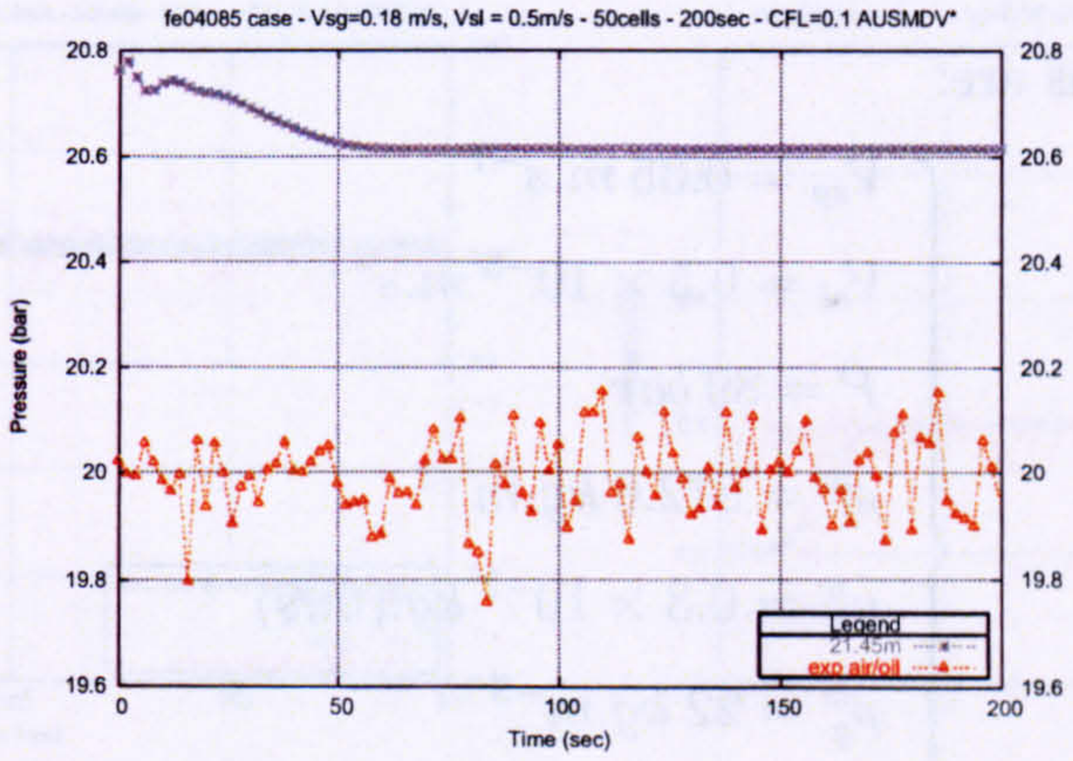

(b) 21.45m

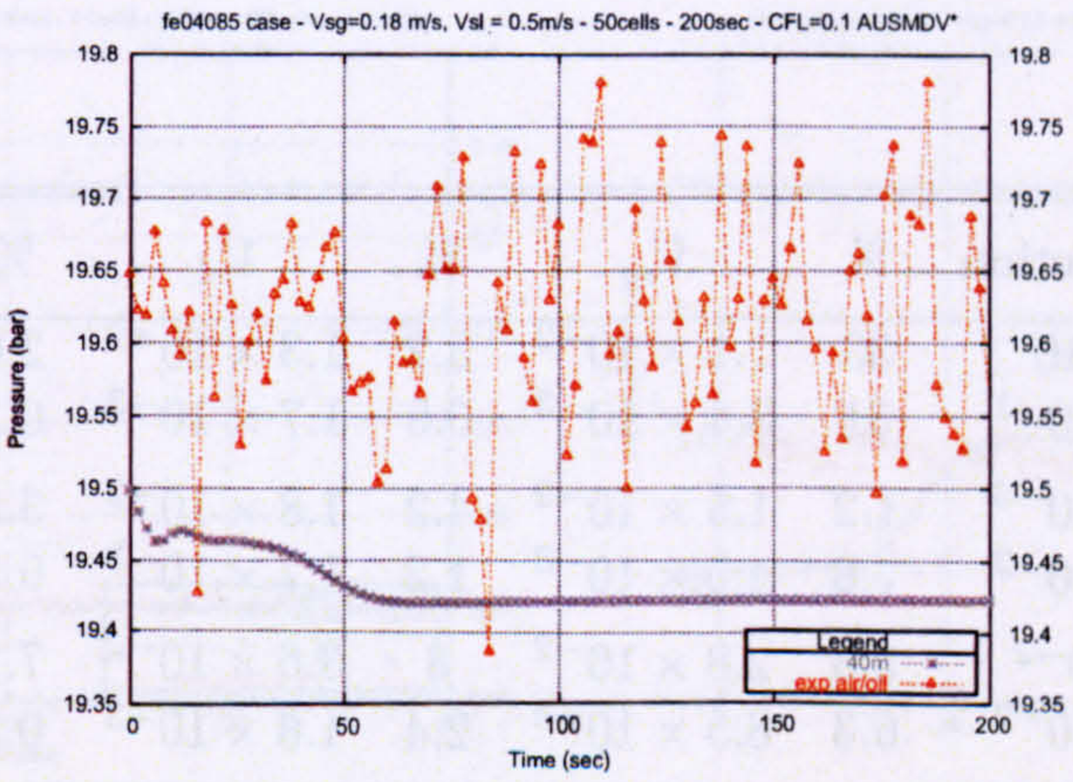

(c) 40m

Figure D.4 : *Trondheim fe04085 test-case - Pressure time profiles.*

	Void fraction	%	V_{sg}	%	V_{sl}	%	P	%
$15.5m$	3.107×10^{-1}	55	1.3×10^{-3}	0.7	1.5×10^{-5}	≤ 0.01	2.18×10^{-1}	1.05
(last 100s)	3.11×10^{-1}	55	1.19×10^{-2}	6.2	3.35×10^{-2}	0.7	2.08×10^{-1}	1.0
$21.45m$	9.63×10^{-2}	27	7.8×10^{-5}	≤ 0.01	1.24×10^{-3}	0.25	6.4×10^{-1}	3.2
(last 100s)	9.28×10^{-2}	26	9.8×10^{-3}	5.1	3.32×10^{-3}	0.66	6.32×10^{-1}	3.1
$40m$	1.08×10^{-1}	29	5.46×10^{-3}	2.8	6.34×10^{-3}	1.2	1.91×10^{-1}	0.9
(last 100s)	1.01×10^{-1}	27	1.16×10^{-3}	0.6	3.2×10^{-3}	0.6	1.88×10^{-1}	0.96

Table D.2 : *Testcase fe04085 ($V_{sg} = 0.19\, m.s^{-1}$ - $V_{sl} = 0.5\, m.s^{-1}$ - $P_{out} = 18.8\, bar$) - Error between the numerical and the experimental results.*

D.3 Case fe04276

The testcase conditions are:

$$\begin{cases} V_{sg} = 0.35\, m.s^{-1} \\ V_{sl} = 0.5 \times 10^{-3}\, m.s^{-1} \\ P = 89\, bar \\ \rho_l^w = 672.6\, kg.m^{-3} \\ \mu_l^w = 0.3 \times 10^{-2}\, kg.(m.s)^{-1} \\ \rho_g^w = 22\, kg.m^{-3} \\ \mu_g = 0.997 \times 10^{-5} \\ \sigma = 0.0141\, N.m^{-1} \end{cases} \tag{D.3}$$

	Void fraction	%	V_{sg}	%	V_{sl}	%	P	%
$15.5m$	1.92×10^{-1}	33	1.1×10^{-2}	3.2	1.3×10^{-2}	2.6	2.2×10^{-1}	0.2
(last 100s)	1.8×10^{-1}	31	3.4×10^{-3}	0.9	1.7×10^{-3}	0.3	1.3×10^{-1}	0.1
$21.45m$	4.8×10^{-3}	1.2	1.5×10^{-2}	4.2	1.8×10^{-2}	3.5	6.9×10^{-1}	0.7
(last 100s)	2.9×10^{-2}	7.6	4.5×10^{-3}	1.2	1.7×10^{-3}	0.3	6.1×10^{-1}	0.7
$40m$	2×10^{-2}	5.3	2.8×10^{-2}	8	3.6×10^{-2}	7.2	4.3×10^{-3}	≤ 0.01
(last 100s)	2.4×10^{-2}	6.3	8.5×10^{-3}	2.4	1.6×10^{-3}	0.3	3.2×10^{-2}	≤ 0.01

Table D.3 : *Testcase fe04276 ($V_{sg} = 0.35\, m.s^{-1}$ - $V_{sl} = 0.5\, m.s^{-1}$ - $P_{out} = 89\, bar$) - Error between the numerical and the experimental results.*

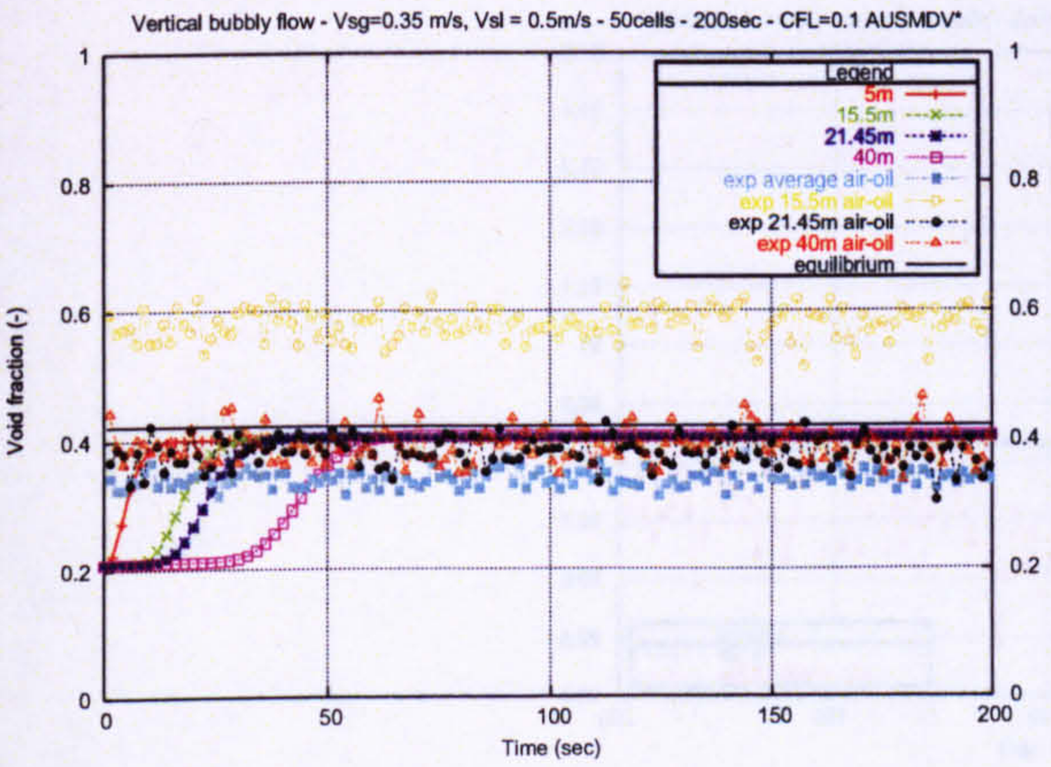

(a) all

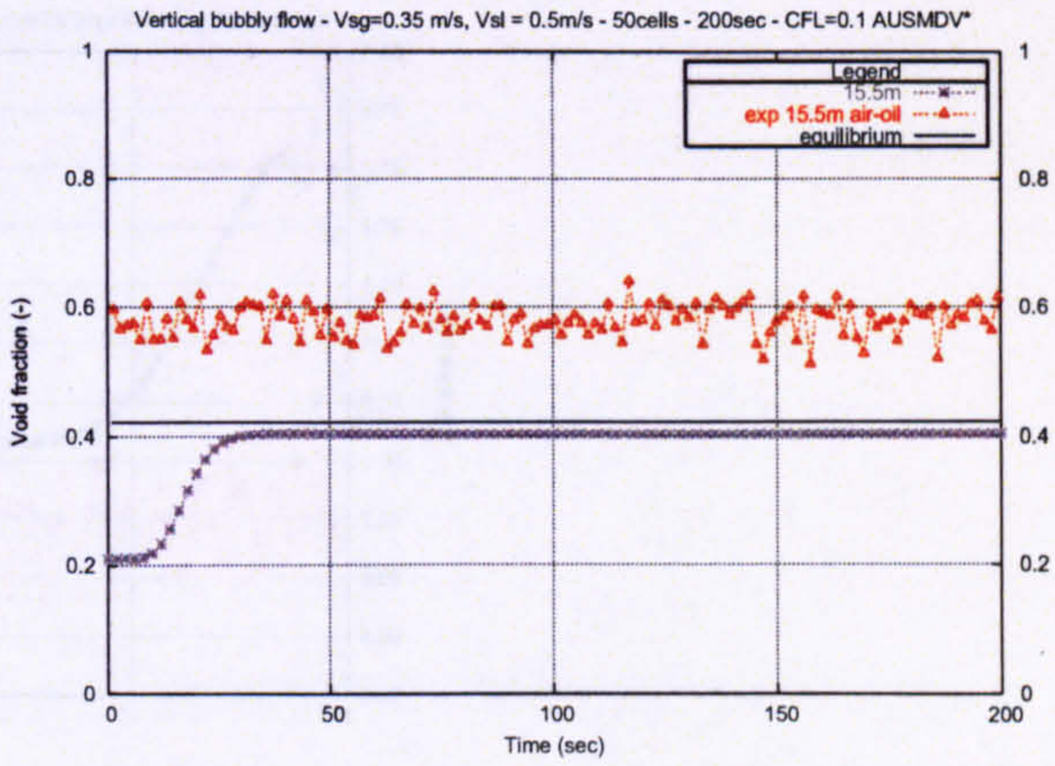

(b) 15.5m

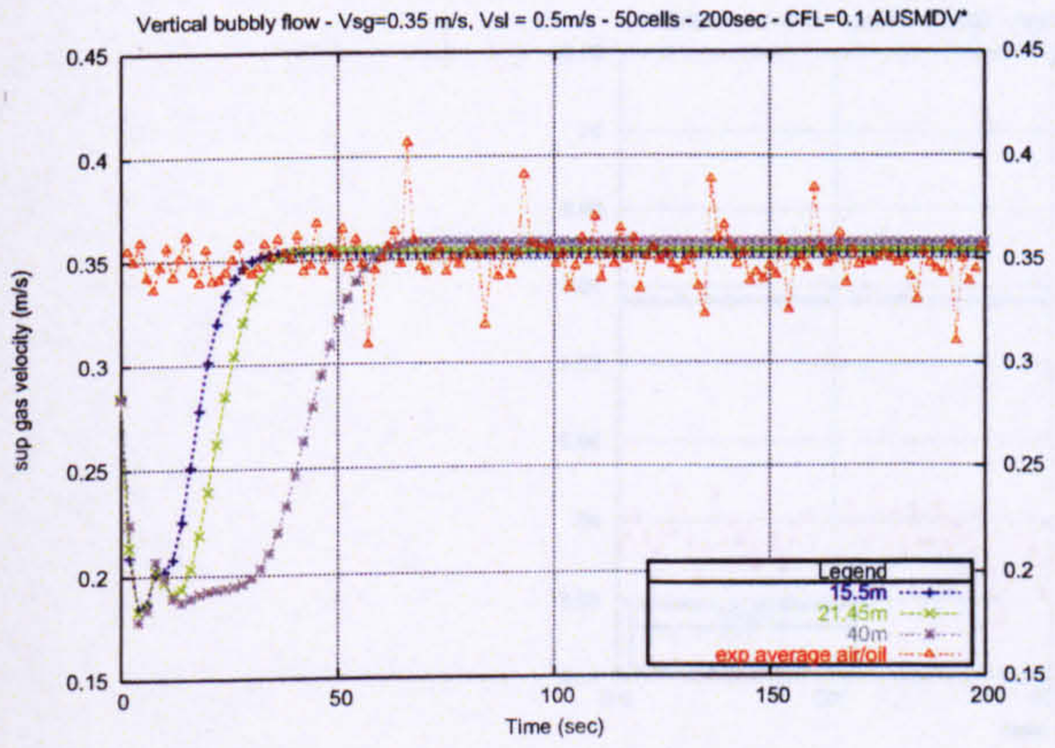

(c) V_{sg}

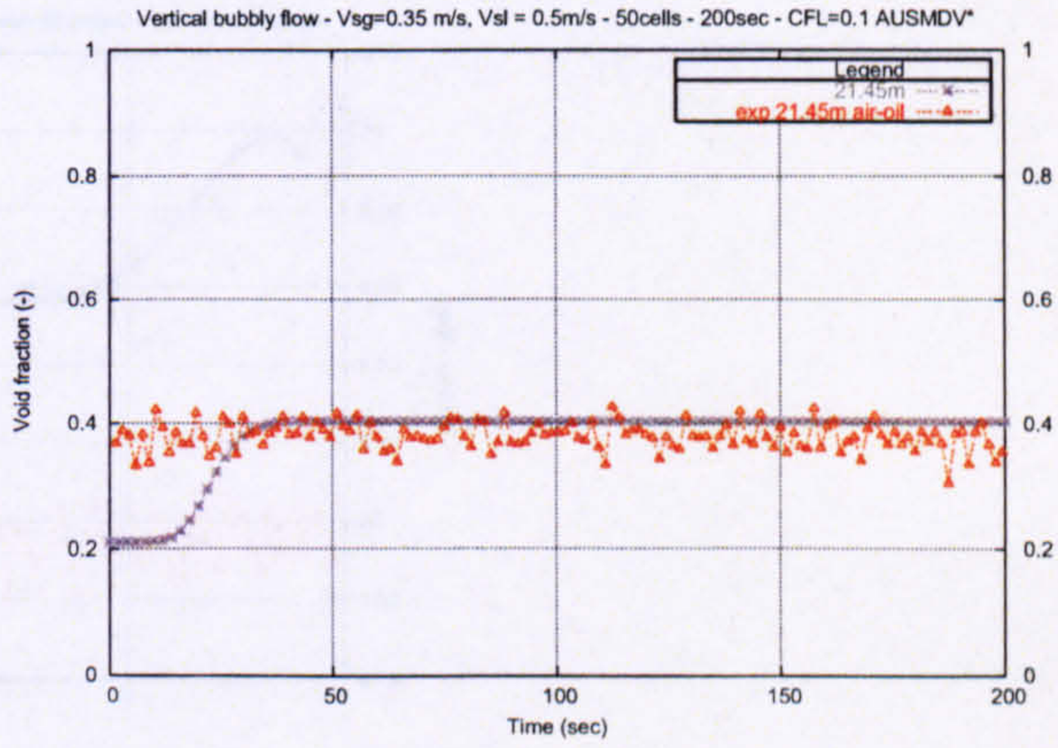

(d) 15.5m

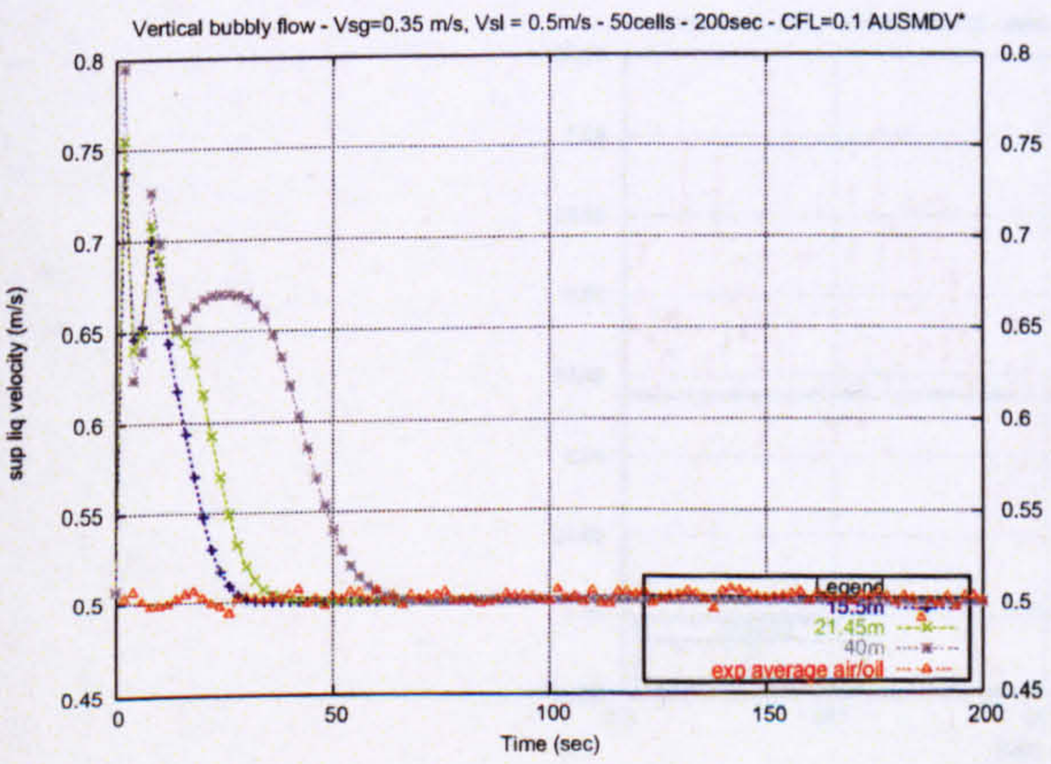

(e) V_{sl}

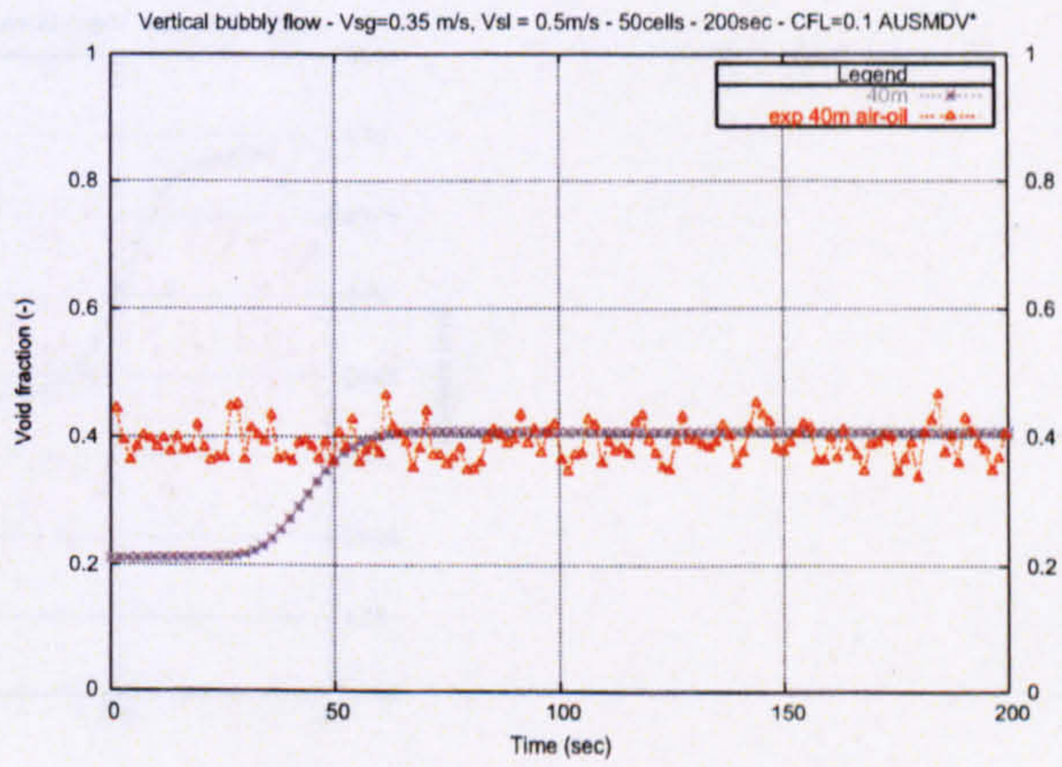

(f) 15.5m

Figure D.5 : *Trondheim fe04276 test-case - Time profiles.*

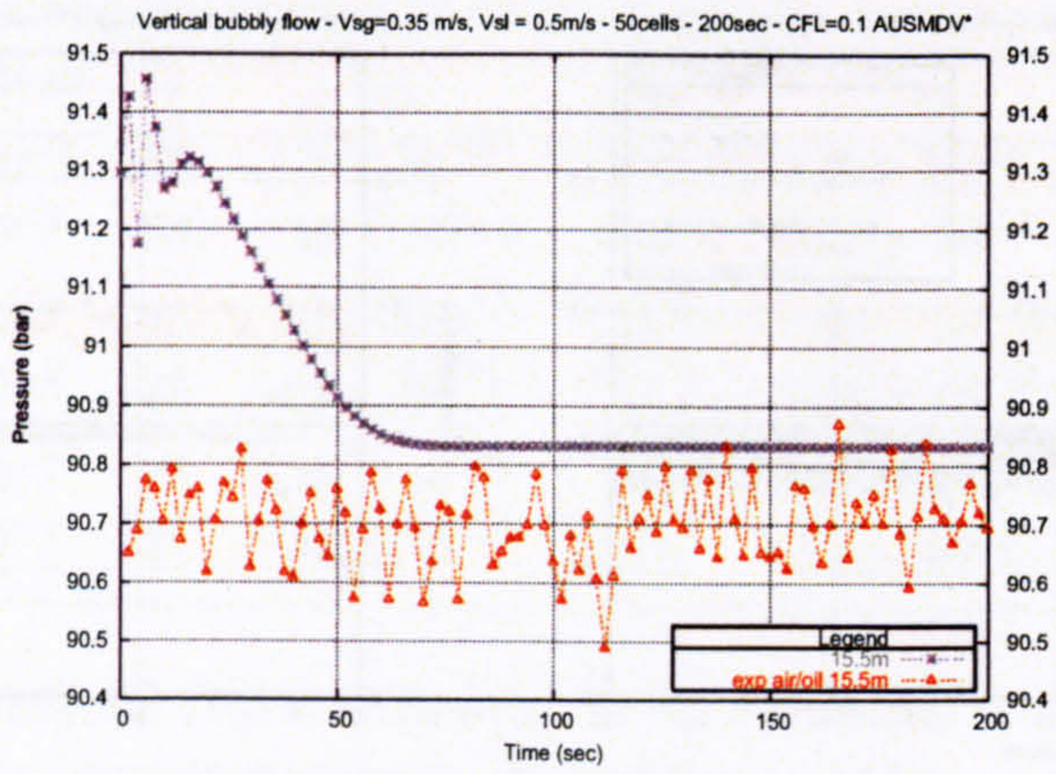

(a) 15.5m

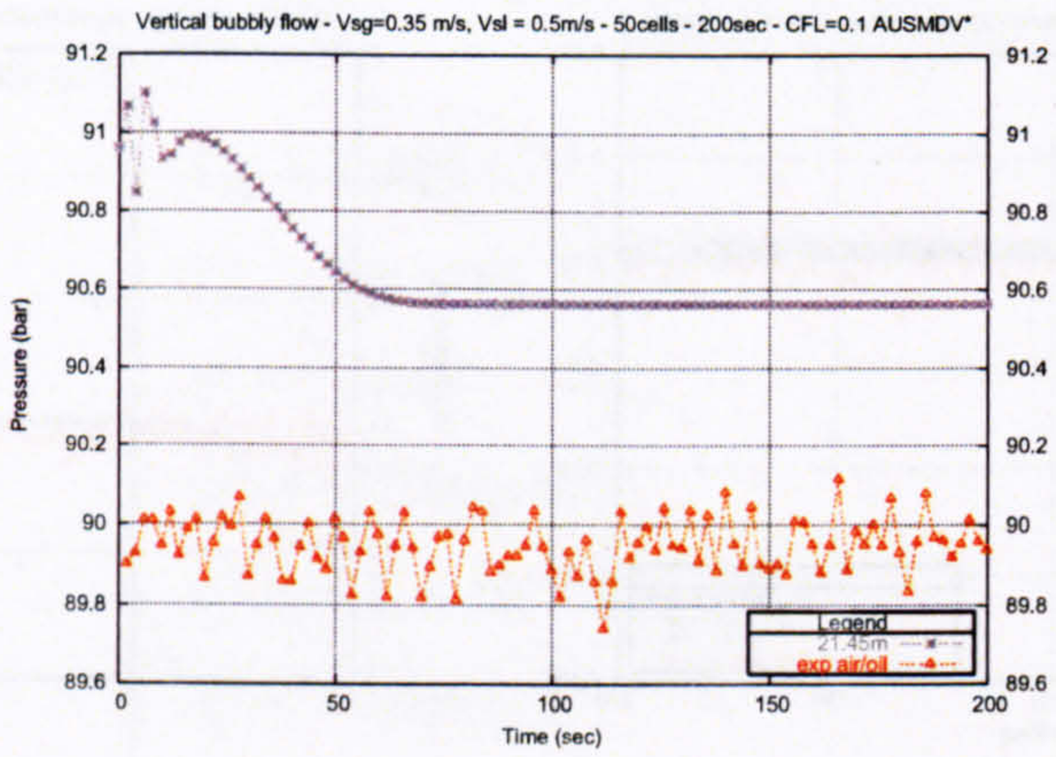

(b) 21.45m

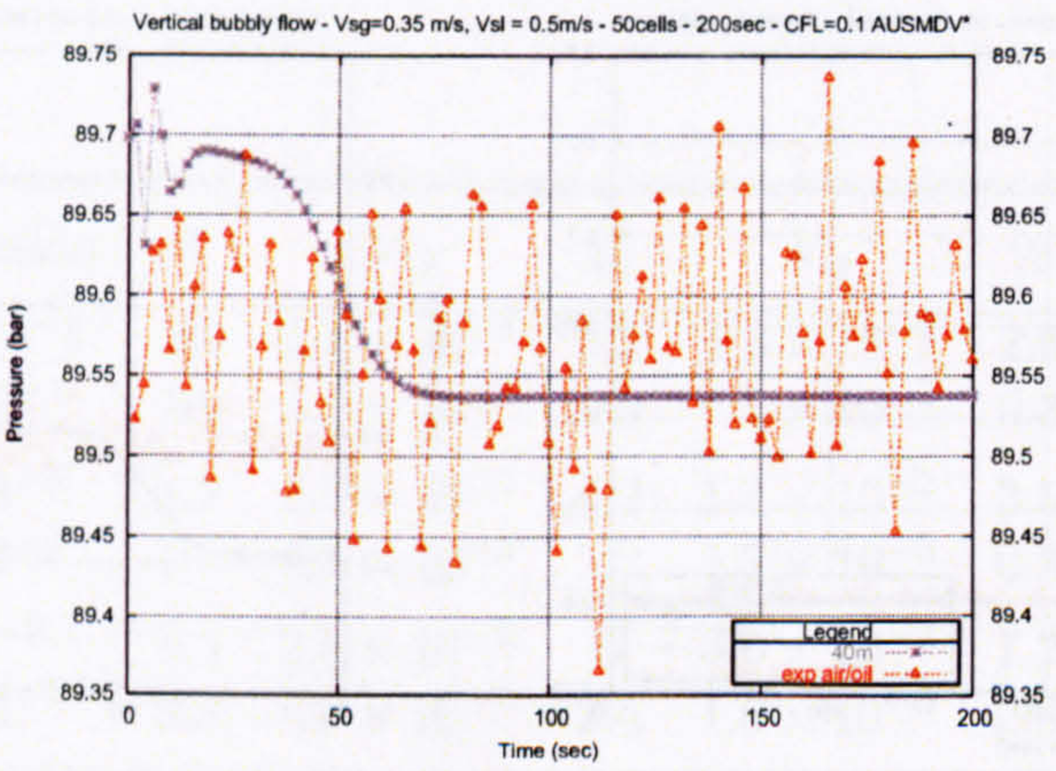

(c) 40m

Figure D.6 : *Trondheim fe04276 test-case - Pressure time profiles.*